

Experimental and analytical analysis of the shear capacity of prestressed steel fibre reinforced concrete beams

Maure De Smedt

Thesis submitted for the degree of
Master of Science in de
Ingenieurwetenschappen:
Bouwkunde, optie Civiele Techniek

Thesis supervisors:

Prof. dr. ir. L. Vandewalle
Dr. ir.-arch. K. De Wilder

Assessors:

Ing. P. van der Zee
Ing. A. Hoekstra

Mentor:

Dr. ir.-arch. K. De Wilder

© Copyright KU Leuven

Without written permission of the thesis supervisors and the author it is forbidden to reproduce or adapt in any form or by any means any part of this publication. Requests for obtaining the right to reproduce or utilize parts of this publication should be addressed to Faculteit Ingenieurswetenschappen, Kasteelpark Arenberg 1 bus 2200, B-3001 Heverlee, +32-16-321350.

A written permission of the thesis supervisors is also required to use the methods, products, schematics and programs described in this work for industrial or commercial use, and for submitting this publication in scientific contests.

Preface

Vijf jaren van hard werken en veel doorzettingsvermogen in de opleiding tot burgerlijk ingenieur bouwkunde worden met deze thesis afgerond. Ik heb deze weg echter niet alleen afgelegd en heb het geluk dat velen mij hierbij steunden, elk op hun manier. Ik wil hen graag allemaal bedanken, met in het bijzonder de volgende personen.

Drie jaar geleden begonnen mijn eerste lessen 'Beton'. Bedankt, professor Lucie Vandewalle, om toen de kiem te leggen voor mijn enthousiasme over het onderwerp en om mij doorheen deze tocht te blijven bijleren en aanmoedigen. Bedankt, Kristof De Wilder, om mij te betrekken in het onderzoek naar staalvezelversterkt beton, voor de degelijke begeleiding met bijhorende kritische bemerkingen en vooral om mij te blijven motiveren. Ik waardeer mijn beide promotoren voor de kans om aan dit onderzoek te werken en voor hun menselijkheid in deze academische wereld.

Het uitvoeren van het experimentele werk had nooit tot een goed einde gebracht kunnen worden zonder het ter beschikking stellen van de proefstukken door de firma Ergon nv, waarvoor dank. Ik ben ook Tom, Jimmy en Stephan van het Laboratorium Reyntjens dankbaar voor hun begeleiding bij de proeven en hun flexibiliteit om altijd te helpen. Daarnaast zorgden Tom en Vincent, mijn medestudenten van het thesisonderwerp, voor een goede samenwerking en het uitwisselen van alle nuttige informatie. Dankzij al deze mannen werden de vele labo-uren een fijne tijd.

Tot slot ben ik mijn ouders, Vake en Moeke, oprecht dankbaar voor alle kansen om deze thesis en mijn studies aan te vatten en succesvol af te ronden. Zonder jullie liefde en ingesteldheid '*Plus est en vous*' was ik niet geworden tot wie ik nu ben. Ook mijn zussen, Mirte en Jente, verdienen een woord van dank voor het verdragen van hun zenuwslopende 'nooit tijd hebbende zus' en mij op de nodige momenten te laten lachen. Daarnaast een dankjewel aan Laurens zijn familie, voor de warmte en de boeiende gesprekken, en aan Laurens zelf, mijn rots in de branding, voor de onvoorwaardelijke steun op letterlijk ieder uur van de dag en de nacht.

Leuven, juni 2016.

Maure De Smedt

Contents

Preface	i
Abstract	vii
Samenvatting	ix
List of Figures and Tables	xi
List of Symbols	xvii
1 Introduction	1
1.1 Problem statement	1
1.2 Focus of the thesis	2
1.3 Outline of the text	3
2 Literature review on shear and SFRC	5
2.1 Introduction	5
2.2 Shear in concrete	6
2.2.1 Background	6
2.2.2 Shear transfer mechanisms	7
2.2.3 Failure modes	11
2.2.4 Influencing parameters	13
2.2.5 Influence of a prestressing force	15
2.2.6 Survey on shear experiments and databases	16
2.2.7 Analytical models	17
2.2.8 Design Code: Eurocode 2	17
2.3 SFRC	20
2.3.1 Background	20
2.3.2 Description of the material	21
2.3.3 Behaviour of the material	23
2.3.4 Identification of the material properties	29
2.4 Shear in SFRC	32
2.4.1 Survey on analytical models and shear experiments of SFRC	32
2.4.2 Design codes or models	33
2.4.3 Design Code: Model Code 2010	39
2.5 Conclusion	42

3	Experimental research	43
3.1	Aims of the research	43
3.2	Experimental specimens	46
3.2.1	Beam design	46
3.2.2	Materials	46
3.2.3	Production process	49
3.3	Material properties identification	51
3.3.1	Mean and characteristic values	52
3.3.2	Cube compressive strength	53
3.3.3	Cylindrical compressive strength	54
3.3.4	Modulus of elasticity	56
3.3.5	Flexural tensile strength	58
3.3.6	Tensile splitting strength	62
3.3.7	Uniaxial tensile strength	65
3.4	Experimental setup	67
3.5	Adopted instrumentation	70
3.5.1	Demountable mechanical strain gauges (DEMEC)	70
3.5.2	LDVTs and optical photoelectric sensor	73
3.5.3	Bragg grated optical fibres (FBG)	76
3.5.4	Stereo-vision digital image correlation (3D-DIC)	79
3.6	Calculation of the load pattern	84
3.7	Results	87
3.7.1	B401	87
3.7.2	B402	89
3.7.3	B403	91
3.7.4	B404	93
3.7.5	B405	95
3.7.6	B406	97
3.7.7	Amount of steel fibres	100
3.8	Conclusion	102
4	Analytical study	103
4.1	Introduction	103
4.2	Parameter study	103
4.2.1	Overview of the main experimental results	104
4.2.2	Influence the amount of steel fibres V_f	106
4.2.3	Influence of the amount of prestressing σ_{p0}	108
4.2.4	Influence of the measured material properties	111
4.2.5	Comparison with shear test results of De Wilder	114
4.3	Discussion of the crack loads	116
4.3.1	Experimentally observed crack loads	116
4.3.2	Comparison with calculated crack loads	117
4.3.3	Comparison with experimentally observed failure loads	118
4.3.4	Calculated crack loads and calculated failure loads	118
4.4	Design Codes of the shear capacity (of SFRC)	120

4.4.1	Eurocode 2	120
4.4.2	Model Code 2010 (A)	121
4.4.3	Discussion	124
4.5	Analytical models of the shear capacity of SFRC	126
4.5.1	DRAMIX Guideline	126
4.5.2	RILEM TC 162-TDF	129
4.5.3	CNR-DT 204/2006	133
4.5.4	Model proposed by Soetens	135
4.5.5	Model Code 2010 (B)	137
4.5.6	General comparison	138
4.6	Conclusion	141
5	Conclusions	143
5.1	General	143
5.2	Recommendations for further research	144
A	List of shear experiments on SFRC beams from literature	149
B	Calculation scheme and additional test results	155
B.1	Calculation of the predicted crack load	155
B.2	Amount of steel fibres	159
	Bibliography	163

Abstract

Steel fibre reinforced concrete (SFRC) is a cementitious composite material, consisting of a concrete matrix with discrete, randomly distributed steel fibres. Its application can be cost- and time-effective by (partially) replacing the conventional reinforcement. Despite the wide research and the continuously increasing structural applications of SFRC, the use is still restricted with respect to its potentials. This is mainly caused by the incomplete understanding of the complex behaviour and the lack of analytical models and international building codes for SFRC structural elements, specifically in the case of shear behaviour.

This research therefore aims to contribute to the understanding of the mechanical shear behaviour of prestressed SFRC beams, based on experimental and analytical investigations. Six beams are subjected to a four-point bending test. The main investigated parameters are (1) steel fibre dosage, (2) the amount of prestressing and (3) the amount of shear reinforcement. Not only failure mode and load are observed, but also shear behaviour is considered by deformations, displacements and cracking pattern properties during the loading. Both conventional measurement devices (i.e. demountable mechanical strain gauges, linear variable differential transformers and optical photoelectric sensor) and advanced optical techniques (Bragg grating optical fibres and stereo-vision digital image correlation) are used. Additionally, material identification tests are performed to characterise the material properties.

The experimentally determined results are analysed by a parameter study and a crack load discussion. Increasing the fibre dosage results in a larger post-cracking behaviour, a more gradual energy dissipation and an increased shear capacity. Increasing the prestress level results in an extended elastic region, a lower inclination of cracks and an increased shear capacity. Furthermore, the failure loads are compared to predictions using analytical models found in Eurocode 2, Model Code 2010, DRAMIX Guideline, RILEM, CNR and the model proposed by Soetens. All calculations of the shear capacity underestimate the actual failure load. The underestimation increases for a higher prestress level. In some models, the influence of a higher fibre dosage is better estimated and vice versa for others. Omitting partial safety factors and using mean material properties, an average experimental-to-predicted failure load ratio of 1.43 was found with a coefficient of variation of 7.2% for Eurocode 2 and Model Code 2010. The other models differ in shear design approach and including parameters, resulting in varying mean experimental-to-predicted ratios and model uncertainties.

Samenvatting

Staalvezelversterkt beton (SFRC) is een cementgebonden composietmateriaal, bestaande uit een betonmatrix met korte, willekeurig verspreide staalvezels. Door de hoge sterkte en duurzaamheid kan het kosten- en tijdbesparend zijn voor het (gedeeltelijk) vervangen van traditionele wapening. Ondanks het vele onderzoek en de toenemende structurele toepassingen van SFRC, is het gebruik ervan nog beperkt ten opzichte van zijn mogelijkheden. Dit wordt voornamelijk veroorzaakt door de onvolledige kennis van het complexe gedrag en het gebrek aan analytische modellen en internationale ontwerpcodes voor SFRC structurele elementen, in het bijzonder voor dwarskracht.

Dit onderzoek beoogt daarom bij te dragen aan het beter begrijpen van het mechanisch gedrag van voorgespannen SFRC balken belast met dwarskracht, steunend op experimenteel en analytisch onderzoek. Zes balken zijn onderworpen aan een vierpuntsbuigproef. De voornaamste onderzochte parameters zijn (1) de hoeveelheid staalvezels, (2) de hoeveelheid voorspanning en (3) de hoeveelheid dwarskrachtwapening. Niet alleen de faalmode en -last zijn geobserveerd, maar ook het gedrag onder dwarskrachtbelasting is beschouwd door middel van vervormings-, verplaatsings- en scheurpatroongegevens tijdens het belasten. Zowel traditionele meettechnieken (zogenaamde *dmountable mechanical strain gauges*, *linear variable differential transformers* and *optical photoelectric sensor*) als geavanceerde optische meettechnieken (zogenaamde *Bragg grated optical fibres* en *stereo-vision digital image correlation*) zijn gebruikt. Daarnaast zijn ook de materiaaleigenschappen bepaald door middel van materiaalproeven.

De experimentele resultaten zijn geanalyseerd op basis van een parameterstudie en een bespreking van de scheurlasten. Een toenemende vezeldosering resulteert in een uitgebreider nascheurgedrag, een meer graduele energiedissipatie en een verhoogde dwarskrachtweerstand. Een toenemende voorspanning resulteert in een uitgebreidere elastische zone, een lagere scheurhelling en een verhoogde dwarskrachtweerstand. Bovendien zijn de faallasten vergeleken met analytische voorspellingen volgens Eurocode 2, Model Code 2010, DRAMIX Richtlijn, RILEM, CNR en het model ontwikkeld door Soetens. Alle berekende dwarskrachtcapaciteiten onderschatten de werkelijke faallast. Deze onderschatting neemt toe bij een grotere voorspanning. Voor sommige modellen is het effect van meer vezels beter ingerekend, voor de anderen is het net omgekeerd. Bij het weglaten van de partiële veiligheidsfactoren en het gebruik van gemiddelde materiaalparameters is de gemiddelde verhouding van

experimentele tot voorspelde faallast gelijk aan 1,43 met een coëfficiënt van variatie van 7,2%, voor Eurocode 2 en Model Code 2010. De andere modellen verschillen in het ontwerp van de dwarskrachtweerstand en het inrekenen van beïnvloedende parameters, resulterend in een variërende gemiddelde verhouding van experimentele tot voorspelde faallast en modelonzekerheden.

List of Figures and Tables

List of Figures

2.1	Internal forces on an elementary part.	6
2.2	Schematic representation of the aggregate interlock [72].	8
2.3	Overview of the failure modes due to dowel action [32].	9
2.4	Different arch development for point loads and distributed loads [32].	10
2.5	Truss analogy of Ritter [53] and Morsch [35]. Tension is denoted with solid lines and compression with dashed lines. C denotes a compressive force, T a tensile force and z the internal lever arm. [13]	11
2.6	Schematic representation of different failure modes. C denotes a compressive force and T a tensile force (adapted from [13]).	12
2.7	Different shapes and types of steel fibres (adapted from [30,37]).	22
2.8	Schematic representation of the pull-out response of a hooked-end fibre by Pompo [46].	24
2.9	Schematic representation of the pull-out response of a hooked-end and straight fibre by Löfgren [30].	24
2.10	Schematic representation of the behaviour of FRC and plain concrete in compression (HSC is high-strength concrete, NSC normal concrete strength) [19,30].	26
2.11	Different failure mechanisms of steel fibres embedded in a concrete matrix (adapted from [58]).	27
2.12	Tensile behaviour of SFRC: (left) softening and (right) hardening, where P_{cr} indicates the crack load [19].	27
2.13	Simplified post-cracking constitutive laws (continuous and dashed lines refer to softening and hardening behaviour respectively) [19].	28
2.14	Experimental setup of EN 14651 (dimensions in mm) [19].	30
2.15	Typical load- $CMOD$ curve, in black for SFRC and in grey for plain concrete [19].	31
2.16	Other load- $CMOD$ curves for SFRC with indication of the maximum load in the defined interval [9].	31
2.17	Inclination of the shear cracks in function of the amount of prestressing according to different analytical models (with $f_{ck} = 50$ MPa and the geometrical properties of the experimentally tested specimens).	38

LIST OF FIGURES AND TABLES

3.1	Schematic overview of the experimental research, classified according to the amount of prestressing (σ_{p0}), with ($\rho_w \neq 0$) or without ($\rho_w = 0$) shear reinforcement, the amount of steel fibres V_f and with their name (B40x).	44
3.2	Flowchart of the experimental research. The numbers in blue correspond to the sections in which these parts are described.	45
3.3	Longitudinal view of the experimental specimens (note: SFRC specimens are shaded grey; units in mm; DEMEC points are indicated with \circ).	47
3.4	Cross sections and reinforcement layout of the experimental specimens (note: SFRC specimens are shaded grey; units in mm).	47
3.5	Configuration of the two lines and three concrete mixtures of the production process.	50
3.6	Four steps of the production process.	50
3.7	Experimental setup for testing of the cubes, cylinders and prisms to determine hardened material properties.	52
3.8	Experimental results of the cube compressive strength for three cubes per beam. The red dotted line indicates the mean value for each beam.	54
3.9	Experimental results of the cylindrical compressive strength for three cylinders per beam. The red dotted line indicates the mean value for each beam.	55
3.10	Comparison of the experimentally obtained mean values of the cube and cylindrical compressive strength per beam. The black lines indicates the standard deviation for each beam.	55
3.11	Experimental results of the modulus of elasticity for three cylinders per beam. The red dotted line indicates the mean value for each beam.	57
3.12	Experimental results of the flexural tensile strength for three prisms per beam. The red dotted line indicates the mean value for each beam.	59
3.13	Experimentally obtained $CMOD - \sigma$ curves for the beams with steel fibres. (Note: mean residual flexural tensile strengths at $CMOD$ equal to 0.5, 1.5, 2.5 and 3.5 mm are indicated with \circ .)	60
3.14	Comparison of the experimentally obtained mean values of the flexural tensile and tensile splitting strength per beam. The black lines indicates the standard deviation for each beam.	64
3.15	Experimental results of the tensile splitting strength for six half prisms per beam. The red dotted line indicates the mean value for each beam.	64
3.16	Uniaxial tensile strength per beam. The black lines indicates the standard deviation for each beam.	66
3.17	Experimental setup for the test specimens.	68
3.18	Schematic representation of the experimental setup.	68
3.19	Safety measures during testing.	69
3.20	Cyclic loading pattern with V_{cr} indicating the first cracking load (example for beam B405).	69
3.21	Schematic representation of the experimental setup (front view) with indication of the measurement methods LVDT, OPT and DIC.	71

3.22	Schematic representation of the experimental setup (back view) with indication of the Bragg grating optical fibre: location of the adopted optical fibres OPTFIB1 and OPTFIB2, mechanical fixing points (■) and Bragg gratings (FBG).	71
3.23	Half of a beam with indication of the DEMEC point by \circ , with notations and distances.	71
3.24	Different aspects of the DEMEC measurement method.	74
3.25	Pictures of the left and right LVDTs and the optical photoelectric sensor, before the loading procedure.	74
3.26	Strains (\circ) between the day of removal of the formwork (DEMEC 1) and the day of full-scale testing (DEMEC 5), with first order polynomial fit (-) and 95% prediction interval (dotted line).	75
3.27	Anchorage and covering of Bragg grating optical fibres (B404).	76
3.28	Measured strains in bottom (left) and top (right) flange with Bragg grating optical fibres for the first loading cycle of beam B404 (up to 53 kN).	78
3.29	Measured strains in bottom (left) and top (right) flange with Bragg grating optical fibres for the fourth loading cycle of beam B404 (up to 132 kN).	78
3.30	Measured strains in top flange with Bragg grating optical fibres for the fifth loading cycle of beam B404 (up to 145 kN).	78
3.31	Different steps of applying the speckle pattern for DIC measurements.	81
3.32	Different parts of the setup of the DIC systems.	82
3.33	Examples of calibration images of B401.	82
3.34	Reconstructed surface geometry from the DIC measurement of the left side of beam B401 before loading ($V = 0$ kN).	83
3.35	Typically obtained results from DIC: horizontal ($u(x, y)$) and vertical ($v(x, y)$) displacement field of the left side of beam B401 at load $V = 236$ kN.	83
3.36	Predicted and applied loading pattern (example of beam B405).	85
3.37	Retained stress level in the strands (\circ) between the day of removal of the formwork and the day of full-scale testing, with first order polynomial fit (-) and 95% prediction interval (dotted line).	86
3.38	Applied loading pattern and observed load-displacement curve (at location of the loading point) of B401.	88
3.39	Different parts of the failure of beam B401.	88
3.40	Applied loading pattern and observed load-displacement curve (at location of the loading point) of B402.	90
3.41	Different parts of the failure of beam B402.	90
3.42	Applied loading pattern and observed load-displacement curve (at location of the loading point) of B403.	92
3.43	Different parts of the failure of beam B403.	92
3.44	Applied loading pattern and observed load-displacement curve (at location of the loading point) of B404.	94
3.45	Different parts of the failure of beam B404.	94

3.46	Applied loading pattern and observed load-displacement curve (at location of the loading point) of B405.	96
3.47	Different parts of the failure of beam B405.	96
3.48	Applied loading pattern and observed load-displacement curve (at location of the loading point) of B406.	98
3.49	Different parts of the failure of beam B406.	98
3.50	Cracking patterns at failure of the three beams, view on the frontside.	99
3.51	Cracking patterns at failure of the SFRC beams, view on the backside.	99
3.52	Schematic view of the amount of fibres per surface area (in $1/\text{cm}^2$), measured at cores crossing the crack planes.	101
4.1	(Refer to Figure 3.1) Reminder of the tested beams, classified according to their parameters and with their name (B40x).	104
4.2	Experimentally obtained load-displacement curves (at location of the loading point) of the tested beams.	105
4.3	Experimentally obtained failure loads of the six tested beams.	106
4.4	The amount of fibres influences the number of cracks and the ductility of the failure.	107
4.5	The amount of prestressing influences the inclination of the cracks and the ductility of the failure.	110
4.6	The amount of prestressing influences the width of the cracks (top figures), measured by placing virtual extensometers over the crack in the DIC measurements (bottom figures).	110
4.7	Influence of the experimentally obtained cylindrical compressive strength on the measured failure loads.	112
4.8	Influence of the experimentally obtained modulus of elasticity on the measured failure loads.	112
4.9	Influence of the experimentally obtained uniaxial tensile strength on the measured failure loads.	113
4.10	Influence of the experimentally obtained residual tensile strength at $CMOD_3 = 2.5$ mm on the measured failure loads.	113
4.11	Overview of the experimentally obtained failure loads of some tested beams (blue) and some shear test results of De Wilder [13] (green).	115
4.12	Experimentally obtained crack loads of the six tested beams.	116
4.13	Experimental failure loads compared to the analytical predictions according to MC2010A.	123
4.14	Experimental failure loads compared to the analytical predictions according to EC2/MC2010.	125
4.15	Experimental failure loads compared to the analytical predictions according to the DRAMIX Guideline.	128
4.16	Experimental failure loads compared to the analytical predictions according to RILEM.	131
4.17	Experimental failure loads compared to the analytical predictions according to RILEM - a/d refinement.	132

4.18	Experimental failure loads compared to the analytical predictions according to CNR.	134
4.19	Experimental failure loads compared to the analytical predictions according to the model proposed by Soetens.	136
4.20	Experimental failure loads compared to the analytical predictions according to the different analytical models of the shear capacity of SFRC.	140
B.1	Template to calculate the predicted crack load (blue fields have to be filled in, white fields are fixed values and grey fields are calculated by the formulas).	158
B.2	Location of the drilled cores for B402.	161
B.3	Location of the drilled cores for B403.	161
B.4	Location of the drilled cores for B405.	162
B.5	Location of the drilled cores for B406.	162

List of Tables

2.1	Overview of the main influencing parameters per shear transfer mechanism (adapted from [13]).	13
3.1	Overview of the experimental program and the investigated parameters.	48
3.2	Concrete mixture composition of the experimental specimens.	48
3.3	Reinforcement properties of the experimental specimens [13].	49
3.4	Experimentally determined material properties of the (SFR)C mixtures.	51
3.5	Experimentally determined mean residual tensile strengths of the SFRC.	61
3.6	Characteristic residual tensile strengths and verification of the requirements according to Model Code 2010 (MC2010), based on Normal and log-normal distribution.	62
3.7	Experimentally determined mean tensile splitting strength of B401, B402 and B404.	63
3.8	Calculated mean uniaxial tensile strengths, based on flexural tensile and tensile splitting strength.	66
3.9	Predicted crack loads.	84
3.10	Main results of B401.	87
3.11	Main results of B402.	89
3.12	Main results of B403.	91
3.13	Main results of B404.	93
3.14	Main results of B405.	95
3.15	Main results of B406.	97
4.1	Overview of the experimental program and the investigated parameters.	106
4.2	Comparison of some tested beams and some shear test results of De Wilder [13].	115
4.3	Experimental crack load and crack mode compared with calculations.	118

LIST OF FIGURES AND TABLES

4.4	Experimental crack load and crack mode compared with the failure load and mode.	119
4.5	Calculated crack load compared with the calculated failure load.	119
4.6	Experimental failure loads compared to the analytical predictions according to EC2.	121
4.7	Experimental failure loads compared to the analytical predictions according to CNR.	123
4.8	Experimental failure loads compared to the analytical predictions according to EC2/MC2010.	125
4.9	Experimental failure loads compared to the analytical predictions according to the DRAMIX Guideline.	128
4.10	Experimental failure loads compared to the analytical predictions according to RILEM.	131
4.11	Experimental failure loads compared to the analytical predictions according to RILEM - a/d refinement.	132
4.12	Experimental failure loads compared to the analytical predictions according to CNR.	134
4.13	Experimental failure loads compared to the analytical predictions according to the model proposed by Soetens.	136
4.14	Comparison of the different analytical shear capacity models for SFRC.	140
B.1	Amount of steel fibres for drilled cores of B402, B403, B405 and B406.	160

List of Symbols

Following list gives an overview of the most commonly used symbols and abbreviations in the text.

Test specimen properties

a	Shear span
a/d	Shear span-to-effective depth ratio
A	Cross sectional area
A_c	Cross sectional area of concrete
A_f	Cross sectional area of a steel fibre
A_s	Cross sectional area of steel
A_{sl}	Cross sectional area of the longitudinal reinforcement
A_{sw}	Cross sectional area of the shear reinforcement
A_{sw}/s	Area of the shear reinforcement per unit length
A_p	Cross sectional area of the prestressing strands
b	Width of a cross-section
$b(y)$	Width of a cross-section at height y
b_w	Web width of the specimen
d	Effective depth of the specimen
d_g	Maximum aggregate size
d_f	Nominal diameter of the steel fibres
d_s	Nominal diameter of the conventional reinforcement
d_p	Nominal diameter of the prestressing reinforcement
D_{max}	Diameter of the largest aggregate
e_p	Distance between the neutral axis and the prestressing reinforcement
F	Fibre factor
h	Height of the specimen
h_f	Flange height of the specimen
h_{sp}	Remaining height at location of the notch
I	Second moment of area
L	Length of the specimen

LIST OF SYMBOLS

L_f	Length of a steel fibre
N_f	Number of steel fibres
s	Spacing (e.g. between steel fibres or reinforcement)
S	First moment of area
V_f	Fibre dosage
z	Internal lever arm

λ_f	Aspect ratio of the steel fibres
ρ_f	Fibre reinforcement ratio
ρ_l	Longitudinal reinforcement ratio
ρ_w	Shear reinforcement ratio
σ_{p0}	Initial stress in the prestressing steel
σ_{cp}	Compressive stress from a prestressing force

Material properties

E_{cm}	Mean secant modulus of elasticity of concrete
$E_{c\infty}$	Mean tangent modulus of elasticity of concrete
E_s	Modulus of elasticity of reinforcing steel
E_p	Modulus of elasticity of prestressing steel
f_c	Concrete cylindrical compressive strength
f_{cd}	Design value of the cylindrical compressive strength
f_{ck}	Characteristic value of the cylindrical compressive strength
f_{cm}	Mean value of the cylindrical compressive strength
$f_{c,cube}$	Concrete cube compressive strength
$f_{cm,cube}$	Mean value of the cube compressive strength
f_{ctd}	Design value of the uniaxial tensile strength
f_{ctk}	Characteristic value of the uniaxial tensile strength
$f_{ctk,ax}$	Characteristic value of the uniaxial tensile strength
f_{ctm}	Mean value of the uniaxial tensile strength
$f_{ct,fl}$	Flexural tensile strength
$f_{ctk,fl}$	Characteristic value of the flexural tensile strength
$f_{ctm,fl}$	Mean value of the flexural tensile strength
$f_{ct,sp}$	Tensile splitting strength
$f_{ctm,sp}$	Mean value of tensile splitting strength
$f_{p0.1m}$	Mean value of the 0.1% proof stress of prestressing reinforcement
f_{pm}	Mean value of the ultimate tensile strength of prestressing reinforcement
f_{tm}	Mean value of the ultimate tensile strength of reinforcing steel
f_{yd}	Design value of the yield strength of reinforcing steel
f_{yk}	Characteristic value of the yield strength of reinforcing steel
f_{ym}	Mean value of the yield strength of reinforcing steel

f_{ywd}	Design value of the yield strength of shear reinforcement
f_{ywm}	Mean value of the yield strength of shear reinforcement
$f_{R,j}$	Residual flexural tensile strength of fibre reinforced concrete corresponding to $CMOD_j$ ($j = 0.5 - 3.5$ mm)
$f_{Rk,j}$	Characteristic value of the residual flexural tensile strength of fibre reinforced concrete corresponding to $CMOD_j$ ($j = 0.5 - 3.5$ mm)
$f_{Rm,j}$	Mean value of the residual flexural tensile strength of fibre reinforced concrete corresponding to $CMOD_j$ ($j = 0.5 - 3.5$ mm)
f_{Ftu}	Ultimate residual strength (post-cracking strength for ultimate crack opening) for fibre reinforced concrete
f_{Ftuk}	Characteristic value of the post-cracking strength for ultimate crack opening for fibre reinforced concrete
f_{Ftum}	Mean value of the post-cracking strength for ultimate crack opening for fibre reinforced concrete
α	Coefficient of thermal expansion
α_{fl}	Conversion factor for the uniaxial tensile strength based on the flexural tensile strength
α_{sp}	Conversion factor for the uniaxial tensile strength based on the tensile splitting strength
ϵ_{su}	Strain at failure of the conventional reinforcement
ϵ_{pu}	Strain at failure of the prestressing reinforcement
ν	Poisson's ratio
ρ_m	Mean density

Analytical modelling

C	Compressive force
F_p	Prestressing force
k	Size effect factor
k_{dg}	Influence factor for the aggregate size
k_f	Influence factor for the effect of flanges on the shear capacity
M	Bending moment
M_{Ed}	Design value of the applied bending moment
N_{Ed}	Design value of the applied normal force
P	An applied load
P_d	Debonding load
P_m	Maximum pull-out force
R_t	Influence factor for the fibre properties
R^2	Coefficient of determination
s	Standard deviation

LIST OF SYMBOLS

T	Tensile force
V	Shear force
V_{cd}	Design value of the concrete contribution to the shear resistance
V_{cr}	First cracking load
$V_{cr,bending}$	First cracking load due to bending
$V_{cr,w}$	First cracking load due to shear
V_{Ed}	Design value of the applied shear force
V_{fd}	Design value of the steel fibre reinforcement contribution to the shear resistance
V_{Rd}	Design value of the shear resistance
$V_{Rd,c}$	Design value of the shear resistance of a member without shear reinforcement
$V_{Rd,max}$	Design value of the maximum shear resistance of a member
$V_{Rd,s}$	Design value of the shear resistance of a member with shear reinforcement
$V_{u,exp}$	Experimental failure load
$V_{u,pred}$	Predicted failure load
V_{wd}	Design value of the shear reinforcement contribution to the shear resistance
w	Crack width
w_u	Ultimate crack opening
x	Height of the compression zone
δ	Deflection
ϵ_x	Longitudinal strain at mid-depth of the effective depth
γ_i	Safety factor for material i (c stands for concrete, F for the steel fibres)
θ	Angle between the compression strut and the beam axis perpendicular to the shear force
σ_f	Crack interface normal stress
τ	Shear stress
τ_f	Crack interface shear stress
τ_{fd}	Design shear stress capacity due to fibres
Φ	Influence of the steel fibre dosage on the shear capacity

Abbreviations

ACI	American Concrete Institute
ANB	Belgian National Application Document
ASCE	American Society of Civil Engineering
CCD	Charge-Coupled Device
CMOD	Crack Mouth Opening Displacement
CNR	Italian National Research Council
COV	Coefficient of Variation
DAfStb	Deutscher Ausschuss für Stahlbeton
DEMEC	Demountable Mechanical strain gauge
DIC	Digital Image Correlation
EC2	Eurocode 2
FBG	Bragg grating optical fibre
<i>fib</i>	Fédération Internationale du Béton
FRC	Fibre Reinforced Concrete
LOP	Limit of Proportionality
LVDT	Linear Variable Differential Transformer
OPT	Optical Photoelectric sensor
MC2010	Model Code 2010
SFRC	Steel Fibre Reinforced Concrete

Chapter 1

Introduction

1.1 Problem statement

Steel fibre reinforced concrete, further denoted as SFRC, is a cementitious composite material, consisting of a concrete matrix with discrete, randomly distributed steel fibres. SFRC is characterised by an enhanced post-cracking tensile residual strength due to the bridging of crack surfaces by the fibres. Advantages such as an improved ductility, a higher energy absorption capacity and an increased flexural strength, depending on the fibre content and the aspect ratio, are generally accepted nowadays. On the other hand, the increased material cost for fibres and high strength concrete has also to be taken in account.

However, the use of SFRC can be cost- and time-effective, by (partially) replacing the conventional (shear) reinforcement with steel fibres dispersed in the fresh concrete mix. The manufacturing of stirrups and reinforcement cages is time consuming and requires a lot of manual labour. Especially in **precast industry**, SFRC is of economic interest because of its cost- and time-effectiveness. Since most of the precast structural elements are pretensioned, it is profitable to investigate prestressed SFRC elements.

Although the idea of adding (steel) fibres to concrete for reinforcement is quite old, SFRC was first studied in the 1960s by Romualdi and Batson [54] and Romualdi and Mandel [55]. Despite the wide research and the continuously increasing structural applications of SFRC, the use is still restricted with respect to its potentials. This is mainly caused by the lack of **analytical models** and international building codes for SFRC structural elements. An exception is the Model Code 2010 [19], which is a considerable step forward in the utilisation of SFRC. These design guidelines are derived from fundamental and applied research of steel fibre reinforced concrete as a structural material. Most investigations focus on the bending behaviour of SFRC structural elements. The shear behaviour and capacity on the other hand are less investigated.

Even for traditional concrete structural elements, **shear behaviour and capacity** are complex phenomena, consisting of interrelated shear transfer mechanisms and affected by different influencing parameters. Various design codes have been developed to determine the shear capacity of plain concrete and the (minimal) amount of conventional shear reinforcement, based on (semi-)empirical and analytical models. For steel fibre reinforced concrete, only a few semi-empirical models of the shear capacity exist nowadays.

The incomplete knowledge and lack of international building codes, especially for the shear behaviour of SFRC, causes its restricted use for structural applications with respect to its potentials. Experimental research, valuable data and analytical models of the shear behaviour and capacity of prestressed SFRC beams are scarce as well. In conclusion, further investigation is needed to validate, verify and optimize the design procedures of SFRC.

1.2 Focus of the thesis

In the problem statement, the need of investigation of the shear behaviour of prestressed SFRC is described. Therefore, the subject of this master thesis is the *experimental and analytical analysis of the shear capacity of prestressed steel fibre reinforced concrete beams*. Prestressed SFRC beams are tested with a four-point bending test to obtain measurements of the shear capacity in function of different parameters as fibre dosage and amount of prestressing force.

The aim is to investigate how the mechanical behaviour of prestressed SFRC beams subjected to shear loading can be described and which factors influence this behaviour. Besides the experimental research, some of the few existing analytical models are analysed and compared with the observed results.

The objectives of this research are defined as follows:

- To obtain a reliable and valuable set of experimental results of the shear resistance of prestressed SFRC beams. Not only failure load and failure mode are measured, but also shear behaviour is considered by deformations, displacements and cracking pattern properties during the shear loading.
- To determine the influence of the main investigated parameters on the failure properties. These main parameters are fibre dosage, amount of prestressing and amount of conventional shear reinforcement.
- To compare the experimentally obtained results with data from literature and with predictions according to design codes and analytical models. Based on this comparison, some remarks should be made to enhance the safe application of prestressed SFRC beams.

The following methodology is adopted to achieve the objectives:

- The research starts with performing a literature survey to get a state-of-the-art on the combination of shear behaviour and capacity of concrete and steel fibre reinforced concrete.
- After the literature survey, the experimental research is initiated at the Reyntjens Laboratory of the Civil Engineering Department of KU Leuven. In general, six I-shaped prestressed SFRC beams without variable height are tested, each with slightly different properties. The experimental setup, test specimens and measurement methods will be discussed in more detail.
- When all the experiments are done, the results are processed by calculating stress losses and the expected crack and failure load, and by performing a parameter study.
- Finally, the reported experimental results are compared to analytical models found in the literature survey. Based on the deviations between both, improvements or adjustments are examined.

1.3 Outline of the text

This first chapter introduces the problem statement of this master thesis, together with the scope and the defined research objectives. A brief overview of the adopted methodology is given as well.

Chapter 2 contains the literature survey, divided into three parts: shear behaviour and capacity of structural concrete elements, steel fibre reinforced concrete and the combination of both in design codes and analytical models. The first part describes the shear transfer mechanisms, influencing parameters and failure modes. Also some analytical models and the effect of prestressing are discussed. The second part deals with the material SFRC and its behaviour in different loading cases. The third part presents some experiments, analytical models from literature and design codes of (prestressed) concrete beams, whether or not reinforced with steel fibres or conventional stirrups.

Chapter 3 describes the experimental research, starting with an overview of the research aims. Secondly, the design and the geometry of the experimental specimens are discussed. Further on, the materials and the material identification tests are explained. The next part presents the experimental setup of the four-point bending test and the adopted instrumentation. The main measurement techniques are *dismountable mechanical strain gauges*, *linear variable differential transformers*, *optical photoelectric sensor*, *Bragg grated optical fibres* and *digital image correlation*. Lastly, the experimental results and predictions are given and analysed.

Chapter 4 includes the analytical study of the experimental results. This contains an investigation on the influence of the main parameters and a discussion of the calculated and experimentally obtained crack loads. Furthermore, a comparison is made between the predicted and experimentally observed results of different analytical models and design codes for the shear capacity. The discussed models are the Eurocode 2, the Model Code 2010, the DRAMIX Guideline, the RILEM σ - ε -design method, the CNR model and the model proposed by Soetens.

Chapter 5 finally presents the conclusions of this research and contains some recommendations for further investigation.

Chapter 2

Literature review on shear and SFRC

2.1 Introduction

This chapter aims to introduce the framework of the research and to explain briefly the state-of-the-art of the different aspects of the research topic, based on a literature survey. Therefore, this literature review is divided into three parts.

Firstly, the subject *shear in concrete* is discussed in Section 2.2. Shear behaviour and capacity of structural concrete elements are complex phenomena, thus the different shear transfer mechanisms and the failure modes are explained. Furthermore, the influencing parameters of these mechanisms and the influence of a prestressing force are elaborated. Also a brief overview of the main shear experiments in literature is given. Additionally, analytical models for the shear design and the shear design procedure according to Eurocode 2 are presented.

Secondly, the subject *steel fibre reinforced concrete* is discussed in Section 2.3. The background and the historical development are given. Thereafter, the material is described based on the concrete, the fibres and the bonding in between. Furthermore, the different aspects of the mechanical behaviour of SFRC are elaborated, namely the pull-out, post-cracking, compression, tensile, flexural and shear behaviour. Lastly, the identification of the material properties is discussed, with the determination of the flexural tensile strengths in more detail.

Thirdly, the *combination of shear and SFRC* is discussed in Section 2.4. Existing analytical models and an overview of performed shear experiments in literature are presented. Thereafter, more generally accepted design codes and models are further elaborated, together with the design procedure of Model Code 2010. These models are valid for prestressed SFRC beams, whether or not reinforced with steel fibres or conventional stirrups.

2.2 Shear in concrete

2.2.1 Background

Shear (V) is an internal force applied perpendicular to the longitudinal axis of an element. It appears in combination with a varying bending moment [64], as derived hereafter. Figure 2.1 shows an elementary part dx subjected to a distributed load. The rotational equilibrium around point A results in:

$$V(x) \cdot dx + M(x) = M(x) + dM(x) + p(x) \cdot dx \cdot \frac{dx}{2} \quad (2.1)$$

Neglecting the second order terms (dx^2) leads to:

$$V(x) = \frac{dM(x)}{dx} \quad (2.2)$$

As a result, shear tests can be done by applying a varying bending moment, for example in a three- or four-point bending test, since a linear varying bending moment diagram leads to a constant shear force.

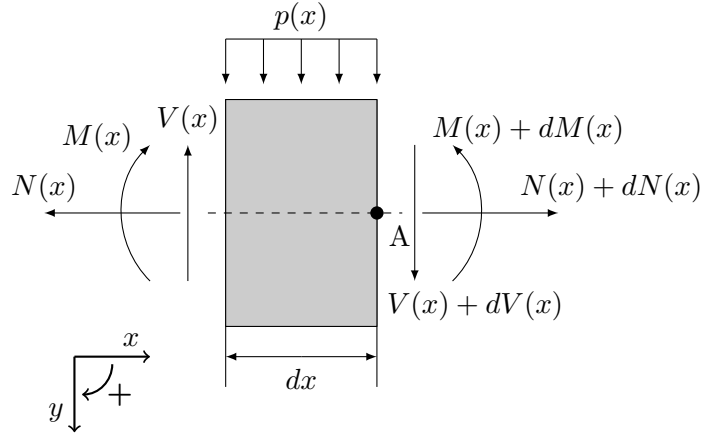


FIGURE 2.1: Internal forces on an elementary part.

The shear force induces shear stresses over the cross-section to maintain the equilibrium, but these shear stresses are not constant along the height of the cross-section [22, 64]. For a homogeneous, isotropic and uncracked beam, the distribution of the shear stress τ over the height y is calculated according to the formula of Jourawski:

$$\tau(y) = \frac{V \cdot S(y)}{b(y) \cdot I} \quad (2.3)$$

Hereby, $S(y)$ is the first moment of area, I is the second moment of area and $b(y)$ is the width of the cross-section at height y .

The combination of a shear force and bending moment (and sometimes also normal force) leads to normal and shear stresses across the cross-section of a flexural element. The combination of these stresses results in principal stresses, namely the maximal normal stresses acting perpendicular to the planes where no shear stresses occur. The principal tensile stress and the principal compressive stress are always perpendicular to each other. When the principal tensile stress exceeds the tensile strength of the concrete, cracks are formed. In case of pure shear, the inclination of the cracks at the neutral axis equals 45° . Once a cross-section is cracked, the structural behaviour becomes non-linear.

The shear capacity is the combination of mechanisms that withstand the applied shear force. Between cracking and failure, the theory of elasticity is no longer valid, as well as the formula of Jourawski. However, at that moment shear transfer mechanisms contribute to the shear capacity of a structural concrete element.

2.2.2 Shear transfer mechanisms

The ASCE-ACI Committee 426 (1973) [25] and the ASCE-ACI Committee 445 (1998) [47] defined five shear transfer mechanisms in a reinforced and/or prestressed concrete beam, not taking into account the contribution of the shear reinforcement [32]:

- (1) Shear stresses in uncracked concrete, i.e. the flexural compression zone;
- (2) Interface shear transfer (also called aggregate interlock or crack friction);
- (3) Dowel action of the longitudinal reinforcement;
- (4) Arch action;
- (5) Residual tensile stresses transmitted directly across cracks.

A cracked concrete beam is influenced by many parameters and the contribution of each transfer mechanism separately is difficult (or rather impossible) to define. Taylor [18, 62] concluded the aggregate interlock to contribute 33 to 50%, the shear stresses in uncracked concrete 20 to 40% and the dowel action 15 to 25%. On the other hand, Sarkar [56] concluded the aggregate interlock to contribute 30 to 40%, the shear stresses in uncracked concrete 10 to 20% and the dowel action 40 to 50%.

Shear stresses in uncracked concrete

In uncracked regions of a structural concrete element with a linear horizontal strain distribution, the shear force is transferred by inclined principal compressive and tensile stresses. In cracked regions, this state of stress is still valid in the uncracked compression zone. The integration of the shear stresses (τ) over the depth of the compression zone (x) gives a shear force component, sometimes considered as the explanation for the concrete contribution.

$$V = \int_0^x b(y) \cdot \tau(y) dy \quad (2.4)$$

This shear force component is not equal to the vertical component of an inclined compression strut. In a slender member without axial compression, the shear force in the compression zone does not contribute significantly to the shear capacity because the depth of the compression zone is relatively small [48, 62].

Interface shear transfer

The physical explanation of the interface shear transfer for normal-density concrete is called aggregate interlock and is described in the report of ASCE-ACI Committee 426 (1973) [25]. Aggregate interlock is the phenomenon where aggregates are protruding from the crack surface and providing resistance against slip (Figure 2.2). It is a consequence of the fact that cracks go through the cement matrix, but not through the aggregates themselves. However, the cracks go through the aggregate in lightweight and high-strength concrete and the cracks still have the ability to transfer shear. Therefore, the term interface shear transfer is more appropriate. It also indicates that this mechanism depends on the surface conditions and is not only a material characteristic.

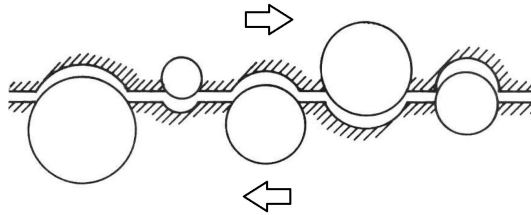


FIGURE 2.2: Schematic representation of the aggregate interlock [72].

The mechanism of interface shear transfer involves the relationship between four parameters: (a) crack interface shear stress τ_f ; (b) normal stress σ_f ; (c) crack width w and (d) crack slip δ . They are often related to the concrete compressive strength. Several researchers developed models during the last three decades [13, 32, 47, 60]. For example the two-phase model of Walraven [71, 72] relates the shear stress to the normal stress with a friction parameter in function of the concrete compressive strength f_c , the crack width w , the largest diameter of the aggregates D_{max} and the crack slip δ :

$$\tau_f = \mu(f_c, w, D_{max}, \delta) \cdot \sigma_f \quad (2.5)$$

Dowel action

Dowel action of the longitudinal reinforcement is the resistance of a reinforcing bar, crossing a crack, to shear displacement. It is a consequence of the stiffness of the reinforcement perpendicular to its longitudinal axis. The prohibited displacement of the crack surfaces causes stresses in the concrete around the bar, namely compressive stresses just below the reinforcing bar and tensile stresses in the horizontal plane of the reinforcement.

As a consequence, dowel action in elements without transverse reinforcement is limited by the tensile strength of the concrete cover supporting the dowel. On the other hand, dowel action can be significant in elements with large amounts of longitudinal reinforcement, particularly when distributed in more than one layer. Based on the occurring stresses, two failure modes due to the dowel action are distinguished (Figure 2.3): (1) splitting of the side and/or bottom concrete cover (also referred as *Failure Mode I*) and (2) crushing of the concrete under the dowel (also referred as *Failure Mode II*).

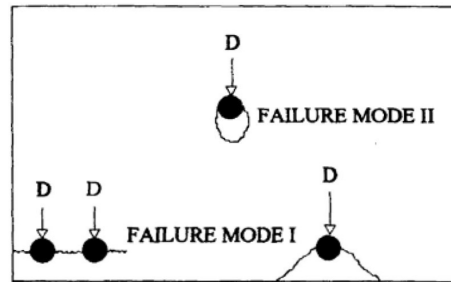


FIGURE 2.3: Overview of the failure modes due to dowel action [32].

Residual tensile stresses

This mechanism has been identified after the report of ASCE-ACI Committee 426 [25] was issued. Normally, the tensile strength of concrete is neglected in strength calculations of concrete members, since it is relatively low and subjected to a wide scatter. However, the shear resistance of concrete elements without conventional shear reinforcement appears to depend on the tensile stresses in the concrete. The basic explanation of the residual tensile stresses is that a first crack in concrete is not a clean break. Small pieces of concrete remain bridging the crack and continue to transfer a tensile force up to the crack widths are in the range of 0.05 to 0.15 mm [47]. After micro-cracking, a crack forms as the tensile strength is reached. However, the tensile stress does not instantly become zero as it would be in a very brittle material. Rather a quasi-brittle behaviour is observed. Shear design models based on fracture mechanics consider this mechanism of residual tensile stresses as the primary shear transfer mechanism [47]. Also other models consider the contribution of residual tensile stresses, for example Reineck's tooth model [48].

Arch action

Arch action is the direct transfer of a part of the applied load to the supports. It appears in both cracked and uncracked concrete. The arch action increases for loads closer to the supports, namely if the shear span-to-effective depth a/d -ratio decreases. It will become significant for beams with a small span and a large height, particularly if a/d is smaller than 2.5. Point loads are transferred by means of

an inclined compressive strut and distributed loads are transferred by means of a compressive arch (Figure 2.4). These compressive regions require a horizontal reaction at the supporting points, which is provided by the flexural reinforcement in simply supported beams. Hence, the anchorage of the reinforcement is heavily loaded and failure of the beam often occurs due to the loss of anchorage of the reinforcement.

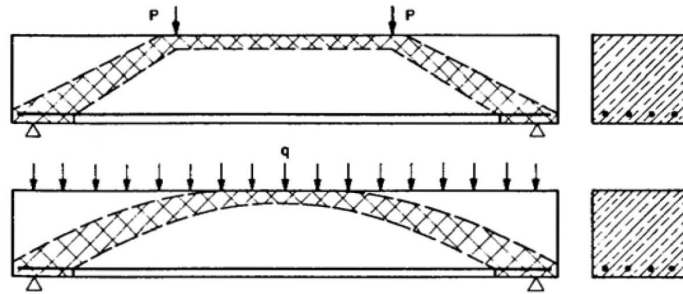


FIGURE 2.4: Different arch development for point loads and distributed loads [32].

Shear reinforcement

Conventional shear reinforcement mostly consists of stirrups. The tensile force in these stirrups will contribute to the shear capacity. Ritter [53] and Morsch [35] developed the truss analogy to describe the mechanism of shear transfer in concrete elements with transverse reinforcement. As shown in Figure 2.5, this model exists of a parallel chord truss with compressive diagonals inclined at 45° . The combination of the inclined compressive struts (in the concrete) and the vertical tension ties (i.e. stirrups) resist the applied shear force whereas the top (i.e. concrete compression zone) and bottom (i.e. longitudinal reinforcement) chord of the truss resist the applied bending moment.

Additionally, shear reinforcement influences the aforementioned shear transfer mechanisms. The interface shear transfer improves due to the limited diagonal cracks opening by presence of stirrups. The dowel action improves because the longitudinal reinforcement is supported by the stirrups. The shear transfer by residual tensile stresses enhances due to the limited crack openings and the stirrups prevent a breakdown of bond when splitting cracks develop in the anchorage zone. Furthermore, a stirrup has to be anchored adequately to develop the yield strength over its full length. In practice, they are bent around the longitudinal bars. The truss mechanism in concrete beams only functions after the formation of diagonal cracks. The primary role of stirrups is transferring the shear across a potential diagonal failure crack. [32]

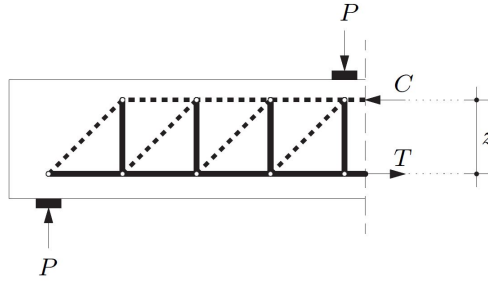


FIGURE 2.5: Truss analogy of Ritter [53] and Mörsh [35]. Tension is denoted with solid lines and compression with dashed lines. C denotes a compressive force, T a tensile force and z the internal lever arm. [13]

2.2.3 Failure modes

The combination of the shear transfer mechanisms results in the shear capacity to withstand the applied shear force. If the applied load exceeds the shear capacity of the (reinforced) concrete element, failure occurs. As a shear force results of a varying bending moment, this bending moment will often cause vertical cracks at first in the zone with the maximum bending moment (in the middle at the bottom side of a beam). Afterwards, when increasing the load, the bending cracks near the supporting points rotate to an angle of 45° with the horizontal axis, due to the influence of shear. Enlarging of the bending cracks causes *flexural shear failure*, shown in Figure 2.6e.

On the other hand, diagonal tension cracks can sometimes occur in the zone between the supporting point and the loading point before the bending moment causes vertical cracks. This is for example the case for beams with a cross-section with a relatively thin web. Enlarging of the shear cracks causes brittle failure due to shear. Four types of brittle failure modes in shear are to be distinguished for reinforced or prestressed concrete beams [38, 65].

- (1) *Failure due to diagonal tension* (Figure 2.6a): when the diagonal cracks open, the shear reinforcement is activated. These stirrups will fail if their yield stress is reached.
- (2) *Failure due to web crushing* (Figure 2.6b): in case of beams with a relatively small web thickness and large shear reinforcement, the concrete compressive strength in the inclined struts can be reached before the yield strength of the stirrups, leading to web-compression failure due to crushing of the concrete.
- (3) *Anchorage shear failure* (Figure 2.6c): the bond of the longitudinal reinforcement is lost near the support due to splitting of the concrete. Mostly, horizontal cracks along the reinforcement are observable.
- (4) *Failure due to crushing of the compression zone* (Figure 2.6d): when the bending-shear cracks become larger, the height of the compression zone decreases. A too small remaining height causes reaching the concrete compressive strength at the top fibre.

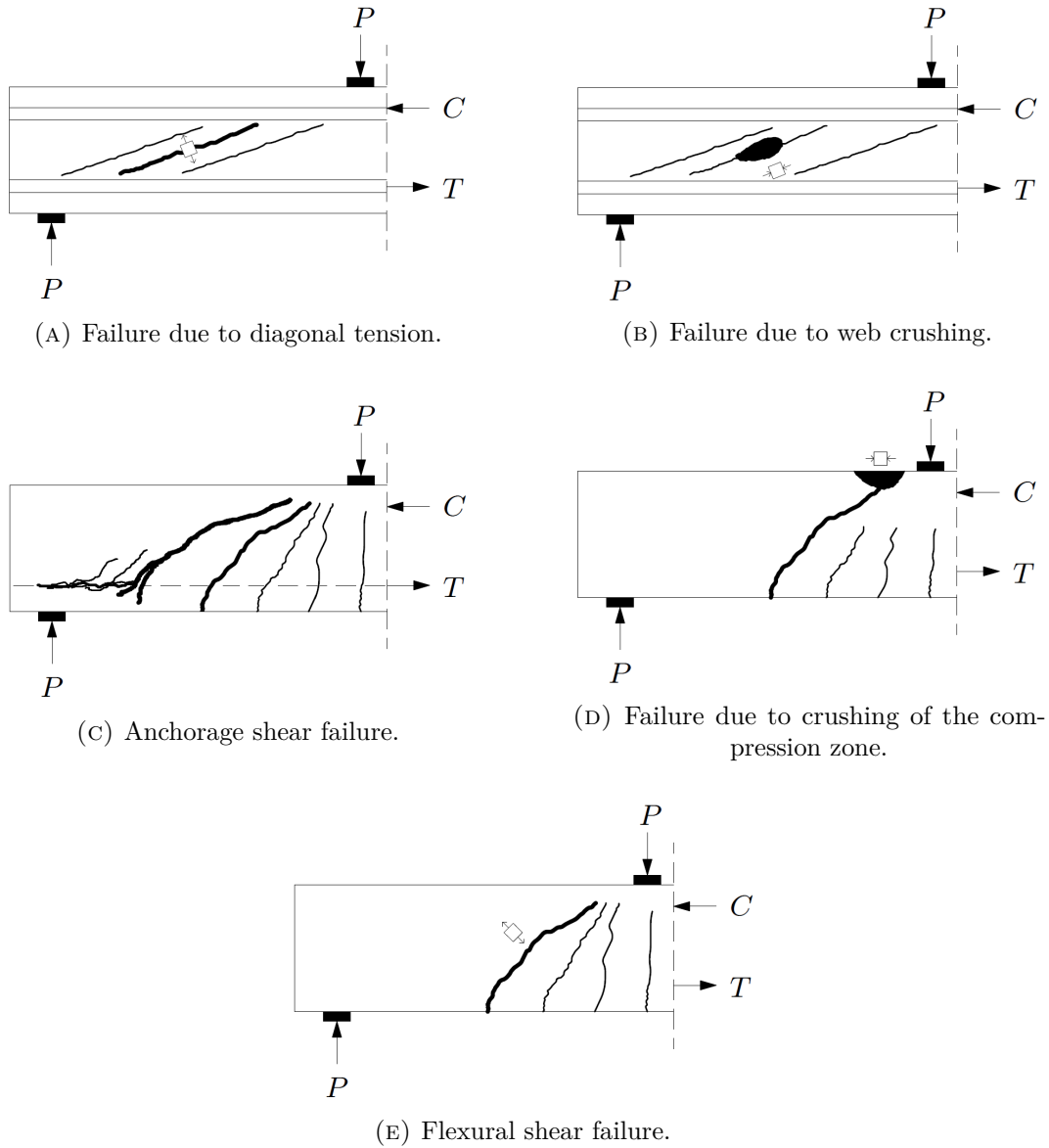


FIGURE 2.6: Schematic representation of different failure modes. C denotes a compressive force and T a tensile force (adapted from [13]).

2.2.4 Influencing parameters

Not only the different interrelated shear transfer mechanisms make the shear capacity of concrete elements difficult, but also the influence of different parameters on these mechanisms. The most important parameters [32, 47, 64, 65] are briefly discussed. Table 2.1 gives an overview of the parameters and the affecting shear mechanisms.

TABLE 2.1: Overview of the main influencing parameters per shear transfer mechanism (adapted from [13]).

Parameter [†]	Shear transfer mechanism					
	Uncracked concrete	Interface transfer	Dowel action	Residual tension	Arch action	Shear re-inforcement
f_{ck}	x	x	x	x	x	
d		x			x	
a/d					x	
ρ_l	x	x	x	x		
ρ_w		x	x	x		x
σ_{cp} [•]	x	x		x		x

Note: [†]: The used symbols are defined in the following paragraphs and [•] in Section 2.2.5.

Concrete quality and strength (f_{ck})

The concrete quality and strength includes the compressive strength (denoted by f_{ck}) and the tensile strength. The former is important since the compression zone contributes to withstanding the shear force, for example in the mechanism of shear stresses in uncracked concrete and in the arch action. A larger compressive strength is related to a larger tensile strength, which is advantageous for the mechanisms of dowel action and residual tensile stresses. An increased tensile strength delays the formation of cracks. However, the use of high-strength concrete to enhance the shear capacity is not incontestable as the cracks will go through the aggregates and will cause a smoother crack surface (a clean break) where the friction and interface shear transfer are smaller than for rougher crack surfaces.

Effective depth (d)

The effective depth of a cross-section is denoted by d and is the distance between the most compressed top fibre and the center of gravity of the longitudinal reinforcement in tension. A larger effective depth mostly implies a larger uncracked compressive zone to contribute to the shear resistance. On the other hand, a larger height leads to larger crack widths whereby the interface shear transfer and the residual tensile stresses mechanisms will decrease. A second aspect is the size effect. Many experiments on the shear behaviour are performed with relatively small specimens for practical reasons. However, the results of these tests are not directly valid for full size specimens. There is a significant size effect on the shear strength of elements without transverse reinforcement.

Shear span-to-effective depth ratio (a/d)

The shear span-to-effective depth ratio is denoted by a/d , with a the distance between the loading point and the supporting point (the shear span) and d the effective depth. This geometrical parameter is important for the shear capacity, as the shear stress at failure becomes smaller in slender beams than in deeper beams. This is caused by the arch action. For deeper beams, in particular when a/d is smaller than 2.5, it is easier for the shear to be transmitted directly to the supports by a compression strut. Hereby, also the support conditions are important. Furthermore, the a/d -ratio is used to describe the shear failure mechanism of simply supported, plain concrete beams:

6	<	a/d	Failure due to the vertical bending cracks.	
2.5	<	a/d	< 6	Failure due to inclined bending-shear cracks.
		a/d	< 2.5	Failure due to crushing or splitting of the concrete.

Longitudinal reinforcement ratio (ρ_l)

The longitudinal reinforcement ratio is denoted by ρ_l and calculated as:

$$\rho_l = \frac{A_{sl}}{b_w \cdot d} \quad (2.6)$$

with A_{sl} the area of longitudinal reinforcement, b_w the web width and d the effective depth. The amount of longitudinal reinforcement influences almost all shear transfer mechanisms. A higher ρ_l -ratio enhances the shear capacity by a decreased crack width and spacing (resulting in larger interface shear transfer), shorter flexural cracks (resulting in a larger compression zone) and a increased dowel action. Although a high amount of longitudinal reinforcement improves the shear capacity, it also makes the failure more sudden and brittle, as a consequence of the crushing of concrete. The capacity of moderately long beams ($a/d > 5$) with low amount of longitudinal reinforcement ($\rho_l < 1\%$) will be governed by a flexural failure and yielding of the reinforcement, which is a more ductile and predictable failure mode. Nowadays, ρ_l is mostly limited to 2%.

Shear reinforcement ratio (ρ_w)

The shear reinforcement ratio is denoted by ρ_w and calculated as:

$$\rho_w = \frac{A_{sw}}{b_w \cdot s} \quad (2.7)$$

with A_{sw}/s the area of shear reinforcement per unit length and b_w the web width. Indeed, the presence of shear reinforcement enhances the shear capacity as explained previously in the part of the mechanism of shear reinforcement (refer to Section 2.2.2).

2.2.5 Influence of a prestressing force

An axial force is the last main influencing parameter of the shear capacity, as shown in Table 2.1 where the axial force is denoted by σ_{cp} . This parameter influences the formation and inclination of cracks. An applied compressive load increases the shear resistance whereas an applied tensile load decreases the resistance.

The increase of the shear capacity due to the compressive force follows from the increased load at which the first cracks occur and the decreased principal tensile stresses. Furthermore, for a significant axial compression the depth of the compression zone of uncracked concrete greatly increases and thus the contribution of the compression zone to the shear capacity becomes more important. Also the interface shear transfer and the residual tensile stresses mechanisms are enhanced due to the smaller crack openings thanks to the larger compression zone. However, how much the shear capacity is influenced by an axial load and what the influence is on the ductility of the element is still a matter of debate.

The most used axial force is a prestressing force. This compressive load results from pretensioning the longitudinal steel strands or bars, before or after the concrete element is cast (for example in precast industry). The compressive stress from the prestressing force on the concrete is denoted by σ_{cp} . Besides increasing the crack load, axial compression also influences the strut inclination. Normally, shear cracks appear in the web of a beam at 45° with the horizontal axis. Therefore, the truss analogy of Ritter [53] and Morsch [35] models the compressive diagonals inclined at 45° . However, the inclination of the shear cracks tends to be significantly smaller than 45° in the presence of axial compression, based on Mohr's Circle. Hence, more shear reinforcement elements are activated by the flatter diagonal cracks. For an axial tension, the effect is opposite and the crack inclination is larger than 45° .

As a result, shear design of a prestressed beam with the truss analogy will lead to conservative results. On the other hand, elements subjected to a large axial compression and shear (and eventually without shear reinforcement) can fail in a very brittle manner at the instance of first diagonal cracking. For these brittle failures, a more conservative design is desired.

Besides the effect of an axial compressive force, the presence of prestressing reinforcement also increases the longitudinal reinforcement ratio ρ_l and the shear transfer mechanisms related with this parameter, especially the dowel action.

It is concluded that a prestressing force has a positive influence, as it increases the shear capacity due to an increased compression zone, decreased tensile stresses, smaller crack openings, smaller crack inclinations and an increased longitudinal reinforcement ratio. On the other hand, a higher prestressing force causes a more brittle failure. Although these effects are known and generally accepted nowadays, modelling the influence of prestressing (or an axial force in general) remains difficult.

2.2.6 Survey on shear experiments and databases

For the development of analytical models regarding the shear capacity based on the different shear transfer mechanisms and influencing parameters, researchers mostly rely on the regression analysis of test results. As a consequence, the used shear test database is of major importance. Researchers often gather their own database by experimental testing. As a result, the models could not be applicable for other specimens than tested and comparing different models could become a problem. Furthermore, the procedures to select and to save data are different, for example which parameters are taken into account. For these reasons, a number of shear databases were constructed to collect as much as possible shear test data in a uniform manner. [13,73]

Reineck et al. [49–52,63] published a database with corresponding extensions during more than ten years. The first one in 1999 [49] contained reinforced concrete elements without shear reinforcement to evaluate the empirical equation for the German Standard DIN 1045-1. In 2003 [51], the database was extended and included 933 rectangular reinforced concrete beams without shear reinforcement subjected to one or two point loads. During the years, it was further developed to the ACI-DAfStb Database in 2013 [50], where also more detailed longitudinal reinforcement information is comprised. The database included shear tests on reinforced concrete elements without stirrups, 128 subjected to distributed loading and 1365 to point loading. 338 of these 1365 are non-slender elements (i.e. $a/d < 2.4$) [52]. In 2015 [63], the research group of Reineck compiled a database of 278 shear tests on non-slender reinforced concrete elements with vertical stirrups.

In 2005, Hawkins et al. [21] proposed a database of 1444 reinforced and 743 prestressed concrete elements. The elements are rectangular, I-shaped or T-shaped, with and without shear reinforcement and subjected to point loads or uniform loads. Further, Collins et al. [12] collected a database of 1849 shear tests, based on earlier compilations, in 2008. The reinforced rectangular or T-shaped elements without shear reinforcement were subjected to point loads or uniform loads. Lastly, in 2013, Nakamura et al. [38] compiled a database of 1696 shear tests of prestressed concrete elements with and without shear reinforcement collected from 1954 to 2010.

To conclude, some remarks have to be made. Firstly, the large number of shear tests in the databases does not mean that all of them are useful, for example due to an ill-documented experimental program with missing necessary data. Secondly, for the development of a certain model, a careful selection of test data is important to gather the proper shear test results, for example based on the correct failure mode. Thirdly, a lot of shear test results are reported by a limited amount of detailed data. Mostly, the geometrical and material properties are reported with the experimentally obtained failure load, failure mode and sometimes the cracking pattern. Detailed behaviour characteristics (e.g. displacement and deformation data during the loading procedure, first crack load and post-cracking behaviour) to investigate the shear behaviour are mostly missing.

2.2.7 Analytical models

The complex phenomenon of shear is discussed in the previous sections based on the shear transfer mechanisms, the failure modes and the influencing parameters. Various researchers proposed models for shear in structural concrete elements, taking into account these aspects and based on the test data gathered in the databases. Also design codes to determine the shear capacity of an element and the (minimal) amount of conventional shear reinforcement are developed all over the world. However, a discussion of all existing shear models falls outside the scope of the present research. The most important design code in Europe (Eurocode 2 [41]) is discussed in the following section and will be used in the analysis of the experimental research. Therefore, only a very brief overview of the main models is given.

Different types of models exist, namely empirical models, analytical models, finite element models or models based on fracture mechanics. The analytical models are mostly distinguished for elements with or without shear reinforcement, as the effect of shear transfer mechanisms varies in presence of shear reinforcement (refer to Section 2.2.2). The following list enumerates the main models. Most of them have a variant for concrete elements with or without shear reinforcement.

- Truss analogy approaches, originally proposed by Ritter [53] and Mörsh [35]. There is a distinction between the 45° model or the variable angle truss model.
- Strut-and-tie models, originally proposed by Schlaich et al. [57]. An alternative approach is the stress field method, proposed by Muttoni et al. [36].
- Upper bound plasticity models, proposed by Nielsen [43].
- Compression field approaches, including the compression field theory [11], the modified compression field theory [70], the rotating-angle softened truss model [4], the disturbed stress field model [69], the fixed angle softened truss model [23] and the simplified modified compression theory [5].
- Tooth model approach, originally proposed by Kani [26], for elements without shear reinforcement. An alternative approach is proposed by Reineck [48].
- Strain based models, originally proposed by Park et al. [44], for concrete elements without shear reinforcement.

Further details on all the different models can be found in [13, 21, 32, 34, 47, 60, 73].

2.2.8 Design Code: Eurocode 2

Eurocode 2 - EN 1992-1-1:2010 (denoted as EC2) [41] is one of the current international design codes and includes a shear design procedure based on the variable angle truss model as originally proposed by Ritter [53] and Mörsh [35]. The shear capacity equations are explained for prestressed beams with horizontal strands and conventional shear reinforcement. The following symbols are defined:

- $V_{Rd,c}$ is the design value of the shear resistance of the member without shear reinforcement.
- $V_{Rd,s}$ is the design value of the shear force which can be sustained by the yielding shear reinforcement.
- $V_{Rd,max}$ is the design value of the maximum shear force which can be sustained by the member, limited by crushing of the compression struts.

In general, the shear capacity of a member with shear reinforcement V_{Rd} is taken equal to $\min(V_{Rd,s}; V_{Rd,max})$, thereby neglecting the contribution of the plain concrete $V_{Rd,c}$. However, in regions where the design shear force V_{Ed} is smaller than the shear resistance of the plain concrete ($V_{Ed} < V_{Rd,c}$), no shear reinforcement is necessary. When no shear reinforcement is required, a minimum amount should nevertheless be provided.

Beams without shear reinforcement

For a cracked section, the design shear resistance of a region with prestressed reinforcement and without shear reinforcement ($V_{Rd} = V_{Rd,c}$) is calculated as:

$$V_{Rd,c} = \left[\frac{0.18}{\gamma_c} \cdot k \cdot (100 \cdot \rho_l \cdot f_{ck})^{\frac{1}{3}} + 0.15 \cdot \sigma_{cp} \right] \cdot b_w \cdot d \quad (2.8)$$

σ_{cp} denotes the remaining concrete compressive stress due to the applied prestressing force in MPa, b_w the web width in mm and k is a factor taking into account the size effect (refer to Section 2.2.4):

$$k = \left(1 + \sqrt{\frac{200}{d}} \right) \leq 2.0 \quad (2.9)$$

The design shear resistance $V_{Rd,c}$ must be larger than the minimum value $V_{Rd,c,min}$:

$$V_{Rd,c,min} = \left[0.035 \cdot k^{3/2} \cdot f_{ck}^{1/2} + 0.15 \cdot \sigma_{cp} \right] \cdot b_w \cdot d \quad (2.10)$$

It is clear that all influencing parameters of the shear transfer mechanisms (Section 2.2.2) as discussed in Section 2.2.4 appear in the calculation of the shear capacity: f_{ck} , d and the size effect, a/d is used to determine the factor 0.18, ρ_l and σ_{cp} (Section 2.2.5).

On the other hand, a section of a prestressed single span member without shear reinforcement can be uncracked in bending. In that case, the shear resistance is limited by the tensile strength of the concrete. Consequently, the shear capacity is calculated with:

$$V_{Rd,c} = \frac{I \cdot b_w}{S} \sqrt{(f_{ctd})^2 + \alpha_l \cdot \sigma_{cp} \cdot f_{ctd}} \quad (2.11)$$

f_{ctd} denotes the design uniaxial tensile strength in N/mm², S the first moment of area in mm³ and I the second moment of area in mm⁴. α_l is a correction factor taking into account the bond properties of the prestressed strands, here equal to 1. The aforementioned formula is only valid for prestressed concrete elements.

Beams with shear reinforcement

The shear resistance of a prestressed member with shear reinforcement (vertical shear bars or stirrups) is equal to the design value of the shear force which can be sustained by the yielding shear reinforcement ($V_{Rd} = V_{Rd,s}$). It is calculated as:

$$V_{Rd,s} = \frac{A_{sw}}{s} \cdot z \cdot f_{ywd} \cdot \cot \theta \quad (2.12)$$

A_{sw} is the cross-sectional area of the shear reinforcement, s is the spacing of the stirrups and f_{ywd} is the design yield strength of the shear reinforcement. z is the internal lever arm, approximately equal to $0.9 \cdot d$.

The design shear resistance $V_{Rd,s}$ must be smaller than or equal to the maximum value $V_{Rd,max}$ (i.e. the shear force required to obtain crushing of the compression struts):

$$V_{Rd,max} = \alpha_{cw} \cdot \nu_1 \cdot f_{cd} \cdot b_w \cdot z \cdot \frac{\cot \theta}{1 + \cot^2 \theta} \quad (2.13)$$

α_{cw} is a factor taking into account the state of the stress in the compression chord, ν_1 is a strength reduction factor for concrete cracked in shear and f_{cd} is the design value of the cylindrical concrete compressive strength.

θ is the angle between the inclined concrete compressive stresses in the web (assumed equal to the inclined shear cracks) and the horizontal axis. It may be chosen freely, but is limited according to EC2 to:

$$1 \leq \cot \theta \leq 2.5 \quad (2.14)$$

In practice, the maximum value of $\cot \theta$ will be chosen for the analysis of a prestressed concrete member. In the Belgian national application document [42] however, the maximum value can be calculated applying a purely empirical extension, which takes into account the influence of the applied prestressing force on the inclination of the compressive stresses:

$$\cot \theta_{max} = \left(2 + \frac{0.15 \cdot \sigma_{cp} \cdot b_w \cdot d}{\frac{A_{sw}}{s} \cdot z \cdot f_{ywd}} \right) \leq 3 \quad (2.15)$$

For highly prestressed concrete members, a slightly lower angle ($\cot \theta_{max} = 3 \rightarrow \theta_{min} = 18.4^\circ$) can be chosen in comparison to the general formulation found in EC2 ($\cot \theta_{max} = 2.5 \rightarrow \theta_{min} = 21.8^\circ$).

In the calculation of the shear capacity of beams with shear reinforcement, the shear resistance of the plain concrete contribution is neglected. Especially for prestressed concrete elements, this is a disadvantage since the applied prestressing force enhances the shear capacity, as mentioned in Section 2.2.5.

In a previous method, no longer valid and called the Standard Method, θ was chosen equal to 45° , resulting in $\cot \theta$ equal to 1. Also the concrete contribution was added to calculate the shear capacity in this Standard Method.

2.3 SFRC

2.3.1 Background

Steel fibre reinforced concrete (SFRC) is a cementitious composite material, consisting of a concrete matrix with discrete, randomly distributed steel fibres. The idea to reinforce concrete with fibres is quite old, as different types of fibres (e.g. straw or horsehair) even have been used to reinforce brittle materials in the Egyptian and Babylonian eras. In 1874, the idea to strengthen the concrete behaviour by adding metallic waste was patented by Bedard [3]. Hereafter, SFRC was not often used until the beginning of the 1960s when the old idea of adding fibres to reinforce concrete revived. Research by Romualdi and Batson [54] and Romualdi and Mandel [55] heralded the era of using steel fibre concrete composites as known today. Since then, the use of SFRC and research on its material properties and structural response of elements increased [32].

The main benefit of including fibres in hardened concrete is controlling the cracking and enhancing the post-cracking tensile residual strength, due to the bridging of crack surfaces by the fibres [16, 19, 32]. The toughness of the composite is increased as well as the failure strain [34]. The advantages such as an improved ductility, a higher energy absorption capacity and an increased flexural strength, depending on the fibre content and the aspect ratio, are generally accepted nowadays [16, 29, 45]. Therefore, in most of the applications, the use of fibres is not to increase the strength (although the increase of tensile strength is a consequence) but to control and delay the widening cracks and the post-cracking behaviour [34]. In tension, SFRC fails only after the steel fibres break or are pulled out of the cement matrix [32]. Furthermore, fibre reinforcement reduces the construction time and cost because it is easily placed.

Despite the old concept and wide research of SFRC, the use is still restricted with respect to its potentials. This is mainly caused by the lack of international building codes for SFRC structural applications [16, 31, 45]. Currently, the widespread use of SFRC is generally limited to non-structural elements like paving applications in airports, highways, bridge decks and industrial floors [39, 74]. Here, the fibres are added with the aim of withstanding the cracks induced by temperature variation or loading and to increase durability. However, structural use of SFRC is also increasing, especially in precast industry. Examples are tunnel linings, precast piles, beams and slabs. Also thin elements with complicated shapes or too small dimensions to provide enough concrete cover to preserve from corrosion are reinforced with fibres. [34]

Lastly, fibres can be used to replace (partially) conventional reinforcement bars in structural applications, to enhance the ductility of the structure. [16, 19] This application of SFRC is investigated in the present research.

2.3.2 Description of the material

The two-composite material steel fibre reinforced concrete can be described in three parts, namely the concrete, the steel fibres and the bonding in between. These aspects also influence the behaviour and the properties of the material.

Concrete and bonding

Firstly, both normal- and high-strength concrete are used in combination with fibres. Sometimes, the concrete mixture is adapted (e.g. increasing the water to cement ratio, including admixtures or increasing the sand fraction) to maintain the workability after adding the fibres. Also self-compacting concrete can be used. The mechanical properties, such as compressive and tensile strength, of the concrete itself are not influenced by adding steel fibres, except for high fibre dosages (exceeding 80 kg/m^3) [34].

Secondly, the bonding is responsible for the transmission of the force between the concrete matrix and the fibres and influences the mechanical behaviour and capacity of the material. Due to the complex character of SFRC, it is difficult to determine a generalized bond strength. The bonding is provided by (1) the mechanical component due to deformations, (2) the frictional resistance, (3) the physical and/or chemical adhesion and (4) the fibre-to-fibre interaction [1]. The physical and chemical adhesion are usually very weak, whereas the mechanical component has the most significant contribution. It depends on the fibre shape and geometry, takes place after failure of the chemical bond and remains until failure of the fibres due to pull-out or rupture. The frictional resistance is mostly affected by the interface between matrix and fibre and is enhanced by the surface roughness. Fibre-to-fibre interaction occurs if the fibres are in contact with each other due to a high fibre content. [32]

Thirdly, the presence of fibres also influences the porosity of the concrete matrix. Adding fibres affects the packing density and can increase the air-content. This leads to a negative effect on the porosity and if the concrete matrix design is not optimized, it leads eventually to a decrease of overall performance. Moreover, the bond strength of fibres can decrease due to the presence of the entrapped air-bubbles. [60]

Steel fibres

At first, adding fibres to concrete is not restricted to steel fibres. For example natural, organic, synthetic, carbon and glass fibres can be used as well. However, the present research is limited to the use of steel fibres. Furthermore, many types of fibres exist, varying in the following aspects (non-exhaustive) [30, 32, 34, 37, 60]:

- *Longitudinal shape*: some examples are shown in Figure 2.7. These variations exist of mechanical deformations along the length or different shaped ends and mainly aim to develop a better bond between the fibres and the concrete matrix. The most used type is the hooked-end fibre which provides high post-cracking ductility due to plastic deformation of the hook during pull-out.

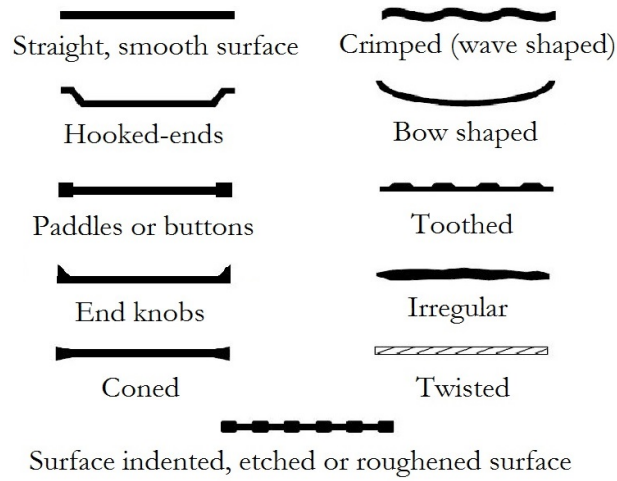


FIGURE 2.7: Different shapes and types of steel fibres (adapted from [30,37]).

- *Dimensions*: mainly the length and the diameter are variable, within a range of 10 to 60 mm and 0.2 to 1 mm respectively. The combination of both parameters is given by the aspect ratio, which is the ratio of the length to the diameter.
- *Cross-section*: this can be circular, rectangular, diamond, square, triangular, flat, polygonal or any substantially polygonal shape.
- *Material composition*: for example carbon or stainless steel.
- *Production*: five types of fibres can be distinguished, namely cold-drawn wire, straight or deformed cut sheet, melt extracted, shaved cold drawn wire and milled from steel blocks, according to the European Standard EN 14889-1:2006.
- *Surface treatments*: roughening the surface can increase the bonding capacity of fibres, for example by surface etching or plasma treating. Coatings, like zinc, are applied to improve the corrosion resistance.
- *Tensile strength*: a broad range of tensile strengths can be obtained, approximately from 1000 to 3000 MPa. It depends on the material, production process and dimensions.

Three main parameters describe the steel fibres of a SFRC mixture. Firstly, the aspect ratio λ_f is the ratio of the length to the diameter of the fibre ($\lambda_f = L_f/d_f$). Secondly, the fibre dosage or volume of fibres V_f is expressed as the amount per cubic meter (kg/m^3). The fibre content can also be expressed as the volume ratio or the fibre volume percentage (%). Thirdly, the fibre factor F is the multiplication of the aspect ratio, the fibre volume percentage and a fibre bond factor (between 0.5 and 1.0, depending on the fibre geometry and the concrete matrix). Besides, also the fibre spacing s can be important.

As a final point, the fibres should have the following properties in order to be effective as a reinforcement in concrete matrices [34, 37]: (1) a tensile strength significantly higher than the matrix (2 to 3 orders of magnitude); (2) a bond strength with the matrix preferably of the same order as or higher than the tensile strength of the matrix; (3) an elastic modulus in tension significantly higher than the matrix. In addition, the Poisson's ratio (ν) and the coefficient of thermal expansion (α) should preferably be of the same order of magnitude for both the fibre and the matrix. For example, if the Poisson's ratio of the fibre is significantly larger than that of the matrix, debonding will occur under tensile load.

2.3.3 Behaviour of the material

The behaviour of steel fibre reinforced concrete is characterised by the pull-out and post-cracking properties. Also the behaviour in compression, tension, flexure and shear are described.

Pull-out

The pull-out behaviour of the steel fibres is one of the most important failure mechanisms of SFRC. As the present experimental research uses of hooked-end fibres, this case is described. The complete mechanism of pull-out can be divided in two parts, namely the debonding phase and the mechanical deformation phase.

Pompo [46] presents the pull-out response of a hooked-end fibre in Figure 2.8. Region I is the debonding phase where shear stresses along the interface of fibres and concrete matrix provide pull-out resistance, until the debonding load P_d . For straight fibres, this load leads to a complete debonding and to the pull-out failure. However, for hooked-end fibres, the hooks provide a mechanical anchorage contribution (equal to $P_m - P_d$) in region II. When the maximum pull-out force P_m is reached, the fibre is completely debonded along its embedded length and further slipping of the fibre causes a decrease of pull-out resistance. The hooked-ends are straightened at first (representing the drop in curve after P_m). In region III, the hook is roughly straightened, providing an almost constant residual pull-out strength due to frictional sliding. In region IV, the embedded length becomes too short, resulting in a complete decay of pull-out force as there is no more transfer of the pull-out force. [46, 60] A similar behaviour is shown by Löfgren [30] in Figure 2.9. However, the deformation of the hooked-end is more pronounced and region II is less distinguishable.

The main influencing parameters of the pull-out behaviour of hooked-end fibres are the embedded length, the tensile strength, the diameter and the hook geometry of the fibre and the concrete compressive strength. Also the fibre inclination with respect to the crack plane and the mutual interaction between fibres are important parameters as well. [24, 61] Numerous investigations and developed pull-out models exist in literature, however, a further discussion falls outside the scope.

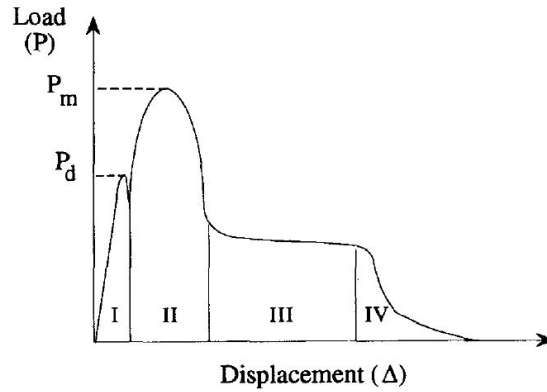


FIGURE 2.8: Schematic representation of the pull-out response of a hooked-end fibre by Pompo [46].

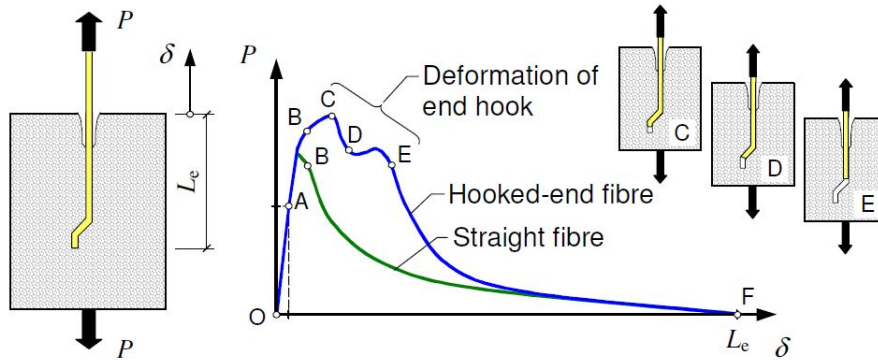


FIGURE 2.9: Schematic representation of the pull-out response of a hooked-end and straight fibre by Löfgren [30].

Post-cracking

Once the concrete cracks because the principal tensile or compressive stresses reach the corresponding strength, the applied load is transferred to the activated fibres. Elements made of SFRC do not immediately fail at the moment of concrete cracking, leading to a post-cracking behaviour. This is one of the major properties of adding steel fibres. They mainly influence the ductility of the concrete, as they bridge and tie cracks from further opening. Hence, the concrete is able to transmit higher forces between the crack planes. The contribution of fibres acts until they are either pulled out or broken. [32, 60]

The post-cracking behaviour is affected by two mechanisms, namely aggregate bridging that is always present in plain concrete and fibre bridging that contributes to energy dissipation in SFRC concrete. The fibre bridging is dominant, but the final strength is the combination of both. Aggregate bridging decays to zero for a crack opening of around 0.3 mm. [30, 34] Furthermore, as fibres deform, additional narrow

cracks develop and continued cracking of the concrete matrix takes place. During this stage, debonding and pull-out of the fibres occur, but the yield strength of the fibres is mostly not reached. If fibres are long and embedded enough to maintain their bond with the matrix, they may fail by yielding or by fracture, depending on their size and spacing. [32, 60]

The post-cracking behaviour and its parameters, determining the performance of SFRC, are characterised and measured by means of material identification tests and therefore explained in Section 2.3.4.

Compression

Figure 2.10 shows the stress-strain relation under compression for plain concrete and SFRC, and for each a distinction between normal and high-strength concrete. The stress-strain relation of plain concrete is nearly linear elastic up to about 30% of the compressive strength, followed by gradual softening. After reaching the compressive strength, the relation shows strain softening until failure takes place by crushing. If the compressive strength increases, a more brittle behaviour is observed and a steep drop of the stress-strain curve occurs.

Adding fibres causes a more pronounced softening branch for normal strength concrete and an increased post-crushing ductility for high-strength concrete, which is more effective. The main effect of fibres on the increase of compression-ductility has been attributed to the enhanced resistance against the longitudinal splitting crack growth after reaching the compressive strength. However, the effect of fibres is highly dependent on the type, the size, the properties and the volume fraction of the fibres and the properties of the concrete matrix. [30, 32, 60]

It is concluded that conventional steel fibres at relatively low fibre dosages (i.e. < 1%) do not affect the pre-peak properties, whereas the strain at crack localisation and the failure strain increase. The residual compressive stresses, ductility and toughness can be increased in function of a higher fibre dosage. However, the compressive strength of concrete itself cannot be improved. Furthermore, SFRC is classified according to the same strength classes as in Eurocode 2 [41].

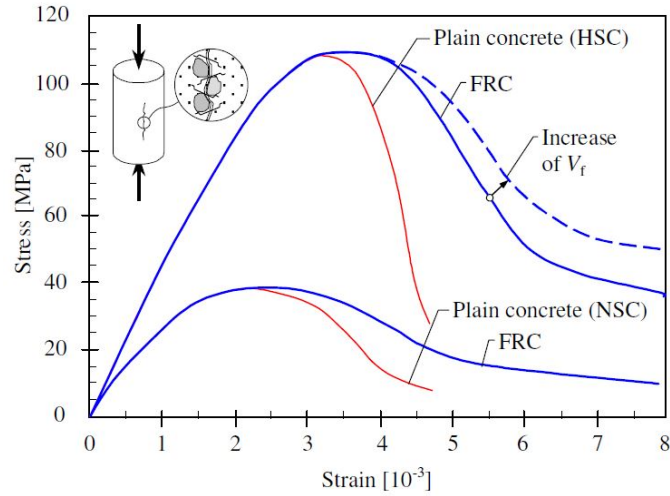


FIGURE 2.10: Schematic representation of the behaviour of FRC and plain concrete in compression (HSC is high-strength concrete, NSC normal concrete strength) [19, 30].

Tension

Although the first developments and research of SFRC aimed to increase the tensile strength of plain concrete, it is generally accepted nowadays that the use of steel fibres only influences the post-cracking tensile behaviour of concrete.

SFRC fails in tension due to either fibre pull-out of the concrete matrix or fibre rupture (Figure 2.11). In the first case, the anchorage length becomes smaller than the required bond length before the fibres reach their tensile strength. However, the pull-out itself is hindered by friction, leading to energy dissipation and a more ductile failure behaviour. In the second case, the fibres are strongly anchored in the concrete matrix and the tensile strength is reached before fibre pull-out. This case is less likely to occur, as the tensile strength of steel fibres is rather high compared to the bonding. Therefore, fibres with greater anchorage quality increase the tensile resistance beyond the first cracking load. [32] Furthermore, the tensile behaviour can be characterised by a tensile stress versus crack opening curve.

The tensile behaviour of SFRC can be classified as softening or hardening, refer to Figure 2.12. Softening behaviour implies the occurrence of a localised single crack that determines the post-peak behaviour and a decrease of stress once the concrete matrix cracks. Hardening behaviour is characterised by multiple cracks and a post-cracking strength larger than the cracking strength. Plain concrete is a softening material. For SFRC with moderate fibre dosages, the tensile strength and modulus of elasticity are not significantly affected. However, the fibres influence the tensile behaviour and the shape of the stress versus crack opening curves varies depending on the type and the amount of the used fibres and the quality of the concrete. [19, 30]

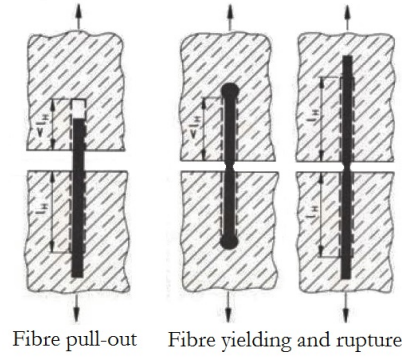


FIGURE 2.11: Different failure mechanisms of steel fibres embedded in a concrete matrix (adapted from [58]).

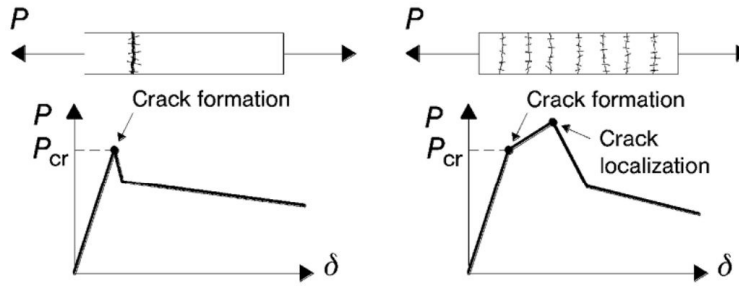


FIGURE 2.12: Tensile behaviour of SFRC: (left) softening and (right) hardening, where P_{cr} indicates the crack load [19].

The constitutive stress versus crack opening law for the post-cracking behaviour of FRC is defined in Model Code 2010 [19]. Two different models can be adopted, namely a rigid plastic or a linear post-cracking behaviour (including softening or hardening). These models are based on the residual tensile strengths $f_{R,1}$ and $f_{R,3}$, resulting from the material identification tests (explained in Section 2.3.4). The rigid-plastic model assumes the ultimate residual tensile strength f_{Ftu} to be a constant value equal to $f_{R,3}/3$, up to a critical crack opening w_u . The linear post-cracking behaviour allows to calculate the softening or hardening after cracking. The tensile stress as a function of the crack opening w is given by (with $CMOD_3$ equal to 2.5 mm):

$$f_{Ftu} = 0.45 \cdot f_{R,1} - \frac{w_u}{CMOD_3} \cdot (0.45 \cdot f_{R,1} - 0.5 \cdot f_{R,3} + 0.2 \cdot f_{R,1}) \geq 0 \quad (2.16)$$

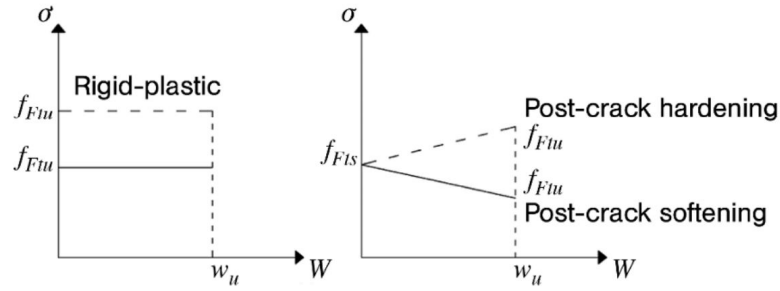


FIGURE 2.13: Simplified post-cracking constitutive laws (continuous and dashed lines refer to softening and hardening behaviour respectively) [19].

Flexure

The influence of steel fibres on flexural strength of concrete is greater than for direct tension and compression. Two flexural strength values are commonly derived from the load-deflection diagram. Firstly, the first-crack flexural strength corresponds to the load at which the load-deformation curve departs from linearity. Secondly, the ultimate flexural strength or modulus of rupture corresponds to the maximum load achieved. Both strengths and the post-cracking load-deformation characteristics are affected by the fibre dosage and the type of fibres. Fibre dosages less than 0.5% and aspect ratios less than 50 seem to have a negligible effect on the strength properties, although the effect on the toughness can still be pronounced. Deformed fibres (e.g. hooked-end) on the other hand provide a better anchorage and an increased flexural strength. [32, 59]

Shear

Shear forces are transferred in concrete beams by the mechanisms discussed in Section 2.2.2. For plain concrete, the aggregate interlock and friction at the crack surfaces are the main mechanisms to transfer shear stresses. For SFRC with moderate fibre dosages, the cracking strength is not affected but once cracking occurs, the fibres are activated, bridge the cracks and start to be pulled out, resulting in a toughening behaviour. The shear transfer capacity can be significantly increased with the fibre dosage. For reinforced concrete, the amount of reinforcement crossing the cracks influences the shear capacity and a similar effect is observed for SFRC. [2, 30]

Summary

Adding fibres has a negligible effect on the strength (in compression, tension, flexure or shear). The primary effect of fibres is their ability to improve the post-cracking behaviour and the toughness (i.e. the capacity of transferring stresses after concrete matrix cracking) and the strains at rupture. SFRC fails due to pull-out (consisting of debonding and mechanical deformation) or rupture of the fibres. All parameters are influenced by the amount and type of fibres.

2.3.4 Identification of the material properties

General

The properties of SFRC should not be represented by a single characteristic (similar to the compression strength of normal concretes), since the fibres mainly influence the post-cracking behaviour without changing the compression strength. Therefore, some kind of toughness property is required and other test methods have to be utilised to characterise it. In addition, the type of properties required depends on the constitutive models that are used in numerical analyses. Furthermore, these tests should be included in (inter)national standards in order to compare test results and to derive design strengths parameters.

Consequently, different material identification tests are investigated during the years to measure uniformly the hardened material properties. Although most of them appear to be equal to the material tests of plain concrete, the measurement method of the tensile strength of SFRC differs, due to the influenced post-cracking behaviour. All identification tests are applied in the present experimental research for the characterisation of the used SFRC mixtures. Therefore, the main tests are listed here, together with the corresponding European Standards. For the practical application is referred to Section 3.3.

- The cube compressive strength $f_{c,cube}$ according to EN 12390-3 [8].
- The cylindrical compressive strength f_c according to EN 12390-3 [8].
- The secant modulus of elasticity E_c according to EN 12390-13 [10].
- The residual flexural tensile strength $f_{R,j}$ at $CMOD_j$ and the flexural tensile strength $f_{ct,fl}$ for SFRC according to EN 14651 [9].

Additionally, also different direct tensile test methods exist. These methods, however, have some difficulties inherent to the experimental setup. As a consequence, the post-cracking behaviour of SFRC is generally determined by the more feasible three-point bending test.

EN 14651: residual flexural tensile strength

The standard test method as given in the European Standard EN 14651 [9] determines the residual flexural tensile strength $f_{R,j}$ and the flexural tensile strength $f_{ct,fl}$, also referred as the limit of proportionality (*LOP*), by means of a three-point bending test on a prism with size 150 mm × 150 mm × 600 mm, a notch of 5 mm × 25 mm in the middle and a span length l of 500 mm. The experimental setup is shown in Figure 2.14. The applied load is monitored as a function of the Crack Mouth Opening Displacement (*CMOD*), as presented in Figure 2.15, or the deflection (δ).

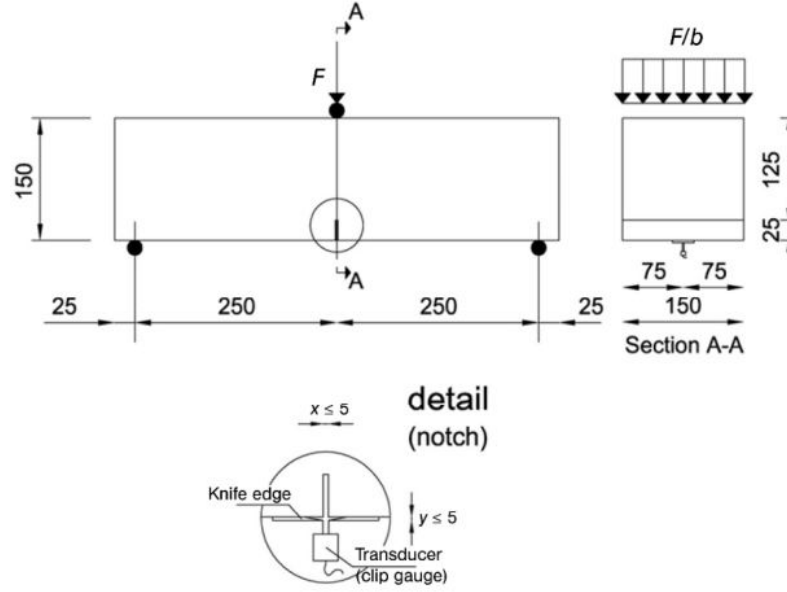


FIGURE 2.14: Experimental setup of EN 14651 (dimensions in mm) [19].

Based on the load- $CMOD$ curve, the residual flexural tensile strengths $f_{R,j}$ in [MPa] are calculated with Equation 2.17 corresponding to $CMOD_j$ (with $j = 1, 2, 3, 4$). $CMOD_1$, $CMOD_2$, $CMOD_3$ and $CMOD_4$ are equal to 0.5, 1.5, 2.5 and 3.5 mm respectively (refer to Figure 2.15). F_j is the load corresponding to $CMOD_j$ in [N]. b is the width of the prism and h_{sp} is the remaining height at the location of the notch, both in [mm].

$$f_{R,j} = \frac{3 \cdot F_j \cdot l}{2 \cdot b \cdot h_{sp}^2} \quad (2.17)$$

The flexural tensile strength $f_{ct,fl}$ in [MPa] is calculated with Equation 2.18. F_L is the maximum load occurring in the range $0 \text{ mm} \leq CMOD \leq 0.05 \text{ mm}$ (refer to Figure 2.16), in [N].

$$f_{ct,fl} = \frac{3 \cdot F_L \cdot l}{2 \cdot b \cdot h_{sp}^2} \quad (2.18)$$

Soetens [60] defines one of the most important issues related to the determination of post-cracking strength parameters of SFRC as the obtained scatter of test results. This scatter is mainly attributed to the variation in mix homogeneity, the orientation and embedded length distribution of fibres in the crack plane, the magnitude of the crack plane area and the concrete strength and fibre dosage variations. Therefore, the obtained test results will be used to derive a characteristic value for design purpose. This is further explained by its application in Section 3.3.1.

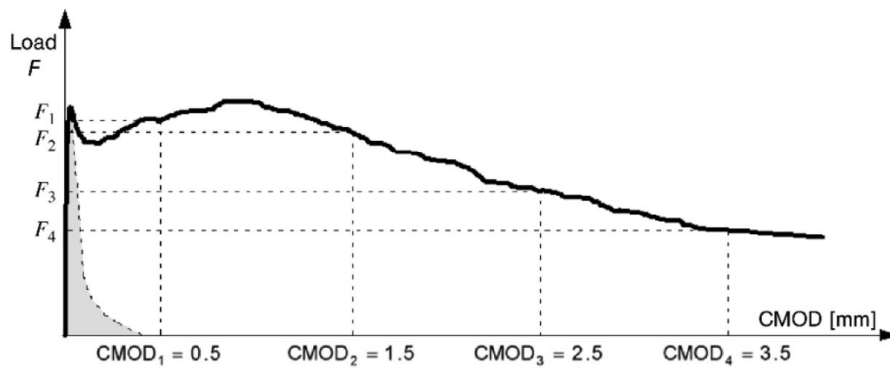


FIGURE 2.15: Typical load-*CMOD* curve, in black for SFRC and in grey for plain concrete [19].

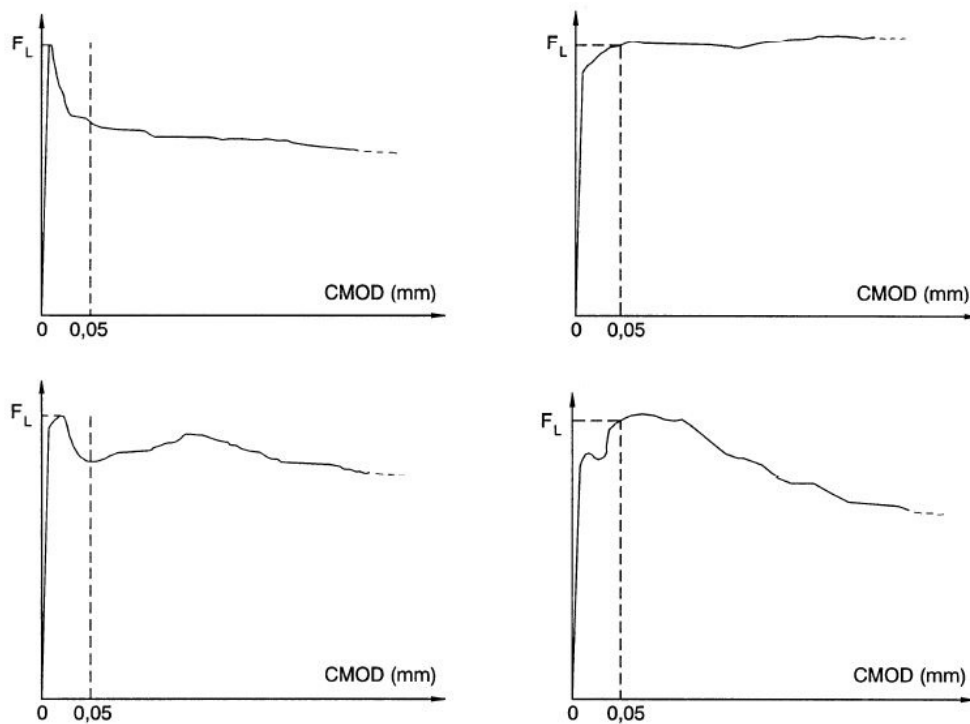


FIGURE 2.16: Other load-*CMOD* curves for SFRC with indication of the maximum load in the defined interval [9].

2.4 Shear in SFRC

The two previous parts of the literature survey, namely shear in concrete and steel fibre reinforced concrete, are now combined in the shear behaviour of (prestressed) SFRC structural elements. In particular the existing analytical models and the performed experiments from literature are summarised in Section 2.4.1. Thereafter, some design codes or models are further elaborated in Section 2.4.2. The Model Code 2010 is described in more detail in Section 2.4.3. These design codes are used to compare with the experimental results in Chapter 4.

2.4.1 Survey on analytical models and shear experiments of SFRC

Since the first research of SFRC in the 1960s by Romualdi and Batson [54] and Romualdi and Mandel [55], SFRC is more and more investigated during the years. Besides, numerous models for the shear capacity of SFRC are developed, mostly (semi-)empirically. Since adding steel fibres to the concrete matrix considerably influences the shear behaviour and capacity, most of the mentioned analytical models of shear in Section 2.2.7 are no longer valid or have to be adapted [34]. An overview of the main experimental investigations and modelling of the shear behaviour and capacity of SFRC beams is given in Appendix A, based on literature. It does not mean to be exhaustive. The 52 listed research programs are performed between 1972 and 2015 and contain SFRC beams with different cross-sections, dimensions and types of reinforcement. Only ten of them are performed with (partially) prestressed SFRC beams, most of which the last fifteen years. Furthermore, many reports published over the past decades confirm the effectiveness of steel fibres as shear reinforcement [32].

However, all these models have some limitations. Firstly, the limited amount of tested specimens and the constraints (choices made in the experimental program) make the resulting models not generally applicable. Secondly, the size of most experimental specimens is relatively small with respect to real elements in building industry, called the size effect. Thirdly, the majority of the existing models does not take into account the effect of a prestressing force on the shear capacity (which is positive, as discussed in Section 2.2.5). In the performed experimental research (described in Chapter 3), only prestressed (SFR)C beams are tested. Therefore, a discussion of non-prestressed models falls outside the scope. Given these points, the focus of this research is put on the more generally accepted models and design codes, also dealing with a level of prestress.

2.4.2 Design codes or models

As concluded in the previous part, the more generally accepted design codes and models dealing with a level of prestress are further elaborated in the present research. There are two ways to evaluate the effect of the presence of steel fibres on the shear capacity [32, 60]. On one hand, a model can incorporate fibre properties, for example the volume of fibres V_f , the aspect ratio of fibres λ_f or the fibre factor F . This method is based on the assumption that steel fibres provide shear strength in excess to the shear strength of plain concrete. The discussed model of this category is the (1) DRAMIX Guideline (1995). On the other hand, a model can incorporate the post-cracking behaviour, measured by material identification tests, instead of fibre properties. This method is based on the assumption that steel fibres directly influence the shear capacity of the concrete. The main discussed design codes or models of this category are the (2) RILEM TC 162-TDF (2003); (3) CNR-DT 204/2006 (2006); (4) Model Code 2010 (2012); and (5) model proposed by Soetens (2015). These five mentioned models will be discussed in the following parts.

Furthermore, the main international building codes are not yet provided with design guidelines for SFRC structural elements, despite the increasing research and the increasing structural applications of SFRC. For example Eurocode 2 (2010) currently does not yet allow SFRC as an alternative for conventional shear reinforcement. Although ACI (American Concrete Institute, 2008) has some requirements for the use of steel fibres, they are so restricted that the application of SFRC is not economical. For example, the concrete compressive strength must be lower than 41 MPa, but most prestressed SFRC elements have a higher strength. Therefore, SFRC is not used as an alternative for conventional shear reinforcement in daily practice. [60]

(1) DRAMIX Guideline (1995)

A technical committee, installed in 1993 on the initiative of the Belgian steel wire manufacturing company N.V. Bekaert, elaborated one of the first guidelines for the design of steel fibre reinforced concrete structures with or without conventional shear reinforcement. The resulting DRAMIX Guideline is based on the state-of-the-art of the research on SFRC until then. The guideline uses the European prestandard ENV 1992-1-1 (Eurocode 2) as a general framework.

The design shear resistance (V_{Rd}) of a section with shear reinforcement is calculated as the sum of the contribution of the concrete (V_{cd}), the contribution of the steel fibre reinforcement (V_{fd}) and the contribution of the vertical and/or inclined shear reinforcement (V_{wd}):

$$V_{Rd} = V_{cd} + V_{fd} + V_{wd} \quad (2.19)$$

The first and the third term, the contribution of concrete and of conventional shear reinforcement respectively, are calculated as defined in European prestandard ENV 1992-1-1, according to the Standard Method. These equations are explained in Section 2.2.8 and repeated here:

$$V_{cd} = \left[\frac{0.18}{\gamma_c} \cdot \left(1 + \sqrt{\frac{200}{d}} \right) \cdot (100 \cdot \rho_l \cdot f_{ck})^{\frac{1}{3}} + 0.15 \cdot \sigma_{cp} \right] \cdot b_w \cdot d \quad (2.20)$$

$$V_{wd} = \frac{A_{sw}}{s} \cdot 0.9 \cdot z \cdot f_{ywd} \quad (2.21)$$

The second term, the contribution of the steel fibres to the shear strength, is calculated with incorporation of the fibre properties aspect ratio and volume of the fibres. The equation is:

$$V_{fd} = k_f \cdot \tau_{fd} \cdot b_w \cdot d \quad (2.22)$$

k_f is a factor taking into account the contribution of the flanges to the shear resistance in I- or T-shaped cross-sections:

$$k_f = 1 + n \cdot \left(\frac{h_f}{b_w} \right) \cdot \left(\frac{h_f}{d} \right) \leq 1.5 \quad (2.23)$$

with

$$n = \frac{(b_f - b_w)}{h_f} \leq \begin{cases} 3 \\ 3 \cdot \frac{b_w}{h_f} \end{cases} \quad (2.24)$$

For uncoated hooked end DRAMIX steel fibres, τ_{fd} is calculated as follows:

$$\tau_{fd} = 0.54 \cdot \frac{f_{ctk,ax} \cdot R_t}{\gamma_c} \quad (2.25)$$

Hereby, $f_{ctk,ax}$ is the characteristic uniaxial tensile strength of concrete and R_t is a factor to calculate the post-cracking stress of SFRC as a fraction of the uniaxial tensile strength. This factor is in function the fibre properties:

$$R_t = \frac{1.1 \cdot V_f \cdot \lambda_f}{180 \cdot 20 + V_f \cdot \lambda_f} \quad (2.26)$$

In addition to the calculation of the design shear resistance, the DRAMIX Guideline provides four requirements for the use of steel fibres.

- (a) A steel fibre reinforced concrete element is a structural element having a minimum fibre content V_f (in volume ratio) of 0.0025.
- (b) Additionally the spacing s between fibres must be smaller then $0.45 \cdot l_f$, with:

$$s = \sqrt[3]{\frac{\pi \cdot d_f^2 \cdot l_f}{4 \cdot V_f}} \quad (2.27)$$

For steel fibres with aspect ratio $\lambda_f \geq 60$, the minimum fibre content of 0.0025 is always determining.

(c) In the case of steel fibres as the only shear reinforcement, the minimum fibre content should be such that the contribution of the steel fibres to the shear resistance is at least the shear resistance of the unreinforced concrete (with γ_c equal to 1.2 for the contribution of steel fibres and 1.5 for the contribution of concrete):

$$0.54 \cdot R_t \cdot k_f \cdot f_{ctk,ax} \cdot \frac{1}{\gamma_c} \geq 1.2 \cdot 0.25 \cdot f_{ctk,ax} \cdot \frac{1}{\gamma_c} \quad (2.28)$$

(d) The fibre dosage must satisfy the condition: $V_f \geq 30 \text{ kg/m}^3$.

The DRAMIX Guideline (1995) incorporates the fibre properties, instead of the post-cracking behaviour. However, this approximation is rather outdated and not longer in accordance with the current developments (of Eurocode 2 for example). Firstly, the same type and amount of fibres in different concrete mixtures result in a different post-cracking behaviour, which is not considered by only taking the fibre properties into account. Secondly, including the post-cracking behaviour is a better approach to design shear resistance since these parameters take into account the scatter of a SFRC mix and therefore lead to a safer design. Thirdly, shear resistance models based on fibre properties are not widely applicable for design purposes since they are only considered to be valid in specific cases. The formulation of the DRAMIX Guideline for example is only valid for uncoated hooked-end DRAMIX steel fibres. [32, 60]

(2) RILEM TC 162-TDF (2003)

The RILEM Technical Committee TC 162-TDF developed the σ - ε -design method in 2000 [67]. This first approach was adapted [66] to the final recommendation in 2003 [68]. The European prestandard ENV 1992-1-1 is used as a general framework in this model. The approach is similar to the DRAMIX Guideline, with the difference of taking into account the post-cracking behaviour instead of fibre properties.

Similar to the DRAMIX Guideline, the design shear resistance (V_{Rd}) of a section with shear reinforcement and with steel fibres is calculated as the sum of the contribution of the concrete (V_{cd}), the contribution of the steel fibre reinforcement (V_{fd}) and the contribution of the vertical shear reinforcement (V_{wd}):

$$V_{Rd} = V_{cd} + V_{fd} + V_{wd} \quad (2.29)$$

The first and the third term are calculated as defined in ENV 1992-1-1, as discussed in the DRAMIX Guideline (refer to Equations 2.20 and 2.21). The second term, the contribution of the steel fibres to the shear resistance, is calculated with:

$$V_{fd} = 0.7 \cdot k_f \cdot k \cdot \tau_{fd} \cdot b_w \cdot d \quad (2.30)$$

The factor k_f is discussed in the DRAMIX Guideline (refer to Equations 2.23 and 2.24) and the factor k in Eurocode 2 (refer to Equation 2.9). τ_{fd} is the design value of the increase in shear strength due to steel fibres and calculated as follows:

$$\tau_{fd} = \frac{0.18}{\gamma_c} \cdot f_{Rk,A} \quad (2.31)$$

Hereby, $f_{Rk,4}$ is the characteristic residual flexural tensile strength of SFRC corresponding to $CMOD_4 = 3.5 \text{ mm}$. This material property of SFRC has to be measured with the standardised three-point bending test on prisms.

A refinement of the previous equations was suggested to take into account the variation of the shear span-to-depth ratio a/d , since this parameter influences the shear capacity. The complete equation of the design shear resistance is equal to:

$$V_{Rd} = \left[\frac{0.15}{\gamma_c} \cdot \sqrt[3]{3 \cdot \frac{d}{a}} \cdot \left(1 + \sqrt{\frac{200}{d}} \right) \cdot (100 \cdot \rho_l \cdot f_{ck})^{\frac{1}{3}} + 0.15 \cdot \sigma_{cp} \right] \cdot b_w \cdot d + \left[0.7 \cdot k_f \cdot \left(1 + \sqrt{\frac{200}{d}} \right) \cdot \frac{1}{\gamma_c} \cdot \frac{d}{a} \cdot \frac{0.5}{0.7} \cdot f_{Rk,4} \right] \cdot b_w \cdot d + V_{wd} \quad (2.32)$$

In addition to the calculation of the design shear resistance, RILEM provides three requirements for the use of steel fibres.

- (a) The proposed model is valid for steel fibre reinforced concrete with compressive strengths of up to C50/60.
- (b) The minimum conventional shear reinforcement can be omitted if sufficient steel fibres are used so that $f_{Rk,4} \geq 1 \text{ N/mm}^2$.
- (c) The minimum shear reinforcement (stirrups and/or steel fibres) must be as such that their shear resistance is at least equal to the shear resistance of plain concrete.

(3) CNR-DT 204/2006 (2006)

The Italian National Research Council (CNR) developed a shear resistance model in 2006, based on the research of Minelli [32]. In this model, the post-cracking behaviour is taken into account and it is assumed that fibres act as a distributed longitudinal reinforcement that enhances the effect of aggregate interlock by a smaller crack width. Therefore, the longitudinal reinforcement ratio is increased in the equation of the shear resistance of plain concrete according to Eurocode 2 (Section 2.2.8) with a factor depending on the residual stress of the SFRC. For elements without design shear reinforcement, with conventional longitudinal reinforcement and with steel fibres, the design shear resistance is given by:

$$V_{Rd} = \left[\frac{0.18}{\gamma_c} \cdot \left(1 + \sqrt{\frac{200}{d}} \right) \cdot \left(100 \cdot \rho_l \cdot \left[1 + 7.5 \cdot \frac{f_{Ftuk}}{f_{ctk}} \right] \cdot f_{ck} \right)^{\frac{1}{3}} + 0.15 \cdot \sigma_{cp} \right] \cdot b_w \cdot d \quad (2.33)$$

The design shear resistance V_{Rd} must be larger than the minimum value $V_{Rd,min}$:

$$V_{Rd,min} = \left[0.035 \cdot \left(1 + \sqrt{\frac{200}{d}} \right)^{3/2} \cdot f_{ck}^{1/2} + 0.15 \cdot \sigma_{cp} \right] \cdot b_w \cdot d \quad (2.34)$$

In addition to the calculation of the design shear resistance, the CNR Guideline provides two requirements for the use of steel fibres.

- (a) The minimum volume fraction of the fibres V_f for structural applications must not be less than 0.003.
- (b) Fibres can replace the conventional shear reinforcement (stirrups) completely if the following limitation is respected:

$$f_{Ftuk} \geq \frac{\sqrt{f_{ck}}}{20} \quad (2.35)$$

This requirement limits the development and the diffusion of the inclined cracking and, as a consequence, can ensure a sufficient member ductility.

(4) Model Code 2010 (2012)

The Model Code 2010 also takes into account the post-cracking behaviour of SFRC. The approach of this model is in accordance with the current developments of the shear design in the latest version of Eurocode 2. The Model Code 2010 contains two design approaches, depending on the level of approximation. These design codes are discussed in more detail in Section 2.4.3.

(5) Model proposed by Soetens (2015)

In his research, Soetens [60] proposed an easy to use alternative model by means of a literature investigation, an analysis of existing design models and a analytical approach of the shear behaviour. The proposed model aims to have a more simplified yet safe shear design for both reinforced and prestressed SFRC elements. The most important shear influencing parameters are incorporated in the calculation of the design shear resistance, namely the shear span-to-depth ratio, the size effect, the dowel action and the prestressing force. The design shear resistance is calculated with:

$$V_{Rd} = \left[0.388 \cdot \sqrt{1 + \frac{\sigma_{cp}}{f_{ctk}}} \cdot \left(1 + \sqrt{\frac{200}{d}} \right) \cdot \left(3 \cdot \frac{d}{a} \cdot \rho_l \right)^{1/3} \cdot \sqrt{f_{cm}} \right] \cdot b_w \cdot z + \left[f_{Ftu}^* \cdot \left(1 + 4 \cdot \frac{\sigma_{cp}}{f_{ck}} \right) \right] \cdot b_w \cdot z \quad (2.36)$$

The first term is the concrete contribution, the second one represents the contribution of the steel fibres. The factor 0.388 is the empirically defined correlation factor between a strain effect factor and the shear capacity of concrete, by means of a linear regression, to avoid an iterative procedure. The fibre contribution is expressed as f_{Ftum} times $\cot(\theta)$. The post-cracking strength for ultimate crack opening is limited to:

$$f_{Ftu}^* = \min \left\{ \begin{array}{l} f_{Ftum} \\ f_{ctm} \cdot \left(1 - \frac{2 \cdot \sigma_{cp}}{f_{cm}} \right) \end{array} \right. \quad (2.37)$$

Furthermore, Soetens defines the inclination of the shear crack in function of the amount of prestressing:

$$\cot(\theta) = \left(1 + 4 \cdot \frac{\sigma_{cp}}{f_{ck}}\right) \quad (2.38)$$

This formulation of $\cot \theta$ is fundamentally different from Eurocode 2 (refer to Section 2.2.8) where $\cot(\theta)$ may be chosen freely between 1 and 2.5 (Equation 2.14). The Belgian national application document (ANB) even increases the maximum value according to Equation 2.15. Figure 2.17 presents these different formulations for a concrete compressive strength of 50 MPa and the geometrical properties of the tested specimens (refer to Chapter 3). The model of Soetens results in a lower value of $\cot \theta$, corresponding to a larger inclination of the shear cracks θ , than the ANB. Mainly for highly prestressed elements, the inclination will decrease. Therefore, it can be expected that the model of Soetens will be less accurate for higher prestressing forces.

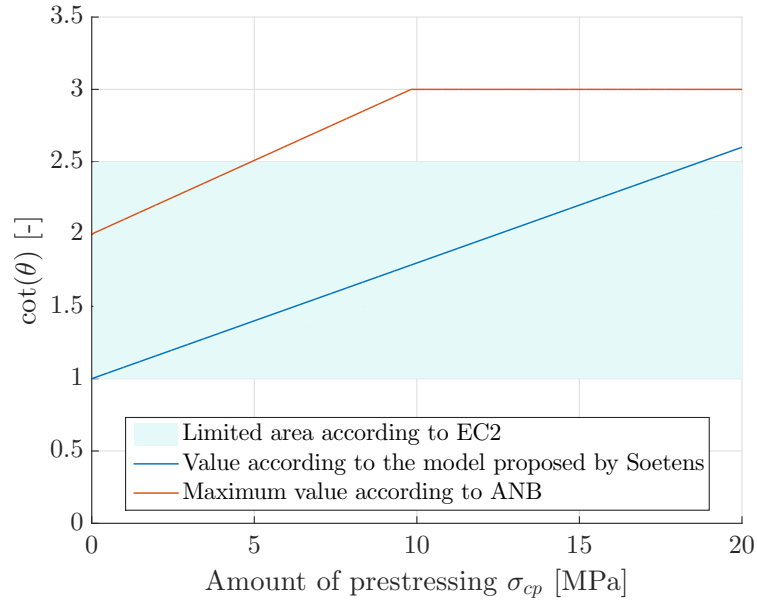


FIGURE 2.17: Inclination of the shear cracks in function of the amount of prestressing according to different analytical models (with $f_{ck} = 50$ MPa and the geometrical properties of the experimentally tested specimens).

2.4.3 Design Code: Model Code 2010

The International Federation for Structural Concrete (*fib*) is a pre-normative organization that developed the Model Code 2010 [19] (denoted as MC2010). The first Model Codes were published in 1978 and 1990. The recent version of 2010 includes new types of reinforcement, such as fibres. Two different analytical models to take into account the effect of steel fibres are proposed in MC2010. They are fundamentally different, although both incorporate the post-cracking behaviour instead of the fibre properties to calculate the effect on the shear capacity of beams without conventional shear reinforcement. The two approaches, A and B, are both discussed. [33]

Besides the two approaches to calculate the design shear resistance, MC2010 provides a requirement for the use of steel fibres. Fibres can replace the conventional shear reinforcement (stirrups) (partially) if the following requirements are fulfilled:

$$f_{R1,k}/f_{ctk,fl} > 0.4 \quad (2.39)$$

$$f_{R3,k}/f_{R1,k} > 0.5 \quad (2.40)$$

Furthermore, the minimum amount of shear reinforcement, provided by either stirrups or fibres, is not required if the following limitation is respected:

$$f_{Ftuk} \geq 0.08 \cdot \sqrt{f_{ck}} \quad (2.41)$$

This requirement limits the development and the diffusion of the inclined cracking and, as a consequence, can ensure a sufficient member ductility.

Model Code 2010 (A)

The first approach, denoted as Model Code 2010 (A) or MC2010A, is based on the current Eurocode 2 formulation for plain concrete and modifies the longitudinal reinforcement ratio with a factor that takes into account the toughness properties of SFRC. This approach is based on the research of Minelli [32] and consequently equal to the model given in the CNR code.

It is assumed that fibres act as a distributed longitudinal reinforcement which enhance the effect of aggregate interlock by a smaller crack width. Therefore, the longitudinal reinforcement ratio is increased in the equation of the shear resistance of plain concrete according to Eurocode 2 (Section 2.2.8) with a factor depending on the residual stress of the SFRC. For elements without design shear reinforcement, with conventional longitudinal reinforcement and with steel fibres, the design shear resistance is given by:

$$V_{Rd} = \left[\frac{0.18}{\gamma_c} \cdot k \cdot \left(100 \cdot \rho_l \cdot \left[1 + 7.5 \cdot \frac{f_{Ftuk}}{f_{ctk}} \right] \cdot f_{ck} \right)^{\frac{1}{3}} + 0.15 \cdot \sigma_{cp} \right] \cdot b_w \cdot d \quad (2.42)$$

With k a factor taking into account the size effect:

$$k = \left(1 + \sqrt{\frac{200}{d}} \right) \leq 2.0 \quad (2.43)$$

f_{Ftuk} is the characteristic value of the ultimate residual tensile strength for SFRC, by considering the crack width $w_u = 1.5$ mm. It can be calculated according to the two different stress-crack opening constitutive laws as discussed before. On one hand, the rigid-plastic model assumes f_{Ftuk} to be a constant value equal to $f_{Rk,3}/3$. On the other hand, the linear post-cracking behaviour (hardening or softening) results in the following equation:

$$f_{Ftuk} = 0.45 \cdot f_{Rk,1} - \frac{w_u}{CMOD_3} \cdot (0.45 \cdot f_{Rk,1} - 0.5 \cdot f_{Rk,3} + 0.2 \cdot f_{Rk,1}) \geq 0 \quad (2.44)$$

Whereby $CMOD_3$ is equal to 2.5 mm. This formulation will be used in the calculations.

The design shear resistance V_{Rd} must be larger than the minimum value $V_{Rd,min}$:

$$V_{Rd,min} = \left[0.035 \cdot k^{3/2} \cdot f_{ck}^{1/2} + 0.15 \cdot \sigma_{cp} \right] \cdot b_w \cdot d \quad (2.45)$$

This simple formulation is based on an empirical approach and commonly used for the design of prestressed concrete beams. It is easily converted to the design of prestressed SFRC beams. However, this approach is not consistent with the general design formulations of MC2010 for reinforced concrete beams without fibres (section 7.3 of Model Code 2010). Therefore, the second approach was developed.

Model Code 2010 (B)

The second approach, denoted as Model Code 2010 (B) or MC2010B, is explained in the commentary section of the Model Code 2010 and consistent with section 7.3 of this code. The model aims to be more physical based and its basis is formed from the simplified modified compression theory (refer to Section 2.2.7). The design shear resistance of plain concrete is extended for elements without design shear reinforcement, with conventional longitudinal reinforcement and with steel fibres:

$$V_{Rd} = \frac{1}{\gamma_F} \cdot \left(k_v \cdot \sqrt{f_{ck}} + k_f \cdot f_{Ftuk} \cdot \cot \theta \right) \cdot b_w \cdot z \quad (2.46)$$

Hereby, the first term takes into account the concrete contribution caused by aggregate interlocking with $\sqrt{f_{ck}}$ limited to 8 MPa. This limitation is provided due to the larger observed variability in shear strength of elements with higher strength concrete, particularly for elements without stirrups.

k_v is a strain effect factor depending on the level of approximation. Model Code 2010 uses different levels of approximation to determine the shear capacity of a structural element. A method with a higher level has more complexity but also a higher accuracy. For the calculation of the shear capacity of SFRC elements, k_v is determined according to the level II approximation, for beams without conventional shear reinforcement ($\rho_w = 0$), as:

$$k_v = \frac{0.4}{1 + 1500 \cdot \epsilon_x} \cdot \frac{1300}{1000 + k_{dg} \cdot z} \quad (2.47)$$

k_{dg} is an aggregate size influence parameter, given by:

$$k_{dg} = \frac{32}{16 + d_g} \leq 0.75 \quad (2.48)$$

where d_g is the maximum aggregate size in mm. If d_g is less than 16 mm, k_{dg} may be taken equal to 1.0.

ϵ_x is the longitudinal strain at the mid-depth of the effective depth. It is estimated by taking half of the strain at the bottom of the beam and is limited by 0.003. If the value of ϵ_x is negative, it must be taken as zero. For elements with prestressed strands and without conventional longitudinal reinforcement, the strain is calculated with:

$$\epsilon_x = \frac{1}{2} \cdot \frac{1}{E_p \cdot A_p} \cdot \left[\frac{M_{Ed}}{z} + V_{Ed} + N_{Ed} \cdot \frac{z - e_p}{z} \right] \quad (2.49)$$

e_p is the distance between the neutral axis and the prestressed reinforcement. M_{Ed} and V_{Ed} are taken as positive quantities and N_{Ed} as negative for compression. The prestressing force F_p is included in the sectional forces as follows:

$$M_{Ed} = V_{Rd} \cdot a - F_p \cdot e_p \quad (2.50)$$

$$N_{Ed} = -F_p \quad (2.51)$$

$$V_{Ed} = V_{Rd} \quad (2.52)$$

To calculate the shear capacity V_{Rd} , the longitudinal strain ϵ_x must be determined (Equation 2.46). To determine ϵ_x , the shear capacity V_{Rd} must be known (Equations 2.50 and 2.52). This results in solving the equations iteratively.

The second term of the calculation of the shear capacity V_{Rd} takes into account the contribution of the fibres with k_f a reduction factor counting for the variation of fibre dispersion and post-cracking behaviour between the material identification tests and the actual beams. The value of k_f is equal to 0.8. f_{Ftuk} is the characteristic value of the ultimate residual tensile strength for SFRC, as explained in the previous part, but calculated with the crack width w_u taken as:

$$w_u = 0.2 + 1000 \cdot \epsilon_x \geq 0.125 \text{ mm} \quad (2.53)$$

The inclination of the shear critical cracks θ may be chosen freely between defined limits equal to:

$$\theta_{\min} \leq \theta \leq 45^\circ \quad (2.54)$$

where the minimum strut inclination angle is determined by the level of approximation. For the used level II of approximation, θ_{\min} equals:

$$\theta_{\min} = 29^\circ + 7000 \cdot \epsilon_x \quad (2.55)$$

The approach of Model Code 2010 (B) is in line with the general design formulations of MC2010 for reinforced concrete beams without fibres (Section 7.3 of Model Code 2010). However it must be solved iteratively, resulting in a more complex approximation.

2.5 Conclusion

In this chapter, the framework of the research is introduced and the state-of-the-art of the different aspects is explained, based on a literature survey.

Firstly, shear in concrete is investigated. Shear force appears in combination with a varying bending moment. After cracking of the concrete, the following mechanisms transfer the shear stresses in a structural concrete element: shear stresses in uncracked concrete, interface shear transfer, dowel action, arch action, residual tensile stresses and eventually the shear reinforcement. Also the different failure modes due to shear force and bending moment are discussed. The main influencing parameters are the concrete quality and strength, the effective depth, the shear span-to-effective depth ratio, the longitudinal and shear reinforcement and lastly the level of prestress. An overview of the main shear experiments, databases and analytical models in literature is made. Lastly, the shear design procedure according to Eurocode 2 is elaborated.

Secondly, the material steel fibre reinforced concrete is discussed, starting with its background and historical development. The material is described based on the concrete, the different types of fibres and the bonding in between. This bonding is of major importance for the mechanical behaviour and the capacity of SFRC. Adding fibres has a negligible effect on the strength (in compression, tension, flexure or shear). Their primary effect is improving the post-cracking behaviour and the toughness and the strains at rupture. SFRC fails due to pull-out (consisting of debonding and mechanical deformation) or rupture of the fibres. All parameters are influenced by the amount and type of fibres. Lastly, the identification of the material properties is discussed, with the determination of the flexural tensile strengths in more detail.

Thirdly, the combination of shear and SFRC is made by a survey of the existing analytical models and performed shear experiments of SFRC in literature. Based on this, five more generally accepted design codes or models are further elaborated, namely the DRAMIX Guideline, the RILEM method, the CNR code, the Model Code 2010 and the model proposed by Soetens. These models are valid for prestressed SFRC beams, whether or not reinforced with conventional stirrups.

This literature survey introduced the main aspects (i.e. mechanisms, influencing parameters and models) of shear behaviour and steel fibre reinforced concrete. The combination of both leads to design codes for the shear capacity of (prestressed) SFRC beams. After performing the experimental research as described in the following chapter, the calculations of the design codes will be compared with the observed results in Chapter 4.

Chapter 3

Experimental research

3.1 Aims of the research

Experimental research is performed to investigate the mechanical behaviour of prestressed SFRC beams, failing in shear. Using various measurement methods, the mechanical behaviour of prestressed SFRC is to be obtained. Six beams with I-shaped cross section are subjected to a four-point bending test with a cyclic loading pattern until failure.

Figure 3.1 gives a schematic overview of the classification of the tested beams based on the investigated parameters. Some characteristics are designed similar to the shear tests of De Wilder [13], in order to compare both experimental programs. Each beam has the same dimensions, three main parameters are investigated:

- Fibre dosage V_f : 0 kg/m³, 20 kg/m³ or 40 kg/m³
- Amount of conventional shear reinforcement ρ_w : 0 or 2.693×10^{-3} [-]
- Amount of prestressing σ_{p0} : 750 MPa or 1488 MPa

With the reported test results, an analytical study and a numerical simulation are performed. The latter is done by Tom Schoofs and Vincent Van de Poel as part of their master thesis. The analytical study contains an investigation of the main parameters and a comparison with results of analytical models, refer to Chapter 4.

Section 3.2 describes the experimental specimens, their design, materials and production process. Identification tests to obtain the hardened material properties are reported in Section 3.3. Section 3.4 presents the experimental setup and the loading pattern of the four-point bending test. Section 3.5 discusses the adopted measurement methods, together with the necessary preparation of the experimental specimens. In Section 3.6, some calculations are made to estimate the prestress losses and the crack load. The results of the tests for each beam are discussed in Section 3.7. The last Section 3.8 summarizes the main conclusions of the experimental research.

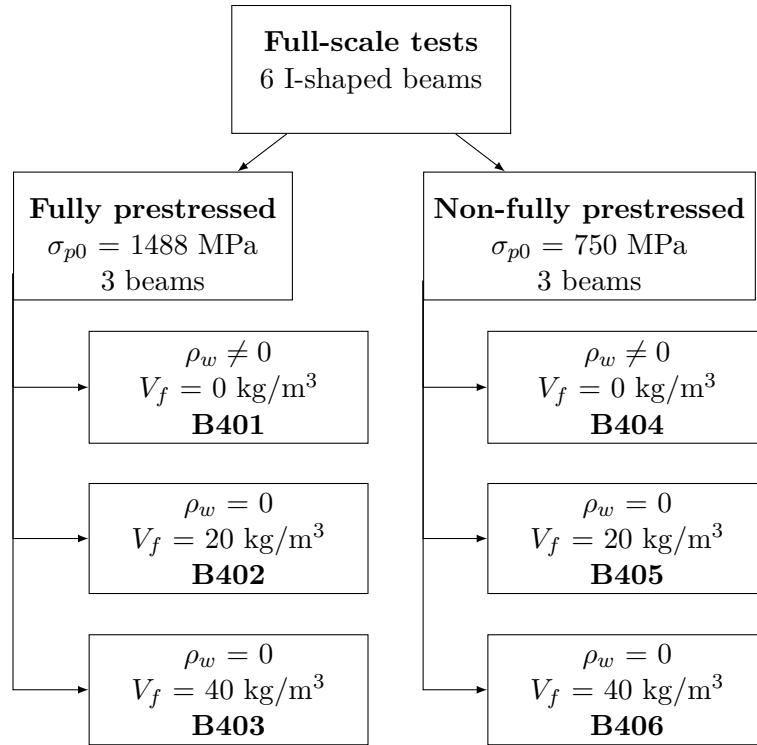


FIGURE 3.1: Schematic overview of the experimental research, classified according to the amount of prestressing (σ_{p0}), with ($\rho_w \neq 0$) or without ($\rho_w = 0$) shear reinforcement, the amount of steel fibres V_f and with their name (B40x).

Figure 3.2 gives a an overview of the experimental research. The flowchart shows, at the left side, the several steps of the production and testing procedure. At the right side, measurements and calculations contributing to the step are mentioned. The different described sections are referred to with their number in blue.

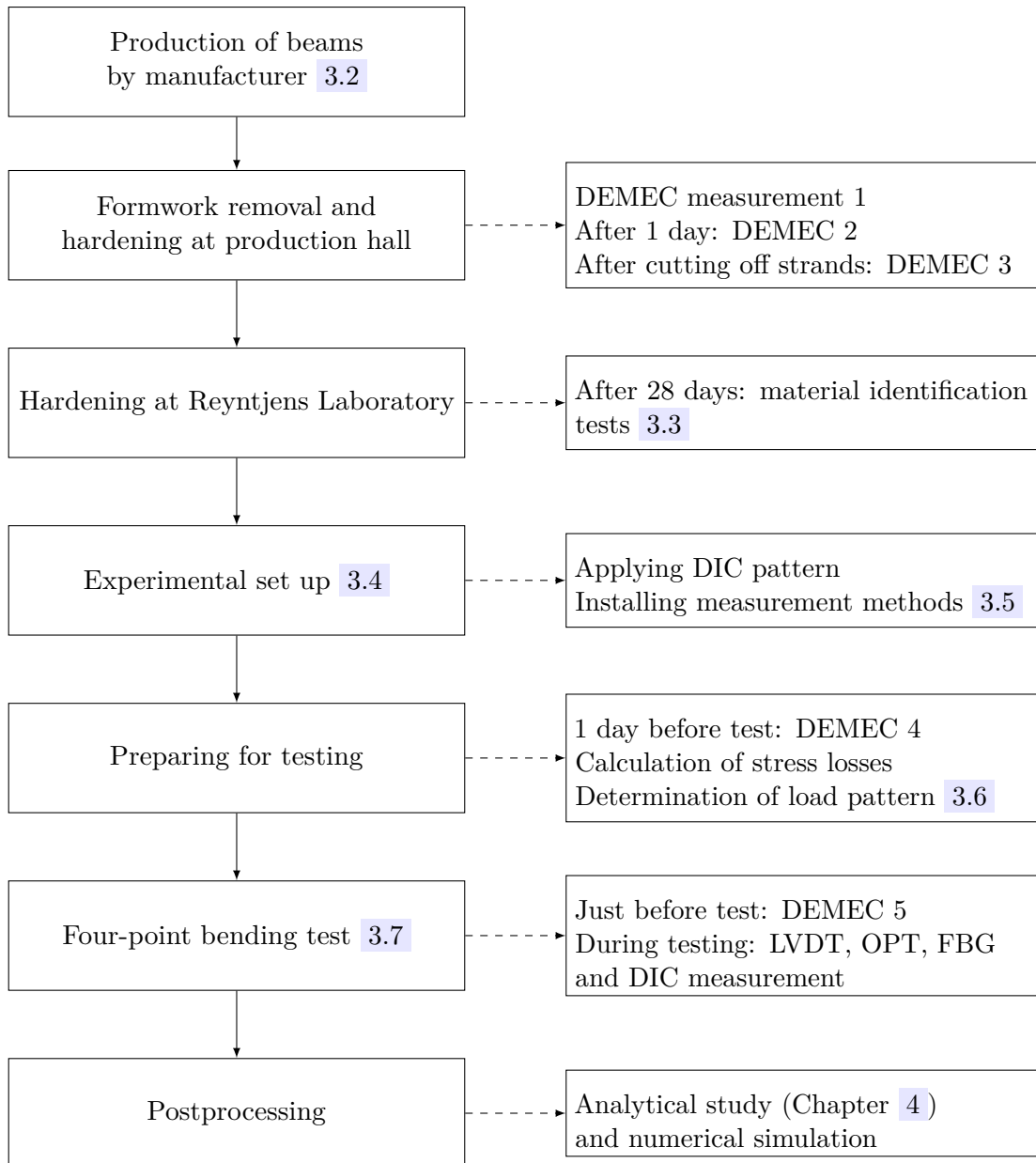


FIGURE 3.2: Flowchart of the experimental research. The numbers in blue correspond to the sections in which these parts are described.

3.2 Experimental specimens

3.2.1 Beam design

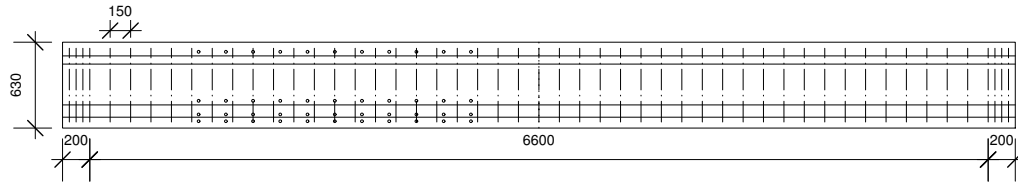
The experimental specimens contain six I-shaped beams with a constant height. Table 3.1 gives an overview of the different characteristics. The beams are denoted with the letter B and a number varying from 401 to 406, as also shown in Figure 3.1. Each beam, with an I-shaped cross section, has a length of 7000 mm, a height of 630 mm, a flange width of 240 mm and a web width of 70 mm. The effective depth equals 557 mm. Figure 3.3 and 3.4 show the longitudinal view and the cross sections of the experimental specimens, with indication of the geometry and the reinforcement layout.

The beams are prestressed with seven-wire low-relaxation (stress loss due to relaxation after 1000 hours ρ_{1000} is less than or equal to 2.5%) strands: seven at the bottom and one at the top of the beams. The strand at the top avoids cracking at the top, induced by the bending moment of the eccentric applied prestressing force. The nominal diameter of one strand is equal to 12.5 mm, the corresponding area of one strand is 93 mm². The amount of prestressing is one of the investigated parameters and differs for the experimental specimens. The stress value in the strands σ_{p0} is equal to 750 MPa for B404, B405 and B406 (an initial prestrain of $3.8 \cdot 10^{-3}$ mm/mm of the strands), and equal to 1488 MPa for B401, B402 and B403 (an initial prestrain of $7.5 \cdot 10^{-3}$ mm/mm of the strands). Although reducing stress levels below the allowable is unconventional in industry, it is applied to investigate the influence of the prestressing force on the shear capacity while the longitudinal reinforcement ratio remains constant.

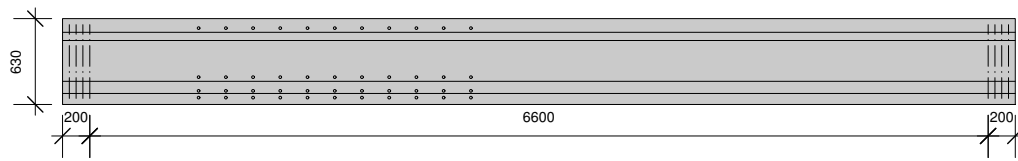
In four of the six beams, the conventional shear reinforcement is replaced by steel fibres (Dramix RC-80/30-CP, length 30 mm, diameter 0.38 mm, tensile strength 3070 MPa). These fibres are added to the fresh concrete mixture in different dosages, namely 20 kg/m³ (B402 and B405) or 40 kg/m³ (B403 and B406). Two beams without steel fibres (B401 and B404) have conventional shear reinforcement, consisting of single-legged stirrups with nominal diameter of 6 mm and centre-to-centre distance of 150 mm. All beams are provided with splitting reinforcement, characterised by a nominal diameter of 8 mm and centre-to-centre distance of 50 mm, in order to withstand the gradual growth of the prestressing force over the beam height.

3.2.2 Materials

Depending on the amount of steel fibres in the beams, three different concrete mixtures are used, as listed in Table 3.2. Each mixture contains early-strength Portland cement CEM I 52.5 R, sand with a maximum size of 2 mm and limestone gravel with a maximum size of 12 mm. Also limestone filler and a high-range water reducer are added. To improve the workability of the concrete mixture with 40 kg/m³ steel fibres, blast furnace slag is used to partially replace cement and the water-cement ratio is increased from 0.44 to 0.57. All mixtures are designed to have a characteristic

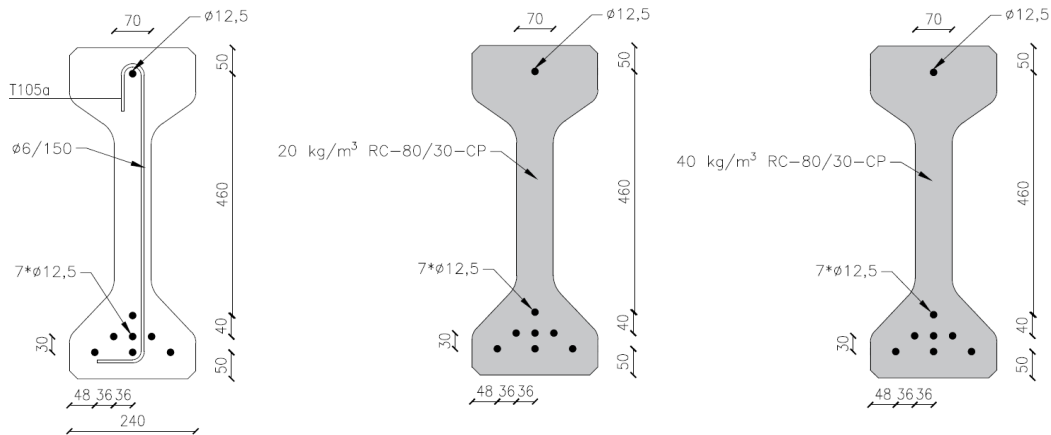


(a) B401 and B404



(b) B402, B403 and B405, B406

FIGURE 3.3: Longitudinal view of the experimental specimens (note: SFRC specimens are shaded grey; units in mm; DEMEC points are indicated with \circ).



(A) B401 and B404

(B) B402 and B405

(C) B403 and B406

FIGURE 3.4: Cross sections and reinforcement layout of the experimental specimens (note: SFRC specimens are shaded grey; units in mm).

3. EXPERIMENTAL RESEARCH

TABLE 3.1: Overview of the experimental program and the investigated parameters.

Beam	L [mm]	h [mm]	d [mm]	b_w [mm]	σ_{p0} [MPa]	a [-]	$\frac{a}{d}$ [-]	ρ_l [-]	ρ_w [$\times 10^{-3}$]	$V_f \bullet$ [kg/m ³]
B401	7000	630	557	70	1488	2200	3.95	0.0167	2.693	0
B402	7000	630	557	70	1488	2200	3.95	0.0167	0	20
B403	7000	630	557	70	1488	2200	3.95	0.0167	0	40
B404	7000	630	557	70	750	2200	3.95	0.0167	2.693	0
B405	7000	630	557	70	750	2200	3.95	0.0167	0	20
B406	7000	630	557	70	750	2200	3.95	0.0167	0	40

Note: \bullet : Bekaert Dramix RC-80/30-CP

TABLE 3.2: Concrete mixture composition of the experimental specimens.

Material	Mixture 1 (B401, B404) Amount [kg/m ³]	Mixture 2 (B402, B405) Amount [kg/m ³]	Mixture 3 (B403, B406) Amount [kg/m ³]
Steel fibres RC-80/30-CP	0.0	20.0	40.0
CEM I 52.5 R	368.0	375.3	306.7
Blast furnace slag	0.0	0.0	128.7
Sand 0/2	700.0	700.0	680.7
Limestone gravel 2/12	1123.0	1090.7	1006.0
Water	106.7	107.3	122.7
Limestone filler	130.7	131.3	149.3
High-range water reducer	5.4	5.4	5.6

cylindrical compressive strength f_{ck} of 50 MPa (concrete class C50/60). Although the concrete is self-compacting, mechanical vibration to obtain a better compaction is applied for the beams with steel fibres (B402, B403 and B405, B406).

The material properties of the reinforcement are given in Table 3.3. It shows the nominal diameter d_p or d_s , the modulus of elasticity E_p or E_s and the strain at failure ϵ_{pu} or ϵ_{su} . For the prestressing reinforcement, 0.1% proof stress and ultimate tensile stress, $f_{p0.1m}$ and f_{pm} respectively, are presented. The same prestressing strands are used at the top and the bottom of the beams. For the conventional reinforcement, yield and ultimate tensile stress, f_{ym} and f_{tm} respectively, are shown. The properties of the prestressing reinforcement are taken from the manufacturer. The properties of shear and splitting reinforcement were tested by De Wilder [13] in previous research, by performing displacement controlled tensile tests. The same reinforcement is used in this research.

TABLE 3.3: Reinforcement properties of the experimental specimens [13].

Reinforcement	Type	d_p	E_p	$f_{p0.1m}$	f_{pm}	ϵ_{pu}
		d_s	E_s	f_{ym}	f_{tm}	ϵ_{su}
		[mm]	[GPa]	[MPa]	[MPa]	[%]
Prestressing reinforcement	7-wire strands	12.5	198.0	1737	1930	5.20
Shear reinforcement	Cold worked	6.0	210.0	608	636	2.73
Splitting reinforcement	Cold worked	8.0	203.0	542	603	5.97

Note: subscript p stands for prestressing and s for conventional reinforcement bars

3.2.3 Production process

All tested beams are fabricated at the precast concrete manufacturer Ergon nv (Lier, Belgium). The production process (Figure 3.6) starts with making concrete at the manufacturing site, where steel fibres are added as the last component. In the following step, the SFRC mixture is transported to the production hall and cast into the formworks (Figure 3.6a) from a concrete bucket (Figure 3.6b). The beams with steel fibres are briefly mechanically vibrated. Together with each beam, small specimens are made of the same mixture to determine the hardened material properties as reported in Section 3.3.

In the production hall, two lines are used depending on the amount of prestressing. One batch of 1.5 m^3 (steel fibre reinforced) concrete is used for two beams. This configuration is schematically presented in Figure 3.5, together with the dates of casting and formwork removal.

After one day of hardening, the formwork of the beams is removed (Figure 3.6c). When the cube compressive strength exceeds the limit of 45 N/mm^2 , the prestressing force is transferred to the (SFRC) beams by cutting the strands (Figure 3.6d). The pieces are stored at the manufacturer for hardening and transported to the Reyntjens Laboratory of the Civil Engineering Department of KU Leuven (Leuven, Belgium) for testing after at least 28 days. During this production process, several measurements are performed, which are reported in Section 3.5.

3. EXPERIMENTAL RESEARCH

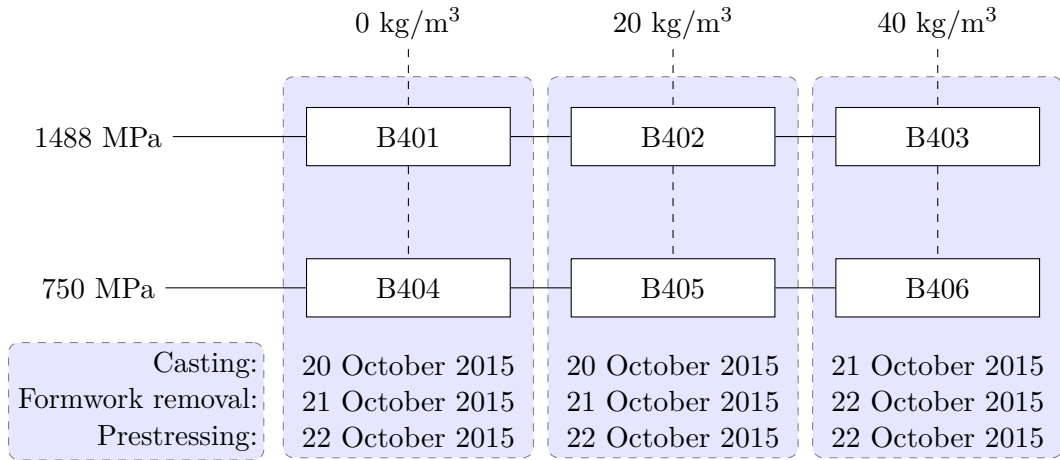


FIGURE 3.5: Configuration of the two lines and three concrete mixtures of the production process.



(A) Formwork with reinforcement.



(B) Casting the formwork with SFRC.



(C) Formwork removal.



(D) Transferring prestressing force.

FIGURE 3.6: Four steps of the production process.

3.3 Material properties identification

One batch of (steel fibre reinforced) concrete is made in an amount of 1.5 m³. For the six beams, three batches of concrete are used, one per fibre dosage (refer to Figure 3.5). Together with each beam, some additional small specimens are cast from the same batch, in order to determine the hardened properties by material identification tests. For each beam, the following samples are made:

- 3 cubes of 150 x 150 x 150 mm³ to determine the mean cube compressive strength $f_{cm,cube}$ according to EN 12390-3 [8] (Figure 3.7a).
- 3 cylinders of height 300 mm and diameter 150 mm to determine the secant modulus of elasticity E_{cm} and the mean cylindrical compressive strength f_{cm} according to EN 12390-13 [10] and EN 12390-3 [8] respectively (Figure 3.7b).
- 3 prisms of 150 x 150 x 600 mm³ to determine the flexural tensile strength $f_{ctm,fl}$ for plain concrete and the residual flexural tensile strength $f_{Rm,j}$ at $CMOD_j$ for SFRC, according to EN 12390-5 [7] and EN 14651 [9] respectively (Figure 3.7c).

Table 3.4 gives an overview of the experimentally determined material properties of the reported test beams, together with the mean density and the age at the four-point bending test of the beam. The different material properties and testing methods are further explained in the following parts. Firstly, some background information on the mean and characteristic values of the material properties is given.

TABLE 3.4: Experimentally determined material properties of the (SFR)C mixtures.

Specimens	$f_{cm,cube}$ [MPa] (#•,s••)	f_{cm} [MPa] (#,s)	E_{cm} [GPa] (#,s)	$f_{ctm,fl}$ [MPa] (#,s)	ρ_m [kg/m ³] (#,s)	Age [days]
B401	79.4 (3, 3.49)	75.6 (3, 0.94)	45.4 (3, 1.89)	9.5 (3, 0.40)	2431 (6, 7.52)	38
B402	65.0 (3, 1.28)	73.8 (3, 7.14)	39.5 (3, 1.05)	5.0 (3, 0.24)	2364 (6, 18.34)	43
B403	67.7 (3, 1.03)	69.7 (3, 4.63)	41.1 (3, 1.21)	5.5 (3, 0.18)	2395 (6, 9.38)	47
B404	97.9 (3, 0.85)	68.1 (2, -)	47.8 (2, -)	5.5 (3, 0.18)	2434 (6, 11.68)	52
B405	78.1 (3, 1.18)	79.4 (3, 3.47)	41.1 (3, 1.07)	4.2 (3, 0.17)	2363 (6, 11.29)	56
B406	89.5 (3, 0.12)	77.4 (3, 12.27)	44.5 (3, 4.59)	5.6 (3, 0.28)	2389 (6, 9.56)	57

Note: •: # denotes the number of tested specimens,
••: s denotes the standard deviation

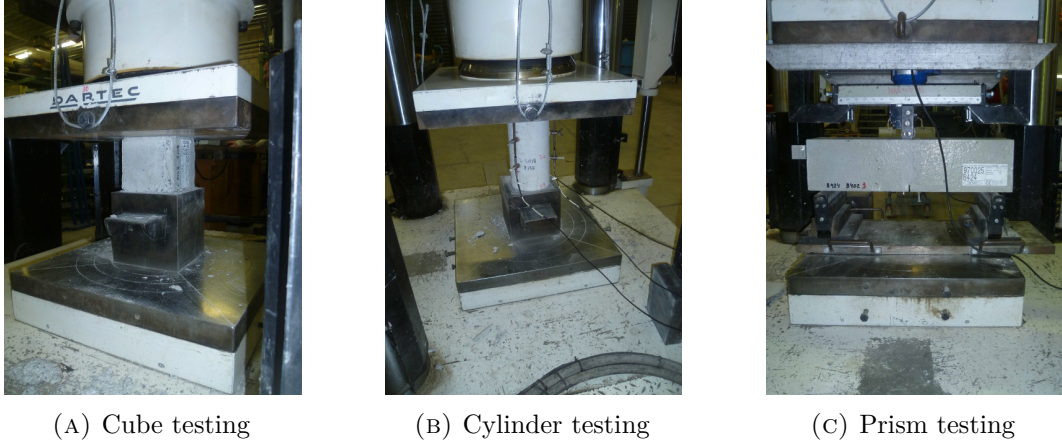


FIGURE 3.7: Experimental setup for testing of the cubes, cylinders and prisms to determine hardened material properties.

3.3.1 Mean and characteristic values

Material identification tests result in average values and standard deviations of the material properties. However, the characteristic values are mostly used for material classification. This value is the 5% fractile value of the assumed statistical distribution of the material property. For design calculations, these characteristic values are transformed to design values with the use of partial safety factors.

Generally, a Normal (or Gaussian) distribution is assumed. In this case, characteristic values f_k are calculated with Equation 3.1 [40]. f_m denotes the mean value of the material property (Equation 3.2, n is the number of specimens) and s is the standard deviation (Equation 3.3), as shown in Table 3.4. k is a constant value in function of the number of tests and the coefficient of variation COV. All properties are tested on three pieces ($n = 3$), which results in $k = 3.37$ for COV unknown. Equation 3.1 implies a lower characteristic value if the scatter of the test results is higher.

$$f_k = f_m - k \cdot s \quad (3.1)$$

$$f_m = \frac{1}{n} \cdot \sum_{i=1}^n (f_i) \quad (3.2)$$

$$s = \sqrt{\frac{1}{n-1} \cdot \sum_{i=1}^n (f_i - f_m)^2} \quad (3.3)$$

For small values of material properties, for example the tensile strength of concrete, the Normal distribution can lead to (unrealistic) negative characteristic values. Adopting a log-normal distribution has the advantage that no negative values can occur. In this case, characteristic values are calculated with Equation 3.4 [40]. The mean value in the log-normal distribution $f_{m,ln}$ is defined with Equation 3.5 and the s_{ln} with Equation 3.6.

$$f_{k,ln} = \exp(f_{m,ln} - k \cdot s_{ln}) \quad (3.4)$$

$$f_{m,ln} = \frac{1}{n} \cdot \sum_{i=1}^n \ln(f_i) \quad (3.5)$$

$$s_{ln} = \sqrt{\frac{1}{n-1} \cdot \sum_{i=1}^n (\ln(f_i) - f_{m,ln})^2} \quad (3.6)$$

These formulation will be used in some of the next sections to determine characteristic values for material classification. A remark which has to be made is that all measured material properties will be used for calculations, without including the effect of the age at day of testing and the conditions of hardening (temperature and relative humidity). These parameters are unknown and it would be more inaccurate to estimate them all than to use the measured properties.

3.3.2 Cube compressive strength

The mean cube compressive strength $f_{cm,cube}$ is measured according to EN 12390-3 [8], in load-control with a hydraulic press (Dartec, maximum capacity 5 MN) (refer to Figure 3.7a). The constant loading rate equals 0.6 MPa/s, which is equivalent to 13.5 kN/s for cubes with a side of 150 mm². The cube compressive strength (in MPa) is calculated with Equation 3.7. F_{max} is the maximum load at failure in [N] and $A_{c,cube}$ is the cross-sectional area of the cube in [mm²].

$$f_{c,cube} = \frac{F_{max}}{A_{c,cube}} \quad (3.7)$$

Figure 3.8 gives the results for three cubes per beam, with indication of the mean value in the red dotted line. The cubes of beams B401, B402 and B403 are tested at an age of 30 days, the cubes of beams B404, B405 and B406 at an age of 48 days. All concrete mixtures have a designed concrete class C50/60. The characteristic cube compressive strengths (calculated with Equation 3.1) vary between 60.6 MPa (B402) and 95.0 MPa (B404). Indeed, the results show a characteristic cube compressive strength equal to or higher than 60 MPa.

Concrete without steel fibres (B401 and B404) have a higher strength, due to the less entrapped air caused by the presence of fibres. Although a higher amount of fibres results in a higher cube compressive strength (comparing B403 to B402 and B406 to B405), this is mainly caused by the concrete mixtures instead of the presence of fibres. The strength of B404, B405 and B406 is larger compared to the cubes of the same concrete batch (B401, B402 and B403 respectively) because of their age of 48 days instead of 30 days. The hardening process continues in time, with an increasing strength as result.

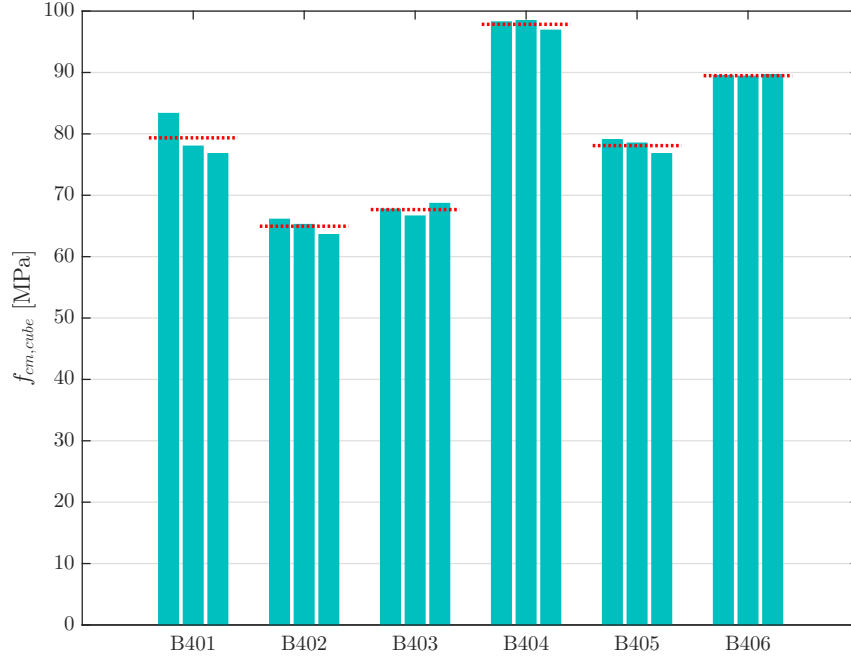


FIGURE 3.8: Experimental results of the cube compressive strength for three cubes per beam. The red dotted line indicates the mean value for each beam.

3.3.3 Cylindrical compressive strength

The mean cylindrical compressive strength f_{cm} is measured according to EN 12390-3 [8], in load-control with a hydraulic press (Dartec, maximum capacity 5 MN) (refer to Figure 3.7b). The constant loading rate equals 0.6 MPa/s, which is equivalent to 10.6 kN/s for cylinders with diameter of 150 mm². The cylindrical compressive strength (in MPa) is calculated with Equation 3.8. F_{max} is the maximum load at failure in [N] and $A_{c,cylinder}$ is the cross-sectional area of the cylinder in [mm²].

$$f_c = \frac{F_{max}}{A_{c,cylinder}} \quad (3.8)$$

Figure 3.9 gives the results for three cylinders per beam, with indication of the mean value in the red dotted line. The cylinders of beams B401, B402 and B403 are tested at an age of 30 days, the cylinders of B404, B405 and B406 at 62 days. All concrete mixtures have a designed concrete class C50/60. The characteristic cylinder compressive strengths are equal to or higher than the designed values, namely varying between 49.7 MPa (B402) and 72.4 MPa (B401). The high standard deviation of B402 (7.14) causes a slightly lower value of B402 (49.7 MPa).

During loading of the second cylinder of beam B404, a large crack occurred without failure of the specimen. These test results are not taken into account. For $n = 2$ and COV unknown, there are not enough tests to determine the characteristic value.

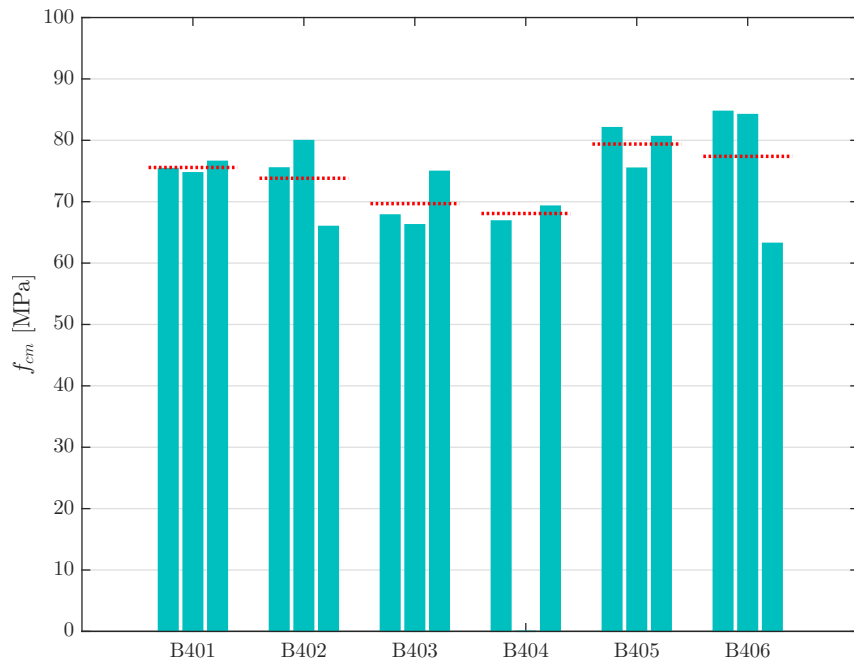


FIGURE 3.9: Experimental results of the cylindrical compressive strength for three cylinders per beam. The red dotted line indicates the mean value for each beam.

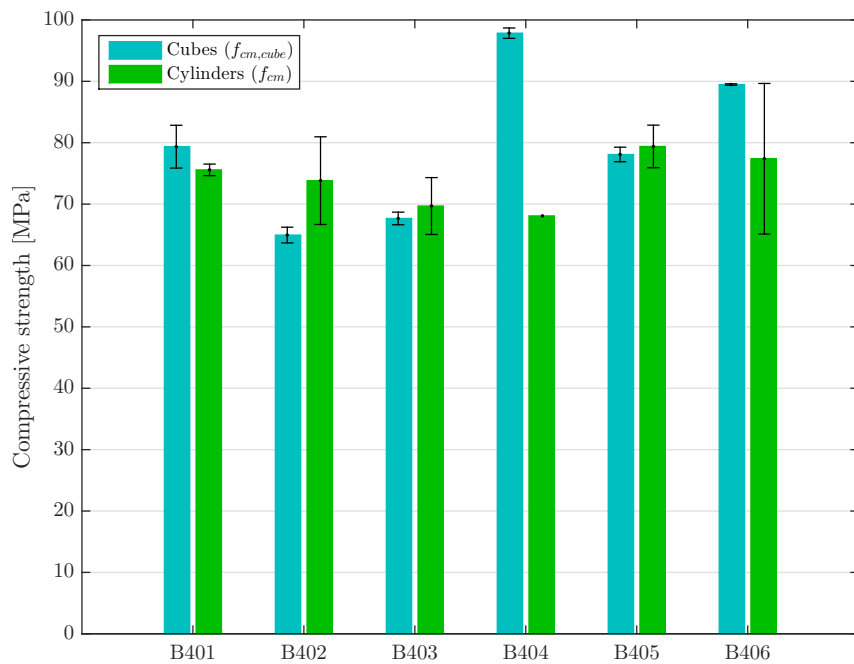


FIGURE 3.10: Comparison of the experimentally obtained mean values of the cube and cylindrical compressive strength per beam. The black lines indicates the standard deviation for each beam.

The differences in results between the beams are less distinct, compared to the conclusions described in Section 3.3.2. On the other hand, the variation in cylinder compressive strength of one beam is larger compared to the cube compressive strength, which also results in a larger standard deviation (refer to Table 3.4). Figure 3.10 shows the mean cube and cylindrical compressive strengths, together with the standard deviations, per beam. Normally, the cube compressive strength of concrete is larger than the cylindrical one, since a measured compressive strength becomes lower if the test specimen is higher or more slender. A widely used conversion estimates the cylindrical compressive strength as 79% of the cube's one. However, for high strength concrete, the difference becomes smaller. This is visible in the results (Figure 3.10). For beam B401, B404 and B406, the cube compressive strength is the largest. For beam B402, B403 and B405, the cylindrical compressive strength is slightly larger. Other contributing aspects to this difference are the degree of unevenness of the contact surface during testing and the satisfactory or unsatisfactory failure of the specimen. A high degree of unevenness or an unsatisfactory failure leads to a smaller compressive strength.

3.3.4 Modulus of elasticity

The mean modulus of elasticity E_{cm} is measured according to EN 12390-13 [10], using a hydraulic press (Dartec, maximum capacity 5 MN) (refer to Figure 3.7b). Before the cylinders are tested to determine their compressive strength, the E-modulus is measured. Three linear variable differential transformers (LVDTs) with base length 100 mm are placed on the outside of the cylinder, at 120° . A cyclic loading pattern is applied, consisting of the following parts:

1. 90 s with a constant stress of 0.50 N/mm^2 , equivalent to 8.8 kN for the cylinders.
2. A loading part with constant loading rate of 0.6 MPa/s , equivalent to 10.6 kN/s , until one third of the cylinder compressive strength f_c is reached. f_c is predicted with a conversion factor applied to the cube compressive strength, since the cubes are tested before the cylinders. This results in a stress level of $\frac{1}{3}0.79f_{cm,cube} \text{ [N/mm}^2\text{]}$, equivalent to $\frac{1}{3}0.79f_{cm,cube}\pi r^2 \text{ [kN]}$.
3. The stress level of $\frac{1}{3}0.79f_{cm,cube}$ is kept during 90 s.
4. An unloading part with the same constant loading rate of 10.6 kN/s until the stress level of 0.50 N/mm^2 is reached.
5. The cycle described in parts 1 to 4 is repeated twice. As such, the loading pattern contains three cycles.
6. After the last cycle, another 90 s of 0.50 N/mm^2 is applied. Afterwards, the cylinder compressive strength is measured by loading the cylinder until failure, with a loading rate of 10.6 kN/s (described in Section 3.3.3).

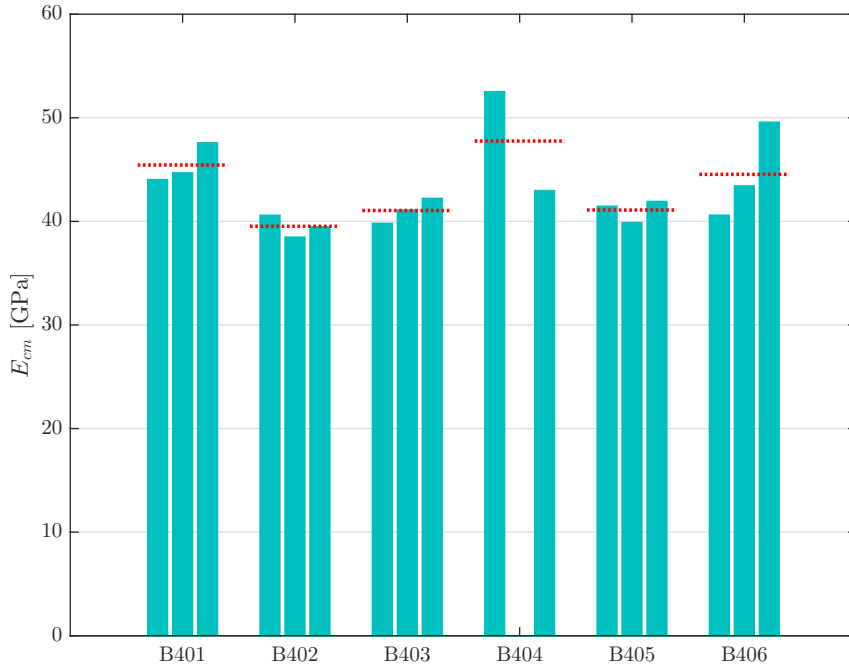


FIGURE 3.11: Experimental results of the modulus of elasticity for three cylinders per beam. The red dotted line indicates the mean value for each beam.

Based on the measurements of the three LVDTs, the average strain ϵ_m between the low ($\sigma_b = 0.5$ MPa) and high ($\sigma_a = \frac{1}{3}f_c$) stress level is calculated for the last two cycles. Together with the applied stress levels, the E-modulus is computed with Equation 3.9.

$$E_c = \frac{\sigma_a - \sigma_b}{\epsilon_m} \quad (3.9)$$

Figure 3.11 gives the results for three cylinders per beam, with indication of the mean value in the red dotted line. The cylinders of beams B401, B402 and B403 are tested at an age of 30 days, the cylinders of beams B404, B405 and B406 at an age of 62 days. During the cyclic loading of the second cylinder of beam B404, a large crack occurred without failure of the specimen. Therefore, these test results are not taken into account.

The conclusions are similar to the one discussed in Section 3.3.2. A lower E-modulus for SFRC (B402, B403 and B405, B406) is caused by entrapped air due to the presence of the fibres and the concrete mixtures for the higher amount of fibres have a higher E-modulus (B403 compared to B402 and B406 to B405). The E-modulus evolves in time as well, the older the cylinder, the higher the E-modulus (B404 compared to B401, B405 to B402 and B406 to B403).

3.3.5 Flexural tensile strength

In general, the mean flexural tensile strength $f_{ctm,fl}$ is measured with a three-point bending test on prisms. This experimental setup is easier compared to the measurement of the uniaxial tensile strength. The test procedure depends on the tested material, namely plain concrete or steel fibre reinforced concrete.

Plain concrete - B401 and B404

$f_{ctm,fl}$ of plain concrete is measured according to EN 12390-5 [7], in load-control with a hydraulic press (Dartec, maximum capacity 5 MN). The distance between the supporting rollers l equals 450 mm. The constant loading rate is 0.05 MPa/s at the bottom fibre, equivalent to 0.25 kN/s for prisms with a side of 150 mm². The $f_{ctm,fl}$ (in MPa) is calculated with Equation 3.10. F_{max} is the maximum load at failure in [N] and h , b are the height and width of the prisms in [mm].

$$f_{ct,fl} = \frac{3 \cdot F_{max} \cdot l}{2 \cdot b \cdot h^2} \quad (3.10)$$

Steel fibre reinforced concrete - B402, B403 and B405, B406

$f_{ctm,fl}$ of SFRC is measured according to EN 14651 [9]. The displacement controlled test is performed with a hydraulic press (Dartec, maximum capacity 5 MN) (refer to Figure 3.7c). A notch, 5 mm wide and 25 mm high, is sawn in the middle of the lower side of the prism, in order to initiate a crack at this location. The distance between the supporting rollers l equals 500 mm. During the test, the crack mouth opening displacement $CMOD$ and the deflection δ are measured with LVDTs. Both measurements can be used to control the test, in this case the rate of increase of $CMOD$ is used. Firstly, the $CMOD$ is increased with 0.05 mm/min until 0.1 mm is reached. Then, the rate is raised to 0.2 mm/min. When a $CMOD$ of 4 mm is obtained, the LVDTs are removed and the prism is loaded until failure.

With the measured $CMOD$ and applied load, a crack mouth opening displacement-stress curve ($CMOD - \sigma$ curve) can be drawn and some material properties can be derived. The flexural tensile strength $f_{ctm,fl}$, also referred as the limit of proportionality LOP , (in MPa) is calculated with Equation 3.11. F_L is the maximum load occurring in the range $0 \text{ mm} \leq CMOD \leq 0.05 \text{ mm}$, in [N]. b is the width of the prism in [mm] and h_{sp} is the remaining height at the location of the notch.

$$f_{ctm,fl} = \frac{3 \cdot F_L \cdot l}{2 \cdot b \cdot h_{sp}^2} \quad (3.11)$$

For SFRC, also residual tensile strengths $f_{R,j}$ are defined, corresponding to $CMOD_j$ (with $j = 1, 2, 3, 4$). $CMOD_1$, $CMOD_2$, $CMOD_3$ and $CMOD_4$ are equal to 0.5, 1.5, 2.5 and 3.5 mm respectively. $f_{R,j}$ is calculated with Equation 3.12. F_j is the load corresponding to $CMOD_j$ in [N].

$$f_{R,j} = \frac{3 \cdot F_j \cdot l}{2 \cdot b \cdot h_{sp}^2} \quad (3.12)$$

Results

Figure 3.12 gives the results for three prisms per beam, with indication of the mean value in the red dotted line. The prisms of beams B401, B402 and B403 are tested at an age of 35 days, the prisms of beams B404 and B405 at an age of 48 days and the prisms of B406 at an age of 58 days. The most remarkable result is the high flexural tensile strength of B401, especially compared to B404, which contains concrete from the same batch and is tested at an older age. Therefore, additional indirect tensile strength testing by the splitting test on the remaining halves of the prisms of B401, B402 and B404 are performed, refer to Section 3.3.6.

Table 3.5 presents the mean residual tensile strengths of B402, B403, B405 and B406. Figure 3.13a to 3.13d show the crack mouth opening displacement-stress curve ($CMOD - \sigma$ curve) of each prism, with indication of the mean residual tensile strengths. Figure 3.13e and 3.13f resume the curves of specimens with 20 or 40 kg/m³ of steel fibres respectively, with indication of the mean $CMOD - \sigma$ curve for each material in black. The figures show that concrete with 20 kg/m³ of steel fibres results in a softening behaviour, while 40 kg/m³ of steel fibres results in a hardening behaviour, under bending loads. Softening behaviour implies the formation of one large crack, while hardening implies the formation of more smaller cracks. Besides, the addition of more steel fibres causes a smaller standard deviation between the $CMOD - \sigma$ curve, comparing figure 3.13f to 3.13e.

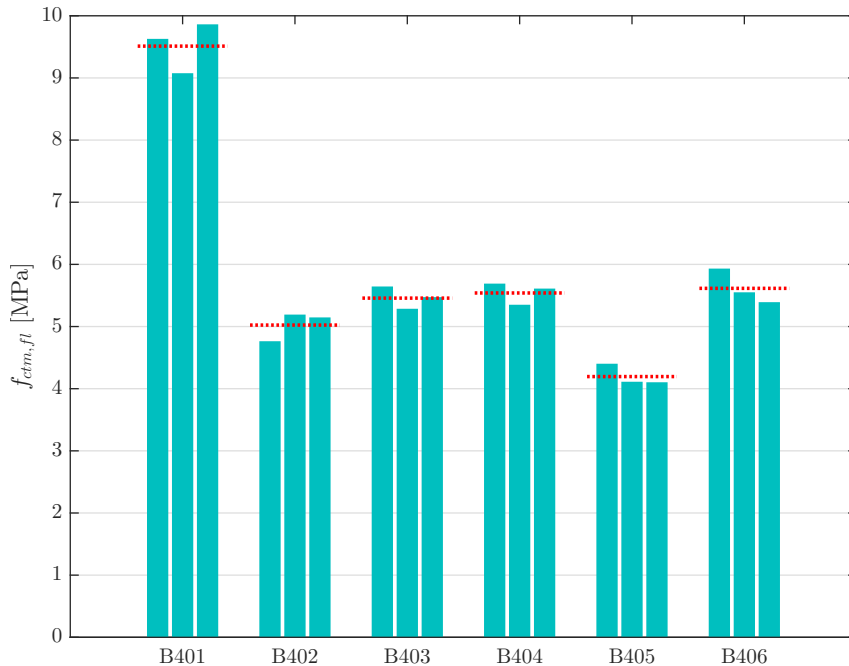
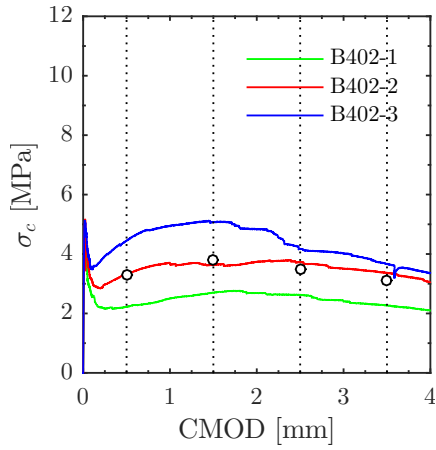
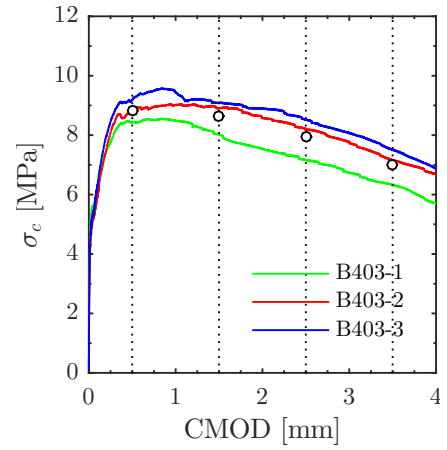


FIGURE 3.12: Experimental results of the flexural tensile strength for three prisms per beam. The red dotted line indicates the mean value for each beam.

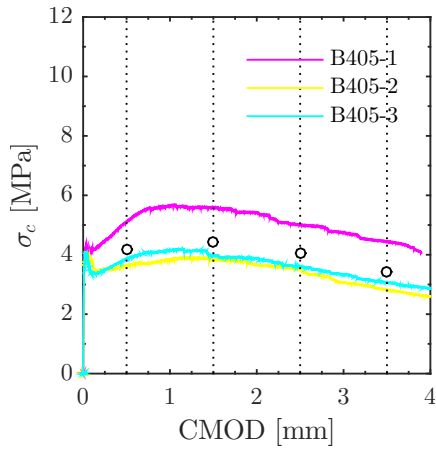
3. EXPERIMENTAL RESEARCH



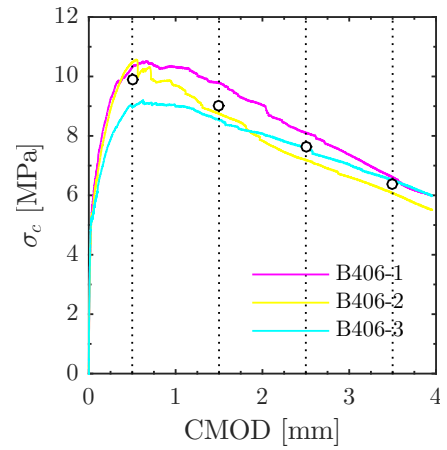
(A) B402 (20 kg/m³ steel fibres)



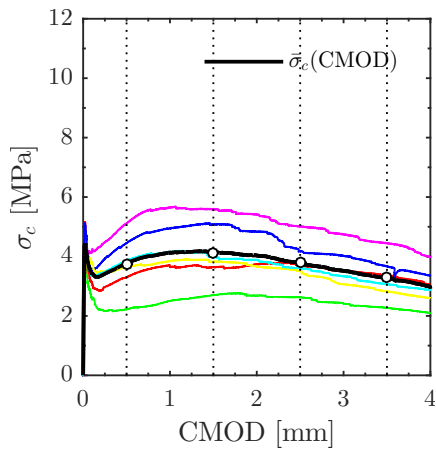
(B) B403 (40 kg/m³ steel fibres)



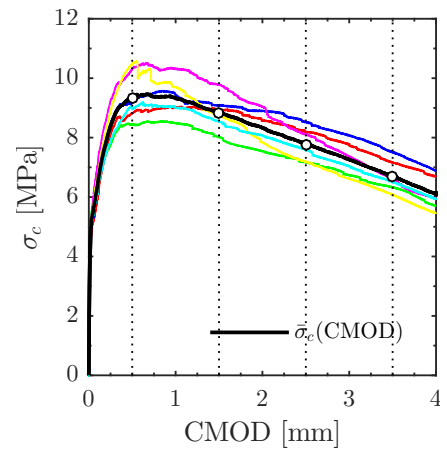
(C) B405 (20 kg/m³ steel fibres)



(D) B406 (40 kg/m³ steel fibres)



(E) Total of 20 kg/m³ steel fibres



(F) Total of 40 kg/m³ steel fibres

FIGURE 3.13: Experimentally obtained $CMOD - \sigma$ curves for the beams with steel fibres. (Note: mean residual flexural tensile strengths at $CMOD$ equal to 0.5, 1.5, 2.5 and 3.5 mm are indicated with \circ .)

TABLE 3.5: Experimentally determined mean residual tensile strengths of the SFRC.

Beam (# [•] , k)	$f_{Rm,1}$ [MPa] ($s^{\bullet\bullet}$)	$f_{Rm,2}$ [MPa] (s)	$f_{Rm,3}$ [MPa] (s)	$f_{Rm,4}$ [MPa] (s)	$f_{ctm,fl}$ [MPa] (s)
B402 (3, 3.37)	3.32 (1.11)	3.80 (1.20)	3.50 (0.80)	3.10 (0.73)	5.02 (0.24)
B403 (3, 3.37)	8.81 (0.38)	8.66 (0.58)	7.97 (0.69)	6.99 (0.59)	5.46 (0.18)
B405 (3, 3.37)	4.20 (0.79)	4.46 (0.97)	4.04 (0.85)	3.44 (0.87)	4.19 (0.17)
B406 (3, 3.37)	9.92 (0.82)	9.03 (0.68)	7.61 (0.47)	6.39 (0.28)	5.61 (0.28)

Note: [•]: # is the number of tested specimens, ^{••}: s is the standard deviation.

Requirements and classification according to Model Code 2010

According to Model Code 2010 [19], refer to Section 2.4.3, fibre reinforcement can substitute conventional reinforcement at ultimate limit state if Equation 3.13 is fulfilled. The first requirement expresses the needed capacity of SFRC to restrain the occurrence of a first crack. The second one expresses the needed ductility and post-cracking tensile stresses for higher crack widths.

$$\begin{aligned} f_{Rk,1}/f_{ctk,fl} &> 0.4 \\ f_{Rk,3}/f_{Rk,1} &> 0.5 \end{aligned} \quad (3.13)$$

The characteristic values of the residual stresses are first calculated according to the Normal distribution, with Equation 3.1. As the residual tensile strengths are rather small, the Normal distribution could possibly lead to negative values. Therefore, the calculations are also made with the log-normal distribution (Equation 3.4). Both results are given in Table 3.6. The Normal distribution does lead to negative values for $f_{Rk,1}$ of B402. Due to the small characteristic residual tensile strengths, the log-normal distribution results in larger characteristic values. Therefore, the log-normal distribution is used to discuss the results of B402.

Table 3.6 show the results of Equation 3.13, for both statistical distributions. All requirements are fulfilled, except the first one of B402. The Normal distribution results in a negative residual tensile strength and corresponding negative ratios, which have no physical meaning. The log-normal distribution gives a ratio of 0.23, not greater than the required 0.4. In this case, the amount of steel fibres is not sufficient to replace the conventional reinforcement according to Model Code 2010. The deviation of beam B402 can be attributed to the high coefficient of variation of 30%. The requirement would be fulfilled if COV decreases to 16%. Therefore, accurate fabrication and testing are needed to avoid a high standard deviation (and COV).

3. EXPERIMENTAL RESEARCH

TABLE 3.6: Characteristic residual tensile strengths and verification of the requirements according to Model Code 2010 (MC2010), based on Normal and log-normal distribution.

		B402	B403	B405	B406
$f_{Rk,1}$	[MPa]	-0.40 (1.00)	7.52 (7.60)	1.55 (2.27)	7.14 (7.42)
$f_{Rk,3}$	[MPa]	0.80 (1.51)	5.63 (5.89)	1.18 (2.03)	6.04 (6.19)
$f_{ctk,fl}$	[MPa]	4.23 (4.28)	4.58 (4.88)	3.62 (3.66)	4.68 (4.76)
$f_{Rk,1}/f_{ctk,fl}$	> 0.4	-0.10 (0.23)	1.55 (1.56)	0.43 (0.62)	1.53 (0.85)
$f_{Rk,3}/f_{Rk,1}$	> 0.5	-1.98 (1.52)	0.75 (0.77)	0.76 (0.90)	0.85 (0.83)
Classification	(MC2010)	/ (1e)	7b (7b)	1.5b (2c)	7b (7b)

Note: values between brackets are calculated according to the log-normal distribution (Equation 3.4), the other ones according to the Normal distribution (Equation 3.1).

For beam B405, the first requirement is just fulfilled in the Normal distribution (0.43 compared to 0.4). Although the log-normal distribution results in higher characteristic values and a ratio closer to the limit (0.62 instead of 0.43), the change of statistical distribution may not be used in an attempt to obtain favourable results. To conclude, beams with 20 kg/m³ of steel fibres just do or just do not fulfil the requirements of Model Code 2010 to replace conventional shear reinforcement. For a safe application of steel fibres, a higher amount should be used.

Lastly, Model Code 2010 [19] also gives a classification system for the post-cracking strength of SFRC, based on the characteristic residual tensile strengths that are significant for serviceability ($f_{Rk,1}$) and ultimate conditions ($f_{Rk,3}$). The classification exists of two parameters, namely a number representing the strength interval of $f_{Rk,1}$ and a letter between a and e representing the $f_{Rk,3}/f_{Rk,1}$ -ratio. Results of the beams are given in Table 3.6, based on the Normal and log-normal distribution. For example B403 and B406 (7b) have a strength $f_{Rk,1}$ in the range 7-8 MPa and a $f_{Rk,3}/f_{Rk,1}$ -ratio between 0.7 and 0.9.

3.3.6 Tensile splitting strength

As reported in the previous section, the experimental results of the flexural tensile test of beam B401 are extremely high (mean value of 9.5 MPa, measured at 35 days), especially compared to the results of beam B404. These two beams are made of the same concrete batch and the prisms of beam B404 are tested at 48 days, resulting in a mean flexural tensile strength of 5.5 MPa. Photographs and measurement data were thoroughly checked, but no explanation was found. Therefore, additional indirect tensile strength testing by the splitting test on the remaining halves of the prisms of B401 and B404 are performed. The specimens of beam B402 are also tested, to investigate the tensile splitting test of SFRC.

The mean tensile splitting strength $f_{ctm,sp}$ is measured according to EN 12390-6 [6], in load-control with a hydraulic press (Dartec, maximum capacity 5 MN). The constant loading rate equals 0.25 kN/s. The tensile splitting strength (in MPa) is calculated with Equation 3.14, based on six specimens for each beams (two halves of three prisms). F_{max} is the maximum load at failure in [N]. L and b are the length of the line of contact and the cross-sectional dimension, both equal to 150 mm.

$$f_{ct,sp} = \frac{2 \cdot F_{max}}{\pi \cdot L \cdot d} \quad (3.14)$$

Figure 3.14 gives the results of the mean tensile splitting strengths $f_{ctm,sp}$ compared to the mean flexural tensile strengths $f_{ctm,fl}$, together with the standard deviation. The numerical values are presented in Table 3.7 and the individual results of $f_{ct,sp}$ are shown in Figure 3.15. The tensile splitting strength is tested at 184 days, for the three beams.

Firstly, the standard deviations of the six tested specimens for each beam are larger compared to the standard deviations of $f_{ctm,fl}$. The variation in specimen dimensions can attribute to this difference. The prisms of the flexural tensile test have the same dimensions, but their remaining halves have not. Secondly, $f_{ctm,sp}$ is normally smaller than $f_{ctm,fl}$, which is the case for B401 and B404. SFRC deviates from this, although the difference is only 0.3 MPa. Thirdly, the tensile splitting test indicates that the measured flexural tensile strength of B401 is extremely high. In general, $f_{ctm,sp}$ is approximately equal to $0.65 \cdot f_{ctm,fl}$.

Based on this additional testing results, it can be concluded that tensile tests on (steel fibre reinforced) concrete can give a large scatter and should be performed as accurate as possible. For beams with plain concrete, B401 and B404, the tensile splitting test gives more realistic results to calculate the uniaxial tensile strength (Section 3.3.7) than the flexural tensile test. Adding steel fibres enhances post-cracking tensile residual strength due to bridging of crack surfaces by the fibres, resulting in a larger tensile strength.

TABLE 3.7: Experimentally determined mean tensile splitting strength of B401, B402 and B404.

Specimens	$f_{ctm,fl}$ [MPa] (# [•] , s ^{••})	$f_{ctm,sp}$ [MPa] (#, s)
B401	9.5 (3, 0.40)	3.5 (6, 0.88)
B402	5.0 (3, 0.24)	5.3 (6, 0.59)
B404	5.5 (3, 0.18)	2.9 (6, 0.59)

Note: [•]: # denotes the number of tested specimens, ^{••}: s denotes the standard deviation

3. EXPERIMENTAL RESEARCH

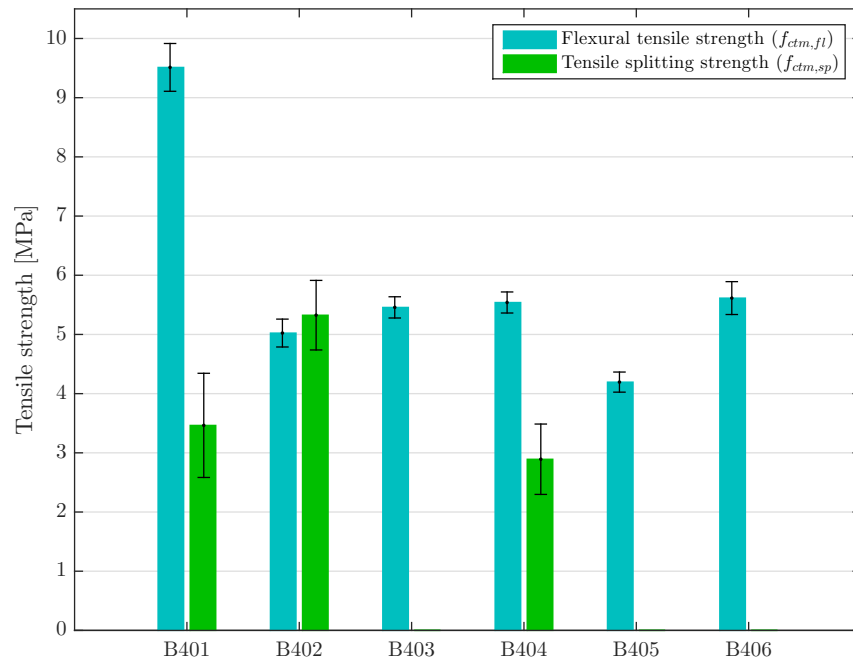


FIGURE 3.14: Comparison of the experimentally obtained mean values of the flexural tensile and tensile splitting strength per beam. The black lines indicates the standard deviation for each beam.

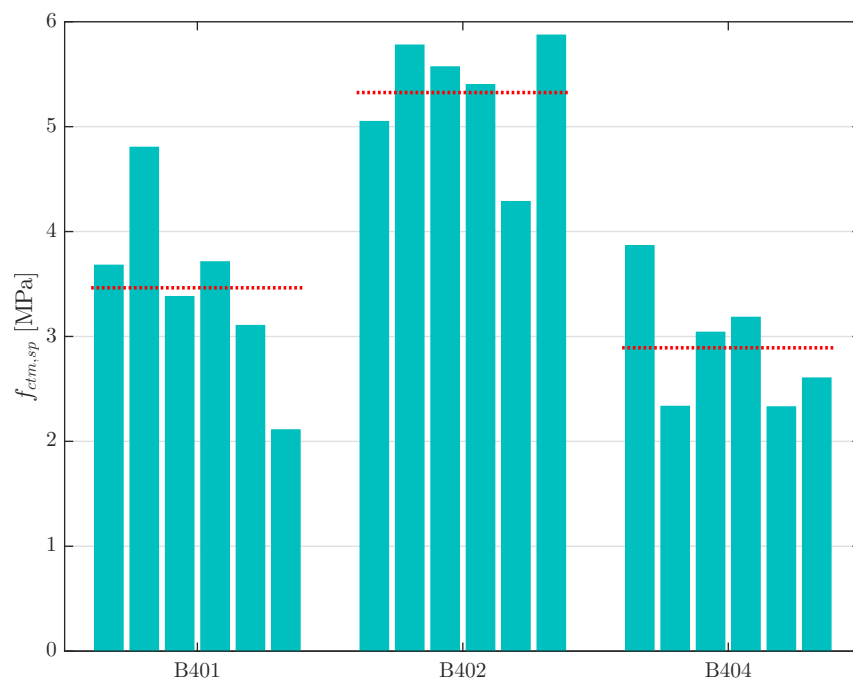


FIGURE 3.15: Experimental results of the tensile splitting strength for six half prisms per beam. The red dotted line indicates the mean value for each beam.

3.3.7 Uniaxial tensile strength

The uniaxial tensile strength f_{ctm} is not directly measured, but estimated from the mean flexural tensile strength $f_{ctm,fl}$ with Equation 3.15 [19] or from the mean tensile splitting strength $f_{ctm,sp}$ with Equation 3.16 [19].

$$f_{ctm} = \alpha_{fl} \cdot f_{ctm,fl} \quad (3.15)$$

$$f_{ctm} = \alpha_{sp} \cdot f_{ctm,sp} \quad (3.16)$$

The conversion factor α_{fl} is calculated by using Equation 3.17, whereby h_b denotes the beam depth in mm. For the prisms of plain concrete (B401 and B404), this depth is equal to 150 mm. The SFRC prisms (B402, B403, B405 and B406) are tested with a notch, resulting in a beam depth of 125 mm.

$$\alpha_{fl} = \frac{0.06 \cdot (h_b)^{0.7}}{1 + 0.06 \cdot (h_b)^{0.7}} \quad (3.17)$$

The conversion factor α_{sp} is equal to 1.0 [19].

Table 3.8 shows the results of the calculation of the uniaxial tensile strength. The correction factor α_{fl} varies between 0.64 (SFRC) and 0.67 (plain concrete). A three-point bending test (with or without notch) induces the first crack at the middle of the prism, which is not necessarily the most weak place of the prism. The experimental setup for a uniaxial tensile test is more complex, but the test induces cracks at the weakest place, instead of a fixed one. The test results therefore in a lower tensile strength, which is taken into account with the conversion factor α_{fl} smaller than 1.

The uniaxial tensile strength is about 65% of the flexural tensile strength and will be used for beams with steel fibres B402, B403, B404, B405 and B406 in calculations (Section 3.6). For beam B401, the uniaxial tensile strength based on the tensile splitting strength is used in calculations due to the unrealistic high experimental results of the flexural tensile strength. The uniaxial tensile strengths used for calculations are finally shown in Figure 3.16, with the standard deviations of the measurements.

A remark on the aforementioned calculation method has to be made. In literature, it is sometimes stated that Equation 3.15 is not valid for SFRC, because of the presence of the notch in the prisms for the measurement of the flexural tensile strength. Sawing these notches can induce micro-cracks which could reduce the strength of the prisms. It has been proposed to use Equation 3.18 instead [20]. Due to the disagreement in literature, this adaptation has not been followed.

$$f_{ctm} = 0.9 \cdot f_{ctm,fl} \quad (3.18)$$

3. EXPERIMENTAL RESEARCH

TABLE 3.8: Calculated mean uniaxial tensile strengths, based on flexural tensile and tensile splitting strength.

		B401	B402	B403	B404	B405	B406
$f_{ctm,fl}$	[MPa]	9.51	5.02	5.46	5.54	4.19	5.61
α_{fl}		0.67	0.64	0.64	0.67	0.64	0.64
f_{ctm}	[MPa]	6.34	3.20	3.48	3.69	2.68	3.58
$f_{ctm,sp}$	[MPa]	3.46	5.33		2.89		
α_{sp}		1	1		1		
f_{ctm}	[MPa]	3.46	5.33		2.89		
f_{ctm}^\bullet	[MPa]	3.46	3.21	2.84	3.69	2.68	3.58

Note: \bullet : these values of f_{ctm} will be used in calculations.

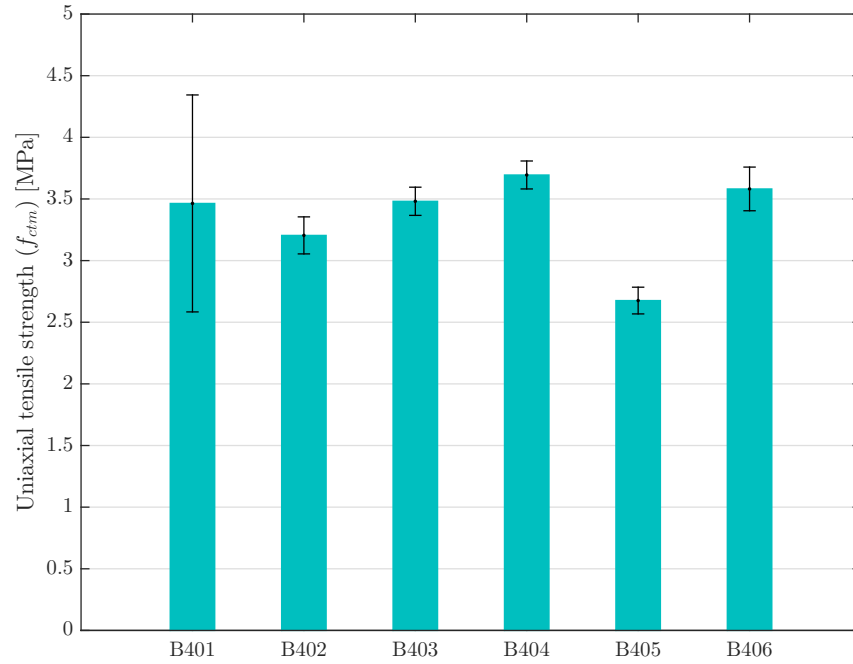


FIGURE 3.16: Uniaxial tensile strength per beam. The black lines indicates the standard deviation for each beam.

3.4 Experimental setup

The six I-shaped beams are subjected to a four-point bending test at the Reyntjens Laboratory of the Civil Engineering Department of KU Leuven, as shown in Figure 3.17. A hydraulic press is used (Instron, maximum capacity 2.5 MN), of which the load is distributed in two point loads by means of a steel transfer beam (HEB 400). Between the transfer beam and the test specimen, two bearing cylinders are used to form the two point loads. These cylinders and the transfer beam are fixed to the hydraulic press (Figure 3.19a), in order to prevent falling down and causing damage when failure of the tested specimen occurs. An other safety measure is the presence of wooden blocks between the surrounding steel frame and the specimen (Figure 3.19b), in order to prevent lateral overturning of the specimen and damaging the cylinders of the hydraulic press. Between the experimental setup and the adjacent controlling computer, safety screens are placed (Figure 3.19c). Lastly, a safety zone is defined which is not accessible during testing (Figure 3.19d).

Figure 3.18 shows a schematic view of the experimental setup. The beams are 7000 mm long and the distance between the supporting points equals 5000 mm. The remaining parts outside the supports have a length of 1000 mm. As such, the zone to gradually develop the prestressing force over the height of the beam does not coincide with the zone to investigate the shear behaviour. Moreover, this setup is less likely to cause failure of the beam due to debonding of the prestressing reinforcement.

The shear span a is equal to 2200 mm for all the beams (Table 3.1) to obtain a shear span-to-effective depth ratio (a/d -ratio) of 3.95. This a/d -ratio is preferred within the range of 2.5 to 6 in order to ensure shear failure. If $a/d < 2.5$, beams are more likely to fail due to an excessive compression force at the supports. If $a/d > 6$, the bending failure mode is dominant, with vertical bending cracks. With a/d equal to 3.95, a safe distance to aforementioned limits is kept to avoid a useless setup to investigate the shear behaviour. In the shear span zone a , the bending moment follows a linear course from zero at the supports to its maximal value at the loading points. The shear force is constant and maximal, causing shear cracks at an angle lower than 45° for prestressed concrete.

The four-point bending tests are carried out in load control. A cyclic pattern with monotonically loading and unloading is applied. Figure 3.20 gives an example of this loading pattern for beam B405. Before each test, the crack load V_{cr} is predicted, with average material properties and with omitting partial safety factors, as explained in Section 3.6. The progressive damage loading scheme exists of a cycle up to half of the predicted crack load ($0.5V_{cr}$), a second cycle up to the predicted crack load (V_{cr}) and in the third cycle, the load is continuously increased until failure occurs ($V_{u,exp}$). The loading rate $\dot{P} = \frac{dP}{dt}$ equals 0.25 kN/s, the unloading rate equals 0.25 kN/s for the first cycle and 1.00 kN/s for the second cycle. These are equivalent to a shear force rate $\dot{V} = \frac{dV}{dt}$ of 0.125 kN/s and 0.50 kN/s respectively. The loading rate is rather slowly, to approximate a quasi-static loading and to avoid dynamic effects.

3. EXPERIMENTAL RESEARCH



FIGURE 3.17: Experimental setup for the test specimens.

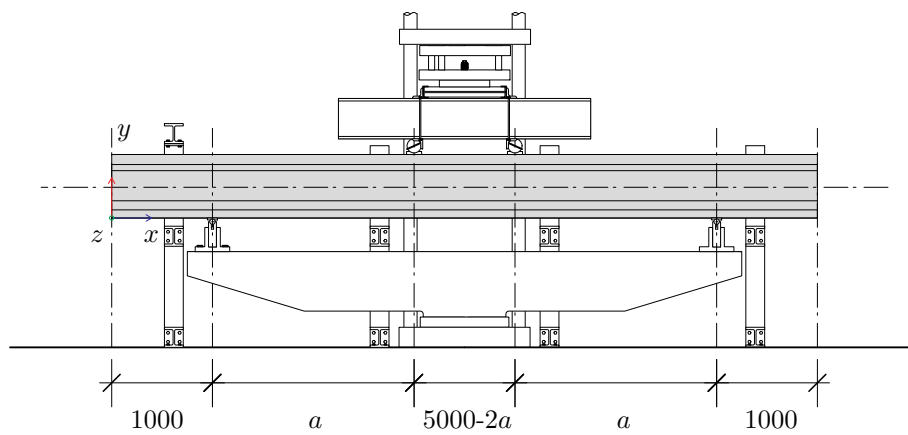


FIGURE 3.18: Schematic representation of the experimental setup.

Before and during testing, some measurement methods are used to obtain properties of shear behaviour, failure load and mode. These methods are explained in Section 3.5 and contain (1) *Demountable Mechanical strain gauges* (DEMEC), (2) *Linear Variable Differential Transformers* (LVDTs), (3) *Bragg grated optical fibres* (FBG) and (4) *Digital Image Correlation* (DIC).

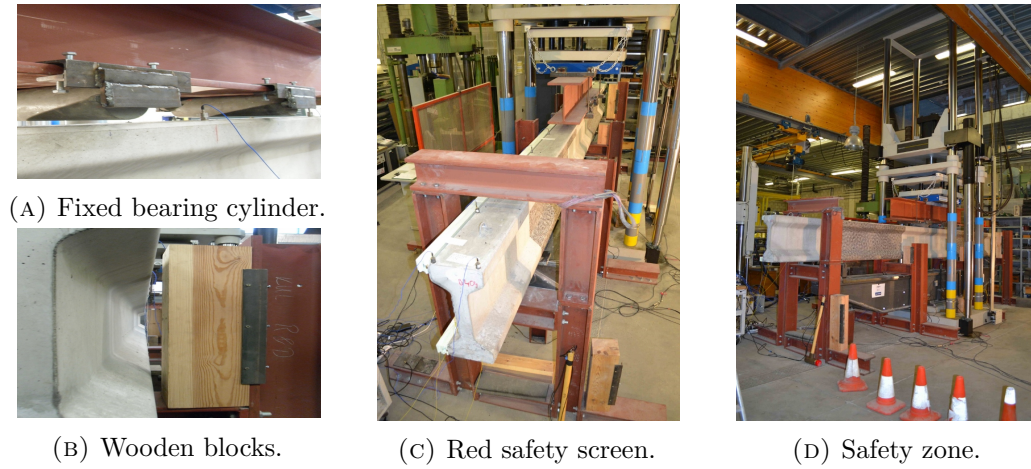


FIGURE 3.19: Safety measures during testing.

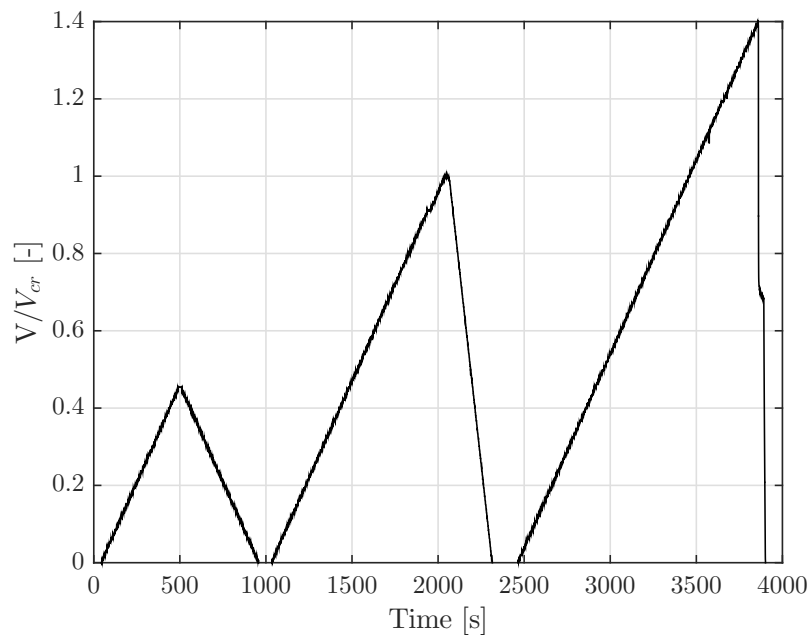


FIGURE 3.20: Cyclic loading pattern with V_{cr} indicating the first cracking load (example for beam B405).

3.5 Adopted instrumentation

Before and during the full-scale testing, different measurement techniques are used in order to obtain a valuable set of experimental results of the shear resistance and behaviour. Not only failure load and failure mode are recorded, but also shear behaviour is considered by deformations, displacements and cracking pattern properties to understand the complete mechanical behaviour during the entire shear loading procedure. The conventional techniques usually give a restricted amount of data in one or two dimensions. Therefore, advanced optical measurement techniques are also used, able to gather a large amount of information and to analyse the full-field displacement and deformation field. Undermentioned measurement methods are used and explained in the following subsections:

- DEMEC points (demountable mechanical strain gauges) to measure deformations during the hardening process, refer to Section 3.5.1 and Figure 3.3.
- LVDTs (linear variable differential transformers) to measure continuous displacements at the supports during testing, refer to Section 3.5.2 and Figure 3.21.
- Optical photoelectric sensor (OPT) to measure continuous displacements at midspan during loading procedure, refer to Section 3.5.2 and Figure 3.21.
- Bragg grating optical fibres (FBG) to measure horizontal strains in the flanges of B403 and B404 during loading procedure, refer to Section 3.5.3 and Figure 3.22.
- 3D-DIC (stereo-vision digital image correlation) to measure mechanical response and deformations during loading procedure, refer to Section 3.5.4 and Figure 3.21.
- During testing, the beams are filmed and photographed at critical moments.

3.5.1 Demountable mechanical strain gauges (DEMEC)

Demountable mechanical strain gauge points are used to determine the deformations and strains during the hardening process, by measuring at different times. Since the prestressing reinforcement undergoes the same deformation as the concrete, both immediate and time dependent stress losses of the prestressing reinforcement are calculated (refer to Section 3.6).

Figure 3.3 shows the location of the DEMEC points, indicated with \circ . Four lines with 11 points are placed, one at the top and three at the bottom of the beam. Each row is denoted from top to bottom with the letter A, B, C or D. The points on each row are numbered from left to right with 1 to 11. Figure 3.23 shows half of a beam with the location, numbering and distances of the DEMEC points. The 44 points are glued on the beam's side surface with a two-component adhesive. Figure 3.24e shows a picture of the results.

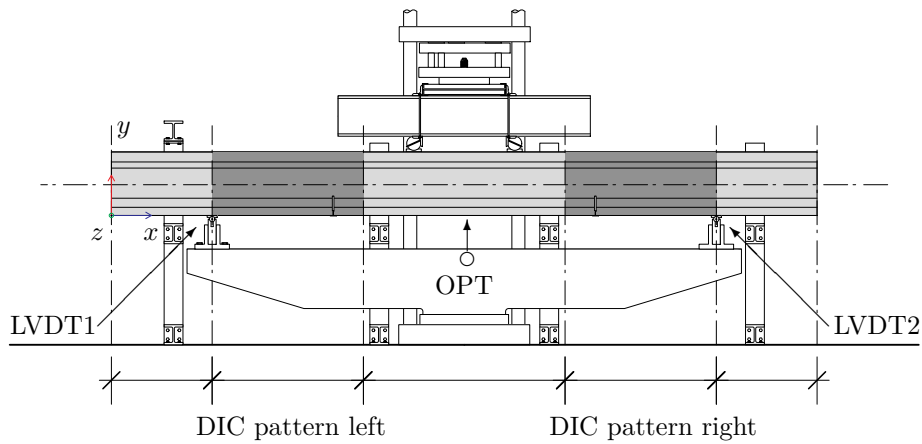


FIGURE 3.21: Schematic representation of the experimental setup (front view) with indication of the measurement methods LVDT, OPT and DIC.

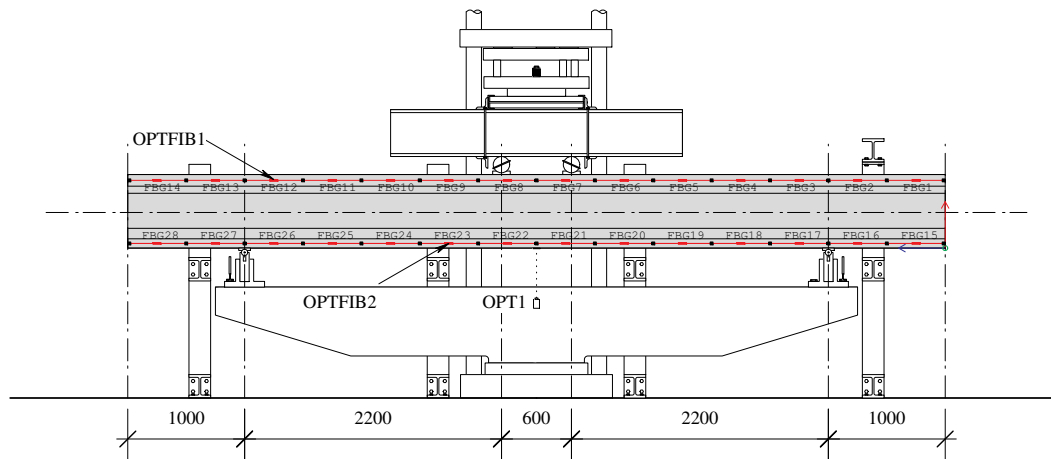


FIGURE 3.22: Schematic representation of the experimental setup (back view) with indication of the Bragg grated optical fibre: location of the adopted optical fibres OPTFIB1 and OPTFIB2, mechanical fixing points (■) and Bragg gratings (FBG).

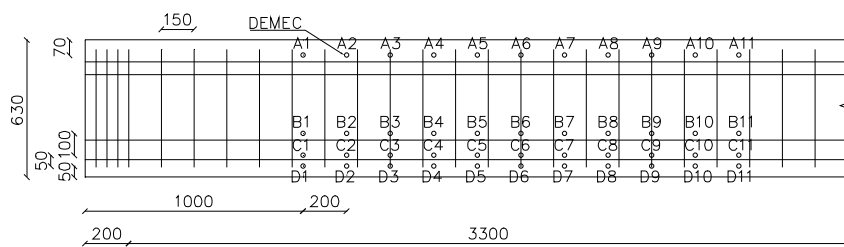


FIGURE 3.23: Half of a beam with indication of the DEMEC point by ◦, with notations and distances.

The complete DEMEC measurements consist of different steps:

0. After removing the formwork of the beam (one day after casting), DEMEC points are immediately glued on the concrete. Therefore, the positions are measured and indicated (Figure 3.24a) and subsequently, the concrete is cleaned of dust by shortly grinding (Figure 3.24b). The DEMEC points are exactly located and glued with the two-component adhesive (Figure 3.24c).
1. After attaching the DEMEC points, the first measurement (DEMEC 1) is made. The spacing between the points should be 200 mm and is measured with precision of 0.001 mm (Figure 3.24d). This is de reference measurement, just after manufacture of the beams.
2. A second measurement DEMEC 2 is made just before releasing the prestressing reinforcement. For beam B403 and B406, DEMEC 1 and 2 are at the same time, whereas DEMEC 2 is one day later than DEMEC 1 for the other four beams.
3. Just after releasing the prestressing reinforcement, the third measurement DEMEC 3 is made. The difference in distances between DEMEC 1/2 and DEMEC 3 gives the deformation due to transferring the prestressing force of 750 or 1488 MPa to the concrete beams.
4. DEMEC 4 measurement is made one day before full-scale testing of the beam, in order to calculate the stress losses (apart from relaxation) to determine the predicted first crack and failure load, V_{cr} and $V_{u,pred}$ respectively, based on the remaining stress in the strands.
5. The last measurement DEMEC 5 is made just before the full-scale test, in order to obtain the most correct information of the deformations at moment of testing, 38 (B401) to 57 (B406) days after casting.

By measuring the distance between two DEMEC-points at different times, the strains can be calculated with Equation 3.19. t_0 indicates the first measurement (DEMEC 1 for B401, B402, B404 and B405; DEMEC 1 and 2 are the same for B403 and B406) and t indicates another measurement (DEMEC 3, 4 or 5). The strains are positive if the distance between two DEMEC-points increases and negative if the distance decreases.

$$\varepsilon = \frac{L_t - L_{t_0}}{L_{t_0}} \quad (3.19)$$

After releasing the prestressing force (by cutting the strands), the concrete matrix undergoes an elastic deformation which causes immediate stress losses. The time dependent losses occurs due to the combination of shrinkage, creep and relaxation. The calculation of these stress losses based on the strains are explained in Section 3.6.

Figure 3.26 presents the strains over the height of the six beams, between the day of removal of the formwork and the day of full-scale testing (the corresponding age is mentioned in Table 3.4). The first order polynomial fit with regression function, the 95% prediction interval and the coefficient of determination R^2 are given. All strains are negative since concrete beams shorten due to the immediate and time dependent effects of prestressing, shrinkage, creep and relaxation.

B401, B402 and B403 (left side of Figure 3.26) have an amount of prestressing of 1488 MPa, whereas B404, B405 and B406 (right side of Figure 3.26) have an amount of 750 MPa. A lower amount of prestressing causes lower strains, as a smaller force is transferred to the concrete. Seven prestressed strands are placed at the bottom of the beam, only one at the top (refer to Section 3.2.1). Thereby, a larger force is applied to the lower part of the beam, causing a larger strain than at the top.

There is only a small difference between the beams with 0 and 20 kg/m³ steel fibers (comparing B401 to B402, and B404 to B405). B403 and B406 with 40 kg/m³ show larger strains within the same prestressing amount. To improve the workability of this fresh SFRC mixture, blast furnace slag was added and the water-cement ratio increased (refer to Table 3.2). A higher amount of water causes also a higher drying shrinkage resulting in larger strains. Beside, the transfer of prestressing force to SFRC happens at an earlier age for these two beams (after one day in contrast to two days). Given that the concrete is less hardened, the deformations can be larger.

However the distances between DEMEC points are measured accurately and precisely up to 0.001 mm, measurement errors can occur in following ways. First, the DEMEC points have to be glued exactly at the defined place. Since this is a challenging task, small deviations are possible. Second, some DEMEC points can be lost during transport. The missing values are replaced by the mean value of the other measurements at the same row. However, in case of beam B404, the upper and lower row (A and D respectively) were covered by the Bragg grating optical fibres at the day of testing, so that no accurate measurements could be performed (refer to Figure 3.26 (B404)). Third, mistakes can be made if the measurement device is not held perfectly parallel with the concrete surface. Empirical testing showed a large variation in values while slightly turning the device. Lastly, errors can occur in post-processing of the measurements, namely during reading the measurement device, writing down the values or transferring them to the computer.

3.5.2 LDVTs and optical photoelectric sensor

Linear variable differential transformers at each support are used to measure continuous displacements of the tested beams without deformation of the rigid experimental setup. An optical photoelectrical sensor (Baumer Photoelectric OADM 12U6460 with resolution 96×10^{-3} mm) is used at midspan of the beam. These locations are indicated at Figure 3.21 and Figure 3.25 shows the LVDTs and the optical sensor.

3. EXPERIMENTAL RESEARCH

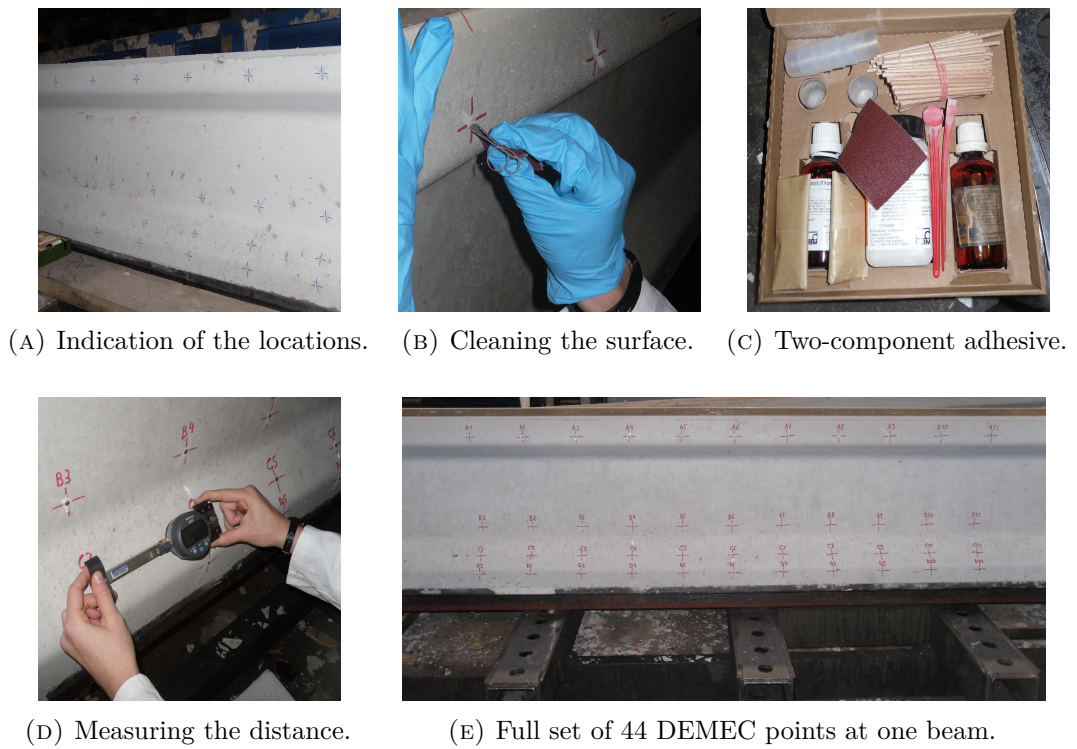


FIGURE 3.24: Different aspects of the DEMEC measurement method.

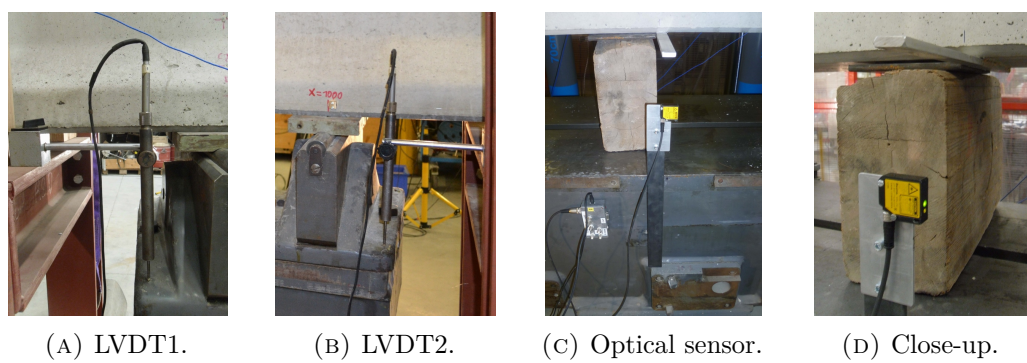


FIGURE 3.25: Pictures of the left and right LVDTs and the optical photoelectric sensor, before the loading procedure.

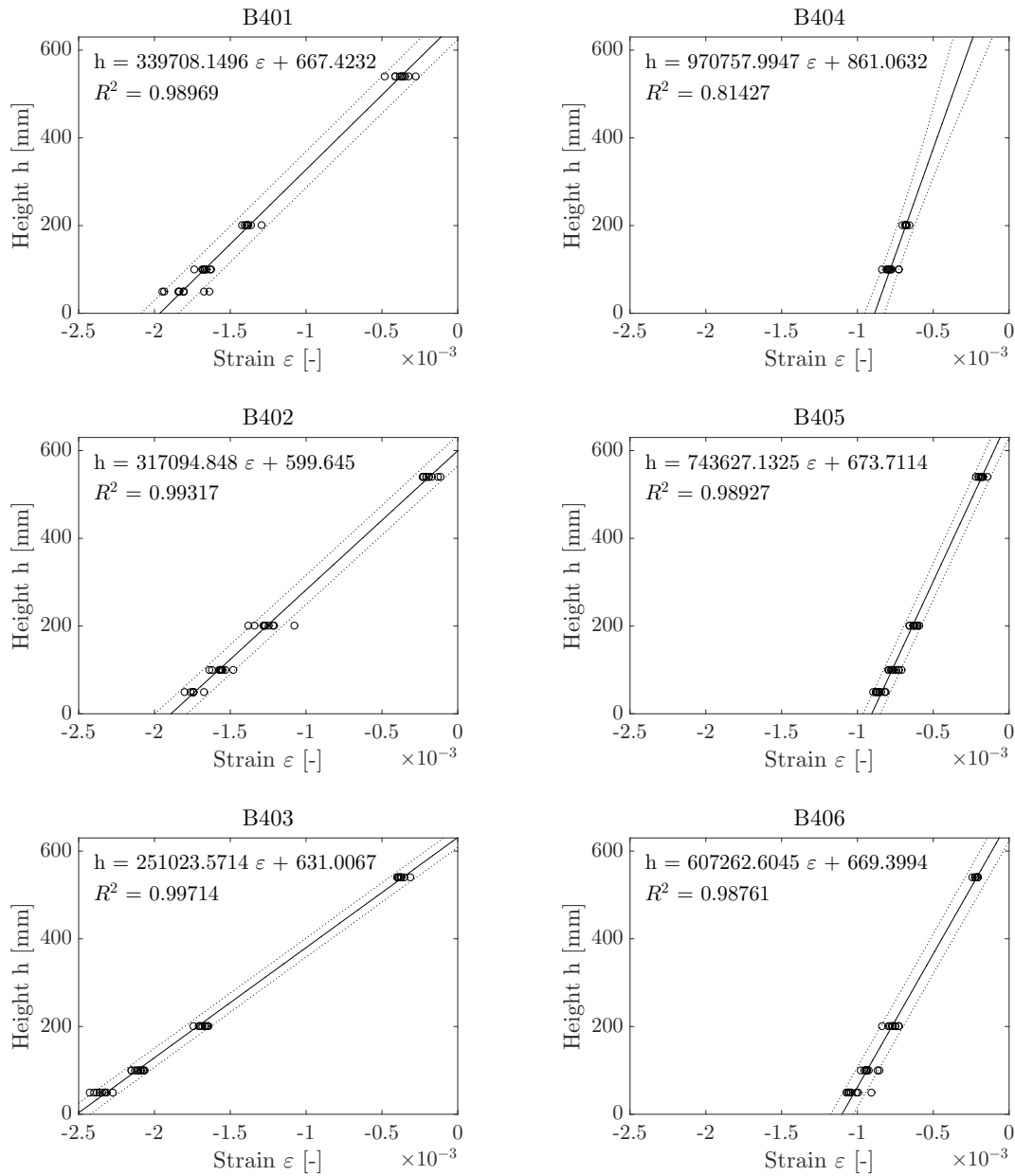


FIGURE 3.26: Strains (o) between the day of removal of the formwork (DEMEC 1) and the day of full-scale testing (DEMEC 5), with first order polynomial fit (-) and 95% prediction interval (dotted line).

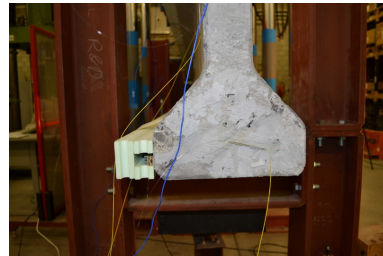
3.5.3 Bragg grated optical fibres (FBG)

During testing of beam B403 and B404, Bragg grated optical fibres (FBG) were used to accurately measure the horizontal strains in the flanges (refer to Figure 3.22). On beam B403, the fibre is used at the top flange and on beam B404 at the top and bottom flange. Strain monitoring with optical fibres engraved with Bragg gratings relies on the analysis of the wavelength spectrum which is reflected by the Bragg gratings. If a change in length of the optical fibre occurs, a shift in the reflected wavelength is induced, where a positive shift in wavelength is related to elongation of the fibre.

Here, one (top flange, B403) or two (top and bottom flange, B404) optical fibres (FOS&S, type SMW-01) based on Draw Tower Grating technology were applied. The optical fibres have a primary ORMOCER coating. A high resolution FBG interrogator was applied for readouts of wavelengths between 1525 nm and 1565 nm. Each optical fibre was equipped with 14 FBG sensors with a base length of 500 mm. The fibres are mechanically fixed into brass anchoring blocks (Figure 3.27a), which are glued onto the concrete side surface using a two-component adhesive. This setup allows for the fibre to be removed prior to failure to avoid damage. Finally, an extruded polystyrene cover was placed over the fibres to thermally shield the sensors from the environment (Figure 3.27b). The strain resolution of the presented setup is approximately equal to 1 μ S. [14]



(A) Mechanically anchored optical fibre.



(B) Covered optical fibre.

FIGURE 3.27: Anchorage and covering of Bragg grated optical fibres (B404).

Figures 3.28, 3.29 and 3.30 give results of the measurements on beam B404 for the top and bottom optical fibre and for different loading cycles of beam B404 (Figure 3.44a). Since the beam is tested with a four-point bending test, the bottom flange elongates due to tension (resulting in positive strains) and the top flange shortens due to compression (resulting in negative strains). The measured strains are grouped per color, as the FBG's are placed symmetrically on the length of the beam (refer to Figure 3.22). FBG1 to FBG7 are represented with a full line, their symmetrical opponent FBG8 to FBG14 with a dotted line in the same color.

Figure 3.28 presents the measured strains during the first loading cycle up to 53 kN (Figure 3.44a). The concrete beam is uncracked as the applied load is approximately half of the first crack load. The measurements show that the strain at the middle of the beam (FBG7&8, bottom and top) is the largest and decreases towards the outsides. Elongation values of $2.25 \cdot 10^{-4}$ are measured in the middle of the bottom flange and shortening values of $1.52 \cdot 10^{-4}$ in the middle of the top flange.

The strains can be calculated with Equation 3.20, for uncracked sections. V is the applied load of 53 kN and a is the shear span of 2200 mm. v is the distance between neutral axis and bottom or top, 312 and 298 mm respectively, and I is the second moment of area. E_c is the measured modulus of elasticity (refer to Section 3.3.4), varying between 43 and 53 GPa. Therefore, the results of the strain values varies in the range $1.60 \cdot 10^{-4}$ - $1.93 \cdot 10^{-4}$ at the bottom and in the range $1.52 \cdot 10^{-4}$ - $1.84 \cdot 10^{-4}$ at the top. For the top flange, the measured strain value is equal to the calculated one with the highest E-modulus ($1.52 \cdot 10^{-4}$). For the bottom flange, the lowest modulus of elasticity gives the best fitting result.

$$\varepsilon = \frac{\sigma_c}{E_c} = \frac{M \cdot v}{I \cdot E_c} = \frac{V \cdot a \cdot v}{I \cdot E_c} \quad (3.20)$$

Figure 3.29 presents the measured strains during the fourth loading cycle up to 132 kN (Figure 3.44a). It is visible that the first cracks appear in the middle of the concrete beam, due to the large strains of the middle FBG's (FBG7&8 and FBG6&9). Therefore, these are cracks due to bending. Figure 3.30 on the other hand presents the measured strains in the top flange during the fifth loading cycle up to 145 kN (Figure 3.44a). Here, it is visible that cracks appear between supporting and loading point, where the shear force is maximal, due to the large variation in strains of FBG5&10 and FBG4&11.

3. EXPERIMENTAL RESEARCH

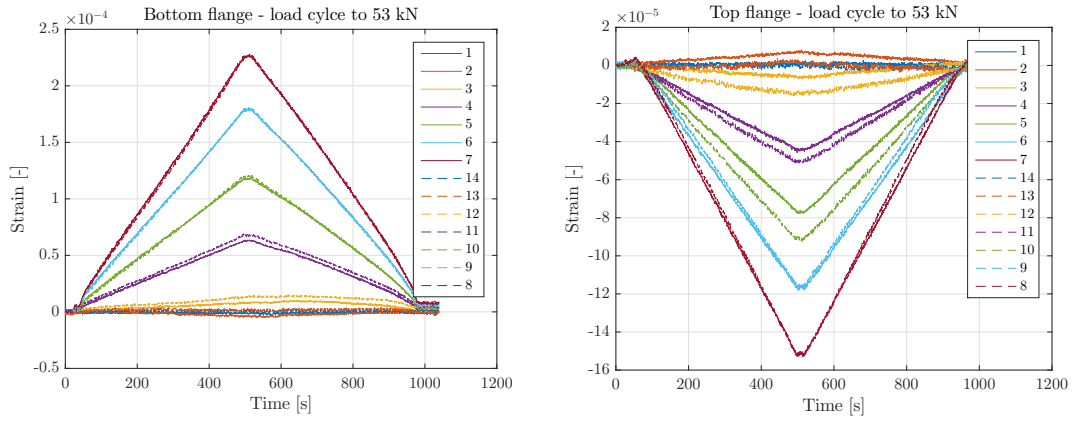


FIGURE 3.28: Measured strains in bottom (left) and top (right) flange with Bragg grating optical fibres for the first loading cycle of beam B404 (up to 53 kN).

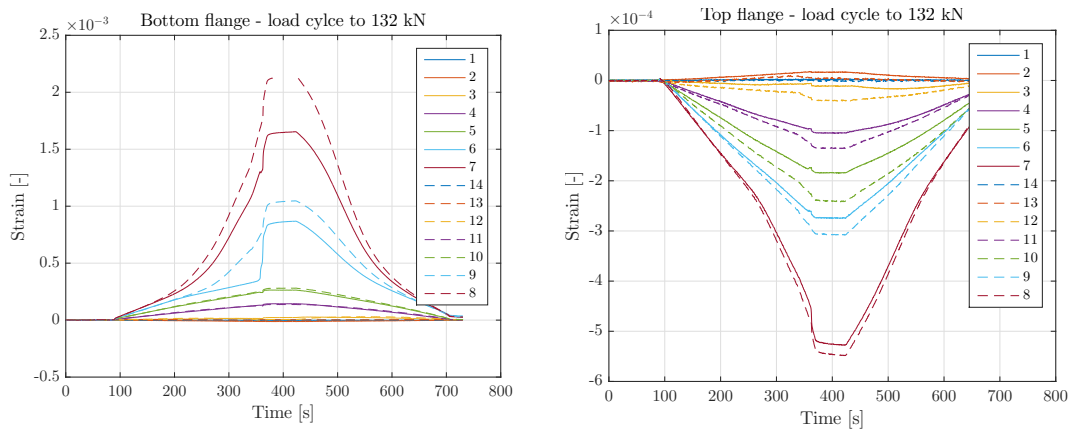


FIGURE 3.29: Measured strains in bottom (left) and top (right) flange with Bragg grating optical fibres for the fourth loading cycle of beam B404 (up to 132 kN).

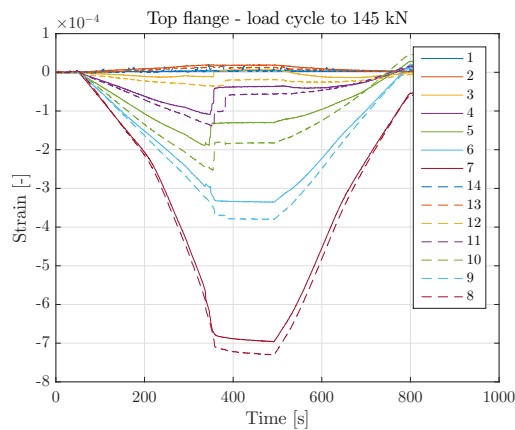


FIGURE 3.30: Measured strains in top flange with Bragg grating optical fibres for the fifth loading cycle of beam B404 (up to 145 kN).

3.5.4 Stereo-vision digital image correlation (3D-DIC)

Stereo-vision Digital Image Correlation (DIC) is an advanced optical and contactless measurement method to analyse the full-field displacement and deformation field in three dimensions, during the complete loading procedure.

Measurement principle

The basic principle is to take images in the undeformed (i.e. reference image) and deformed (i.e. during testing) state of an area of interest and to calculate the displacements by correlating these images. Here, the selected area of interest is the shear critical area, at both sides of the beams. The correlation is quantified as the zero-normalized sum of squared differences for every point within the area, which is independent of scale and offset in lighting. Therefore, the surface area is covered with a non-uniform high-contrast pattern, namely a black and white speckle pattern. A numerical technique generated an optimized speckle pattern, to control speckle size and spatial distribution, in order to avoid correlation problems due to non-uniqueness of a subset. The relatively large speckle size is required due to the large area of interest and the speckle pattern has to be reproducible on a 3D surface.

Two stereo-vision DIC systems are used to investigate both zones with shear force. Each area of interest is approximately 1500 mm by 630 mm. A DIC system consists of two CCD 8-bit cameras (AVT Stingray F-201 B; 1628 by 1236 pixels resolution) with lenses having a focal length of 12 mm mounted on a tripod. Two simultaneously capturing cameras are used for stereo-vision measurements. The cameras are positioned next to each other and at a perpendicular distance of approximately 2700 mm from the web of the test specimen. To ensure good lighting conditions, uniform light intensity and small exposure times, a 500 W quartz iodine lamp was provided per zone. The image acquisition rate of each camera is 1 Hz with an exposure time of 12 ms. All images of the four cameras are transferred to a desktop computer over FireWire and synchronized with the analogue data (applied force and corresponding stroke) of the hydraulic press.

The subset-based method to correlate two images of the speckle pattern considers a pixel and its neighbourhood in the undeformed image $F(x_i, y_j)$ and searches the same subset in the deformed image $G^t(x_i, y_j)$ at time (i.e. load) t . The dimensions of each subset are 27 by 27 pixels, where each pixel has the physical dimension of approximately 1 mm. After capturing images, the correlation process and the post-processing of the data are done using MatchID 3D (in-house, specialized software of KU Leuven, Campus Ghent) [27, 28]. Strains are calculated by smoothing the displacement data over a certain zone to damp out the effect of noise and local uncertainties. Strains are averaged over approximately 150 by 150 mm (51 by 51 displacement data points, with the step size of 3 pixels and the physical dimension of one pixel). This relatively large base length is justified when dealing with heterogeneous materials that exhibit a profound cracking behaviour such as concrete. [14]

Experimental setup

The first step is to apply the speckle pattern onto the surface of the beam. If the pattern is attached carefully to the material underneath, the displacement and deformation of the pattern is the same as the surface material. The speckle pattern is applied with a heat-sensitive stencil printing technique consisting of three layers: a vinyl base layer, the inverse of the speckle pattern and a top protective heat-sensitive polypropylene layer. The base layer is removed carefully (Figure 3.31a) while the concrete surface of the beam is cleaned of dust and preheated. Secondly, the inverse pattern and top layer are attached on the surface. Each pattern is always placed at the same position and in the same direction. Due to heating, the inverse speckle pattern is stucked to the beam and the top layer can be removed (Figure 3.31b and 3.31c). Thereafter, mat (to avoid reflections of light) black paint is sprayed over the pattern (Figure 3.31d and 3.31e). After drying of the paint, the inverse pattern is removed (Figure 3.31f) and the speckle pattern as desired is painted on the area of interest (Figure 3.31g).

The second step is to set up the DIC system (Figure 3.32). Two systems with each two CCD cameras (Figure 3.32a and 3.32b) and a lamp are used. The position of the lamp is empirically optimized by replacing the lamp until good lighting conditions are obtained (Figure 3.32c). All devices are connected with the desktop computer (Figure 3.32d). The apertures of the camera lenses are experimentally optimized based on their histograms. A histogram of a digital image indicates the number of pixels with a certain grey value. For 8-bit cameras, there are 256 grey values where 0 denotes a black pixel and 255 a white pixel. By illuminating and changing the apertures, the histograms for both cameras are equalized.

The third step is to calibrate the cameras of the DIC systems to reconstruct the surface of the measured object. Therefore, calibration images are taken with a rectangular grid of 12 x 9 circles with a known diameter and an intermediate distance of 45 mm. An example of calibration images is shown in Figure 3.33. As such, the intrinsic and extrinsic camera parameters are identified. With the MatchID software package [27, 28], an estimation of the calibration error can be made, expressed as the standard deviation. The standard deviation of the in-plane displacements was equal to 17.0×10^{-3} mm respectively 8.0×10^{-3} mm. The standard deviation of the out-of-plane displacement is an order of magnitude higher due to triangulation errors (100.9×10^{-3} mm). However, the applied loading is primarily carried by in-plane stresses, resulting primarily in in-plane deformations and displacements. Therefore, out-of-plane displacements are not further considered.



(A) Removing base layer.



(B) Removing top layer.



(C) Inverse speckle pattern.



(D) Spraying black paint.



(E) Painted area of interest.



(F) Removing pattern.



(G) Result of the painted speckle pattern.

FIGURE 3.31: Different steps of applying the speckle pattern for DIC measurements.

3. EXPERIMENTAL RESEARCH

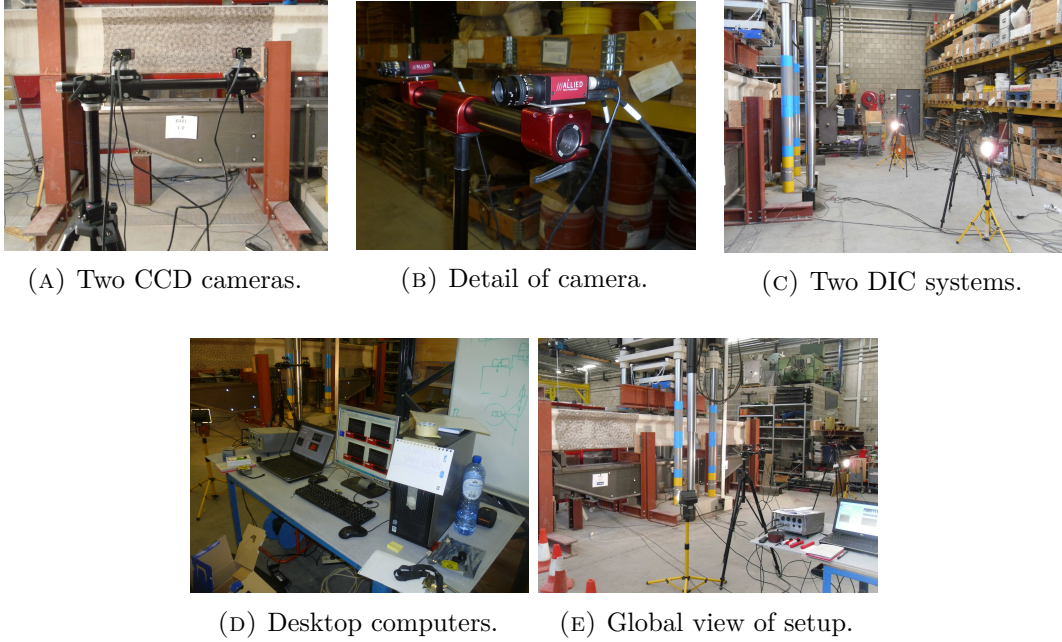


FIGURE 3.32: Different parts of the setup of the DIC systems.

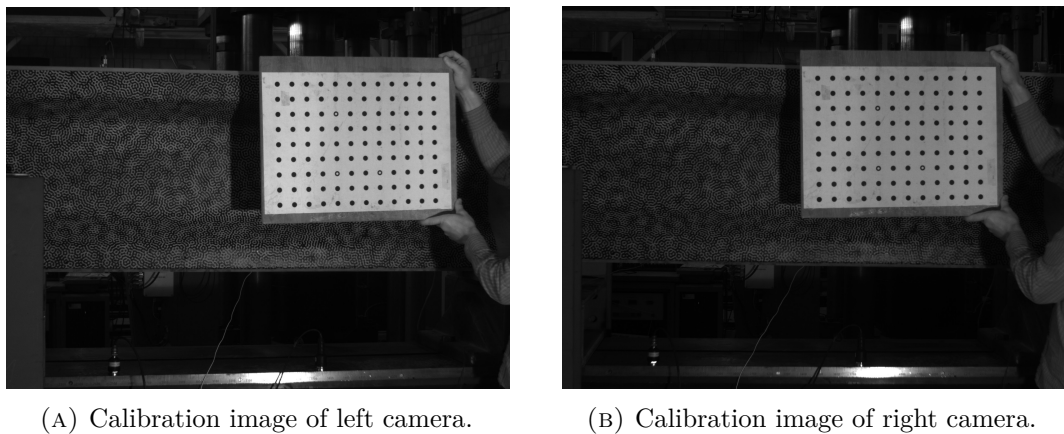


FIGURE 3.33: Examples of calibration images of B401.

Results

After the setup of the DIC systems, the four-point bending test is started and images of both areas of interest are taken each second. For each state of deformation captured by the cameras, the applied shear load is known. Based on the measurements according to the z -axis, also the geometry of the surface of the beams can be reconstructed. The curve of the I-shaped cross-section is visible in Figure 3.34 for the left side of beam B401 at the first image (i.e. before the loading procedure started). After post-processing with MatchID 3D, the continuously monitored displacement field results in the shear deformations and the shear crack propagation. Figure 3.35 shows the horizontal and vertical displacement field of the left side of beam B401 at loading of $V = 236$ kN (i.e. before failure at 256 kN). The horizontal displacement of the beam varies between 2.86 mm in the direction of the loading points at the top side and 0.84 mm in the direction of the supporting points at the bottom side. The vertical displacement of the beam varies between 13.36 mm downwards near the loading points and 1.74 mm downwards near the supporting points. These directions are typical for the four-point bending test. The formation of the inclined shear crack is observable in the web of the beam due to the difference in displacements at both sides. Furthermore, virtual extensometers could be placed over the observed main cracks to obtain the relationship between shear load and crack deformation. A result of this method is shown and discussed in Section 4.2.3, Figure 4.6.

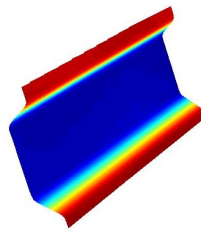


FIGURE 3.34: Reconstructed surface geometry from the DIC measurement of the left side of beam B401 before loading ($V = 0$ kN).

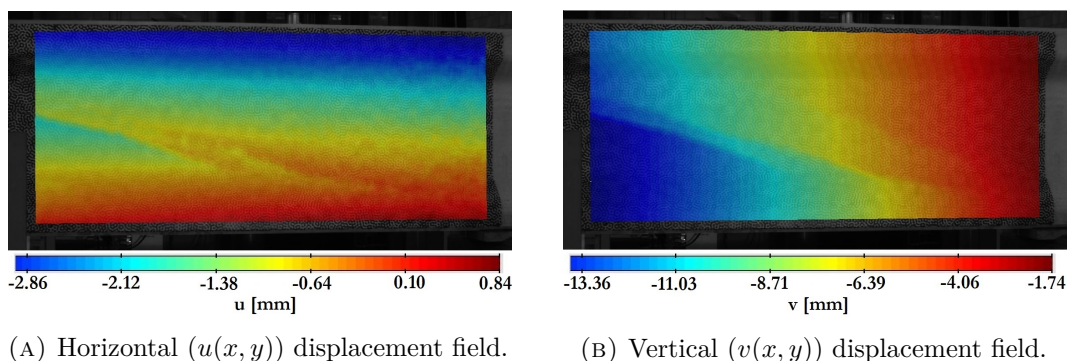


FIGURE 3.35: Typically obtained results from DIC: horizontal ($u(x, y)$) and vertical ($v(x, y)$) displacement field of the left side of beam B401 at load $V = 236$ kN.

3.6 Calculation of the load pattern

Load pattern

As described in Section 3.4, a cyclic pattern with monotonically loading and unloading is applied. The progressive damage loading scheme is calculated just before the test, based on the DEMEC measurements of the deformations (refer to Section 3.5.1).

The predicted first crack load V_{cr} is used to determine this loading pattern (refer to Figure 3.20). The first cycle goes to half of the crack load ($0.5V_{cr}$), the second cycle to the predicted crack load (V_{cr}) and in the third cycle, the load increases continuously until failure ($V_{u,exp}$). As the load of the press is distributed in two point loads, the applied press load P_{cr} is twice as large as the calculated crack load V_{cr} of the beams. The loading rate $\dot{P} = \frac{dP}{dt}$ is 0.25 kN/s, the unloading rate 0.25 kN/s for the first cycle and 1.00 kN/s for the second cycle. These are equivalent to a shear force rate $\dot{V} = \frac{dV}{dt}$ of 0.125 kN/s and 0.50 kN/s respectively.

Predicted crack load V_{cr}

Appendix B.1 explains the followed calculation formulas and scheme of the crack load V_{cr} . It is calculated with the average material properties from the material identification tests (Section 3.3) and with omitting partial safety factors. Table 3.9 presents the results of the calculation for each beam. In all cases, the load due to the bending moment M_{cr} determines the crack load. The effect of the amount of steel fibres is restricted, it only influences the material properties. The results of beam B401 are the largest, due to the large measured tensile strength (refer to Section 3.3.5). The crack load of B401, B402 and B403 are almost twice as large as the results of B404, B405 and B406, due to the double amount of prestressing (1488 MPa compared to 750 MPa). Figure 3.36 shows the loading pattern of beam B405, both the predicted and the experimentally applied one.

TABLE 3.9: Predicted crack loads.

		B401	B402	B403	B404	B405	B406
$V_{cr,w}$	[kN]	221.5	212.0	216.1	181.9	145.7	176.0
$V_{cr,bending}$	[kN]	177.4	178.9	166.6	99.9	94.4	95.8
V_{cr}	[kN]	177.4	178.9	166.6	99.9	94.4	95.8
P_{cr}	[kN]	354.8	357.8	333.2	199.8	188.8	191.6

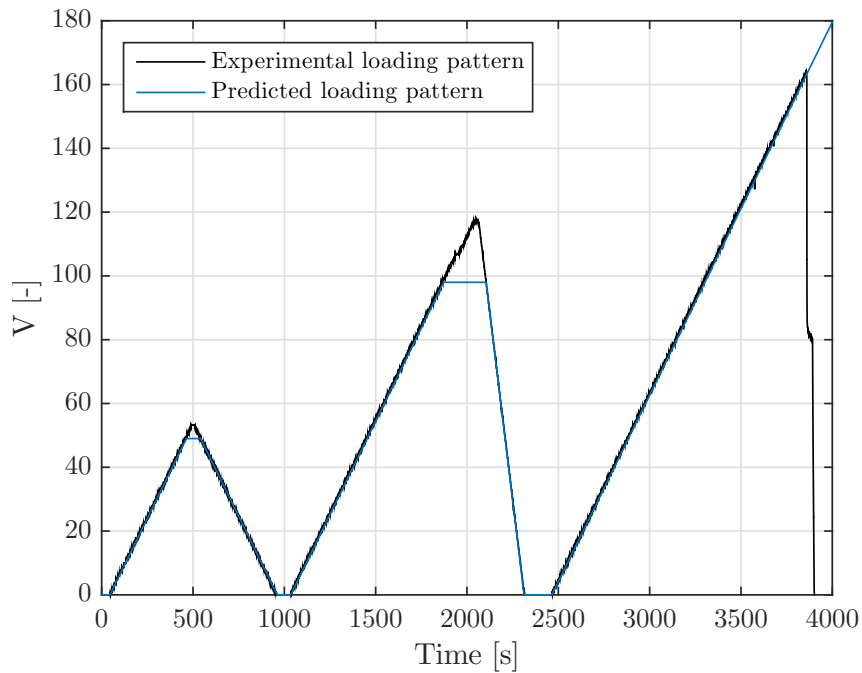


FIGURE 3.36: Predicted and applied loading pattern (example of beam B405).

Prestress losses

Figure 3.26 showed the results of the DEMEC measurements between the day of removal of the formwork and the day of testing, by plotting the measured strains over the height of the beam. The beam's shortening (indicated by negative strains) is approximated with a linear regression function: $h = a \cdot \varepsilon + b$ with a the gradient and b the intercept. The strains are converted to stress losses with the modulus of elasticity of the prestressing reinforcement (Hooke's law). Together with the initial prestress of 1488 or 750 MPa, the retained stress level over the beam's height is calculated and presented in Figure 3.37. Approximately 5% of the initial prestressing force is lost in the top strand for all beams, which is relatively small. In the seven bottom strands, an average of 80% of the initial stress is retained for beam B401, B402, B404 and B405. Beam B403 and B406 have the lowest remaining stress of 73 and 76% respectively, due to the largest measured strains (refer to Section 3.5.1).

3. EXPERIMENTAL RESEARCH

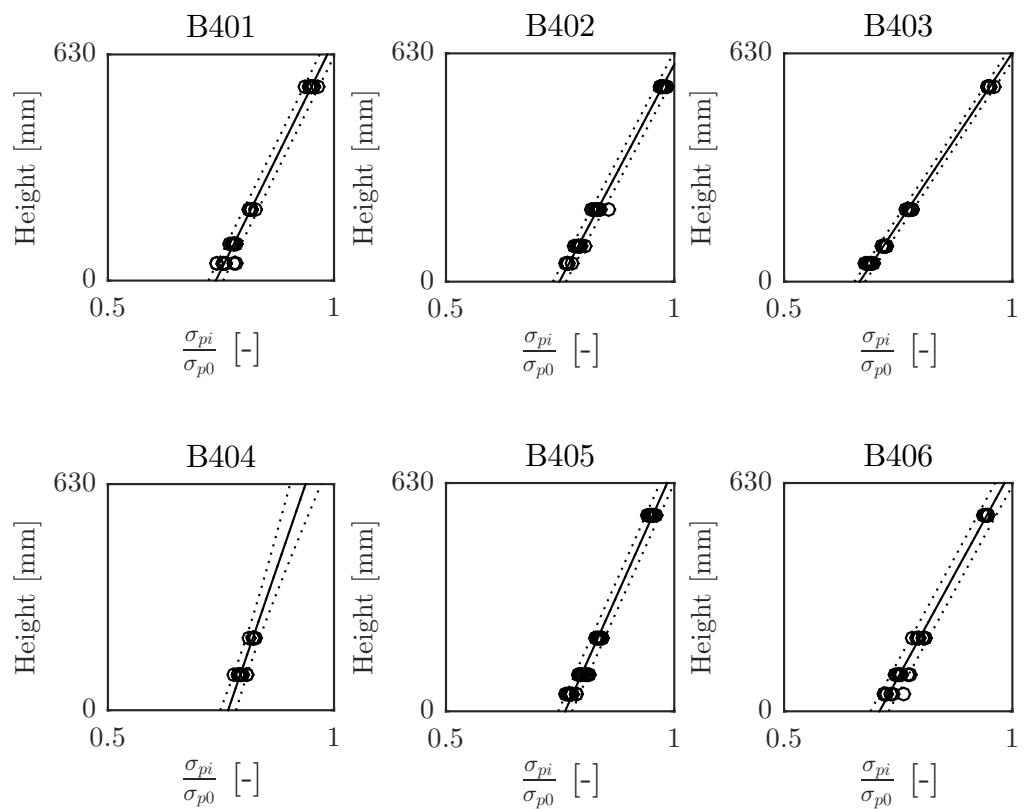


FIGURE 3.37: Retained stress level in the strands (\circ) between the day of removal of the formwork and the day of full-scale testing, with first order polynomial fit (-) and 95% prediction interval (dotted line).

3.7 Results

In this section, the main experimental results of the six tested beams are presented. The following aspects are reported for each beam: overview of the main parameters, applied load pattern, obtained load-displacement curve, discussion of failure load and mode, and observed cracking pattern. A parameter study of and comparison between the tested beams is performed in Chapter 4.

3.7.1 B401

Table 3.10 presents the main investigated properties, the dates of manufacturing and testing, the experimentally observed results of material properties and the failure load and mode. Figure 3.38 presents the applied loading scheme and the observed load-displacement response at location of the loading point of the hydraulic press.

TABLE 3.10: Main results of B401.

Investigated properties		
V_f	[kg/m ³]	0
ρ_w	[$\times 10^{-3}$]	2.693
σ_{p0}	[MPa]	1488
Dates		
Day of manufacturing		20 October 2015
Day of testing		27 November 2015
Age at testing day	[days]	38
Experimentally observed results		
f_{cm}	[MPa]	75.6
f_{ctm}	[MPa]	3.5
$V_{u,exp}$	[kN]	256.4
Failure mode		S-DT*

*: Shear (S) failure mode due to Diagonal Tension (DT)

The first crack of beam B401 (Figure 3.39a) occurred at 177.5 kN, causing a variation of stiffness in the load-deflection curve (Figure 3.38b). At both sides of the beam, cracks at an angle of approximately 20° grow in the web until failure at one side of the beam. In the unloading phase of the second cycle, the cracks close, but the stiffness is not recovered. Due to the high prestressing force, the inclination of the crack is lower than 45°. A schematic view of the cracking pattern at failure is given in Figure 3.50a.

Beam B401 failed at a load of 256.4 kN, in a shear failure mode due to diagonal tension (S-DT), as designed (Figure 3.39c). Inclined web cracking causes yielding and rupture of the conventional shear reinforcement (Figure 3.39b). Mainly one major crack occurs, leading to a very brittle failure (Figure 3.39d). There is no possibility of redistribution of internal forces and the energy is released instantly.

3. EXPERIMENTAL RESEARCH

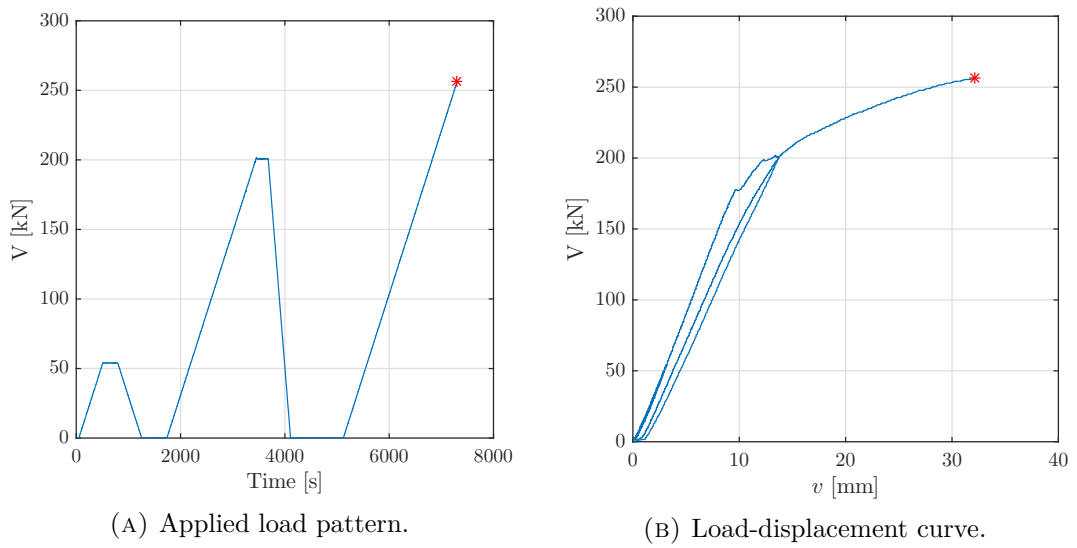


FIGURE 3.38: Applied loading pattern and observed load-displacement curve (at location of the loading point) of B401.

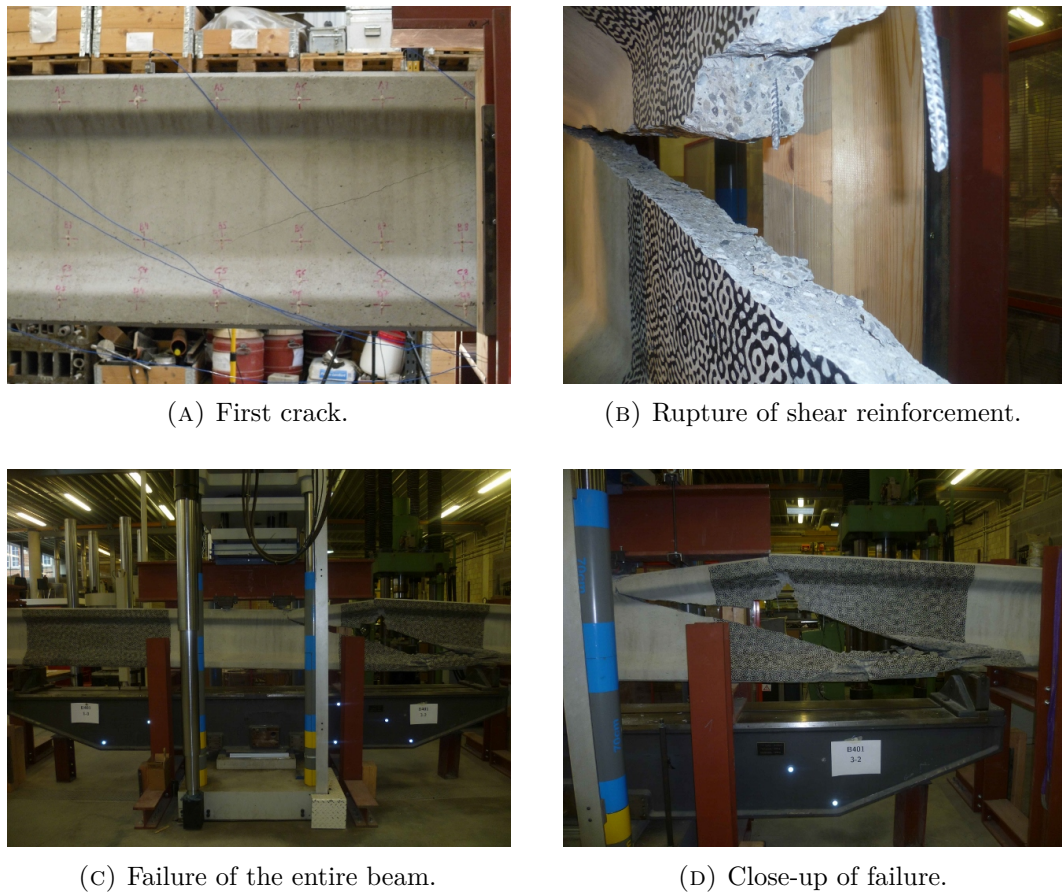


FIGURE 3.39: Different parts of the failure of beam B401.

3.7.2 B402

Table 3.11 presents the main investigated properties, the dates of manufacturing and testing, the experimentally observed results of the material properties and the failure load and mode. Figure 3.40 presents the applied cyclic loading scheme and the observed load-displacement response at location of the loading point of the hydraulic press.

TABLE 3.11: Main results of B402.

Investigated properties		
V_f	[kg/m ³]	20
ρ_w	[$\times 10^{-3}$]	0
σ_{p0}	[MPa]	1488
Dates		
Day of manufacturing		20 October 2015
Day of testing		2 December 2015
Age at testing day	[days]	43
Experimentally observed results		
f_{cm}	[MPa]	73.8
f_{ctm}	[MPa]	3.2
$V_{u,exp}$	[kN]	218.5
Failure mode		S-DT*
*: Shear (S) failure mode due to Diagonal Tension (DT)		

The first inclined web crack of beam B402 (Figure 3.41a) occurred at 184.0 kN, causing a variation of stiffness in the load-deflection curve (Figure 3.40b). A larger shear crack at the other side of the beam is observed at 215.0 kN, right before failure. In the unloading phase of the second cycle, the cracks close, but the stiffness is not recovered. A schematic view of the cracking pattern at failure is given in Figure 3.50b and 3.51a.

Beam B402 failed at a load of 218.5 kN, in a shear failure mode due to diagonal tension (S-DT), as designed (Figure 3.41c). The steel fibres are pulled out of the concrete matrix, but fibre rupture was not observed (Figure 3.41b). The addition of steel fibres leads to multiple cracks and a more ductile failure (Figure 3.41d). There is a redistribution of internal forces and a more gradual energy dissipation due to the post-cracking behaviour of SFRC.

3. EXPERIMENTAL RESEARCH

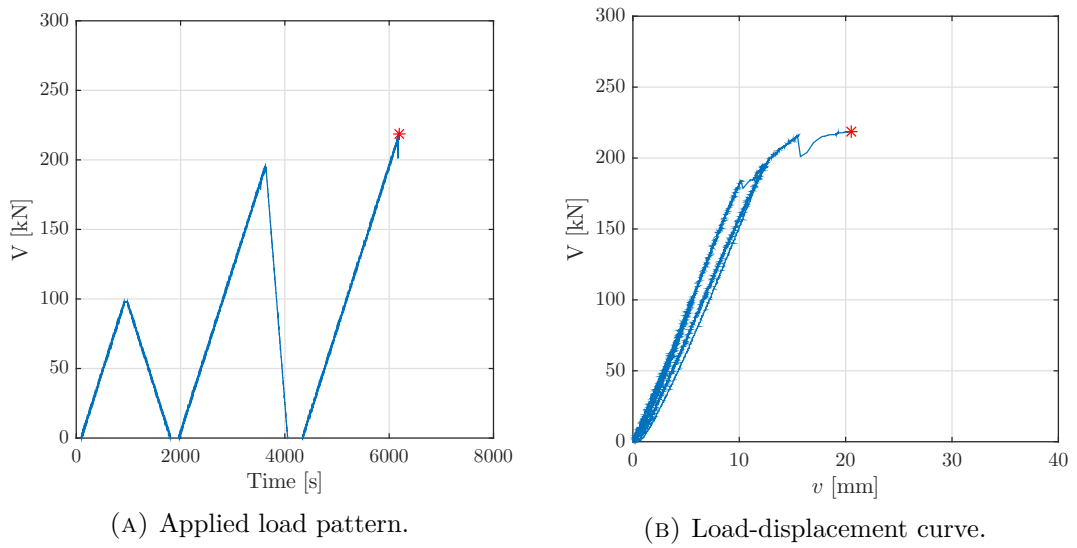


FIGURE 3.40: Applied loading pattern and observed load-displacement curve (at location of the loading point) of B402.

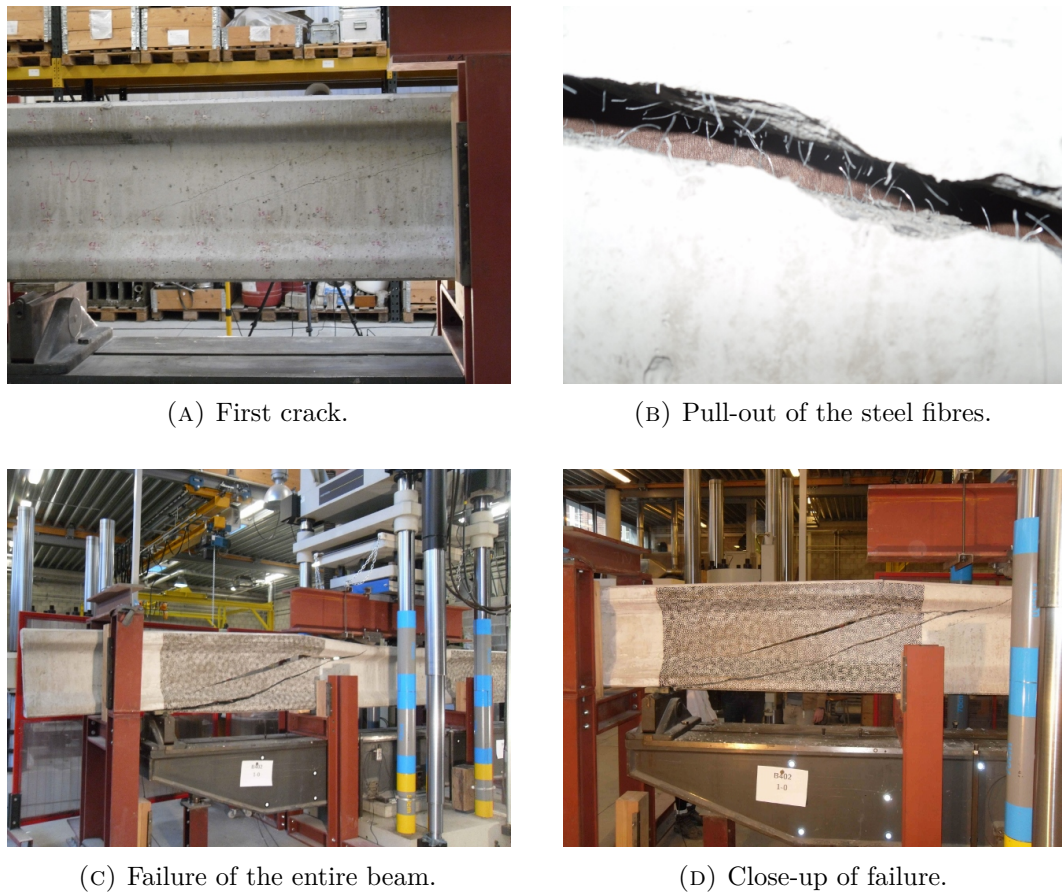


FIGURE 3.41: Different parts of the failure of beam B402.

3.7.3 B403

Table 3.12 presents the main investigated properties, the dates of manufacturing and testing, the experimentally observed results of the material properties and the failure load and mode. Figure 3.42 presents the applied cyclic loading scheme and the observed load-displacement response at location of the loading point of the hydraulic press.

TABLE 3.12: Main results of B403.

Investigated properties		
V_f	[kg/m ³]	40
ρ_w	[$\times 10^{-3}$]	0
σ_{p0}	[MPa]	1488
Dates		
Day of manufacturing		21 October 2015
Day of testing		7 December 2015
Age at testing day	[days]	47
Experimentally observed results		
f_{cm}	[MPa]	69.7
f_{ctm}	[MPa]	2.8
$V_{u,exp}$	[kN]	254.4
Failure mode		S-DT*
*: Shear (S) failure mode due to Diagonal Tension (DT)		

The first inclined web cracks of beam B403 occurred at 216.5 kN, causing a variation of stiffness in the load-deflection curve (Figure 3.42b). Beam B403 has multiple cracks (Figure 3.43b), instead of one large crack as in beam B401. However, all large cracks were observed at one side of beam B403, only small cracks occurred at the other side. A schematic view of the cracking pattern at failure is given in Figure 3.50c and 3.51b.

Beam B403 failed at a load of 254.4 kN, in a shear failure mode due to diagonal tension (S-DT), as designed (Figure 3.43c). The steel fibres are pulled out of the concrete matrix, but fibre rupture was not observed (Figure 3.43a). The addition of a higher amount of steel fibres than beam B402 leads to even more cracks and an even more ductile failure. There is a higher redistribution of internal forces and a more gradual energy dissipation due to the post-cracking behaviour of SFRC.

3. EXPERIMENTAL RESEARCH

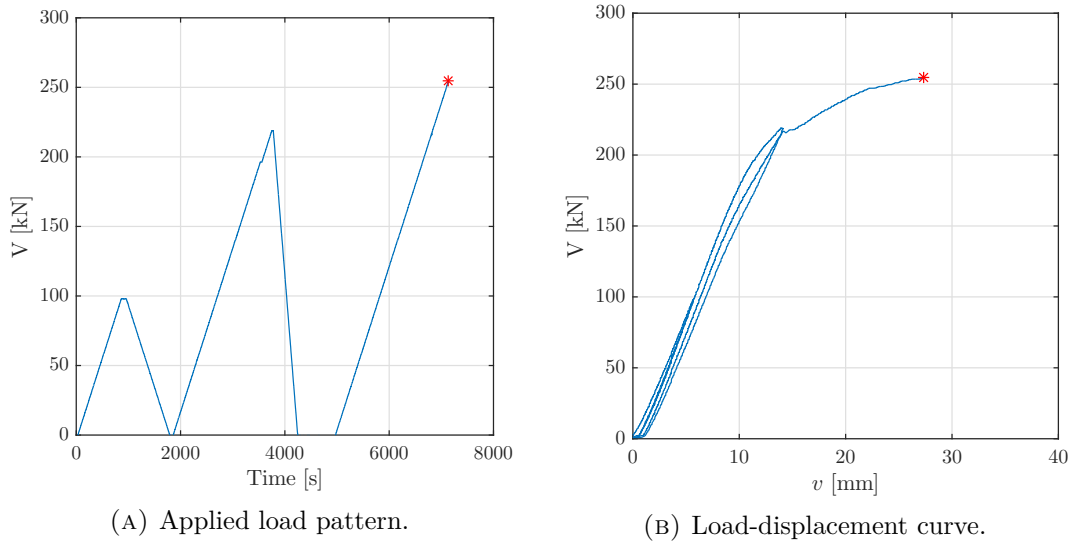


FIGURE 3.42: Applied loading pattern and observed load-displacement curve (at location of the loading point) of B403.



FIGURE 3.43: Different parts of the failure of beam B403.

3.7.4 B404

Table 3.13 presents the main investigated properties, the dates of manufacturing and testing, the experimentally observed results of the material properties and the failure load and mode. Figure 3.44 presents the applied cyclic loading scheme and the observed load-displacement response at location of the loading point of the hydraulic press. The loading scheme has been modified with more cycles, where the third, fourth and fifth cycle goes to 10% more of the previous one.

TABLE 3.13: Main results of B404.

Investigated properties		
V_f	[kg/m ³]	0
ρ_w	[$\times 10^{-3}$]	2.693
σ_{p0}	[MPa]	750
Dates		
Day of manufacturing		20 October 2015
Day of testing		11 December 2015
Age at testing day	[days]	52
Experimentally observed results		
f_{cm}	[MPa]	68.1
f_{ctm}	[MPa]	3.7
$V_{u,exp}$	[kN]	202.5
Failure mode		S-DT*
*: Shear (S) failure mode due to Diagonal Tension (DT)		

The first crack of beam B404 occurred at 128.5 kN (during the fourth cycle), due to bending. These vertical cracks start at the bottom of the middle of the beam, which could also be concluded from Section 3.5.3. The first shear cracks (Figure 3.45a) occurred at 137.5 kN (during the fifth cycle). At both sides of the beam, cracks at an angle of approximately 30° grow in the web until failure at one side of the beam. Due to the lower prestressing force than beam B401, the inclination of the cracks is higher.

Beam B404 failed at a load of 202.5 kN, in a shear failure mode due to diagonal tension (S-DT), as designed (Figure 3.45c). Comparable to the failure of beam B401, inclined web cracking causes yielding and rupture of the conventional shear reinforcement (Figure 3.45b). Mainly one major crack occurs, leading to a brittle failure (Figure 3.45d). However, this failure is less brittle than at beam B401, due to the lower prestressing force. There is no possibility of redistribution of internal forces and the energy is released instantly.

3. EXPERIMENTAL RESEARCH

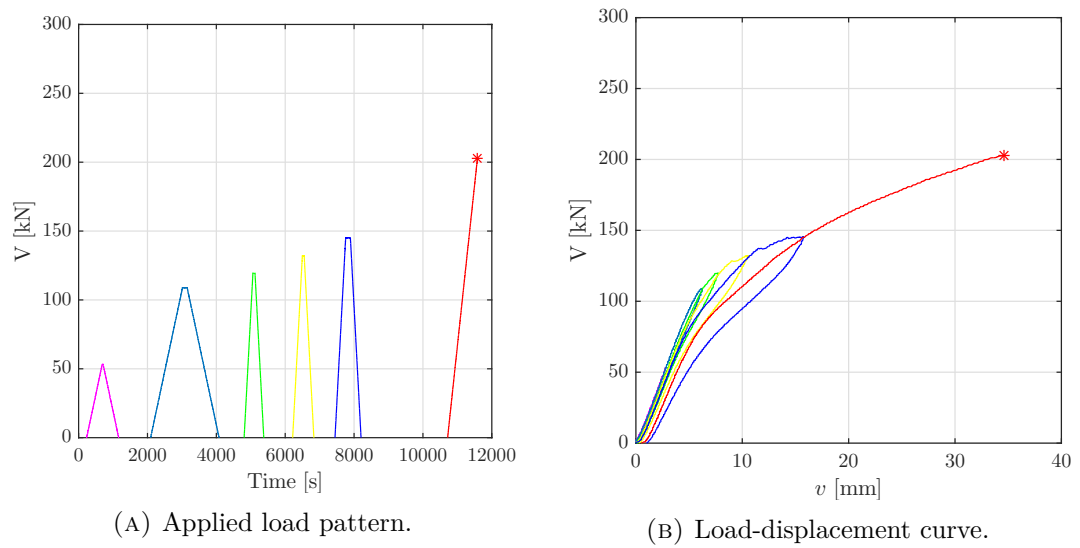


FIGURE 3.44: Applied loading pattern and observed load-displacement curve (at location of the loading point) of B404.

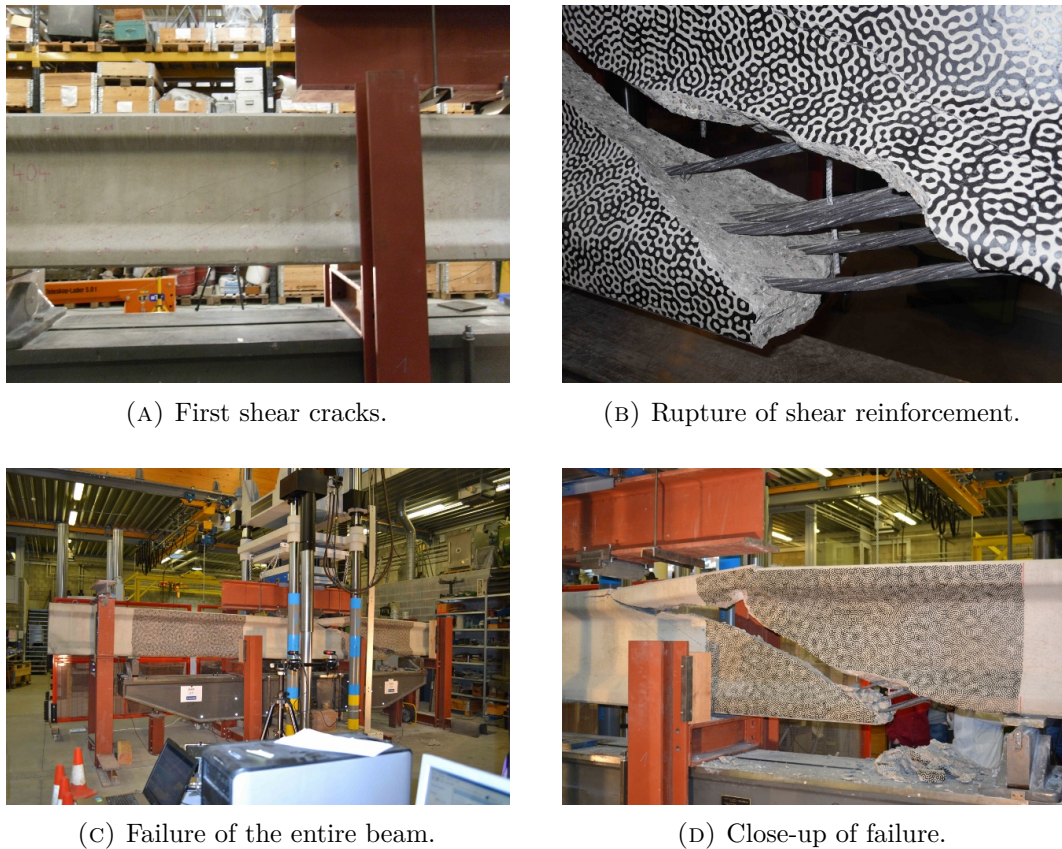


FIGURE 3.45: Different parts of the failure of beam B404.

3.7.5 B405

Table 3.14 presents the main investigated properties, the dates of manufacturing and testing, the experimentally observed results of the material properties and the failure load and mode. Figure 3.46 presents the applied cyclic loading scheme and the observed load-displacement response at location of the loading point of the hydraulic press.

TABLE 3.14: Main results of B405.

Investigated properties		
V_f	[kg/m ³]	20
ρ_w	[$\times 10^{-3}$]	0
σ_{p0}	[MPa]	750
Dates		
Day of manufacturing		20 October 2015
Day of testing		15 December 2015
Age at testing day	[days]	56
Experimentally observed results		
f_{cm}	[MPa]	79.4
f_{ctm}	[MPa]	2.7
$V_{u,exp}$	[kN]	164.1
Failure mode		S-DT*
*: Shear (S) failure mode due to Diagonal Tension (DT)		

The first inclined web cracks of beam B405 (Figure 3.47a) occurred at 131.0 kN and at the other side at 142.5 kN (Figure 3.47b). As these shear loads were reached in the third cycle, there is only a small variation of stiffness in the load-deflection curve during the second cycle (Figure 3.46b). This variation is because of non-visible vertical cracks at the bottom of the middle of the beam, due to bending. A schematic view of the cracking pattern at failure is given in Figure 3.51c.

Beam B405 failed at a load of 164.1 kN, in a shear failure mode due to diagonal tension (S-DT), as designed (Figure 3.47c). The addition of steel fibres leads to multiple cracks (Figure 3.47d) and a more ductile failure. There is a redistribution of internal forces and a more gradual energy dissipation due to the post-cracking behaviour of SFRC.

3. EXPERIMENTAL RESEARCH

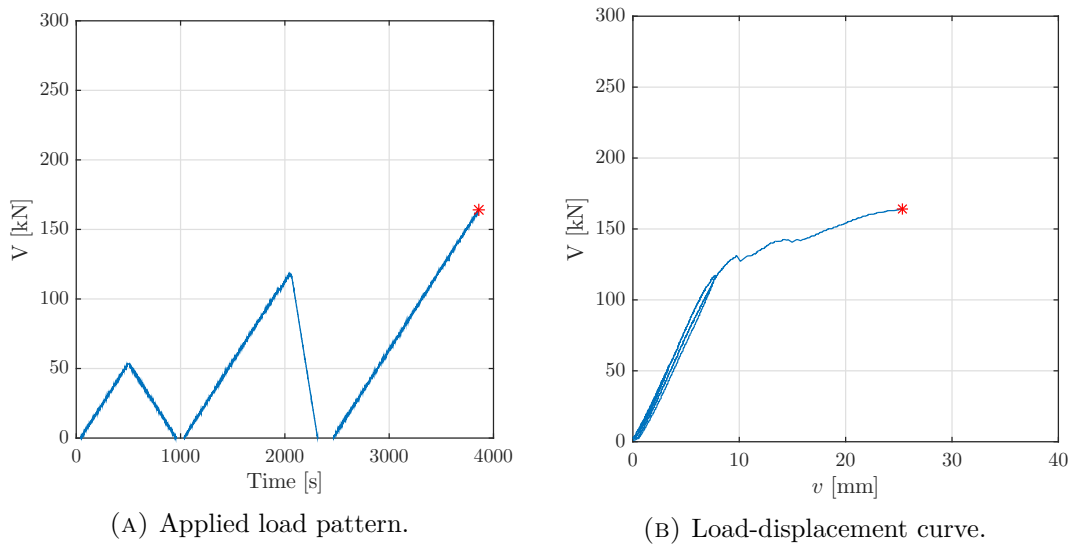


FIGURE 3.46: Applied loading pattern and observed load-displacement curve (at location of the loading point) of B405.

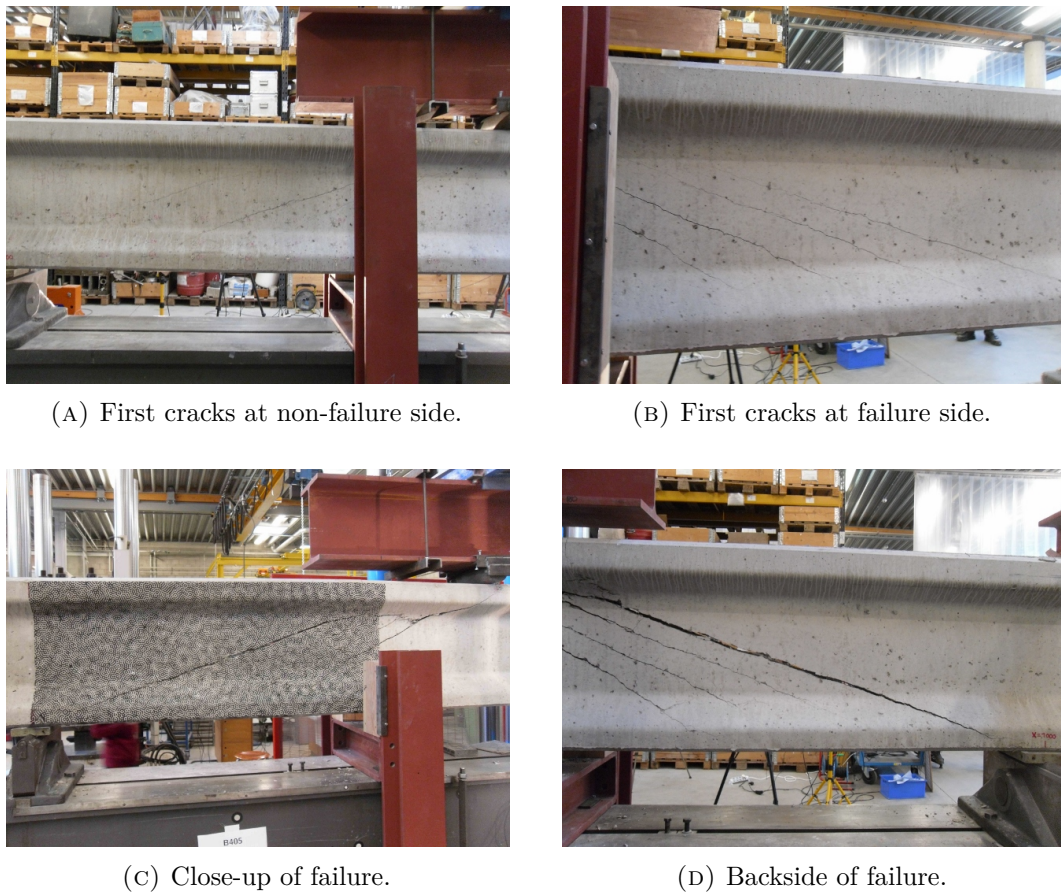


FIGURE 3.47: Different parts of the failure of beam B405.

3.7.6 B406

Table 3.15 presents the main investigated properties, the dates of manufacturing and testing, the experimentally observed results of the material properties and the failure load and mode. Figure 3.48 presents the applied cyclic loading scheme and the observed load-displacement response at location of the loading point of the hydraulic press.

TABLE 3.15: Main results of B406.

Investigated properties		
V_f	[kg/m ³]	40
ρ_w	[$\times 10^{-3}$]	0
σ_{p0}	[MPa]	1488
Dates		
Day of manufacturing		21 October 2015
Day of testing		17 December 2015
Age at testing day	[days]	57
Experimentally observed results		
f_{cm}	[MPa]	77.4
f_{ctm}	[MPa]	3.6
$V_{u,exp}$	[kN]	197.4
Failure mode		S-DT*
*: Shear (S) failure mode due to Diagonal Tension (DT)		

The first inclined web cracks of beam B406 occurred at 144.4 kN, in the third cycle. The small variation of stiffness in the load-deflection curve during the second cycle (Figure 3.46b) is due to vertical cracks at the bottom of the middle of the beam, due to bending, as shown in Figure 3.49a. Again, beam B406 has multiple scattered cracks at both sides of the beam (Figure 3.49b). A schematic view of the cracking pattern at failure is given in Figure 3.51d.

Beam B406 failed at a load of 197.4 kN, in a shear failure mode due to diagonal tension (S-DT), as designed (Figure 3.49c). The steel fibres are pulled out of the concrete matrix, but fibre rupture was not observed. The addition of a higher amount of steel fibres than beam B405 leads to even more cracks (Figure 3.49d) and an even more ductile failure. There is a more prolonged redistribution of internal forces and a more gradual energy dissipation due to the post-cracking behaviour of SFRC.

3. EXPERIMENTAL RESEARCH

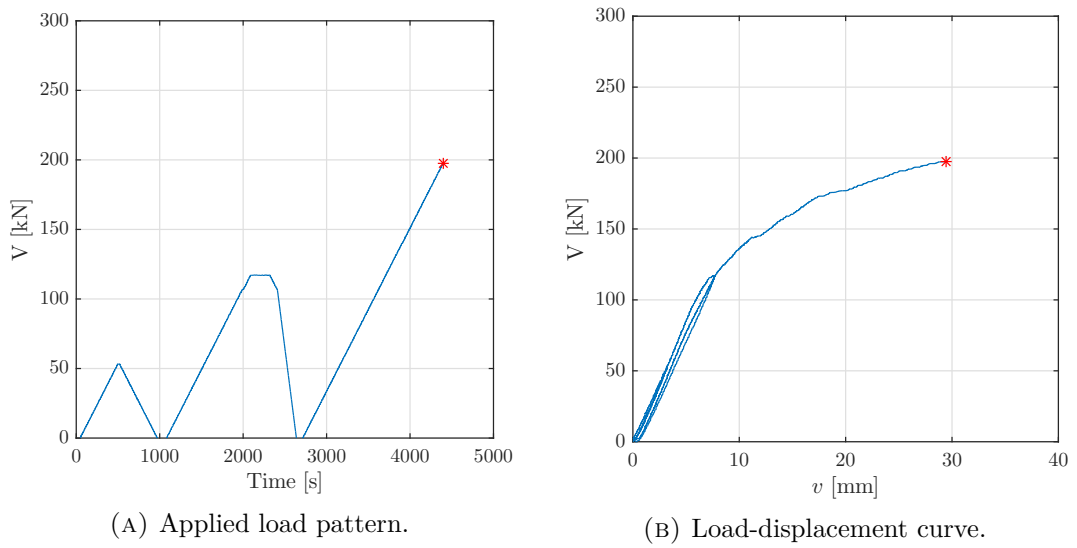


FIGURE 3.48: Applied loading pattern and observed load-displacement curve (at location of the loading point) of B406.

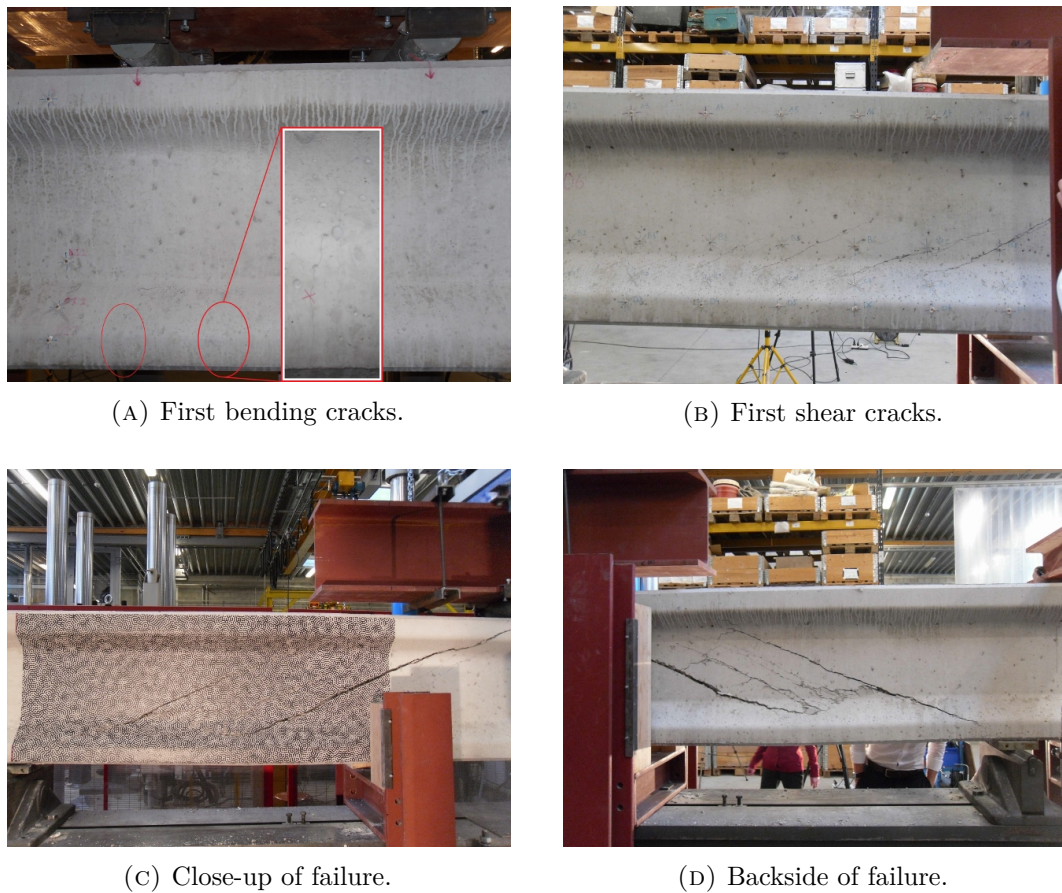


FIGURE 3.49: Different parts of the failure of beam B406.

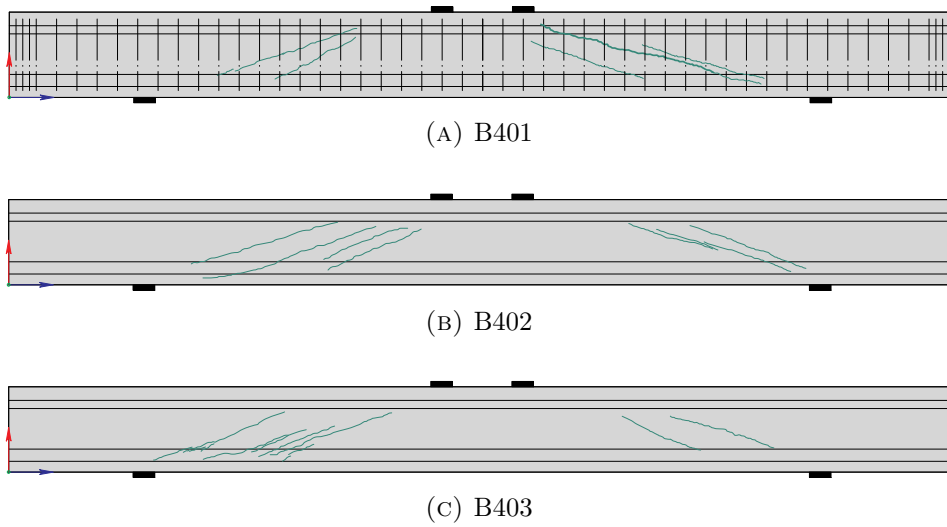


FIGURE 3.50: Cracking patterns at failure of the three beams, view on the frontside.

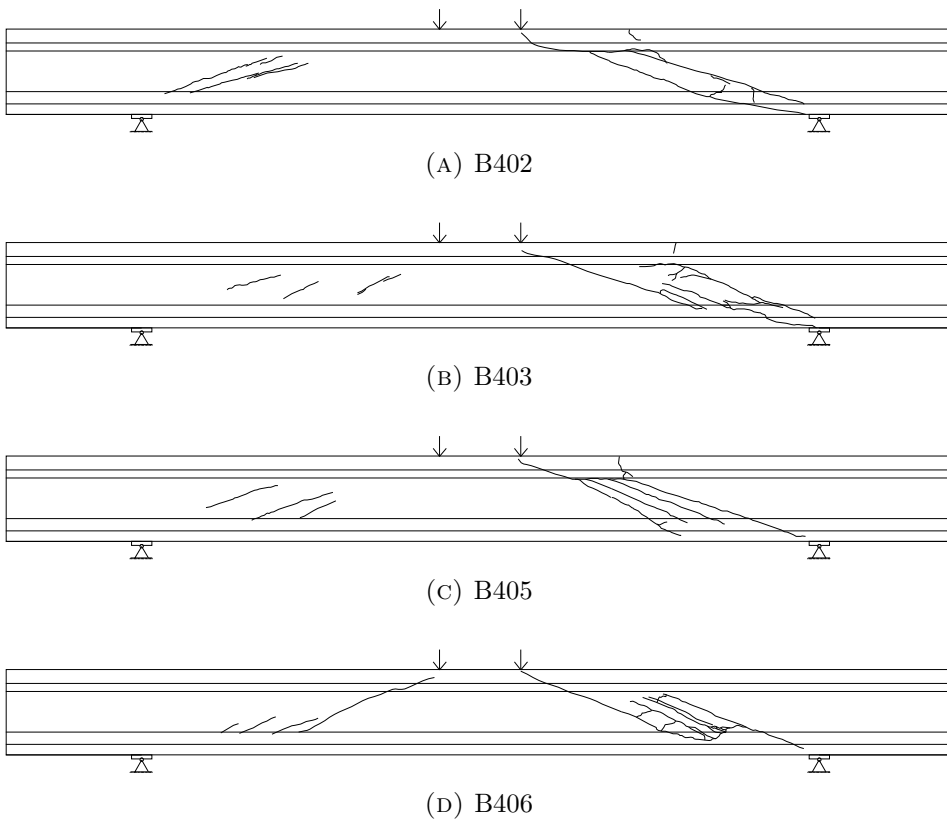


FIGURE 3.51: Cracking patterns at failure of the SFRC beams, view on the backside.

3.7.7 Amount of steel fibres

As the amount of fibres crossing the crack plane influences the failure behaviour, some cores are drilled to determine the number of steel fibres present in a cross-section. After the four-point bending test, seven cores for each beam are localised over the crack openings, drilled out and the steel fibres are counted manually.

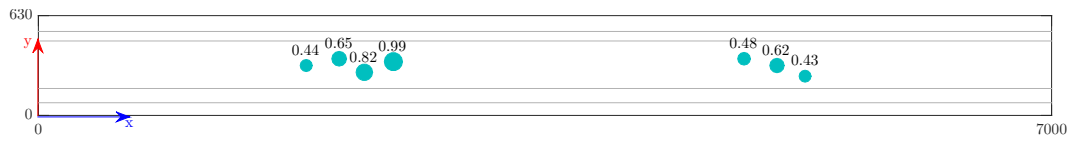
Appendix B.2 gives the results of this procedure. Figures of the locations of the drilled cores are given (Figure B.2, B.3, B.4 and B.5 for beam B402, B403, B405 and B406 respectively). A complete overview of the amount of fibres of the cores is given in Table B.1. Since each core is taken over a crack opening, it consists of two parts. The crack surface A_{tot} is measured and the number of fibres N_f counted, for both parts. This results in an amount of fibres per surface area.

Figure 3.52 gives a schematic view of the results per beam. Each circle denotes for an amount of fibres. The larger the circle, the higher the amount of fibres per surface area. Since beams B402 and B405 contain 20 kg/m³ steel fibres, their values are lower than beams B403 and B406, containing 40 kg/m³ steel fibres. The mean values are 0.63, 1.45, 0.54 and 1.43 [1/cm²] for beam B402, B403, B405 and B406 respectively, with coefficients of variation between 17% and 33% (Table B.1).

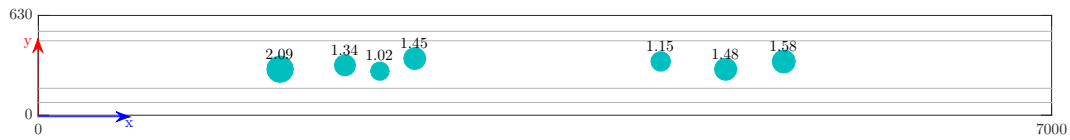
There is no clear indication of locations that have a lower amount of fibres and that can have less resistance to cracking. Only some small differences can be related to the cracking pattern. For beam B402, the first crack at the left side occurred closest to the supporting point. Here, the amount of fibres is smaller than at the second crack (0.44 and 0.63 compared to 0.82 and 0.99). For beam B403, the crack closest to the supporting point occurred as the last one and has a small crack width. This location has the highest amount of fibres (2.09).

All tested beams have the same type of steel fibres, namely Dramix RC-80/30-CP with diameter 0.38 mm. To compare the results to cross-sections of SFRC containing different types of fibres, the fibre reinforcement ratio ρ_f is calculated with Equation 3.21. A_f is the fibre cross sectional area, here equal to 0.11 mm². The results are given in Table B.1 and vary between 0.05% and 0.11% for beams with 20 kg/m³ steel fibres and between 0.11% and 0.24% for beams with 40 kg/m³ steel fibres.

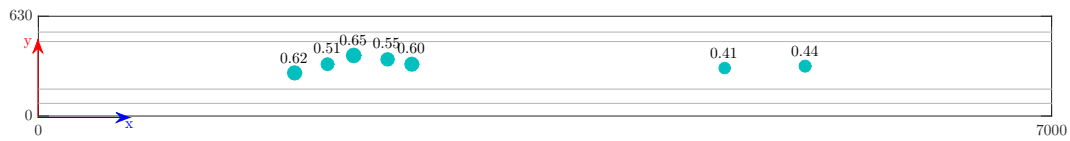
$$\rho_f = \frac{N_f \cdot A_f}{A_{tot}} \quad (3.21)$$



(A) B402 (20 kg/m³ of steel fibres).



(B) B403 (40 kg/m³ of steel fibres).



(C) B405 (20 kg/m³ of steel fibres).



(D) B406 (40 kg/m³ of steel fibres).

FIGURE 3.52: Schematic view of the amount of fibres per surface area (in 1/cm²), measured at cores crossing the crack planes.

3.8 Conclusion

In this chapter, the performed experimental research program is presented. Firstly, the beam design, materials and production process of the six I-shaped prestressed steel fibre reinforced concrete beams are described. The three main investigated parameters are fibre dosage, amount of conventional shear reinforcement and amount of prestressing. Secondly, hardened material properties are determined with material identification tests on cubes, cylinders and prisms. The cube compressive strength, the cylindrical compressive strength, the modulus of elasticity, the flexural tensile strength, the residual tensile strengths, the tensile splitting strength and the uniaxial tensile strength are measured or calculated and extensively discussed, for both plain concrete as steel fibre reinforced concrete.

Thereafter, the experimental setup of the four-point bending test is given, together with the measurement methods. Besides conventional techniques, advanced optical measurement methods are used as well in order to gather a large amount of information of the full-field displacement and deformation field instead of only the failure load and failure mode. The shear behaviour is considered by deformations, displacements and cracking pattern properties to understand the complete mechanical behaviour during the entire shear loading procedure. The conventional techniques are demountable mechanical strain gauges and linear variable differential transformers, the optical techniques are Bragg grating optical fibres and stereo-vision digital image correlation.

Lastly, the first crack load is predicted and the load pattern calculated, based on the measured prestress losses. As the experimental research program is described, the main results of the six tested beams are listed. The load-displacement curve, the observed cracking pattern and the failure load and mode are presented. All beams failed in shear failure mode due to diagonal tension, as designed. For the plain concrete beams, inclined web cracking caused yielding and rupture of the conventional shear reinforcement, leading to very brittle failure. For the SFRC beams, the steel fibres are pulled out of the concrete matrix, leading to multiple cracks and a more ductile failure, due to its post-cracking behaviour. The amount of steel fibres crossing the crack plane is investigated as well.

Based on the different parameters of the tested beams, the results can be compared. Therefore, the next chapter contains a parameter study. Also the experimentally observed and analytically predicted cracking and failure loads, according to different models, will be compared. This analytical study is performed to further investigate the mechanical behaviour of prestressed SFRC beams subjected to shear loading.

Chapter 4

Analytical study

4.1 Introduction

This analytical study aims to improve the understanding of the mechanical behaviour of prestressed SFRC beams subjected to shear loading. However adding steel fibres as an alternative for conventional shear reinforcement is promising, the application is restricted, mainly due to the lack of (experience with) international design codes.

Besides an analytical study, also a numerical simulation by developing a finite element model provides insight in the mechanical behaviour. This is performed by Tom Schoofs and Vincent Van de Poel as part of their master thesis. However, a finite element analysis requires a certain degree of experience and understanding to design concrete structural elements. Therefore, design engineers mainly still rely on the application of analytical models, in particular international building codes.

The previous chapter presented the experimental research program. Investigation of the shear behaviour of prestressed steel fibre reinforced concrete beams is not only limited to obtaining a valuable set of experimental results. In attempt to encourage the use of SFRC for structural applications, also discussions of the measured results and of the existing design guidelines are needed. The former is done by means of a parameter study in Section 4.2. The latter is done by comparing the experimentally obtained results with predictions according to analytical models in Section 4.4 and 4.5. Thirdly, the predicted and measured crack loads are discussed in Section 4.3.

4.2 Parameter study

In this section, the obtained experimental results are investigated by performing a parameter study. Firstly, the main results are summarized. Secondly, the influence of the amount of steel fibres and the influence of the amount of prestressing are described. The effect of the measured material properties is also discussed. Finally, a comparison with the shear test results of De Wilder [13] is made.

4.2.1 Overview of the main experimental results

Six I-shaped prestressed (SFR)C beams were tested with a four-point bending test to study the shear behaviour and capacity. Figure 3.1 is repeated in Figure 4.1, to remind the beam's notations (B401 to B406). The tested beams had three varying parameters that will be investigated, namely:

- Amount of steel fibres V_f : 0 kg/m³, 20 kg/m³ or 40 kg/m³
- Amount of conventional shear reinforcement ρ_w : 0 or 2.693×10^{-3} [-]
- Amount of prestressing σ_{p0} : 750 MPa or 1488 MPa

Firstly, not only the shear capacity but also the shear behaviour is investigated. Therefore, the experimentally obtained load-displacement responses at location of the loading point of the hydraulic press are presented in Figure 4.2. (The individual curves can be found in Section 3.7). Secondly, the shear capacity of the beams is presented. Table 4.1 shows the experimentally obtained failure loads together with the main characteristics of the beams. Figure 4.3 presents these failure loads, classified according to their parameters V_f and σ_{p0} . These figures will be used to discuss the influence of the parameters on the shear behaviour in the next sections.

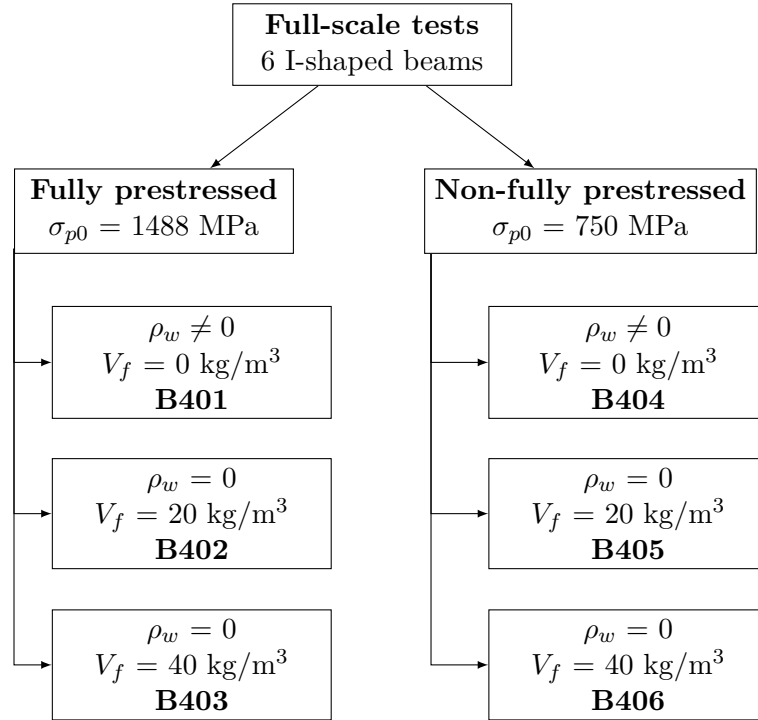


FIGURE 4.1: (Refer to Figure 3.1) Reminder of the tested beams, classified according to their parameters and with their name (B40x).

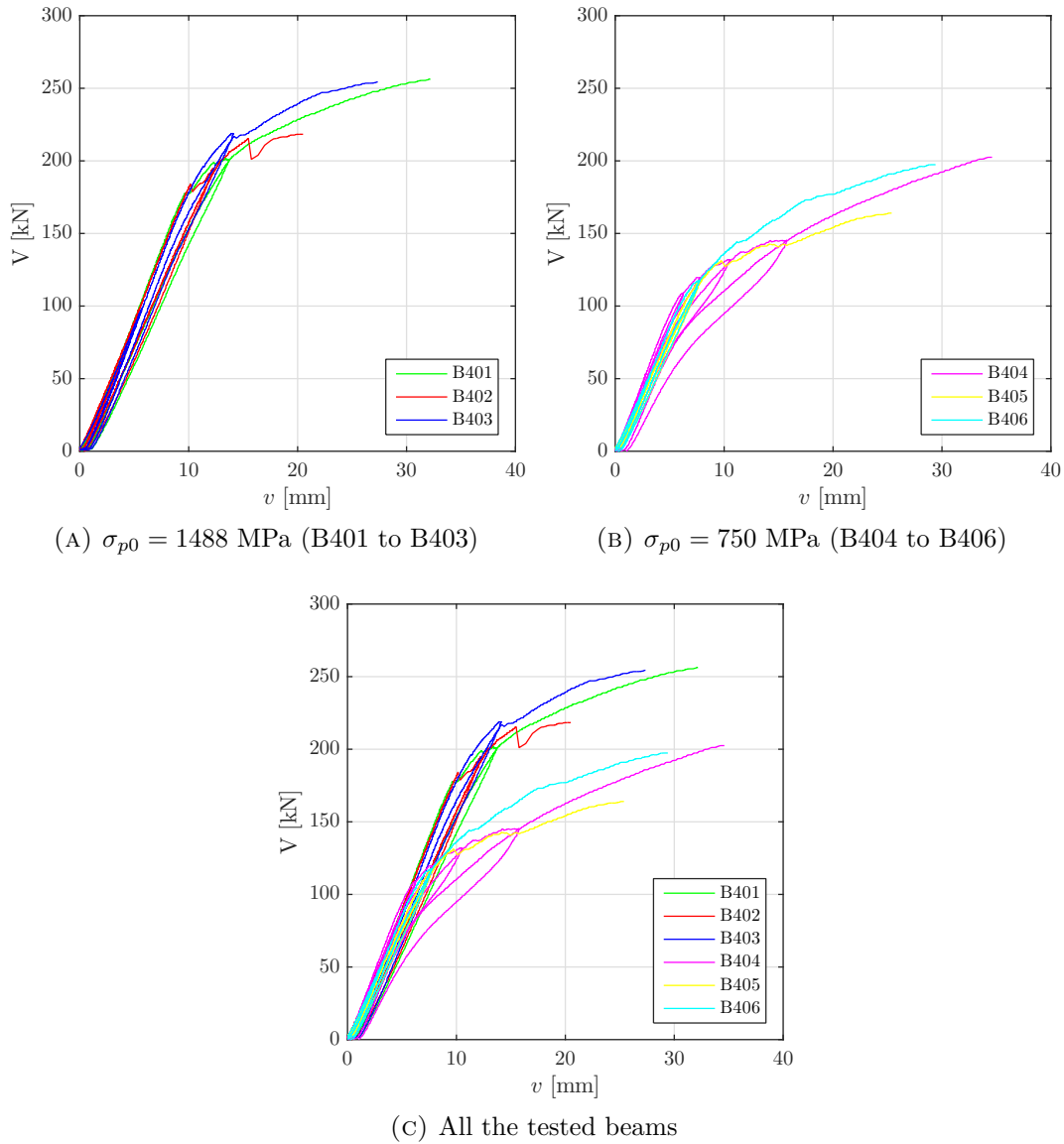


FIGURE 4.2: Experimentally obtained load-displacement curves (at location of the loading point) of the tested beams.

4. ANALYTICAL STUDY

TABLE 4.1: Overview of the experimental program and the investigated parameters.

Beam	L [mm]	d [mm]	b_w [mm]	σ_{p0} [MPa]	$\frac{a}{d}$ [-]	ρ_l [-]	ρ_w [$\times 10^{-3}$]	$V_f \bullet$ [kg/m ³]	$V_{u,exp}$ [kN]
B401	7000	557	70	1488	3.95	0.0167	2.693	0	256.4
B402	7000	557	70	1488	3.95	0.0167	0	20	218.5
B403	7000	557	70	1488	3.95	0.0167	0	40	254.4
B404	7000	557	70	750	3.95	0.0167	2.693	0	202.5
B405	7000	557	70	750	3.95	0.0167	0	20	164.1
B406	7000	557	70	750	3.95	0.0167	0	40	197.4

Note: \bullet : Bekaert Dramix RC-80/30-CP

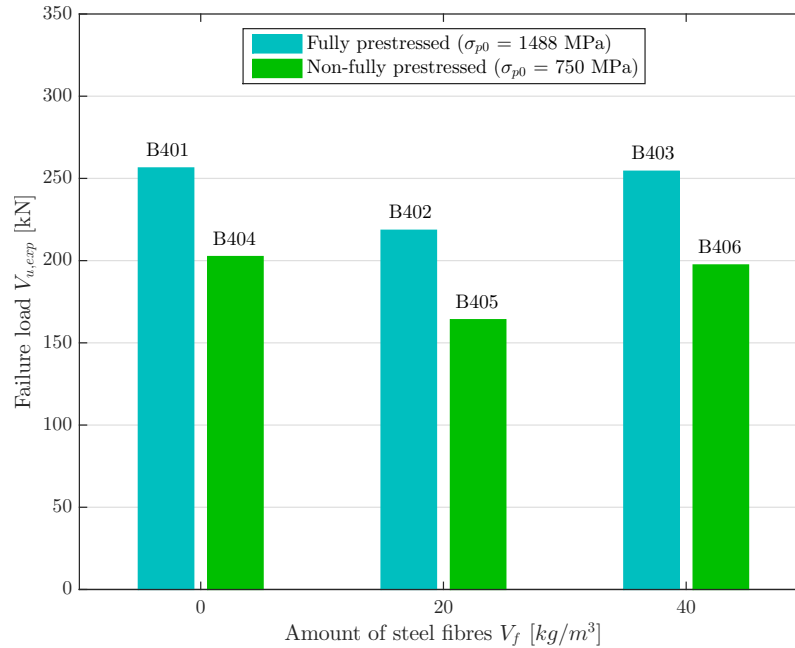


FIGURE 4.3: Experimentally obtained failure loads of the six tested beams.

4.2.2 Influence the amount of steel fibres V_f

The presence of steel fibres mainly contribute to the material properties. They enhance post-cracking tensile residual strength due to the bridging of the crack surfaces. A higher energy absorption and an improved ductility are also known as advantages of adding steel fibres. However, the influence depends on the amount of fibres, as discussed in this section.

Beams B401 and B404 have conventional shear reinforcement and no steel fibres. Beams B402 and B405 contain 20 kg/m³ of steel fibres and beams B403 and B406 contain 40 kg/m³. The difference in amount of steel fibres results in a different shear behaviour and a different shear capacity.

Shear behaviour

The material behaviour is shown in Figure 4.2. Within Figure 4.2a and 4.2b, all characteristics are identical except from the amount of steel fibres. The material behaves similar in the elastic region, independently of the fibre dosage. After the first (shear) cracks, the stiffness is not recovered. Although the first crack load increases with an increasing fibre dosage, this is not dependent on the amount of fibres. The first crack load only depends on the concrete material properties, namely the uniaxial tensile strength. The increase of this strength between the different concrete mixtures (refer to Figure 3.16) causes the increase in first crack load.

The post-cracking behaviour of B402 and B405 is limited, due to the lower amount of fibres than B403 and B406. Both Figures 4.2a and 4.2b depict similar load-displacement curves: B403 (B406) has the largest elastic region and B402 (B405) has a limited post-cracking behaviour. B401 (B404) is in between with the shortest elastic region, but a high post-cracking behaviour due to the presence of stirrups. They transfer the shear forces over the cracked concrete, until yielding and failure of the stirrups themselves occur.

Although the amount of fibres does not directly influence the cracking behaviour, it does influence the failure mode of the beams. All specimens failed in shear due to diagonal tension. However, a clear distinction has to be made between the failure development of beams with shear reinforcement and beams with fibres. B401 and B404 (without steel fibres and with conventional shear reinforcement) have one major crack where all the deformation is localized (Figure 4.4a). The failure is very brittle, highly energy releasing and occurs without the possibility of redistribution of internal forces. On the contrary, multiple cracks occur for beams B402-B403 and B405-B406 (with fibres, Figure 4.4b). The failure is less brittle, even though a shear failure mode is observed. Redistribution of internal forces is to some extent possible and energy dissipation is more gradual, because of the post-cracking behaviour of SFRC. As expected, a higher fibres dosage (B403 and B406) leads to the most cracks, the least brittle failure and the more prolonged redistribution of internal forces. (Figure 4.4c).

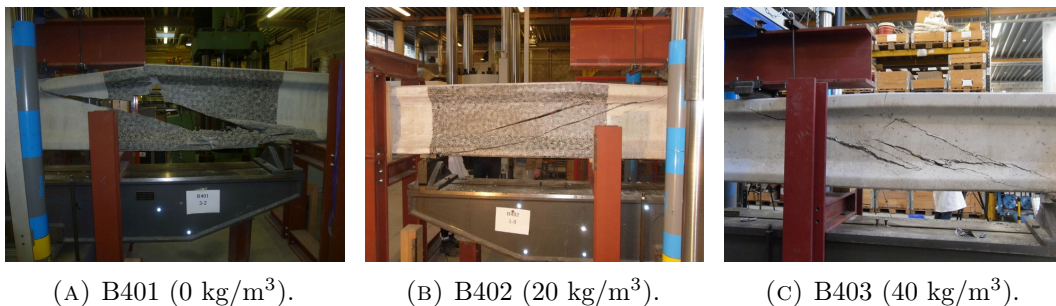


FIGURE 4.4: The amount of fibres influences the number of cracks and the ductility of the failure.

Shear capacity

The failure loads are shown in Table 4.1 and Figure 4.3. All the blue values and all the green ones have the same characteristics and they are grouped according to their amount of steel fibres. It is clear that blue and green values depict a similar trend. An increased amount of fibres, for specimens with a constant prestressing force and without shear reinforcement, results in a higher shear capacity (B402 - B403, B405 - B406), as expected. As calculated in Section 3.7.7, the mean amount of fibres per surface area is 0.59 1/cm^2 (with a coefficient of variation of 27%) and 1.44 1/cm^2 (with a coefficient of variation of 21%) for 20 and 40 kg/m^3 steel fibres respectively. Consequently, a higher fibre dosage causes a larger bridging effect.

The experimental results show that the shear capacities of the specimens with shear reinforcement and the specimens with 40 kg/m^3 steel fibres are comparable (B401 - B403, B404 - B406). Replacing the amount of shear reinforcement $\rho_w = 2.693 \times 10^{-3}$ by 20 kg/m^3 of steel fibres is not sufficient to obtain the same failure load. Section 3.3.5 calculated as well that this fibre dosage does not fulfil the requirements according to Model Code 2010 to substitute conventional reinforcement at ultimate limit state. Replacing by 40 kg/m^3 of steel fibres on the other hand results in a similar shear capacity for the tested specimens, and also fulfils the Model Code 2010 requirements.

Conclusion

To conclude, the main influences of the amount of steel fibres are listed. Increasing the fibre dosage (for specimens with a constant prestressing force and without shear reinforcement) leads to:

- (1) a larger post-cracking behaviour and additional cracks at failure;
- (2) a less brittle failure, a redistribution of the internal forces and a gradual energy dissipation;
- (3) an increased shear capacity.

Furthermore, beams without steel fibres (but with stirrups) have the shortest elastic region and consequently the lowest crack load. However, their post-cracking behaviour due to the stirrups is larger. One major crack and a brittle failure occurs. It can also be concluded that replacing the amount of shear reinforcement $\rho_w = 2.693 \times 10^{-3}$ by 40 kg/m^3 of steel fibres results in a similar shear capacity for the tested specimens.

4.2.3 Influence of the amount of prestressing σ_{p0}

Previous research showed that prestressing of concrete elements has a positive influence on the shear capacity [13]. The underlying principle is that beams withstand a higher shear load if a horizontal pressure is applied. However, the influence depends on the amount of prestressing, as discussed in this section.

Beams B401, B402 and B403 are prestressed at a level of 1488 MPa. Beams B404, B405 and B406 are prestressed at a level of 750 MPa. Although reducing stress levels below the allowable is unconventional in industry, it is applied to investigate the influence of this difference on the shear capacity while the longitudinal reinforcement ratio remains constant. This varying amount of prestressing results in a different shear behaviour and a different shear capacity.

Shear behaviour

The material behaviour, shown in Figure 4.2c, is similar in the elastic region. However, the first crack load decreases with a decreasing prestress level. As a consequence, the elastic region for B404, B405 and B406 is limited. The displacement at midspan of the beams at failure is comparable, independently of the amount of prestressing, although the failure load is different.

Furthermore, the first cracks in the beams with the lowest amount of prestressing are vertical cracks at the bottom of the middle of the beam, due to bending. For beam B404, these cracks were measured with the Bragg grating optical fibres (refer to Section 3.5.3) and for beam B406, the cracks were observable (refer to Figure 3.49a). The tensile stresses at the bottom side of the beam are larger and exceed the tensile strength of the material sooner, due to the lower compression force of prestressed strands at the bottom side.

Despite the first bending cracks, all beams failed in shear due to diagonal tension. Shear cracks grow in the web until failure. Without prestressing force, the inclination of these shear cracks is around 45° . The angles of the shear cracks are estimated based on the geometry of the beams after failure. This results in approximately 30° for beams B404 - B406 (with low prestress level) and approximately 20° for beams B401 - B403 (with high prestress level). As expected, a higher prestressing force causes a lower inclination of the shear cracks. A remark is that this inclination is also depending on the shear span-to-effective depth ratio a/d . Since all beams have the same a/d -ratio, this effect is not taken into account.

Lastly, the amount of prestressing also influences the brittleness of the failure. Due to a higher prestress level, a larger amount of energy is released at failure, causing a more brittle failure. Figure 4.5 compares the failure of B402 to B405. The cracks of B402 are steeper and a more deformed beam is observed. In addition, larger crack widths for a higher level of prestress are measured with the DIC measurement method (refer to Section 3.5.4). Several virtual extensometers are placed over the length of the main crack to obtain the shear load-crack width relation. This is shown in Figure 4.6 for beam B402 and B405. For B402, the crack width increases rapidly in the last part of the load pattern, just before failure occurs. The middle of the crack opens 5 to 6 mm, the outer parts around 3 mm. For B405, the crack width enlarges more gradually. The middle of the crack opens 3 to 4 mm, the outer parts around 1 mm.

4. ANALYTICAL STUDY



FIGURE 4.5: The amount of prestressing influences the inclination of the cracks and the ductility of the failure.

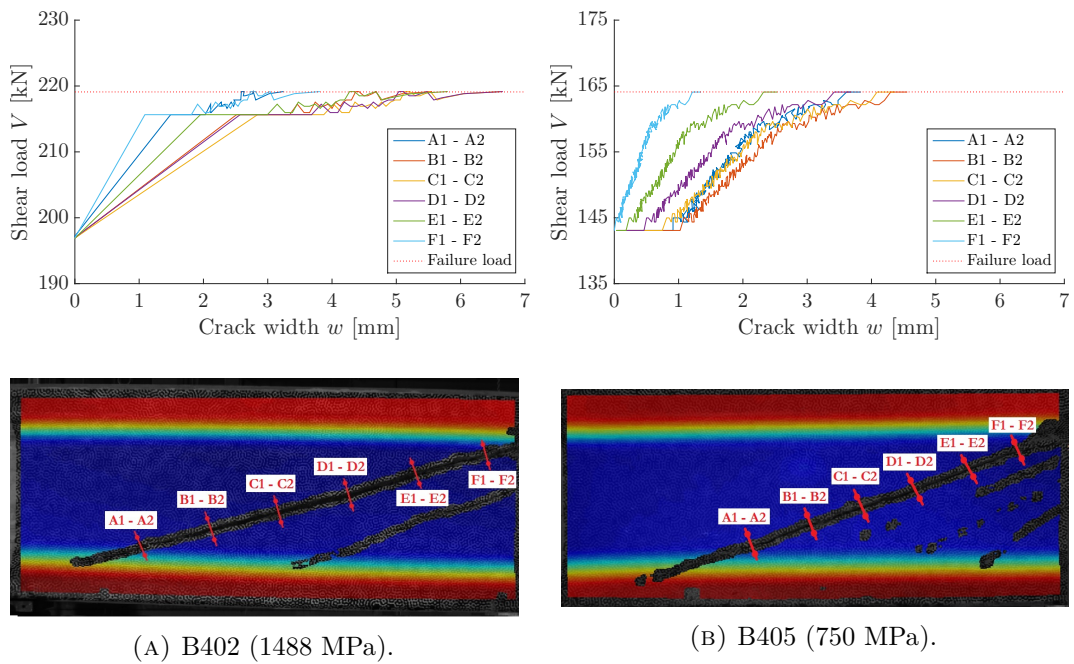


FIGURE 4.6: The amount of prestressing influences the width of the cracks (top figures), measured by placing virtual extensometers over the crack in the DIC measurements (bottom figures).

Shear capacity

The failure loads are shown in Figure 4.3. The amount of prestressing differs per blue and green value, grouped according to their fibre dosage. The longitudinal reinforcement ratio remains constant. It is clear that the three duos depict a similar trend. Decreasing the prestressing force with 50% results in a decreased failure load with 75 to 79% for the tested specimens with (B401 - B404) and without (B402 - B405, B403 - B406) shear reinforcement, and with a constant longitudinal reinforcement ratio. The shear capacity of concrete will increase, amongst other things, by increasing the prestressing force.

Conclusion

To conclude, the main influences of the amount of prestressing are listed. Decreasing the level of prestress (while remaining the longitudinal reinforcement ratio constant) leads to:

- (1) a limited elastic region and a decreased first crack load;
- (2) the occurrence of bending cracks at first;
- (3) a higher inclination of the shear cracks and smaller crack widths;
- (4) a lower amount of released energy and a less brittle failure than fully-prestressed beams.
- (5) a decreased shear capacity (but an unchanged deflection at midspan at failure).

4.2.4 Influence of the measured material properties

The amount of steel fibres and the amount of prestressing were investigated parameters of the experimental research. However, these two characteristics are not the only ones that influence the shear behaviour and capacity. Also the material properties of the hardened (steel fibre reinforced) concrete determine the failure load. Figure 4.7, 4.8, 4.9 and 4.10 show the failure load of the specimens at the left vertical axis and an experimentally obtained material property on the right vertical axis.

In three cases, the relative differences between the material properties (green values) correspond to the relative differences between the failure loads (blue values). This effect is the most distinct for the uniaxial tensile strength (Figure 4.9). Indeed, when this strength is exceeded, cracks occur and failure is initiated. The residual tensile strength (Figure 4.10) behaves in a similar way for the SFRC beams. Also for the modulus of elasticity (Figure 4.8), this effect can be distinguished.

On the other hand, the aforementioned qualitative relationship is not observable for the cylindrical compressive strength (Figure 4.7). For some beams, it even seems to be reversed (a higher compressive strength results in a lower failure load). Consequently, the compressive strength may have a much smaller, a less straight forward or an inverse influence on the failure load of the specimens.

The discussed effect is only valid between beams with the same amount of prestressing (B401 to B403 and B404 to B406), as a higher prestress level causes a larger shear capacity. The influence of the material properties is also related to the amount of steel fibres, as the material identification tests are performed on cubes, cylinders and prisms with the different fibres dosages. For example, B406 has a higher uniaxial and residual strength than B405, because of the 40 kg/m^3 steel fibres compared to the 20 kg/m^3 . These remarks show that all the different parameters of the used material, geometry and reinforcement are interrelated to create a particular shear capacity.

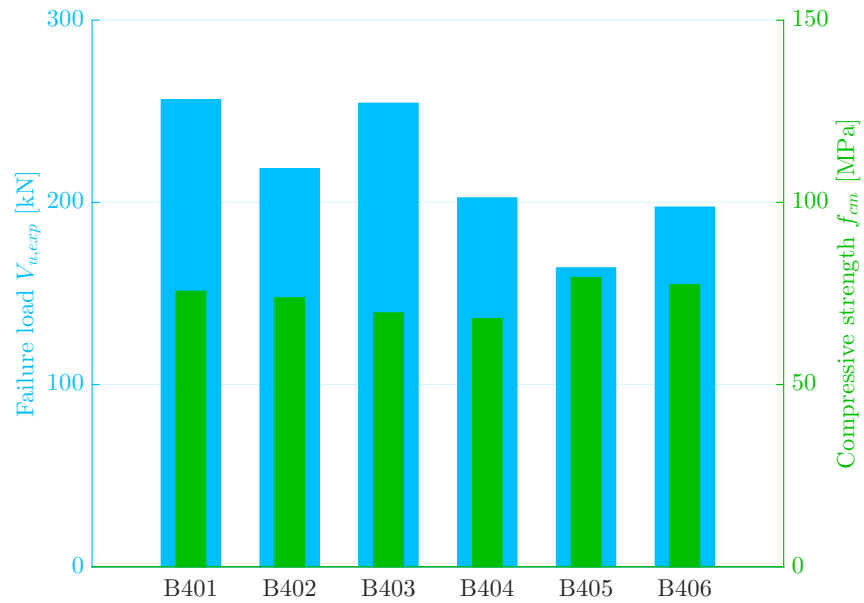


FIGURE 4.7: Influence of the experimentally obtained cylindrical compressive strength on the measured failure loads.

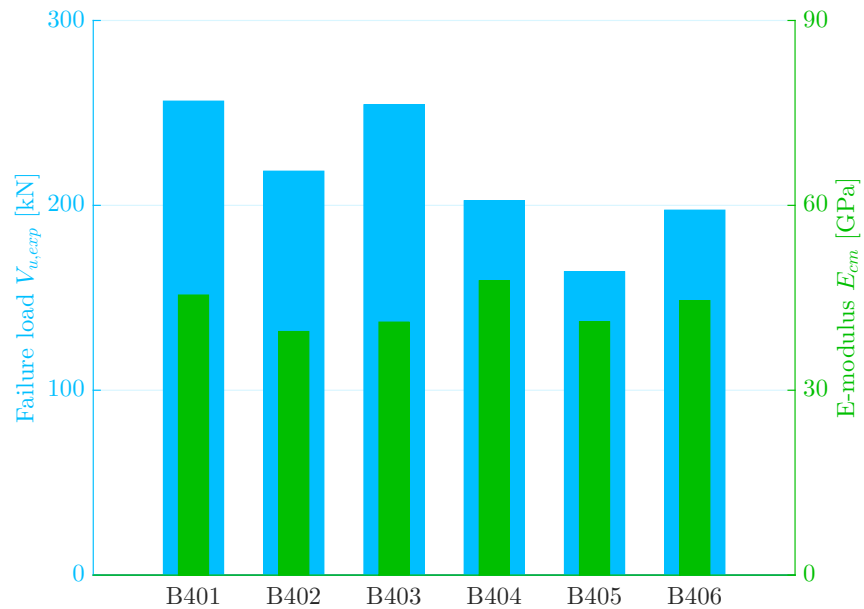


FIGURE 4.8: Influence of the experimentally obtained modulus of elasticity on the measured failure loads.

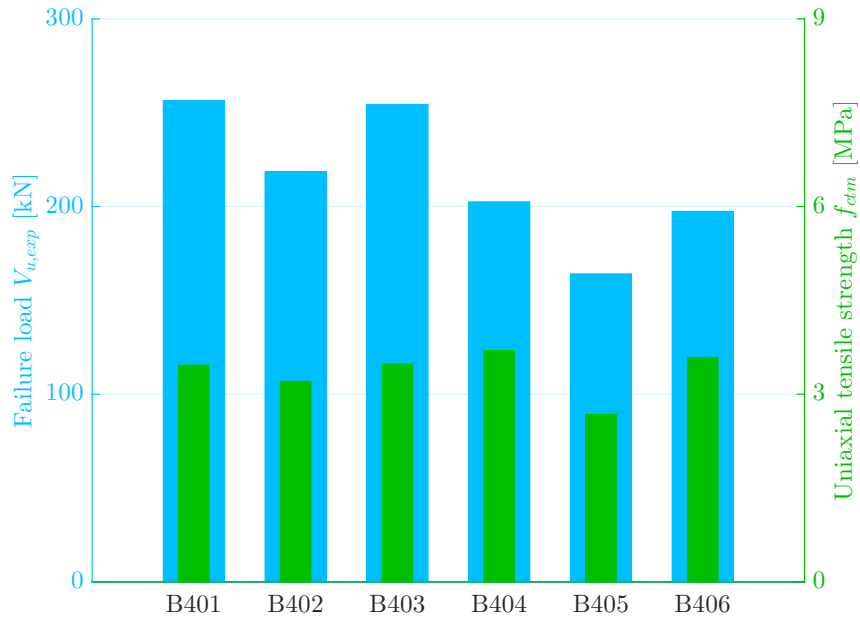


FIGURE 4.9: Influence of the experimentally obtained uniaxial tensile strength on the measured failure loads.

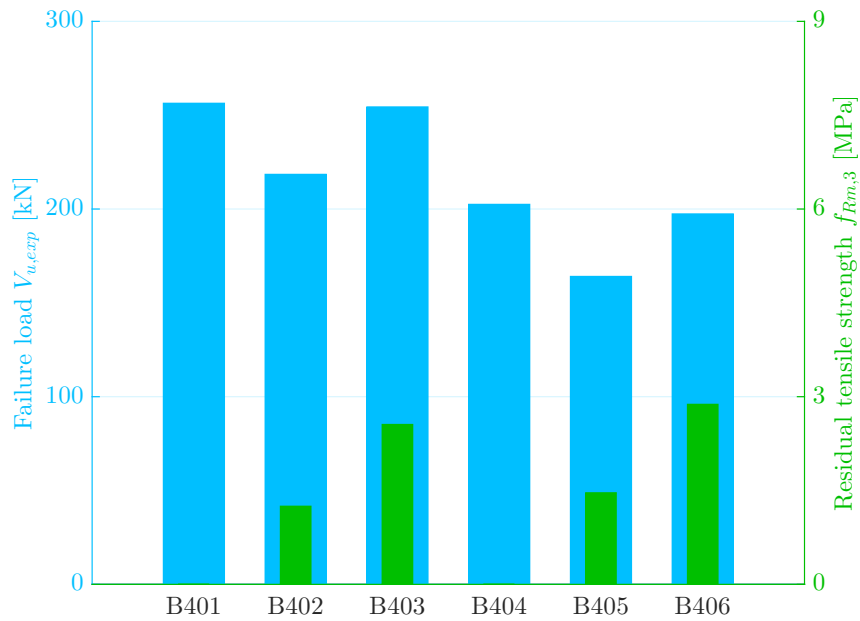


FIGURE 4.10: Influence of the experimentally obtained residual tensile strength at $CMOD_3 = 2.5$ mm on the measured failure loads.

4.2.5 Comparison with shear test results of De Wilder

The research of De Wilder [13] investigated the shear capacity of prestressed and reinforced concrete members. Amongst others, 12 prestressed concrete beams, without steel fibres and with an I-shaped cross-section, were tested in a similar way as in this experimental program (a four-point bending test). They have the same geometry (length, height and widths) as well. The results of four of the I-shaped beams can be compared, because of their almost equal shear span-to-effective depth ratio a/d . As discussed before, the a/d -ratio has an influence on the shear capacity. This experimental program however focusses on the influence of the amount of steel fibres and the amount of prestressing. The discussion of the varying a/d -ratio can be read in [13].

Another difference is the longitudinal reinforcement ratio, since the beams of De Wilder have 9 prestressed strands and the other ones only 8. The amount of prestressing is the same (1488 or 750 MPa). Therefore, the experimental results are normalised with the initial prestressing force to be able to compare the results properly. For the beams with 9 strands at a prestress level of 1488 MPa, the initial prestressing force $F_{p,init}$ equals 1246 kN. 8 prestressed strands result in 1107 kN. The prestress level of 750 MPa leads to 628 kN for 9 strands and 558 kN for 8 strands.

Table 4.2 presents the characteristics of the compared beams. Two main groups are distinguished, namely with the high level of prestress (1488 MPa) and with the low level of prestress (750 MPa). Each group contains two beams with conventional shear reinforcement and without steel fibres (B401 - B102, B404 - B105), although the longitudinal reinforcement ratio varies ($\rho_l = 0.0167$ for B401 - B404 and $\rho_l = 0.0208$ for B102 - B105). In addition, each group also contains a beam without conventional shear reinforcement or steel fibres (B103 and B106, with high ρ_l) and a beam without conventional shear reinforcement and with steel fibres (B403 and B406, with low ρ_l). The experimentally obtained failure loads are divided by the initial prestressing force, resulting in the ratio $\frac{V_{u,exp}}{F_{p,init}}$. This ratio for all the beams is given in the last column of Table 4.2, and shown in Figure 4.11.

Within each group, the results of the shear capacity (independent of the prestressing force) are consistent with the expectations. Firstly, increasing the longitudinal reinforcement ratio results in an increased shear capacity. However, this effect is rather small because the strands are not activated as the shear cracks develop in the web of the beam and are therefore not crossing the horizontal strands. Secondly, removing the conventional shear reinforcement results in a decreased shear capacity. Thirdly, replacing the stirrups by 40 kg/m³ of steel fibres results in an equal shear capacity. The shear capacity and the applied prestressing force are not proportional and therefore, doubling the prestressing force does not double the shear capacity. This explains the difference between the two defined groups. The low level of prestress halves the initial prestressing force while the failure load only decreased with 20 to 30%, resulting in a higher $\frac{V_{u,exp}}{F_{p,init}}$ ratio.

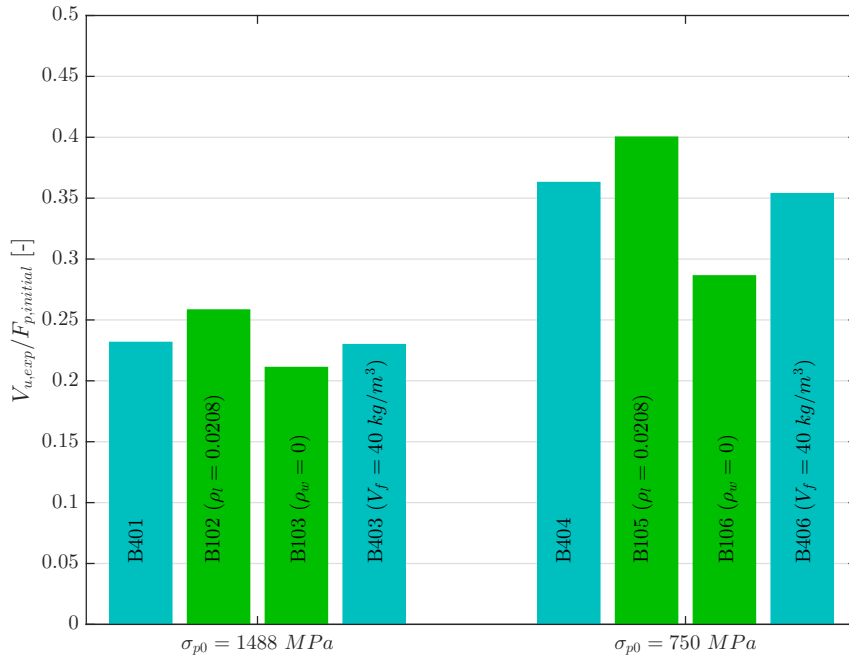


FIGURE 4.11: Overview of the experimentally obtained failure loads of some tested beams (blue) and some shear test results of De Wilder [13] (green).

TABLE 4.2: Comparison of some tested beams and some shear test results of De Wilder [13].

Test [•]	Beam	σ_{p0} [MPa]	$n^{\bullet\bullet}$ [-]	$\frac{a}{d}$ [-]	ρ_l [-]	ρ_w [$\times 10^{-3}$]	V_f [kg/m ³]	$V_{u,exp}$ [kN]	$\frac{V_{u,exp}}{F_{p,init}}$ [-]
EP	B401	1488	7	3.95	0.0167	2.693	0	256.4	0.265
DW	B102	1488	8	3.91	0.0208	2.693	0	321.6	0.291
DW	B103	1488	8	3.91	0.0208	0	0	262.8	0.237
EP	B403	1488	7	3.95	0.0167	0	40	254.4	0.263
EP	B404	750	7	3.95	0.0167	2.693	0	202.5	0.415
DW	B105	750	8	3.91	0.0208	2.693	0	251.2	0.450
DW	B106	750	8	3.91	0.0208	0	0	179.7	0.322
EP	B406	750	7	3.95	0.0167	0	40	197.4	0.404

Note: [•]: EP denotes the preformed experimental program and DW denotes the research of De Wilder [13]; ^{••} denotes the number of prestressed strands at the bottom.

4.3 Discussion of the crack loads

Not only the failure load, but also the crack load is important for the shear behaviour. The observed crack loads $V_{cr,exp}$ are discussed (Section 4.3.1), compared with the calculations V_{cr} (Section 4.3.2) and with the failure loads $V_{u,exp}$ (Section 4.3.3). In addition, a remark on the crack and failure loads is made (Section 4.3.4).

4.3.1 Experimentally observed crack loads

Figure 4.12 shows the experimental first crack loads, classified according to their parameters V_f and σ_{p0} . Firstly, a higher amount of prestressing causes a higher first crack load (blue to green values). This is caused by the prolonged elastic region as the prestressing force counteracts the applied load. Secondly, it seems that the crack loads also differs with the amount of steel fibres, for example a comparable crack load for beams with stirrups or with 20 kg/m^3 steel fibres (B401 - B402 and B404 - B405) and a slightly increased crack load for 40 kg/m^3 (B402 - B403 and B405 - B406). However, this is not correct as the crack load is only dependent of the concrete material properties and the amount of prestressing. Therefore, the differences arise from the different concrete mixtures. Furthermore, the comparable crack load of beams with conventional shear reinforcement or with 20 kg/m^3 steel fibres can not be extended to the failure loads (refer to Figure 4.3), because yielding and rupture of the stirrups will occur later than pull-out of the 20 kg/m^3 steel fibres of the concrete matrix.

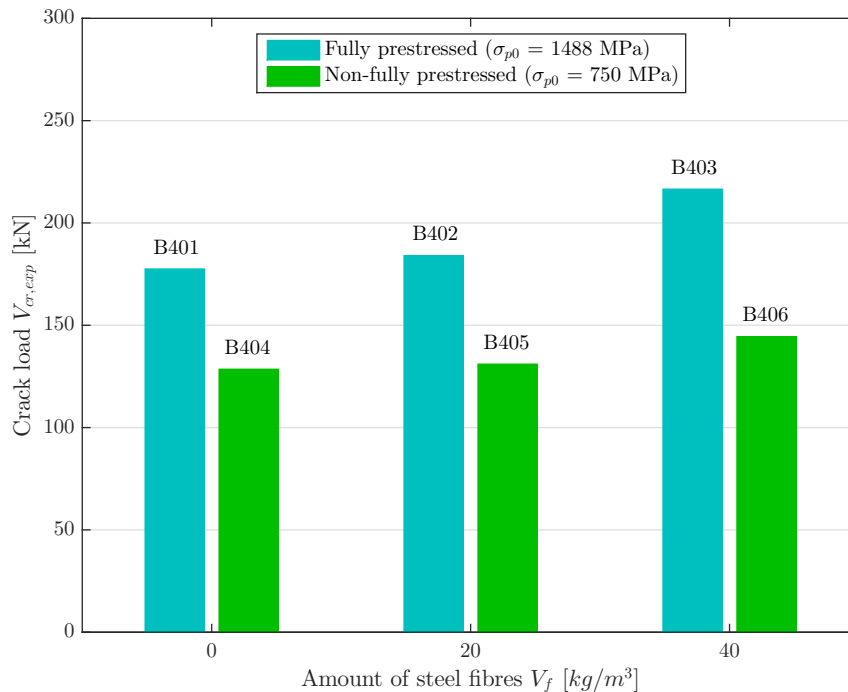


FIGURE 4.12: Experimentally obtained crack loads of the six tested beams.

4.3.2 Comparison with calculated crack loads

As described in Section 3.6, the crack load V_{cr} is calculated according to Appendix B.1, with average material properties and with omitting partial safety factors. It is the minimum of the load that induces inclined cracks in the web of the beam ($V_{cr,w}$) and the load that causes vertical flexural cracks at the bottom of the beam ($V_{cr,bending}$). According to the calculations, all beams would crack due to the bending moment.

Table 4.3 presents the experimental and calculated crack loads and modes. For beam B404 to B406, the first cracks are indeed (non-)visible vertical cracks at midspan (refer to Section 4.2.3). Thereafter, also inclined cracks in the web of the beams occurred. For beam B401 to B403, the first cracks are diagonal cracks in the web of the beams, because of shear due to diagonal tension. In the calculations of the crack load due to the bending moment, the uniaxial tensile strength was used (refer to Appendix B.1). However, the flexural tensile strength could be more appropriate in this case. The calculations were repeated with the measured $f_{ctm,fl}$ instead of f_{ctm} , resulting in V_{cr} equal to 216.2, 190.7 and 179.4 kN for beams B401, B402 and B403 respectively. These values are still smaller than the calculated crack load due to shear $V_{cr,w}$ and therefore, this can not explain the difference in crack mode.

The calculated crack loads are equal to the experimentally observed ones for B401 and B402. For the other beams, the calculated crack loads are smaller than the observed ones, with a ratio between 1.30 and 1.50. This results in a mean experimental-to-calculated crack load of 1.25, with a coefficient of variation of 16%. The formulas to calculate the crack loads include the amount of prestressing and the uniaxial tensile strength. The former is determined with the DEMEC measurements and can be assumed as reasonably accurate. The latter is much more variable, within a beam and to measure (as discussed in Section 3.3.6 and 3.3.7) and can cause the deviations between calculated and experimentally observed values.

For beams B402 and B405, a remarkable observation is made. The shear cracks of both beams did not occur simultaneous at both sides of the beams. After one side has cracked, a large crack occurred on the other side at 215 kN (B402) and 143 kN (B405). These values of 'second shear crack load' are indeed approximately equal to the calculated crack load due to a shear force $V_{cr,w}$ (212.0 and 145.7 kN respectively).

There is no distinct reason why a beam cracks firstly at an particular side. Various effects can contribute to this. For example (a) a local weak spot in the material can cause a lower tensile strength; (b) an inhomogeneous distribution of steel fibres can also create stronger and weaker spots; (c) the shear span-to-effective depth ratio can differs on both sides if the loading point is not positioned exactly with respect to the supporting points (in the side with the larger shear span, and consequently the larger ratio, a larger shear force will develop and the arching action will be smaller); or (d) due to a developing crack at one side, the shear resistance of that side is increased and a larger part of the applied load is transferred to the other side.

TABLE 4.3: Experimental crack load and crack mode compared with calculations.

Beam	Experiment		Calculations			
	$V_{cr,exp}$ [kN]	Crack mode	V_{cr} [kN]	Crack mode	$\frac{V_{cr,exp}}{V_{cr}}$ [-]	$V_{cr,w}$ [kN]
B401	177.5	S-DT [•]	177.4	B	1.00	221.5
B402	184.0	S-DT	178.9	B	1.03	212.0
B403	216.5	S-DT	166.6	B	1.30	216.1
B404	128.5	B ^{••}	99.9	B	1.29	181.9
B405	131.0	B	94.4	B	1.39	145.7
B406	144.4	B	95.8	B	1.51	176.0
$\frac{V_{cr,exp}}{V_{cr}}$ [†]					1.25	
COV [‡]					16.0 %	

Note: [•]: Shear (S) crack mode due to Diagonal Tension (DT); ^{••}: Bending (B) crack mode; [†]: Mean experimental-to-calculated crack load ratio; [‡]: Coefficient of variation

4.3.3 Comparison with experimentally observed failure loads

When cracking occurs before failure, the failure load is larger than the crack load. The question however is how much larger it is. This can be an indication of how many time between the observation of cracks in a structural beam and the failure is left, for example. The comparison is made in Table 4.4. For the beams with conventional shear reinforcement (B401 and B404), the failure load is 44 to 58% larger. For the beams with steel fibres, it is 19% for the high prestress level (B402 and B403) and 25 to 37% for the low prestress level (B405 and B406). On average, the experimental failure loads are 33% larger than the crack loads, with a coefficient of variation of 12%.

The observed results can be associated with the discussed shear behaviour in Sections 4.2.2 and 4.2.3. A larger experimental failure-to-crack load ratio implies a prolonged post-cracking behaviour (refer to Figure 4.2). Decreasing the prestressing force enlarges the post-cracking region, adding more steel fibres also enlarges the post-cracking region and beams with conventional shear reinforcement have a prolonged post-cracking region as well. These conclusions are visible in the ratios as well. For example the beam with the lowest prestressing force and conventional shear reinforcement (B404) has the largest ratio with 1.58.

4.3.4 Calculated crack loads and calculated failure loads

In Section 4.4 are the failure loads calculated according to different analytical models. The design codes Eurocode 2 [41] and Model Code 2010 [19], most applied in Europe, are used, amongst others. The calculation formulas will be explained in the following, only the results are mentioned here to compare with the calculated crack loads due to shear. Table 4.5 shows the comparison between the calculated crack loads due to shear $V_{cr,w}$ and the calculated failure loads $V_{u,pred}$.

TABLE 4.4: Experimental crack load and crack mode compared with the failure load and mode.

Beam	Experiment		Experiment		$\frac{V_{u,exp}}{V_{cr,exp}}$ [-]
	$V_{cr,exp}$ [kN]	Crack mode	$V_{u,exp}$ [kN]	Failure mode	
B401	177.5	S-DT [•]	256.4	S-DT	1.44
B402	184.0	S-DT	218.5	S-DT	1.19
B403	216.5	S-DT	254.4	S-DT	1.18
B404	128.5	B ^{••}	202.5	S-DT	1.58
B405	131.0	B	164.1	S-DT	1.25
B406	144.4	B	197.4	S-DT	1.37
$\overline{\frac{V_{u,exp}}{V_{cr,exp}}}$ [†]					1.33
COV [‡]					11.9 %

Note: [•]: Shear (S) crack mode due to Diagonal Tension (DT); ^{••}: Bending (B) crack mode; [†]: Mean experimental failure-to-crack load ratio; [‡]: Coefficient of variation

All calculated failure loads are smaller than the calculated crack loads, with a mean value of 78% and a coefficient of variation of 8%. At first sight, this is an illogical result. However, this is caused by the different calculation methods and analytical models behind. Crack loads are calculated with the assumption of an uncracked concrete section, while failure loads are calculated in a cracked concrete section. In the latter case, the material already lost some of its strength, resulting in the lower calculated values.

TABLE 4.5: Calculated crack load compared with the calculated failure load.

Beam	$V_{cr,w}$ [kN]	$V_{u,pred}$ [kN] [19, 41]	$\frac{V_{u,pred}}{V_{cr,w}}$ [-]
B401	221.5	174.3	0.79
B402	212.0	148.2	0.70
B403	216.1	161.3	0.75
B404	181.9	146.8	0.81
B405	145.7	129.0	0.89
B406	176.0	137.6	0.78
$\overline{\frac{V_{u,pred}}{V_{cr,w}}}$ [†]			0.78
COV [‡]			7.9 %

Note: [†]: Mean calculated failure-to-crack load ratio; [‡]: Coefficient of variation

4.4 Design Codes of the shear capacity (of SFRC)

After a discussion of the crack loads, also the failure loads are analysed. In the following, the predictions of the shear capacity according to different design codes or analytical models are compared with the experimentally obtained results and discussed. Firstly, the most used design codes in Europe, Eurocode 2 and Model Code 2010, will be used in this section. Eurocode 2 currently only provides guidelines for structural concrete elements without steel fibres. Model Code 2010 also provides guidelines for structural SFRC elements. Both models were discussed in the literature review. Secondly, other analytical model to predict the shear capacity of concrete beams with steel fibres are used in the next part.

For all calculations, the design codes are used to estimate the actual failure load. Therefore, the partial safety factors are omitted and the average material properties are used (as defined in Table 3.4 and 3.8). $V_{u,pred}$ is the predicted shear capacity (failure load), calculated with the design codes. $V_{u,exp}$ is the experimentally obtained failure load (refer to Section 3.7).

For Model Code 2010, also a discussion of the influence of steel fibre dosage on the shear capacity is given. This influence is investigated by recalculating the shear capacity model equations without presence of steel fibres (e.g. by neglecting the term with the contribution of the steel fibres). The influence is denoted as Φ , expressed in percentages, and calculated with:

$$\Phi = \left(1 - \frac{V_{u,pred,without\,fibres}}{V_{u,pred,with\,fibres}} \right) \cdot 100 \quad (4.1)$$

4.4.1 Eurocode 2

For beams without steel fibres and with shear reinforcement (namely beam B401 and B404 in this experimental program), the shear design procedure of Eurocode 2 (EC2) is used, as described in Section 2.2.8.

Calculation

Since beams B401 and B404 are provided with stirrups, only the shear capacity of this reinforcement is taken into account, the concrete contribution is neglected. The shear capacity $V_{u,pred}$ is the smaller value of the shear force required to obtain yielding of the shear reinforcement $V_{R,s}$ and the shear force required to obtain crushing of the compression struts $V_{R,s,max}$:

$$V_{u,pred} = \min \begin{cases} V_{R,s} \\ V_{R,s,max} \end{cases} \quad (4.2)$$

4.4. Design Codes of the shear capacity (of SFRC)

The shear reinforcement ratio of B401 and B404 is relatively low ($\rho_l = 0.017$). Consequently, yielding and rupture of the reinforcement bars will occur earlier than crushing of the compression struts. Therefore, the shear capacity is calculated using:

$$V_{u,pred} = V_{R,s} = \frac{A_{sw}}{s} \cdot z \cdot f_{ywm} \cdot \cot \theta \quad (4.3)$$

The area of reinforcement per unit length $\frac{A_{sw}}{s}$ is determined by the stirrups with a diameter of 6 mm and a spacing of 150 mm. The maximum value of $\cot \theta$ is chosen between 1 and $\cot \theta_{max}$, to include the effect of prestressing. $\cot \theta_{max}$ is calculated with [42]:

$$\cot \theta_{max} = \left(2 + \frac{0.15 \cdot \sigma_{cp} \cdot b_w \cdot d}{\frac{A_{sw}}{s} \cdot z \cdot f_{ywm}} \right) \leq 3 \quad (4.4)$$

For beam B401, the formula results in $\cot \theta = 3.03$ and is limited to 3. For beam B404, the formula results in $\cot \theta = 2.53$. The angle θ is equal to 18.4° and 21.6° respectively. Indeed, the inclination of the shear cracks under a higher prestressing force is lower (refer to Section 2.2.5 and 4.2.3).

Results

Table 4.6 presents the results of the prediction of the shear capacity compared to the experimentally obtained results for B401 and B404. These results are further discussed in Section 4.4.3.

TABLE 4.6: Experimental failure loads compared to the analytical predictions according to EC2.

Beam	Experiment		Prediction	
	$V_{u,exp}$ [kN]	Failure mode [-]	$V_{u,pred}$ [kN]	$\frac{V_{u,exp}}{V_{u,pred}}$ [-]
B401	256.4	S-DT•	174.3	1.47
B404	202.5	S-DT	146.8	1.38

Note: •: Shear (S) crack mode due to Diagonal Tension (DT).

4.4.2 Model Code 2010 (A)

For steel fibre reinforced concrete beams, EC2 currently does not provide a design procedure. Therefore, Model Code 2010 (MC2010) is used for the SFRC beams (namely B402, B403, B404 and B405), as described in Section 2.4.3. MC2010 contains two design approaches, depending on the level of approximation. The most used approach A (MC2010A) is based on the current EC2 formulation and hence will be used in this section. The approach B is discussed in Section 4.5.5.

Calculation

MC2010A takes into account the contribution of steel fibres by increasing the longitudinal reinforcement ratio with a factor depending on the residual stress of the SFRC. The ultimate shear capacity is calculated with:

$$V_{u,pred} = \left[0.18 \cdot k \cdot \left(100 \cdot \rho_l \cdot \left[1 + 7.5 \cdot \frac{F_{Ftum}}{f_{ctm}} \right] \cdot f_{cm} \right)^{\frac{1}{3}} + 0.15 \cdot \sigma_{cp} \right] \cdot b_w \cdot d \quad (4.5)$$

The model also defines a minimum value of the shear resistance. In the calculations, this minimum value is not determinative for the results. The mean value of the ultimate residual tensile strength F_{Ftum} for B402, B403, B405 and B406 equals 1.2, 2.9, 1.5 and 2.9 MPa respectively.

Requirements

The Model Code 2010 also gave a requirement for the use of steel fibres. It was verified in Section 3.3.5 with the following conclusion: beams with 20 kg/m³ of steel fibres just do or just do not fulfil the requirement of Model Code 2010 to replace conventional shear reinforcement. 20 kg/m³ of steel fibres is not sufficient to replace the shear reinforcement for these beams.

Furthermore, the second limitation about the minimum amount of shear reinforcement is fulfilled with the mean material properties. With the characteristic properties, the requirement is not satisfied for beam B402 and beam B405. For a safe application of steel fibres, a higher amount than 20 kg/m³ should be used.

Results

Table 4.7 and Figure 4.13 present the results of the predicted shear capacities (horizontal axis) compared to the experimentally obtained results (vertical axis) for the SFRC beams. The mean experimental-to-predicted failure ratio is 1.44, with a coefficient of variation of 8.8%. In the figure, also a first order polynomial fit and the 95% prediction interval are drawn. The coefficient of determination R^2 with the linear regression equals 0.99. These results are further discussed in Section 4.4.3. The mean influence of the amount of steel fibres Φ_m is 27% and 35%, for the low and high fibre dosage respectively. A higher fibre dosage results in a higher influence and the scatter of the influences is caused by the variation in the measured material properties.

4.4. Design Codes of the shear capacity (of SFRC)

TABLE 4.7: Experimental failure loads compared to the analytical predictions according to CNR.

Beam	Experiment		Prediction		
	$V_{u,exp}$ [kN]	Failure mode [-]	$V_{u,pred}$ [kN]	$\frac{V_{u,exp}}{V_{u,pred}}$ [-]	Φ [%]
B402	218.5	S-DT [•]	148.2	1.47	22
B403	254.4	S-DT	161.3	1.58	32
B405	164.1	S-DT	129.0	1.27	32
B406	197.4	S-DT	137.6	1.43	38
				$\frac{V_{u,exp}}{V_{u,pred}}^{\dagger}$	1.44
				COV [‡]	8.8 %

Note: [•]: Shear (S) crack mode due to Diagonal Tension (DT);
[†]: Mean experimental-to-predicted failure load ratio; [‡]: Coefficient of variation

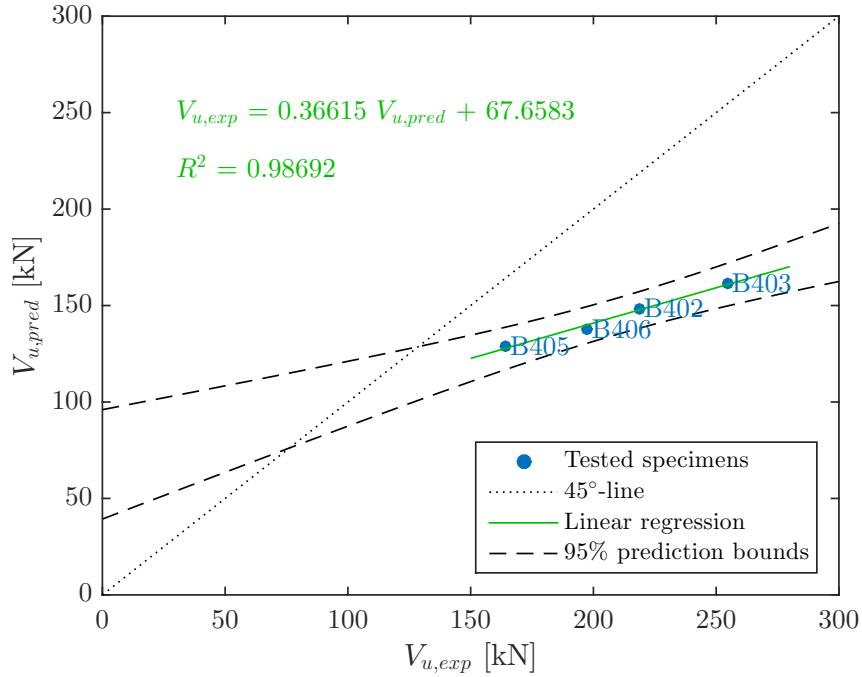


FIGURE 4.13: Experimental failure loads compared to the analytical predictions according to MC2010A.

4.4.3 Discussion

The results of the aforementioned calculations to predict the shear capacity according to EC2 or MC2010 are shown in Table 4.8, as well as the load required to obtain the theoretical bending capacity ($V_{u,flex} = M_R/a$) derived from a plane section analysis. Figure 4.14 presents the results. For the values on the 45°-line, the experimentally obtained value equals the predicted one. Above this line, the beam is predicted to have a higher failure load than experimentally observed and below this line, the predictions are smaller than the experimental results. This last case is also considered as the safe side. The first-order polynomial fit, the 95% prediction interval and the coefficient of determination R^2 are shown. The closer R^2 is to 1, the better the regression fits to the results. The following conclusions concerning the calculation procedures can be made:

- (1) Based on the experimental results, Section 4.2.2 concluded that the shear capacities of the specimens with shear reinforcement and the specimens with 40 kg/m³ steel fibres are comparable (B401 - B403, B404 - B406). This conclusion is also valid for the analytical predictions of the shear capacities. It can be concluded that replacing the amount of shear reinforcement $\rho_w = 2.693 \times 10^{-3}$ by 40 kg/m³ of steel fibres results in a similar shear capacity for the tested specimens.
- (2) The predicted failure loads are always an underestimation of the experimentally observed ones, all results are located below the 45°-line in Figure 4.14. Therefore, the design procedures of EC2 and MC2010 result in safer failure loads, even if partial safety factors are omitted and average material properties are used instead of design values. The mean experimental-to-predicted failure ratio is 1.43, with a coefficient of variation of 7.2% and a correlation of 0.92.
- (3) According to the calculations of EC2, only the shear capacity of the reinforcement is taken into account, the concrete contribution to the shear capacity is neglected. However, the shear capacity of concrete will increase by increasing the prestressing force [15]. The influence of prestressing is solely considered in the determination of $\cot \theta$ (Equation 4.4), although it is limited by the value of 3. This explains the higher experimental-to-predicted ratio of B401 compared to B404.
- (4) The influence of the prestressing force is taken into account in Equation 4.5 from MC2010, but also in this case the ratio $V_{u,exp}/V_{u,pred}$ increases for a higher prestressing force, comparing B402 to B405 and B403 to B406. The influence of the prestressing force is not completely correctly estimated in MC2010, especially for higher prestressing values.
- (5) A similar behaviour is observed concerning the amount of steel fibres: the higher the fibre dosage, the higher the ratio $V_{u,exp}/V_{u,pred}$, comparing B402 to B403 and B405 to B406. The amount of fibres affects the post-cracking behaviour by the mean ultimate residual tensile strength for FRC (f_{Ftum} based on the residual flexural tensile strengths $f_{Rm,1}$ and $f_{Rm,3}$).

4.4. Design Codes of the shear capacity (of SFRC)

TABLE 4.8: Experimental failure loads compared to the analytical predictions according to EC2/MC2010.

Beam	Experiment		Prediction using EC2 and MC2010A			
	$V_{u,exp}$ [kN]	Failure mode [-]	$V_{u,pred}$ [kN]	$V_{u,flex}$ [kN]	$\frac{V_{u,exp}}{V_{u,pred}}$ [-]	Φ [%]
B401	256.4	S-DT [•]	174.3	293.4	1.47	-
B402	218.5	S-DT	148.2	293.4	1.47	22
B403	254.4	S-DT	161.3	293.4	1.58	32
B404	202.5	S-DT	146.8	289.3	1.38	-
B405	164.1	S-DT	129.0	289.3	1.27	32
B406	197.4	S-DT	137.6	289.3	1.43	38
				$\frac{V_{u,exp}}{V_{u,pred}}^{\dagger}$	1.43	
				COV [‡]	7.2 %	

Note: [•]: Shear (S) crack mode due to Diagonal Tension (DT);
[†]: Mean experimental-to-predicted failure load ratio; [‡]: Coefficient of variation

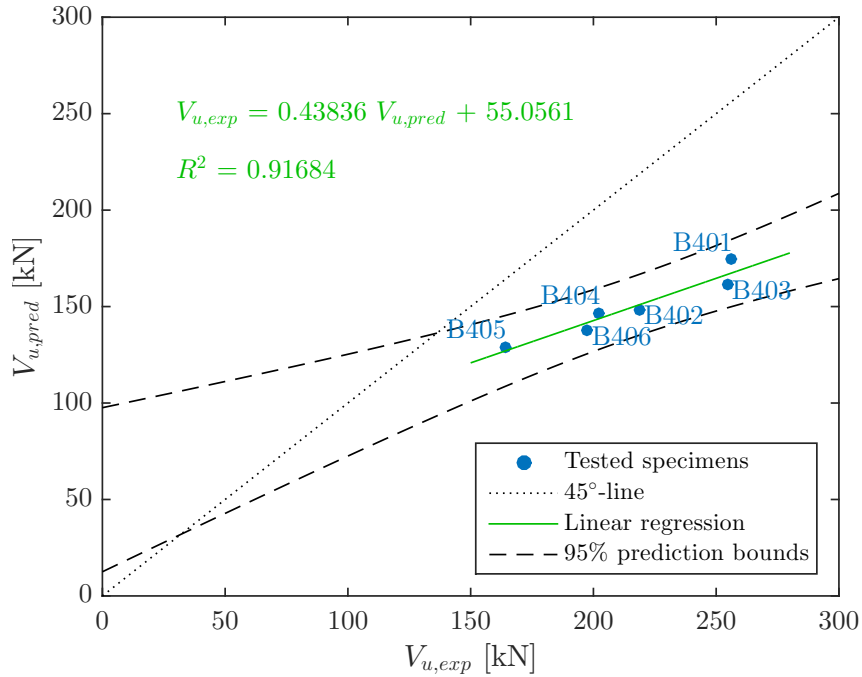


FIGURE 4.14: Experimental failure loads compared to the analytical predictions according to EC2/MC2010.

4.5 Analytical models of the shear capacity of SFRC

In the previous part, the two most used design codes were discussed in detail: Eurocode 2 and Model Code 2010. Alternatively, five other analytical models are applied to calculate the shear capacity of the SFRC beams. All these models were described in the literature review, Section 2.4.1. In the following, the results of each model are compared with the experimentally obtained results and discussed (Section 4.5.1 to 4.5.5). To conclude, a general comparison is made in Section 4.5.6.

For all calculations, there is no contributing part of conventional shear reinforcement to the shear capacity, since stirrups are not present in the beams with steel fibres. Furthermore, all analytical models are used to estimate the actual failure load. Therefore, the partial safety factors are omitted and the average material properties are used (as defined in Table 3.4 and 3.8). $V_{u,pred}$ is the predicted shear capacity (failure load), calculated with one of the described models. $V_{u,exp}$ is the experimentally obtained failure load (refer to Section 3.7).

The influence of steel fibre dosage on the predicted shear capacity is investigated in the same way as in the previous section, namely by recalculating the shear capacity model equations without presence of steel fibres (e.g. by neglecting the term with the contribution of the steel fibres). The influence is denoted as Φ , expressed in percentages, and calculated with:

$$\Phi = \left(1 - \frac{V_{u,pred,without\,fibres}}{V_{u,pred,with\,fibres}} \right) \cdot 100 \quad (4.6)$$

4.5.1 DRAMIX Guideline

Calculation

The DRAMIX Guideline takes into account some steel fibre properties, instead of the post-cracking behaviour. The ultimate shear capacity is calculated with:

$$\begin{aligned} V_{u,pred} = & \left[0.18 \cdot \left(1 + \sqrt{\frac{200}{d}} \right) \cdot (100 \cdot \rho_l \cdot f_{cm})^{\frac{1}{3}} + 0.15 \cdot \sigma_{cp} \right] \cdot b_w \cdot d \\ & + k_f \cdot 0.54 \cdot f_{ctm,ax} \cdot \frac{1.1 \cdot V_f \cdot \lambda_f}{180 \cdot 20 + V_f \cdot \lambda_f} \cdot b_w \cdot d \end{aligned} \quad (4.7)$$

The first part is the same as the contribution of concrete in Eurocode 2. The factor R_t is equal to 0.3 and 0.5 for 20 and 40 kg/m³ of steel fibres respectively. This means that the post-cracking strength of SFRC is estimated as 30 and 50% of the uniaxial tensile strength $f_{ctm,ax}$.

Requirements

Not all the requirements for the use of steel fibres are fulfilled. For the beams with 20 kg/m³ of steel fibres (B402 and B405), the minimum fibre dosage of 30 kg/m³ is not satisfied. Secondly, the contribution of the steel fibres to the shear resistance is smaller than the shear resistance of the unreinforced concrete, with a ratio of 0.84. Given these points, 20 kg/m³ of steel fibres is not sufficient to replace the shear reinforcement for these beams, according to the DRAMIX Guideline. For 40 kg/m³, all requirements are fulfilled, the second one with a ratio of 1.29.

Results and discussion

Table 4.9 and Figure 4.15 present the results of the prediction of the shear capacity compared to the experimentally obtained results. The predicted failure loads are always an underestimation of the experimentally observed ones. Therefore, the design procedure of the DRAMIX Guideline results in safer failure loads, with a mean experimental-to-predicted failure ratio of 1.48. All the beams are located in the bottom right-hand corner, below the 45°-line, in Figure 4.15. This is the safe side of the figure, the beams can withstand a higher load than calculated. In design, when partial safety factors and characteristic material properties are taken into account, this leads to a larger $V_{u,exp}/V_{u,pred}$ ratio. As such, the results can become too conservative, resulting in expensive designs while not needed.

The scatter of the results is relatively small, with a coefficient of variation of 4.6%. The coefficient of determination R^2 with a first order polynomial fit is equal to 0.97. A similar conclusion as in Section 4.4.3 can be drawn: the ratio $V_{u,exp}/V_{u,pred}$ increases for higher prestressing forces, comparing B402 to B405 and B403 to B406. The influence of the prestressing force is not completely correctly estimated, especially for higher prestressing values. For the high level of prestress, the ratio $V_{u,exp}/V_{u,pred}$ also increases for higher steel fibres dosages, comparing B402 to B403. However, this is not valid for B405 and B406.

The mean influence of the amount of steel fibres Φ_m is equal to 22% and 35% for the low and high amount of steel fibres respectively. As expected, the higher the fibre dosage, the higher the influence. Adding 20 kg/m³ of steel fibres increases its contribution with approximately 10%. Although B403 and B406 both contain 40 kg/m³ of fibres, their influence differs with 7%. This is caused by the variation in the measured uniaxial tensile strength (refer to Figure 3.16).

4. ANALYTICAL STUDY

TABLE 4.9: Experimental failure loads compared to the analytical predictions according to the DRAMIX Guideline.

Beam	Experiment		Prediction		
	$V_{u,exp}$ [kN]	Failure mode [-]	$V_{u,pred}$ [kN]	$\frac{V_{u,exp}}{V_{u,pred}}$ [-]	Φ [%]
B402	218.5	S-DT [•]	147.5	1.48	21
B403	254.4	S-DT	162.3	1.57	32
B405	164.1	S-DT	114.0	1.44	23
B406	197.4	S-DT	139.6	1.41	39
			$\frac{V_{u,exp}}{V_{u,pred}}^{\dagger}$	1.48	
			COV [‡]	4.6 %	

Note: [•]: Shear (S) crack mode due to Diagonal Tension (DT);

[†]: Mean experimental-to-predicted failure load ratio; [‡]: Coefficient of variation

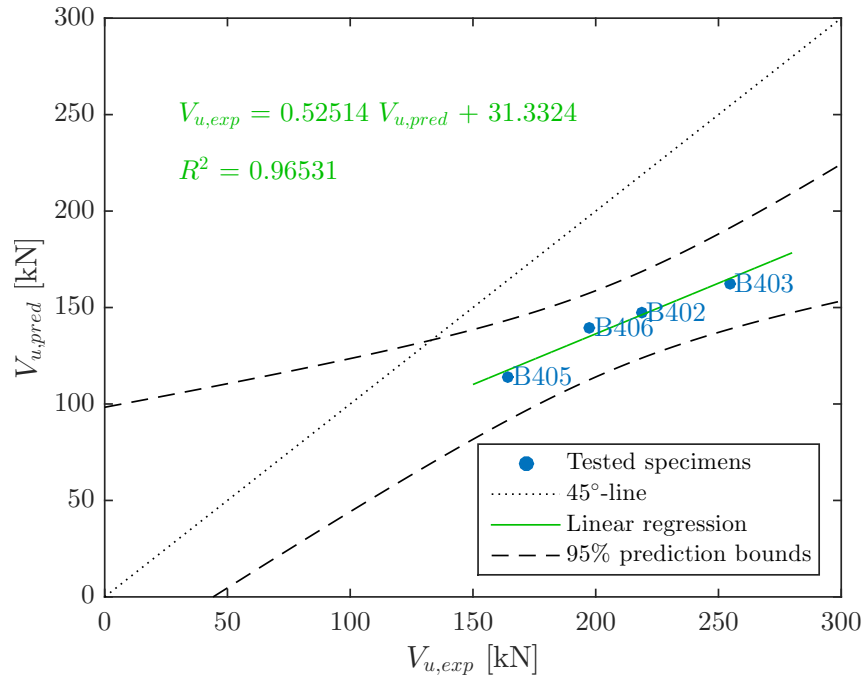


FIGURE 4.15: Experimental failure loads compared to the analytical predictions according to the DRAMIX Guideline.

4.5.2 RILEM TC 162-TDF

Calculation

The RILEM σ - ε -design method takes into account the post-cracking behaviour, instead of steel fibre properties. The ultimate shear capacity is calculated with:

$$V_{u,pred} = \left[0.18 \cdot \left(1 + \sqrt{\frac{200}{d}} \right) \cdot (100 \cdot \rho_l \cdot f_{cm})^{\frac{1}{3}} + 0.15 \cdot \sigma_{cp} \right] \cdot b_w \cdot d \\ + \left[0.7 \cdot k_f \cdot \left(1 + \sqrt{\frac{200}{d}} \right) \cdot 0.18 \cdot f_{Rm,4} \right] \cdot b_w \cdot d \quad (4.8)$$

The first term is the same as Eurocode 2 or the DRAMIX Guideline. The contribution of the steel fibres is larger than the calculations according to the DRAMIX Guideline. Hereby, the influence of the amount of fibres is not directly taken into account, but due to $f_{Rm,4}$ (the mean flexural tensile strength corresponding to $CMOD_4$). As discussed in Section 3.3.5, the higher fibres dosage leads to a hardening behaviour, resulting in larger residual strengths (refer to Figure 3.13).

Requirements

Not all the requirements for the use of steel fibres are fulfilled. For the beams with 20 kg/m³ of steel fibres (B402 and B405), the minimum $f_{Rk,4}$ of 1 N/mm² is not satisfied. The characteristic values, calculated as described in Section 3.3.1, are 0.63 and 0.51 for B402 and B405 respectively. Similar to the DRAMIX Guideline, 20 kg/m³ of steel fibres is not sufficient to replace the shear reinforcement for these beams, according to the RILEM model. For 40 kg/m³, all requirements are fulfilled, with $f_{Rk,4}$ equal to 5.0 (B403) and 5.5 (B406).

Results and discussion

Table 4.10 and Figure 4.16 present the predictions compared to the experimentally obtained shear capacities. Similar to the DRAMIX Guideline, the predicted failure loads are an underestimation of the experimentally observed ones. Therefore, the design procedure of the RILEM model results in safer failure loads, with a mean $V_{u,exp}/V_{u,pred}$ ratio of 1.35. All beams are located below the 45°-line, at the safe side of Figure 4.16. In design, this leads to a larger $V_{u,exp}/V_{u,pred}$ ratio. However, the RILEM model result in a better prediction of the loads than DRAMIX, as the $V_{u,exp}/V_{u,pred}$ ratio decreases from 1.48 to 1.35. As such, RILEM is less conservative.

The scatter of the results is larger than the DRAMIX Guideline, with a coefficient of variation of 6.0%. The coefficient of determination R^2 with a linear regression is 0.90. In this model, the ratio $V_{u,exp}/V_{u,pred}$ increases as well for higher prestressing forces (B402 - B405, B403 - B406). On the contrary, the ratio $V_{u,exp}/V_{u,pred}$ decreases for higher steel fibres dosages (B402 - B403, B405 - B406). The higher the amount of steel fibres, the better their influence is estimated.

The mean influence of the amount of steel fibres Φ_m is equal to 26% and 43% for the low and high amount of steel fibres respectively. As expected, the higher the fibre dosage, the higher the influence. Adding 20 kg/m³ of steel fibres increases its contribution with approximately 15%. However, this influence varies more than in the DRAMIX calculations. This is caused by the larger scatter on the measured $f_{Rm,4}$ (Figure 3.13) than on the measured uniaxial tensile strength (Figure 3.16).

Refinement for a/d

A refinement of the RILEM equations was suggested to take into account the variation of the shear span-to-depth ratio. The ultimate shear capacity is then calculated with:

$$V_{u,pred} = \left[0.15 \cdot \sqrt[3]{3 \cdot \frac{d}{a} \cdot \left(1 + \sqrt{\frac{200}{d}} \right) \cdot (100 \cdot \rho_l \cdot f_{cm})^{\frac{1}{3}} + 0.15 \cdot \sigma_{cp}} \right] \cdot b_w \cdot d \quad (4.9)$$

$$+ \left[0.7 \cdot k_f \cdot \left(1 + \sqrt{\frac{200}{d}} \right) \cdot \frac{d}{a} \cdot 0.5 \cdot f_{Rm,4} \right] \cdot b_w \cdot d$$

Table 4.11 and Figure 4.17 present the results of the prediction of the shear capacity compared to the experimentally obtained results. The main differences with the RILEM model without refinement are discussed.

Firstly, the predicted failure loads are a larger underestimation of the experimentally observed ones than in the previous model. The mean $V_{u,exp}/V_{u,pred}$ ratio increases from 1.35 to 1.67, resulting in even safer failure loads. Therefore, this refined RILEM model is more conservative and probably too conservative for design calculations, where partial safety factors and characteristic material properties are included as well. This observation seems illogical, as a refinement would imply a better estimation.

The reduction of the predictions comes both from the concrete and from the fibre contribution term. In both terms, the factor 0.18 is replaced by a factor in function of a/d , equal to 0.14 and 0.13 respectively. For the experimental program performed in this research, explicitly including the a/d -ratio does not lead to better predictions of the failure loads.

On the other hand, the refined RILEM model yields to more consistent results, as the coefficient of variation is equal to 2.8% and coefficient of determination to 0.98. The ratio $V_{u,exp}/V_{u,pred}$ increases as well for higher prestressing forces (B402 - B405, B403 - B406). The influence of the amount of steel fibres is less distinct.

Lastly, the mean influence of the amount of steel fibres Φ_m is decreased from 26 to 23% and from 43 to 38% for the low and high amount of steel fibres respectively. This means that the concrete contribution and the fibre contribution are not reduced in the same proportion.

4.5. Analytical models of the shear capacity of SFRC

TABLE 4.10: Experimental failure loads compared to the analytical predictions according to RILEM.

Beam	Experiment		Prediction		
	$V_{u,exp}$ [kN]	Failure mode [-]	$V_{u,pred}$ [kN]	$\frac{V_{u,exp}}{V_{u,pred}}$ [-]	Φ [%]
B402	218.5	S-DT [•]	149.9	1.46	23
B403	254.4	S-DT	186.4	1.36	41
B405	164.1	S-DT	125.2	1.31	30
B406	197.4	S-DT	155.6	1.27	45
			$\frac{V_{u,exp}}{V_{u,pred}}^{\dagger}$	1.35	
			COV [‡]	6.0 %	

Note: [•]: Shear (S) crack mode due to Diagonal Tension (DT);
[†]: Mean experimental-to-predicted failure load ratio; [‡]: Coefficient of variation

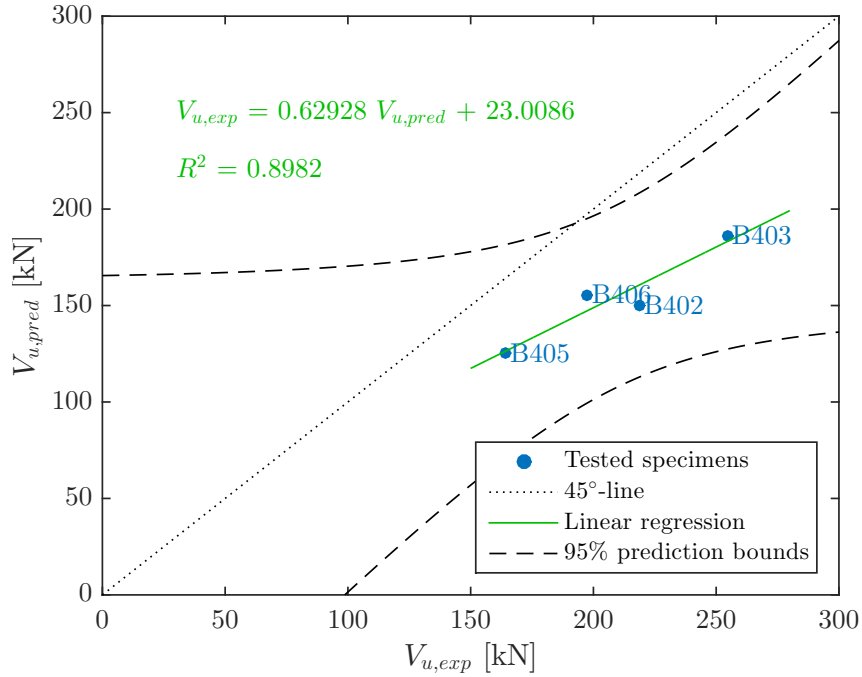


FIGURE 4.16: Experimental failure loads compared to the analytical predictions according to RILEM.

4. ANALYTICAL STUDY

TABLE 4.11: Experimental failure loads compared to the analytical predictions according to RILEM - a/d refinement.

Beam	Experiment		Prediction		
	$V_{u,exp}$ [kN]	Failure mode [-]	$V_{u,pred}$ [kN]	$\frac{V_{u,exp}}{V_{u,pred}}$ [-]	Φ [%]
B402	218.5	S-DT [•]	126.5	1.73	19
B403	254.4	S-DT	150.6	1.78	36
B405	164.1	S-DT	100.4	1.64	26
B406	197.4	S-DT	121.2	1.63	41
			$\frac{V_{u,exp}}{V_{u,pred}}^{\dagger}$	1.67	
			COV [‡]	2.8 %	

Note: [•]: Shear (S) crack mode due to Diagonal Tension (DT);

[†]: Mean experimental-to-predicted failure load ratio; [‡]: Coefficient of variation

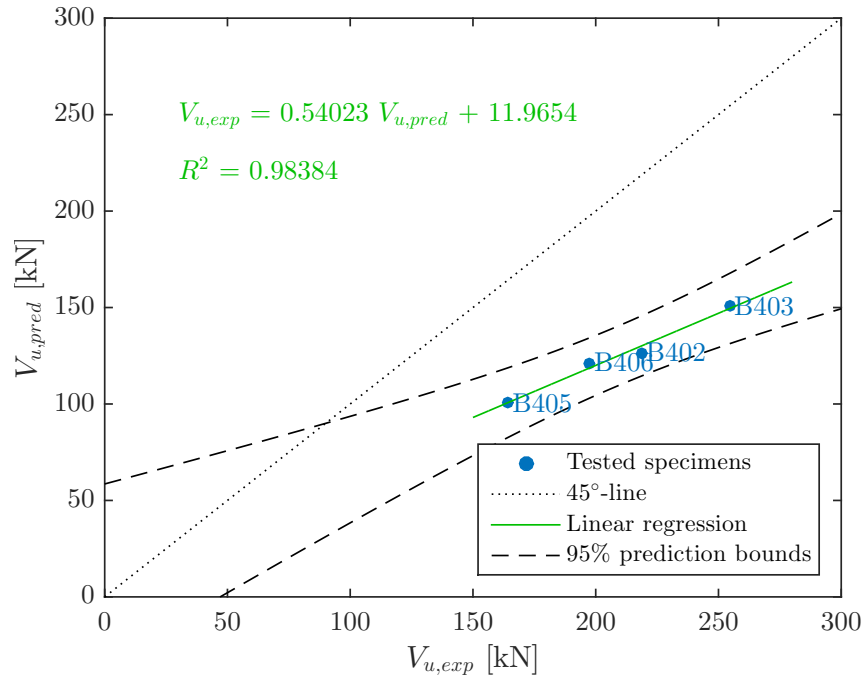


FIGURE 4.17: Experimental failure loads compared to the analytical predictions according to RILEM - a/d refinement.

4.5.3 CNR-DT 204/2006

Calculation

The CNR model takes into account the contribution of steel fibres by increasing the longitudinal reinforcement ratio with a factor depending on the residual stress of the SFRC. The ultimate shear capacity is calculated with:

$$V_{u,pred} = \left[0.18 \cdot \left(1 + \sqrt{\frac{200}{d}} \right) \cdot \left(100 \cdot \rho_l \cdot \left[1 + 7.5 \cdot \frac{F_{Ftum}}{f_{ctm}} \right] \cdot f_{cm} \right)^{\frac{1}{3}} + 0.15 \cdot \sigma_{cp} \right] \cdot b_w \cdot d \quad (4.10)$$

The model also defines a minimum value of the shear resistance. In the calculations, this minimum value is not determinative for the results. The used equation in the CNR model is identical to the formulation of the Model Code 2010 (A), refer to Section 2.4.3. Therefore, the results are the same as discussed in Section 4.4.2.

Requirements

The requirement of the minimum volume fraction of the fibres equal to 0.003 is not fulfilled for the beams with 20 kg/m³ of steel fibres. There, ρ_f is equal to 0.0026. For 40 kg/m³ of steel fibres, the requirement is satisfied with ρ_f equal to 0.0051. The second requirement is fulfilled with the mean material properties. With the characteristic properties, the requirement is not satisfied for beam B402 and just satisfied for beam B405. Once again, 20 kg/m³ of steel fibres is not sufficient to replace the shear reinforcement for these beams, according to the CNR model.

Results and discussion

Table 4.12 and Figure 4.18 present the results of the prediction of the shear capacity compared to the experimentally obtained results. Also for this model, the predicted failure loads are always an underestimation of the experimentally observed ones. This leads to safer failure loads, beams located in the bottom right-hand corner in Figure 4.18 and possibly too conservative results in design calculation. The mean experimental-to-predicted failure ratio is 1.44, larger than with the RILEM model (1.35), but smaller than the DRAMIX Guideline (1.48).

The scatter of the results is the largest of the discussed models until here, with a coefficient of variation of 8.8%. However, the coefficient of determination R^2 with the linear regression is equal to 0.99. Comparable to the previous models, the ratio $V_{u,exp}/V_{u,pred}$ increases for higher prestressing forces (B402 - B405 and B403 - B406). In contrast to the previous models, it is here very clear that the $V_{u,exp}/V_{u,pred}$ ratio also increases for higher steel fibres dosages (B402 - B403 and B405 - B406).

The mean influence of the amount of steel fibres Φ_m is 27% and 35%, for the low and high fibre dosage respectively. These results are in line with the previous discussed models. A higher fibre dosage results in a higher influence and the scatter of the influences is caused by the variation in the measured material properties.

TABLE 4.12: Experimental failure loads compared to the analytical predictions according to CNR.

Beam	Experiment		Prediction		
	$V_{u,exp}$ [kN]	Failure mode [-]	$V_{u,pred}$ [kN]	$\frac{V_{u,exp}}{V_{u,pred}}$ [-]	Φ [%]
B402	218.5	S-DT [•]	148.2	1.47	22
B403	254.4	S-DT	161.3	1.58	32
B405	164.1	S-DT	129.0	1.27	32
B406	197.4	S-DT	137.6	1.43	38
			$\frac{V_{u,exp}}{V_{u,pred}}^{\dagger}$	1.44	
			COV [‡]	8.8 %	

Note: [•]: Shear (S) crack mode due to Diagonal Tension (DT);

[†]: Mean experimental-to-predicted failure load ratio; [‡]: Coefficient of variation

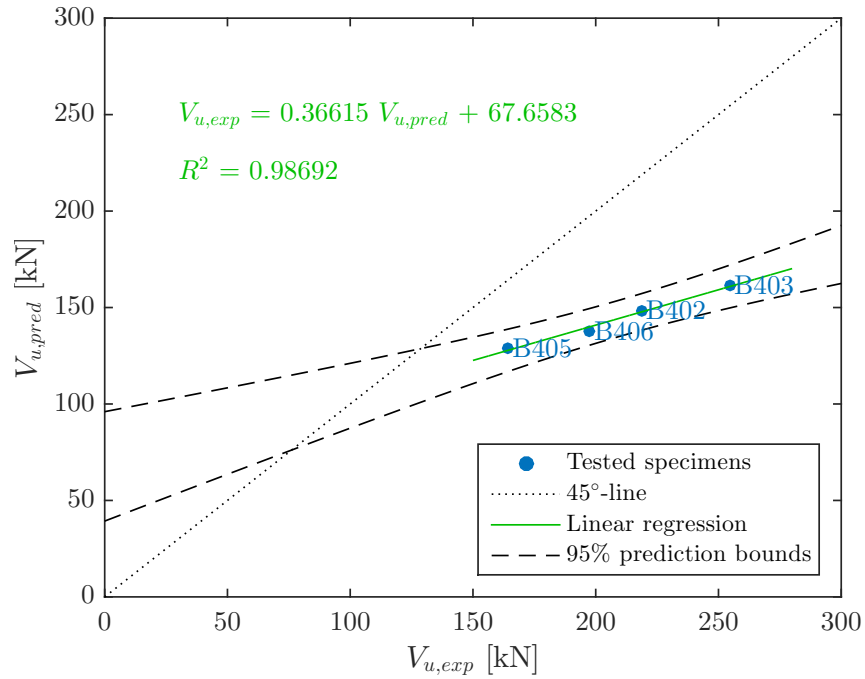


FIGURE 4.18: Experimental failure loads compared to the analytical predictions according to CNR.

4.5.4 Model proposed by Soetens

Calculation

The alternative model proposed by Soetens takes into account the most important shear influencing parameters. The ultimate shear capacity is calculated with:

$$V_{u,pred} = \left[0.388 \cdot \sqrt{1 + \frac{\sigma_{cp}}{f_{ctm}}} \cdot \left(1 + \sqrt{\frac{200}{d}} \right) \cdot \left(3 \cdot \frac{d}{a} \cdot \rho_l \right)^{1/3} \cdot \sqrt{f_{cm}} \right] \cdot b_w \cdot z \quad (4.11)$$

$$+ \left[f_{Ftu}^* \cdot \left(1 + 4 \cdot \frac{\sigma_{cp}}{f_{cm}} \right) \right] \cdot b_w \cdot z$$

The post-cracking strength for ultimate crack opening f_{Ftum} is limited by the value of $f_{ctm} \cdot \left(1 - \frac{2 \cdot \sigma_{cp}}{f_{cm}} \right)$. In the calculations, the value of f_{Ftum} is determining, except for beam B403 where the limited value is used (2.5 MPa compared to 2.9 MPa).

Results and discussion

Table 4.13 and Figure 4.19 present the results of the prediction of the shear capacity compared to the experimentally obtained results. This model gives the most divergent results compared to the other discussed models. Although the predicted failure loads are smaller than the experimentally observed ones, the mean experimental-to-predicted failure ratio is the smallest with 1.16. For beam B406, the prediction is even equal to the experimentally obtained failure load. For the estimation of the ultimate failure load, this results are the most accurate, on average. The model is not too conservative. However, it could be possible that the $V_{u,exp}/V_{u,pred}$ ratio in design calculations remains too small to give reliable results for practical use.

Conversely, the scatter of these results is the largest of the discussed models with a coefficient of variation of 13.2% (even larger than the previous discussed CNR model). The 95% prediction bounds are so wide that they fell off the figure. Furthermore, the coefficient of determination R^2 with the linear regression is equal to 0.59, which is the lowest result of all discussed models. Comparable to the previous models, the ratio $V_{u,exp}/V_{u,pred}$ increases for higher prestressing forces (B402 - B405 and B403 - B406). On the other hand, the $V_{u,exp}/V_{u,pred}$ ratio decreases for higher steel fibres dosages (B402 - B403 and B405 - B406). The lower the amount of steel fibres, the less accurate the results of the proposed model.

The mean influence of the amount of steel fibres Φ_m is 44% and 64%, for the low and high fibre dosage respectively. These results are larger than all previous discussed models. Adding 20 kg/m³ of steel fibres increases its contribution with approximately 20%. For beams with 40 kg/m³ of steel fibres, even more than half of the shear resistance is caused by the presence of the steel fibres. The influence of the plain concrete to the shear resistance in this model is 75 to 90% of the concrete contribution of the other models.

TABLE 4.13: Experimental failure loads compared to the analytical predictions according to the model proposed by Soetens.

Beam	Experiment		Prediction		
	$V_{u,exp}$ [kN]	Failure mode [-]	$V_{u,pred}$ [kN]	$\frac{V_{u,exp}}{V_{u,pred}}$ [-]	Φ [%]
B402	218.5	S-DT [•]	159.6	1.37	43
B403	254.4	S-DT	221.4	1.15	63
B405	164.1	S-DT	144.1	1.14	46
B406	197.4	S-DT	197.9	1.00	65
			$\frac{V_{u,exp}}{V_{u,pred}}^{\dagger}$	1.16	
			COV [‡]	13.2 %	

Note: [•]: Shear (S) crack mode due to Diagonal Tension (DT);

[†]: Mean experimental-to-predicted failure load ratio; [‡]: Coefficient of variation

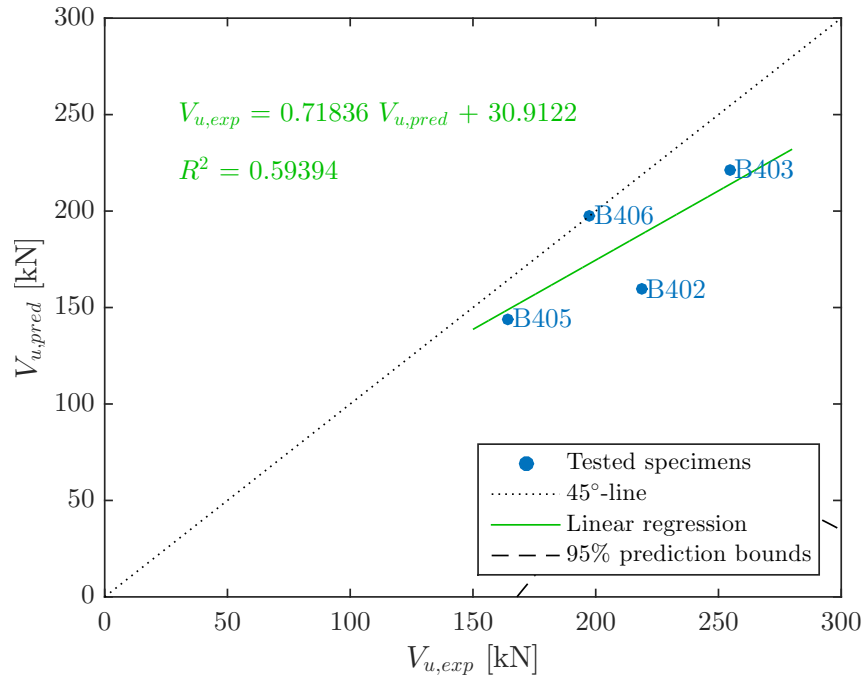


FIGURE 4.19: Experimental failure loads compared to the analytical predictions according to the model proposed by Soetens.

4.5.5 Model Code 2010 (B)

Calculation and discussion

The second approach of the Model Code 2010 (MC2010B) is given in the commentary section and must be solved iteratively. The longitudinal strain at mid-depth ϵ_x is needed to calculate the shear capacity, but ϵ_x is dependent on the applied shear force, as explained in Section 2.4.3. Moreover, the longitudinal strain is limited between 0 and 0.003. This assumes that a tensile force is acting on the fibre at mid-depth. While calculating these formulas, convergence has not been reached and a solution was not found. Since ϵ_x is limited, shear forces resulting in a value outside of the limits make no differences. Two modifications are investigated.

Modifications

Firstly, Soetens [60] mentions that if a compressive force is acting on the fibre at mid-depth of the section, the additional stiffness of the uncracked concrete section A_{ct} , assumed equal to $A_c/2$, could be taken into account. This results in:

$$\epsilon_x = \frac{1}{2} \cdot \frac{1}{E_p \cdot A_p + E_c \cdot A_c/2} \cdot \left[\frac{M_{Ed}}{z} + V_{Ed} + N_{Ed} \cdot \frac{z - e_p}{z} \right] \quad (4.12)$$

However, this formulation only influences negative strains, which are always limited by 0. Therefore, the problem of not reaching convergence remains.

Secondly, another strain distribution over the height is assumed whereby a part of the section is subjected to compressive forces, instead of the strain profile of MC2010B. A new formula to calculate the longitudinal strain at mid-depth of the effective depth ϵ_x is derived for prestressed beams, based on the equilibrium equations:

$$\int_0^x \sigma_c(y) \cdot b(y) \cdot dy - A_p \cdot \sigma_p - A'_p \cdot \sigma'_p = 0 \quad (4.13)$$

$$\int_0^x \sigma_c(y) \cdot b(y) \cdot y \cdot dy + A_p \cdot \sigma_p \cdot (d_p - x) - A'_p \cdot \sigma'_p \cdot (x - d'_p) = V_{Rd} \cdot a \quad (4.14)$$

x is the height of the compressive zone, d_p and d'_p are the distance from the top fibre of the beam to the center of the bottom respectively top reinforcement (A_p and A'_p). The stresses σ_c , σ_p and σ'_p in the concrete, bottom and top reinforcement respectively can be written in function of the corresponding strains ϵ_c , ϵ_p and ϵ'_p , depending on the assumed constitutive stress-strain relationships of concrete and steel. Once the strain profile is calculated by solving these equations, the strain at mid-depth of the section is known as well. Due to the presence of the applied shear force V_{Rd} in Equation 4.14, calculating the shear capacity remains iterative.

However, also the second modification does not result in strains at mid-depth between 0 and 0.003, leading to the same problem of not reaching convergence. To conclude, the second approach of the Model Code 2010 does not lead to predictions of the shear capacity of the beams tested in the present research.

4.5.6 General comparison

Table 4.14 presents the main result of each discussed model, namely the DRAMIX Guideline, the RILEM method, the CNR model, the Model Code 2010 (A) and the model proposed by Soetens. The experimental-to-predicted failure ratio for each beam and the mean value with the coefficient of variation are given. Also the coefficient of determination with a linear regression and the influences of the amount of steel fibres are shown. Furthermore, all models are summarized in Figure 4.20.

Firstly, the predicted shear capacities of all models are an underestimation, located below the 45°-line. This result leads to safe structural designs. The disadvantage is that some results are already very safe (maximum factor of 1.58), although all partial safety factors are omitted and average material properties are used. Therefore, the design values of the shear capacity will be even safer and could be too conservative, leading to expensive designs.

Secondly, it can be concluded that the CNR model and the Model Code 2010 (A) are identical, both in calculation formulas and results. This is logical, since both are based on the research of Minelli [32]. Therefore, the Model Code 2010 will be mentioned in the following for both the Model Code 2010 and the CNR code.

Thirdly, the model proposed by Soetens is the most divergent model. The experimental-to-predicted ratio is the lowest, both the mean value (1.16) as for each beam separately. This implies the model of Soetens to have the best ability to predict the actual shear capacity of prestressed SFRC beams. However, the main drawback is the largest coefficient of variation (13.2%) and the lowest coefficient of determination (0.59). The high scatter on the predictions leads to a higher model uncertainty.

On the contrary, the DRAMIX Guideline has the largest mean experimental-to-predicted value (1.48) and the lowest coefficient of variation (4.6%). As explained before, this rather outdated method includes the fibre properties instead of the post-cracking behaviour, resulting in less accurate predictions of the shear capacity that are only valid in specific cases (e.g. uncoated hooked end DRAMIX steel fibres).

Furthermore, the RILEM method leads to a better prediction of the failure load than the Model Code 2010. The former includes the contribution of the fibres by an additional shear capacity term V_{fd} , based on the post-cracking behaviour. The latter includes the effect of steel fibres by increasing the longitudinal reinforcement ratio, also based on the post-cracking behaviour.

Additionally, the influences of the amount of steel fibres are the highest for the model proposed by Soetens (approximately 44 and 64%). Counting on a larger effect of the steel fibres results in better predictions. The other influences are 20 to 25% for 20 kg/m³ of steel fibres and 32 to 40% for 40 kg/m³. The Model Code 2010 is an exception, with 32% for beam B405 with 20 kg/m³ steel fibres. This is

caused by the low measured uniaxial tensile strength (refer to Figure 3.16). Due to its presence in the denominator, the contribution of the steel fibres is larger. The scatter of the influences is caused by the variation in the measured material properties.

Lastly, the results give an indication of the influence of some properties on the accurateness of the predictions.

- (a) For all models, the $V_{u,exp}/V_{u,pred}$ ratio increases if the prestressing force increases (comparing B405 to B402 and B406 to B403). The influence of the prestressing force is not completely correctly estimated, especially for higher prestressing values. For this point, additional research could be performed.
- (b) On the contrary, an increasing amount of steel fibres leads to an increased $V_{u,exp}/V_{u,pred}$ ratio for the Model Code 2010 and a decreased ratio for the RILEM method and the model of Soetens (comparing B402 to B403 and B405 to B406). For the DRAMIX Guideline, it increases for the high level of prestress and decreases for the low level of prestress. This difference also explains the different slope of the linear regression of Model Code 2010 in Figure 4.20. It can be concluded that the contribution of the steel fibres still remains discordant and rather unknown correctly. In some cases, the influence of a higher amount is better estimated and vice versa for other cases. It also depends on the accurateness of the measurements of the material properties, namely the characteristics of the post-cracking behaviour. Further research on the modelling of the contribution of the amount of steel fibres is recommended.

As a final point, appropriate safety factors for design should be used in combination with the discussed models for the shear capacity of prestressed SFRC beams. This safety factor depends on the model uncertainty and the scatter of the measured material properties. On one hand, it must be large enough to reduce the failure risk sufficiently in order to design and build secure structural elements. On the other hand, a too large safety factor results in over-expensive designs.

4. ANALYTICAL STUDY

TABLE 4.14: Comparison of the different analytical shear capacity models for SFRC.

Parameter		DRAMIX Guideline	RILEM method	CNR model	Model Code 2010	Soetens model
$\frac{V_{u,exp}}{V_{u,pred}}$	B402	1.48	1.46	1.47	1.47	1.37
	B403	1.57	1.36	1.58	1.58	1.15
	B405	1.44	1.31	1.27	1.27	1.14
	B406	1.41	1.27	1.43	1.43	1.00
$\overline{\frac{V_{u,exp}}{V_{u,pred}}}$ [†]		1.48	1.35	1.44	1.44	1.16
COV [‡]	[%]	4.6	6.0	8.8	8.8	13.2
$R^{2\bullet}$		0.97	0.90	0.99	0.99	0.59
$\Phi^{\bullet\bullet}$ [%]	B402	21	19	22	22	43
	B403	32	36	32	32	63
	B405	23	26	32	32	46
	B406	39	41	38	38	65

Note: [†]: Mean experimental-to-predicted failure load ratio; [‡]: Coefficient of variation; [•]: Coefficient of determination; ^{••}: Influence of the steel fibre dosage.

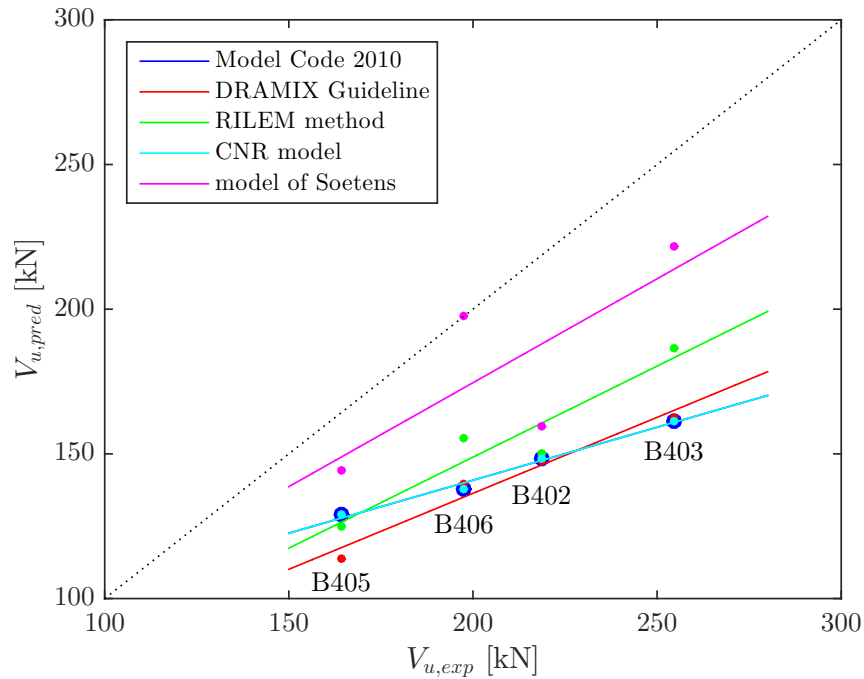


FIGURE 4.20: Experimental failure loads compared to the analytical predictions according to the different analytical models of the shear capacity of SFRC.

4.6 Conclusion

In this chapter, the analytical study of the experimental results (shear behaviour, crack loads and shear capacity) is performed. Firstly, the parameter study investigates the influence of the amount of fibres and the amount of prestressing. Increasing the fibre dosage results in several cracks, a larger post-cracking behaviour, a more gradual energy dissipation and an increased shear capacity. Increasing the prestress level results in an extended elastic region, a lower inclination of cracks with a larger width, a higher amount of released energy and an increased shear capacity. Furthermore, the shear behaviour and capacity are dependent on the measured material properties, however their influence is less distinct. Based on the research of De Wilder [13], the experimental dataset is extended and compared.

Secondly, the experimental crack loads are discussed. Comparing with the calculations shows an equal or smaller prediction than experimentally obtained. Deviations are mainly due to the scatter on the measured uniaxial tensile strengths and bending cracks occur before shear cracks in the non-fully prestressed beams. Comparing with the experimental failure loads shows an increase between crack and failure load of 20% (high prestress level, with steel fibres) to 60% (low prestress level, with stirrups).

Thereafter, the experimental failure loads are compared to analytical predictions based on design codes Eurocode 2 (without steel fibres) and Model Code 2010 (with steel fibres). The calculations are an underestimation, increasing as the prestressing force or the fibre dosage increases. Omitting partial safety factors and using average material properties, an average experimental-to-predicted failure load ratio equal to 1.43 was found with a coefficient of variation equal to 7.2%. Additionally, 20 kg/m³ of steel fibres is not sufficient to replace the shear reinforcement, according to MC2010.

Lastly, other shear capacity models for SFRC are applied and discussed, namely DRAMIX Guideline, RILEM method, CNR model, model proposed by Soetens and Model Code 2010(B). These models result in underestimations as well, which also increase by increasing the prestress level. In some models, the influence of a higher amount of steel fibres is better estimated and vice versa for others. The model of Soetens has on average the best predictions, but with the highest model uncertainty. DRAMIX Guideline has the largest underestimation, but with the smallest scatter. Further research on the contribution of the steel fibres is recommended. Additionally, appropriate safety factors should be determined in combination with the models to balance between a safe and a too conservative design.

In general, it is concluded that 40 kg/m³ steel fibres can replace the conventional shear reinforcement for an equal shear capacity (for the tested prestressed beams). The shear behaviour on the other hand differs in terms of crack load and post-cracking behaviour. Most deviations between results are caused by the scatter of the measured concrete material properties. Modelling of the shear capacity of SFRC still needs further investigation, as well as the influence of higher amounts of prestressing.

Chapter 5

Conclusions

The shear behaviour and shear capacity of prestressed steel fibre reinforced concrete beams and their influencing parameters are investigated, based on experimental and analytical research. This chapter presents the main conclusions and recommendations for further research.

5.1 General

Even for traditional structural concrete elements, shear behaviour and capacity are complex phenomena, consisting of interrelated shear transfer mechanisms and affected by different influencing parameters. Numerous models and experimental results are reported for reinforced concrete beams. However, valuable and complete data of prestressed concrete elements loading in shear are scarce, specifically for steel fibre reinforced concrete. Although a few different (semi-)empirical models of the shear capacity of SFRC exist nowadays, none of them is able to model the mechanisms fully correctly. Therefore, improving the design procedures of SFRC is important to economize and optimize the use of SFRC in structural elements.

The presented experimental research included six I-shaped prestressed concrete beams, four of them are reinforced with steel fibres and two with conventional shear reinforcement. The investigated parameters are fibre dosage, amount of conventional shear reinforcement and amount of prestressing. The material identification tests showed a large scatter, especially for the tensile strengths (flexural, splitting and uniaxial strength). The six beams are subjected to a combination of shear force and bending moment to investigate the shear failure mechanisms. The mechanical behaviour and shear capacity are measured using the displacement and deformation field, by use of conventional (DEMEC-points and LVDTs) and advanced optical (FBGs and 3D-DIC) techniques. All beams failed in a shear failure mode due to diagonal tension, as designed. For the conventional concrete beams, inclined web cracking caused yielding and rupture of the conventional shear reinforcement, leading to a very brittle failure. For the SFRC beams, the steel fibres are pulled out of the concrete matrix, leading to multiple cracks and a more ductile failure.

The analytical research included a parameter study, a discussion of the crack loads, a comparison with the main design codes (Eurocode 2 and Model Code 2010) and an investigation of other shear capacity models for SFRC (DRAMIX Guideline, RILEM method, CNR model and the model proposed by Soetens). Increasing the fibre dosage results in a more profound cracking pattern, a larger post-cracking behaviour, a more gradual energy dissipation and an increased shear capacity. Increasing the prestress level results in an extended elastic region, a lower inclination of cracks with a larger width, a higher amount of released energy and an increased shear capacity. Deviations between the experimental and calculated crack loads are mainly due to the scatter on the measured uniaxial tensile strengths and bending cracks occur before shear cracks in the non-fully prestressed beams. Furthermore, all the calculated predictions of the shear capacity are an underestimation of the actual failure load. The underestimation increases as the prestressing force increases. In some models, the influence of a higher amount of steel fibres is better estimated and vice versa for others. Omitting partial safety factors and using average material properties, an average experimental-to-predicted failure load ratio equal to 1.43 was found with a coefficient of variation equal to 7.2% for EC2 and MC2010. The other models differ in shear design approach and including affecting parameters, resulting in varying average experimental-to-predicted failure load ratios and model uncertainties.

Lastly, it can be concluded from the performed experimental program that 40 kg/m^3 of steel fibres can replace the conventional shear reinforcement to obtain an equal shear capacity for the prestressed beams of the presented cases. The shear behaviour on the other hand differs in terms of crack load and post-cracking behaviour. Most deviations between results are caused by the scatter of the measured concrete material properties.

5.2 Recommendations for further research

The performed experimental and analytical research contributes to the knowledge about shear behaviour of SFRC and existing analytical models of the shear capacity, in order to enhance the safe application of (prestressed) SFRC structural elements. To enlarge this knowledge, recommendations for further research are made.

Firstly, the experimental research was limited to six beams with the same geometry and material and with only three varying parameters. Further research can extend this obtained experimental dataset by testing more and varying beams. For example, the type of used steel fibres (e.g. aspect ratio, shape and strength), the geometry of the beam and reinforcement (e.g. length, shape of the cross section and number of prestressing strands) and the experimental setup (e.g. shear span-to-effective depth ratio and distributed loads) are parameters to investigate. In addition, also the use of synthetic fibres or a combination of conventional and fibre reinforcement are worth to examine. Hereby, it is useful to measure the shear behaviour (deformations, displacements and cracking pattern) instead of only the shear capacity.

Secondly, further research on the analytical models and design codes could be performed. A higher prestressing forces leads to a larger underestimation, thus the models are not able to include the effect of prestressing completely correctly. The same conclusion is made for the amount of steel fibres, especially because for some models the underestimation enlarges for a higher fibre dosage and for others for a smaller fibre dosage. The correct estimation of the effect of steel fibres, based on the post-cracking behaviour, remains absent. In addition, also the appropriate safety factors can be determined since all the models already predict a lower shear capacity than the actual failure load.

Appendices

Appendix A

List of shear experiments on SFRC beams from literature

This appendix contains an overview of the main experimental investigations and modelling of the shear behaviour and capacity of SFRC beams, related to Chapter 2, Section 2.4.1. It is chronologically listed and does not mean to be exhaustive. The list is constructed based on literature and on [17, 32, 34, 60]. The research programs including (partially) prestressed SFRC beams are indicated with the symbol * in front of the reference.

1. Batson, G., Jenkins, E. and Spatney, R. (1972). Steel Fibers as Shear Reinforcement in Beams. *ACI Journal*, 69(10):640-644.
2. Henager, C. H., Asce, M. and Doherty, T.J. (1976). Analysis of Reinforced Fibrous Concrete Beams. *Journal of the Structural Division (ASCE)*, 102(1):177-188.
3. Roberts, T. M. and Ho, N. L. (1982). Shear Failure of Deep Fibre Reinforced Concrete Beams. *The International Journal of Cement Composites and Lightweight Concrete*, 4(3):145-152.
4. Swamy, R. N. and Bahia, H. M. (1985). The Effectiveness of Steel Fibers as Shear Reinforcement. *Concrete International*, 7(3):35-40.
5. Niyogi, S. K. and Dwarakanathan, G. I. (1985). Fiber Reinforced Beams under Moment and Shear. *Journal of Structural Engineering*, 111(3):516-527.
6. Mansur, M. A., Ong, K. C. G., Paramasivam, P. (1986). Shear Strength of Fibrous Concrete Beams without Stirrups. *Journal of Structural Engineering (ASCE)*, 112(9):2066-2079.
7. Sharma, A. K. (1986). Shear Strength of Steel Fiber Reinforced Concrete Beams. *ACI Journal*, 83(4):624-628.
8. * Narayanan, R. and Darwish, I. Y. S. (1987). Use of Steel Fibers as Shear Reinforcement. *ACI Structural Journal*, 84(3):216-227.
* Narayanan, R. and Darwish, I. Y. S. (1987). Shear in Prestressed Concrete Beams Containing Steel Fibres. *The International Journal of Cement Composites and Lightweight Concrete*, 9(2):81-90.

9. Kaushik, S. K., Gupta, V. K. and Tarafdar, N. K. (1987). Behaviour of Fiber Reinforced Concrete Beams in Shear. Proceedings of the International Symposium of Fibre Reinforced Concrete, Madras, India, December 16-19, pp. 133-149.
10. Murty, D. S. R. and Venkatacharyulu, T. (1987). Fibre Reinforced Concrete Beams Subjected to Shear Force. Proceedings of the International Symposium of Fibre Reinforced Concrete, Madras, India, December 16-19, pp. 125-131.
11. Al-Ta'an, S. A. and Al-Feel, J. R. (1990). Evaluation of Shear Strength of Fibre-Reinforced Concrete Beams. Cement and Concrete Composites, 12(2):87-94.
12. Sachan, A. K. and Kameswara Rao, C. V. S. (1990). Behaviour of Fibre Reinforced Concrete Deep Beams. Cement and Concrete Composites, 12(3):211-218.
13. Ashour, S. A., Hasanain, G. S. and Wafa, F. F. (1992). Shear Behavior of High-Strength Fiber Reinforced Concrete Beams. ACI Structural Journal, 89(2):176-184.
14. Li, V., Ward, R. and Hamza, A. (1992). Steel and synthetic fibers as shear reinforcement. ACI Material Journal, 89(5):449-508.
15. Saluja, S. K., Kumar, S., Samra, M. S. and Singh, A. P. (1992). Flexural and Shear Strength of Fibre Reinforced Concrete Beams. Journal of Structural Engineering, 19(3):101-105.
16. Swamy, N. R., Roy, J. and Chiam A. T. P. (1993). Influence of Steel Fibers in the Shear Resistance of Lightweight Concrete I-Beam. ACI Structural Journal, 90(1):103-114.
17. Tan, K. H., Murugappan, K. and Paramasivam, P. (1993). Shear behaviour of steel fiber reinforced concrete beams. ACI Structural Journal, 90(1):3-11.
* Tan, K. H., Paramasivam, P. and Murugappan, K. (1995). Steel Fibers as Shear Reinforcement in Partially Prestressed Beams. ACI Structural Journal, 92(6):643-652.
18. Shin, S. W., Oh, J. G. and Ghosh, S. K. (1994). Shear Behavior of Laboratory-Sized High Strength Concrete Beams Reinforced with Bars and Steel Fibers. Fiber Reinforced Concrete: Developments and Innovations. ACI SP-142, Detroit, USA, pp. 181-200.
19. Batson, G. B. and Youssef, A. G. (1994). Shear Capacity of Fiber Reinforced Concrete Based on Plasticity of Concrete: A Review. Fiber Reinforced Concrete: Developments and Innovations, ACI SP-142, Detroit, USA, pp. 141-165.
20. Imam, M., Vandewalle, L., and Mortelmans, F. (1995). Shear-moment analysis of reinforced high strength concrete beams containing steel fibers. Canadian Journal of Civil Engineering, 22(3):462-470.
Imam, M., Vandewalle, L., Mortelmans, F., and Van Gemert, D. (1997). Shear domain of fibre-reinforced high-strength concrete beams. Engineering Structures, 19(9):738-747.
21. Casanova, P., Rossi, P. and Schaller, I. (1997). Can steel fibers replace transverse reinforcement in reinforced concrete beams? ACI Material Journal, 94(5):341-354.

-
22. Adebar, P. Mindess, S., St.-Pierre, D. and Olund, B. (1997). Shear tests of fiber concrete beams without stirrups. *ACI Structural Journal*, 94(1):68-76.
 23. Kützing, L. (1997). Shear strength of steel fibre reinforced concrete beams and plates. *LACER 2*, University of Leipzig, pp. 263-272.
 24. Lim, D. H. and Oh, B. H. (1999). Experimental and Theoretical Investigation on the Shear of Steel Fibre Reinforced Concrete Beams. *Engineering Structures*, 21(10):937-944.
 25. Khuntia, M., Stojadinovic, B., Subhash, C. G. (1999). Shear strength of normal and high-strength fiber reinforced concrete beams without stirrups. *ACI Structural Journal*, 96(2):282-289.
 26. Gustafsson, J., and Noghabai, K. (1999). Steel fibers as shear reinforcement in high strength concrete beams. *Bi-annual report - Nordic Concrete Research (NCR)*, 1:1-18.
 27. Noghabai, K. (2000). Beams of Fibrous Concrete in Shear and Bending. Experiment and Model. *Journal of Structural Engineering*, 126(2):243-251.
 28. Di Prisco, M. and Ferrara, L. (2001). HPFRC pre-stressed thin-web elements: some results on shear resistance. *Fracture Mechanics of Concrete Structures*. De Borst et al (eds), pp. 895-902.
 29. Kwak, Y. K., Eberhard, M. O., Kim, W. S. and Kim, J. (2002). Shear Strength of Steel Fiber-Reinforced Concrete Beams without Stirrups. *ACI Structural Journal*, 99(4):530-538.
 30. Vandewalle, L. and Dupont, D. (2002) Dwarskrachtcapaciteit van staalvezelbetonbalken (in Dutch). *Cement* 8:92-96.
 31. Rosenbusch, J. and Teutsch, M. (2003). Shear Design with σ - ϵ Method. Test and Design Methods for Steel Fibre Reinforced Concrete. *RILEM TC 162-TDF Workshop*, Bochum, Germany, pp. 105-117.
 32. * Kovács, I. and Balázs, G. L. (2003). Structural behavior of steel fibre reinforced concrete. *FIB Structural Concrete Journal*, 4(2):57-63.
 33. Voo, Y. L., Foster, S. J. and Gilbert, I. R. (2003). Shear Strength of Fibre Reinforced Reactive Powder Concrete Girders without Stirrups. School of Civil and Environmental Engineering, The University of New South Wales, UNSW Sydney, Australia.
* Voo, Y. L., Foster, S. J. and Gilbert, I. R. (2006). Shear Strength of Fibre Reinforced Reactive Powder Concrete Prestressed Girders without Stirrups. *Journal of Advanced Concrete Technology*, 4(1):123-132.
Voo, Y. L., Foster, S. J. (2008). Shear strength of steel fiber reinforced ultra-high performance concrete beams without stirrups. *5th international Specialty Conference on Fibre Reinforced Materials*, pp. 177-184.
 34. Cucchiara, C., La Mendola, L. and Papia, M. (2004). Effectiveness of Stirrups and Steel Fibres as Shear Reinforcement. *Cement and Concrete Composites*, 26(7):777-786.

35. Kearsley, E. P. and Mostert, H. F. (2004). The Effect of Fibres on the Shear Strength of Reinforced Concrete Beams. Proceedings of the Sixth RILEM Symposium on Fibre Reinforced Concrete (FRC). BEFIB 2004, Varenna, Italy, 2:955-964.
36. * Meda, A. Minelli, F., Plizzari, G. A. and Riva, P. (2005). Shear behaviour of steel fibre reinforced concrete beams. *Materials and Structures*, 38:343-351.
37. * Minelli, F. (2005). Plain and Fibre Reinforced Concrete Beams under Shear Loading. Structural Behaviour and Design Aspects. PhD-thesis. University of Brescia, Brescia, Italy.
38. Adhiraky, B. B. and Mutsuyoshi, H. (2006). Prediction of Shear Strength of Steel Fiber RC Beams Using Neural Networks. *Elsevier Edition Construction and Building Materials*, 20(9):801-811.
39. Parra-Montesinos, G. J. (2006). Shear strength of beams with deformed steel fibres. *Concrete International*, pp. 57-61.
40. * De Pauw, P., Taerwe, L., Van De Buerie, N. and Moerman, W. (2008). Replacement of Shear Reinforcement by Steel Fibres in Pretensioned Concrete Beams. *Tailor Made Concrete Structures - Walraven and Stoelhorst edition*. London, U.K., pp. 391-397.
- * De Pauw, P., Taerwe, L., Van den Buerie, N., Moerman, W. (2008). Steel fibre concrete as an alternative for traditional shear reinforcement in pretensioned concrete beams. 7th international RILEM symposium on fibre reinforced concrete: design and applications (BEFIB 2008), pp. 887- 898.
41. Greenough, T., Nehdi, M. (2008). Shear Behavior of Fiber-Reinforced Self-Consolidating Concrete Slender Beams. *ACI Materials Journal*, 105(5):468-477.
42. De Hanai, J. B. and Holanda, K. M. A. (2008). Similarities between Punching and Shear Strength of Steel Fiber Reinforced Concrete (SFRC) Slabs and Beams. *Ibracon Structures and Materials Journal*, 1(1):1-16.
43. Fico, R., Prota, A. and Manfredi, G. (2008). Assessment of Eurocode-like Design Equations for the Shear Capacity of FRP RC Members. (Elsevier Edition) *Composites. Part B*, 39(5):792-806.
44. * Cho, J.-S., Lundy, J., Chao, S.-H. (2009). Shear Strength of Steel Fiber Reinforced Prestressed Concrete Beams. *Structures Congress 2009: Don't Mess with Structural Engineers*, Austin, Texas, pp. 1058-1066.
45. Dinh, H. H., Parra-Montesinos, G. J. and Wight, J. K. (2010). Shear Behavior of Steel Fiber-Reinforced Concrete Beams without Stirrup Reinforcement. *ACI Structural Journal*, 107(5):597-606.
- Dihn, H. H., Parra-Montesinos, G. J. and Wight, J. K. (2011). Shear strength model for steel fiber reinforced concrete beams without stirrup reinforcement. *ASCE Journal of Structural Engineering*, 137(10):1039-1051.
46. Kang, T. H., Kim, W. Kwak, Y.-K. and Hong, S.-G. (2011). Shear testing of steel fiber-reinforced lightweight concrete beams without web reinforcement. *ACI Structural Journal*, 108(5):553-561.

-
47. Ding, Y., You, Z. and Jalali, S. (2011). The Composite Effect of Steel Fibres and Stirrups on the Shear Behaviour of Beams Using Self-Consolidating Concrete. *Engineering Structures*, 33(1):107-117.
Ding, Y., Zhang, F., Torgal, F., Zhang, Y. (2012). Shear behaviour of steel fibre reinforced selfconsolidating concrete beams based on the modified compression field theory. *Composite Structures*, 94(8):2440-2449.
 48. Aoude, H., Mehdi, B., Cook, W. D., Mitchell, D. (2012). Response of Steel Fiber-Reinforced Concrete Beams with and without Stirrups. *ACI Structural Journal*, 109(3):359-368.
 49. Parmentier, B., Cauberg, N., Vandewalle, L. (2012). Shear resistance of macro-synthetic and steel fibre reinforced concrete beams without stirrups. 8th RILEM international symposium on fibre reinforced concrete: challenges and opportunities (BEFIB 2012), Guimaraes, Portugal.
 50. * Cuenca, E., Serna, P. (2013). Shear behavior of prestressed precast beams made of self-compacting fiber reinforced concrete. *Construction and Building Materials*, 45:145-156.
 51. Minelli, F. and Plizzari, G. A. (2013). On the effectiveness of steel fibres as shear reinforcement. *ACI Structural Journal*, 110(3):379-389.
 52. * Soetens, T. (2015). Design models for the shear strength of prestressed precast steel fiber reinforced concrete girders. PhD thesis, Faculty of Engineering Science and Architecture, UGent, Belgium.

Appendix B

Calculation scheme and additional test results

This appendix gives some additional information related to Chapter 3, where the experimental research is presented. The first part explains in detail the calculation formulas and scheme to predict the crack load of the beams. The second part presents the extensive results of the measurements of the amount of steel fibres.

B.1 Calculation of the predicted crack load

This appendix completes Section 3.6 about the calculation of the load pattern. Figure B.1 gives the followed calculation scheme. The first part (Figure B.1a) lists the measured and defined concrete and reinforcement properties and dimensions (as described in Sections 3.2 and 3.3). The second part (Figure B.1b) involves the prestress losses and calculates the crack load.

Based on the DEMEC measurements, a linear regression function is drawn of the strain in function of the height of the beam (refer to Figure 3.26). The strains at the position of the prestressing strands (at bottom and top) are converted to stresses with the modulus of elasticity of the prestressing strands. The shortening of the beam, due to aforementioned effects, corresponds to negative strains and prestress losses. These are subtracted from the initial prestress to obtain the remaining prestress at the moment of testing.

The first crack load is the minimum of the load that induces inclined cracks in the web of the beam ($V_{cr,w}$) and the load that causes vertical flexural cracks at the bottom of the beam (M_{cr}), refer to Equation B.1.

$$V_{cr} = \min(V_{cr,w}; V_{cr,bending}) \quad (\text{B.1})$$

In the first case, the shear force leads to a principal normal stress σ_1 that exceeds the tensile strength (Equation B.2, based on Mohr's Circle). The shear stress before cracking can be calculated with the formula of Jourawski (Equation B.4). Combining Equation B.3 and B.4 results in the crack load due to shear force $V_{cr,w}$ (Equation B.5).

$$\sigma_1 = \sqrt{\frac{\sigma_{cp}^2}{4} + \tau^2} - \frac{\sigma_{cp}}{2} \leq f_{ctm} \quad (\text{B.2})$$

$$\tau = \sqrt{(f_{ctm})^2 + \sigma_{cp} \cdot f_{ctm}} \quad (\text{B.3})$$

$$\tau = \frac{V_{cr,w} \cdot S}{b_w \cdot I} \quad (\text{B.4})$$

$$V_{cr,w} = \frac{I \cdot b_w}{S} \sqrt{(f_{ctm})^2 + \alpha_l \cdot \sigma_{cp} \cdot f_{ctm}} \quad (\text{B.5})$$

σ_{cp} denotes the remaining prestress in MPa, f_{ctm} the uniaxial tensile strength in N/mm² (refer to Table 3.8), S the first moment of area in mm³, I the second moment of area in mm⁴, b_w the web width in mm and α_l a correction factor equal to 1.

In the second case, the bending moment M_{cr} leads to exceeding the tensile strength at the bottom of the beam. The stress at the bottom consists of three parts (Equation B.6): compression due to the prestressing force P , compression due to the eccentricity e of the prestressing force ($M_p = P \cdot e$) and tension due to the applied load ($M_{cr} = V_{cr,bending} \cdot a$). This results in Equation B.7. v denotes the distance from the neutral axis to the bottom side in mm and a the shear span length of 2200 mm.

$$f_{ctm} \geq -\frac{P}{A_c} - \frac{M_p \cdot v}{I} + \frac{M_{cr} \cdot v}{I} \quad (\text{B.6})$$

$$V_{cr,bending} \cdot a = \frac{I}{v} \left(f_{ctm} + \sigma_{cp} + \frac{P \cdot e \cdot v}{I} \right) \quad (\text{B.7})$$

B.1. Calculation of the predicted crack load

CALCULATION OF THE LOAD PATTERN

Concrete properties

Mean cylindrical compressive strength	f_{cm}		[N/mm ²]	From small-scale tests
Mean flexural tensile strength	$f_{ctm,fl}$		[N/mm ²]	From small-scale tests
Mean axial tensile strength	f_{ctm}		[N/mm ²]	From Model Code 2010:

$$f_{ctm} = \alpha_{fl} f_{ctm,fl}$$

With:

$$\alpha_{fl} = \frac{0,06 h_b^{0,7}}{1 + 0,06 h_b^{0,7}}$$

$$h_b = \begin{cases} 150 \text{ mm,} & \text{for plain concrete} \\ 125 \text{ mm,} & \text{for SFRC with notch} \end{cases}$$

E-modulus concrete	E_c		[N/mm ²]	From small-scale tests
Density	ρ		[kg/m ³]	From small-scale tests

Reinforcement steel properties

E-modulus prestressing steel	E_p	198	[GPa]	
Ratio E-moduli	m		[-]	$m = E_p/E_c$
Surface prestressing strand	$A_{p,1}$	93	[mm ²]	
Number of strands at bottom	n	7	[-]	
Total surface of prestressing reinforcement	A_p	651	[mm ²]	$A_p = n A_{p,1}$
Amount of steel fibres	V_f		[kg/m ³]	0, 20 or 40 kg/m ³

Dimensions

Height	h	630	[mm]	
Web width	b_w	70	[mm]	
Center of gravity bottom reinforcement	z	73	[mm]	$z = \frac{1 \cdot 120 + 3 \cdot 80 + 3 \cdot 50}{7}$ from bottom
Effective depth	d	557	[mm]	$d = h - z$
Height top reinforcement	d_2	50	[mm]	
Length	L	7	[m]	
Total surface	A	87450	[mm ²]	
Surface of concrete	A_c	86706	[mm ²]	
Total weight of beam	G_{beam}		[kN/m]	
Neutral axis from top side	y_o		[mm]	
Neutral axis from bottom side	$h - y_o$		[mm]	
First moment of area	S		[mm ³]	
Second moment of area	I		[mm ⁴]	
Shear span	a	2200	[mm]	
Shear span-to-effective depth ratio	a/d	3,95	[-]	

(A) Part 1 of the calculation template: properties and dimensions.

B. CALCULATION SCHEME AND ADDITIONAL TEST RESULTS

Prestressing force			
Initial prestress	$\sigma_{pm0(x)}$	[N/mm ²]	750 or 1488 N/mm ²
Initial prestressing force (8 strands)	P_{m0}	[kN]	
DEMEC measurement			
	$h = a \cdot \varepsilon + b \rightarrow \varepsilon = \frac{h-b}{a}$	a	From linear regression function
		b	From linear regression function
Prestress loss			
Center of gravity reinforcement	h	73	580 [mm]
Strain loss	ε		[-]
Stress loss	$\Delta\sigma_p$		[N/mm ²] $\Delta\sigma_p = E_p \cdot \varepsilon$
Remaining prestress	σ_p		[N/mm ²] $\sigma_p = \sigma_{pm0(x)} + \Delta\sigma_p$
Remaining prestressing force (7 or 1 strands)	P_p		[kN] $P_p = \sigma_p \cdot A_p$
Total remaining prestressing force			
	P	[kN]	$P = P_{p,bottom} + P_{p,top}$
Total remaining prestress on concrete			
	σ_{cp}	[N/mm ²]	$\sigma_{cp} = P/A_c$
First crack load			
The first crack load is the minimum of the load needed to induce shear or bending cracks.			
Shear capacity			
	α_l	1	[-]
Shear capacity	$V_{cr,w,total}$	[kN]	$V_{cr,w,total} = \frac{I \cdot b_w}{S} \sqrt{(f_{ctm})^2 + \alpha_l \sigma_{cp} f_{ctm}}$
Shear capacity taking into account weight	$V_{cr,w}$	[kN]	$V_{cr,w} = V_{cr,w,total} - \frac{G_{beam} L}{2}$
Bending capacity			
Distance neutral axis to bottom side	v	[mm]	$f_{ctm} = -\frac{P}{A_c} - \frac{M_p \cdot v}{I} + \frac{M_{cr} \cdot v}{I}$ \downarrow $M_{cr,totaal} = \frac{I}{v} \left(f_{ctm} + \sigma_{cp} + \frac{P \cdot e \cdot v}{I} \right)$ \downarrow $M_{cr} = M_{cr,totaal} - \frac{G_{beam} L^2}{8}$ \downarrow $V_{cr,bending} = \frac{M_{cr}}{a}$
Eccentricity	e	[mm]	
Bending capacity	$M_{cr,total}$	[kNm]	
Bending capacity taking into account weight	M_{cr}	[kNm]	
Shear capacity corresponding to bending	$V_{cr,bending}$	[kN]	
Predicted first crack load			
	V_{cr}	[kN]	$V_{cr} = \min(V_{cr,w}; V_{cr,bending})$
Corresponding press load			
	P_{cr}	[kN]	$P_{cr} = 2V_{cr}$

(B) Part 2 of the calculation template: prestress losses and crack load.

FIGURE B.1: Template to calculate the predicted crack load (blue fields have to be filled in, white fields are fixed values and grey fields are calculated by the formulas).

B.2 Amount of steel fibres

This appendix completes Section 3.7.7 about the amount of steel fibres in the crack plane of the full-scale beams after testing.

Figures B.2, B.3, B.4 and B.5 show the location of the drilled cores of the SFRC beams B402, B403, B405 and B406 respectively. The schematic view presents the frontside of the beam, with the origin of the coordinate system in the left bottom corner. The photographs are taken at the backside of the beam and show the positions of the cores on the cracks. Each core is denoted with the letter K, the number of the beam and behind the slash mark a number varying between 1 and 7.

Table B.1 gives the numerical results. The location of the cores is denoted by x and y , both in mm, with the origin of the coordinate system in the left bottom corner. A_{tot} is the crack surface of the core in mm^2 and N_f the counted number of fibres crossing this crack surface. The amount of fibres per surface area is denoted as N_f/A_{tot} and ρ_f is the fibre reinforcement ratio (refer to equation 3.21).

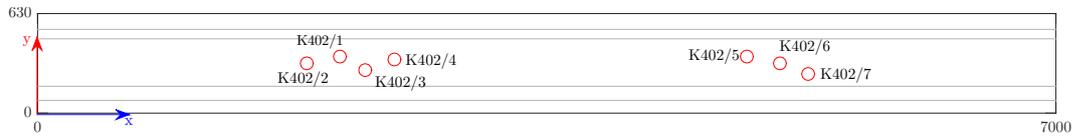
B. CALCULATION SCHEME AND ADDITIONAL TEST RESULTS

TABLE B.1: Amount of steel fibres for drilled cores of B402, B403, B405 and B406.

Cores	x [mm]	y [mm]	A_{tot} [mm ²]	N_f [-]	N_f/A_{tot} [1/cm ²]	ρ_f [%]
K402/1	2080	360	7840	51	0.65	0.07
K402/2	1850	315	7770	34	0.44	0.05
K402/3	2250	270	7700	63	0.82	0.09
K402/4	2450	340	7700	76	0.99	0.11
K402/5	4875	360	7875	38	0.48	0.05
K402/6	5100	315	7875	49	0.62	0.07
K402/7	5300	250	6300	27	0.43	0.05
				$\frac{\bar{N}_f}{A_{tot}}$ •	0.63	
				COV••	33%	
K403/1	1670	290	7700	161	2.09	0.24
K403/2	2120	315	7840	105	1.34	0.15
K403/3	2360	280	7840	80	1.02	0.12
K403/4	2600	360	7665	111	1.45	0.16
K403/5	4300	340	7805	90	1.15	0.13
K403/6	4750	290	7700	114	1.48	0.17
K403/7	5150	340	7700	122	1.58	0.18
				$\frac{\bar{N}_f}{A_{tot}}$ •	1.45	
				COV••	24%	
K405/1	1770	270	7770	48	0.62	0.07
K405/2	2000	330	7315	37	0.51	0.06
K405/3	2180	380	7945	52	0.65	0.07
K405/4	2410	360	7595	42	0.55	0.06
K405/5	2580	330	7630	46	0.60	0.07
K405/6	4740	300	7875	32	0.41	0.05
K405/7	5300	315	7700	34	0.44	0.05
				$\frac{\bar{N}_f}{A_{tot}}$ •	0.54	
				COV••	17%	
K406/1	1730	315	7700	116	1.51	0.17
K406/2	1940	380	7700	120	1.56	0.18
K406/3	2290	270	7700	138	1.79	0.20
K406/4	2600	350	7700	75	0.97	0.11
K406/5	4300	370	7700	120	1.56	0.18
K406/6	4450	315	7700	106	1.38	0.16
K406/7	4600	240	7840	97	1.24	0.14
				$\frac{\bar{N}_f}{A_{tot}}$ •	1.43	
				COV••	18%	

•: Mean amount of fibres per surface area; ••: Coefficient of Variation

B.2. Amount of steel fibres



(A) Schematic view of the frontside of the beam (in mm).

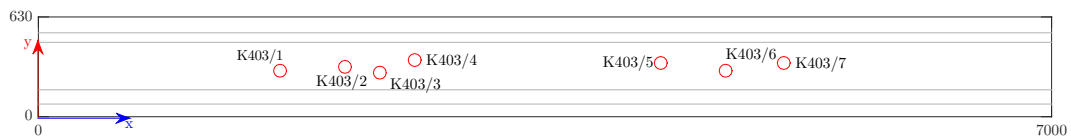


(B) Picture of the backside ($x = 2000$ mm).



(C) Picture of the backside ($x = 5000$ mm).

FIGURE B.2: Location of the drilled cores for B402.



(A) Schematic view of the frontside of the beam (in mm).



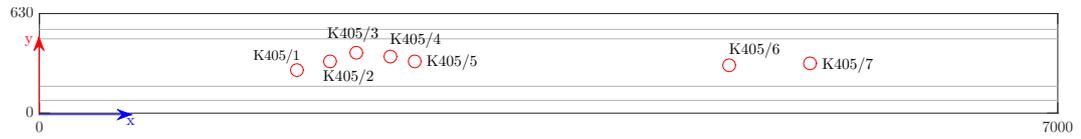
(B) Picture of the backside ($x = 2000$ mm).



(C) Picture of the backside ($x = 5000$ mm).

FIGURE B.3: Location of the drilled cores for B403.

B. CALCULATION SCHEME AND ADDITIONAL TEST RESULTS



(A) Schematic view of the frontside of the beam (in mm).

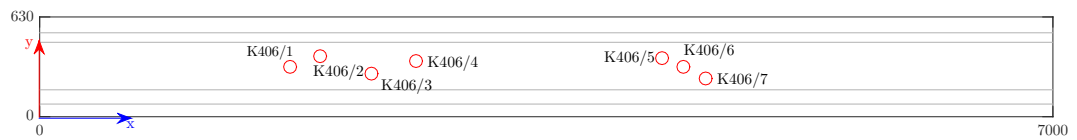


(B) Picture of the backside ($x = 2000$ mm).



(C) Picture of the backside ($x = 5000$ mm).

FIGURE B.4: Location of the drilled cores for B405.



(A) Schematic view of the frontside of the beam (in mm).



(B) Picture of the backside ($x = 2000$ mm).



(C) Picture of the backside ($x = 5000$ mm).

FIGURE B.5: Location of the drilled cores for B406.

Bibliography

- [1] J. M. Alwan, A. E. Naaman, and P. Guerrero. Effect of mechanical clamping on the pull-out response of hooked steel fibers embedded in cementitious matrices. *Concrete Science and Engineering*, 1(1):15–25, 1999.
- [2] B. E. Barragán. *Failure and toughness of steel fiber reinforced concrete under tension and shear*. PhD thesis, Universitat Politècnica de Catalunya, Barcelona, Spain, 2002.
- [3] C. Bedard and P. C. Aitcin. A la recherche d’un béton de 150 MPa. *Canadian Journal Civil Engineering*, 10(4):600–613, 1983.
- [4] A. Belarbi and T. T. C. Hsu. Constitutive laws of concrete in tension and reinforcing bars stiffened by concrete. *ACI Structural Journal*, 91(4):465–474, 1994.
- [5] E. C. Bentz, F. J. Vecchio, and M. P. Collins. Simplified modified compression field theory for calculating shear strength of reinforced concrete elements. *ACI Structural Journal*, 103(4):614–624, 2006.
- [6] CEN. NBN EN 12390-6: Testing hardened concrete - Part 6: Tensile splitting strength of test specimens, 2001.
- [7] CEN. NBN EN 12390-13: Testing hardened concrete - Part 5: Flexural strength of test specimens, 2009.
- [8] CEN. NBN EN 12390-3: Testing hardened concrete - Part 3: Compressive strength of test specimens, 2009.
- [9] CEN. EN 14651: Test method for metallic fiber concrete - measuring the flexural tensile strength (limit of proportionality (LOP), residual), 2014.
- [10] CEN. NBN EN 12390-13: Testing hardened concrete - Part 13: Determination of secant modulus of elasticity in compression, 2014.
- [11] M. P. Collins. Towards a rational theory for RC members in shear. *Journal of the Structural Division - ASCE*, 104(4):649–666, 1978.
- [12] M. P. Collins, E. C. Bentz, and E. G. Sherwood. Where is shear reinforcement required? review of research results and design procedures. *ACI Structural Journal*, 105(5):590–600, 2008.

- [13] K. De Wilder. *Shear capacity of prestressed and reinforced concrete members*. PhD thesis, Faculty of Engineering Science, KU Leuven, Belgium, October 2014.
- [14] K. De Wilder, M. De Smedt, P. Lava, E. Reynders, G. De Roeck, and L. Vandewalle. Experimental analysis of the mechanical behaviour of shear-deficient pretensioned steel-fibre reinforced concrete beams. In *BEFIB 2016 - 9th Rilem International Symposium in Fiber Reinforced Concrete*, Vancouver, Canada, September 2016.
- [15] K. De Wilder, P. Lava, D. Debruyne, Y. Wang, G. De Roeck, and L. Vandewalle. Experimental investigation on the shear capacity of prestressed concrete beams using digital image correlation. *Engineering Structures*, 82(1):89–92, 2015.
- [16] M. di Prisco, G. Plizzari, and L. Vandewalle. Fibre reinforced concrete: new design perspectives. *Materials and Structures*, 42(9):1261–1281, 2009.
- [17] H. H. Dihm, G. Parra-Montesinos, and J. Wight. Shear strength model for steel fiber reinforced concrete beams without stirrup reinforcement. *ASCE Journal of Structural Engineering*, 137(10):1039–1051, 2011.
- [18] Fédération Internationale du Béton (fib). Shear and torsion: Explanatory and viewpoint papers on Model Code chapters 11 and 12 prepared by members of CEB Commission V. *CEB-Bulletin 126*, 1978.
- [19] Fédération Internationale du Béton (fib). *fib Model Code for Concrete Structures 2010*. Wilhelm Ernst und Sohn Verlag für Architektur, Berlin (Germany), 2013.
- [20] L. Ferrara and M. di Prisco. Three- vs. four-point bend tests: a numerical investigation on plain concrete, studi e ricerche, Politecnico di Milano. *Scuola di specializzazione in costruzioni in cemento armato, Italcementi*, 22:73–119, 2001.
- [21] N. M. Hawkins, D. A. Kuchma, R. F. Mast, M. L. Marsh, and K. H. Reineck. NCHRP report 549: simplified shear design of structural concrete members. Technical report, Transportation Research Board of The National Academies, 2005.
- [22] R. C. Hibbeler. *Sterkteleer. Achtste editie (in Dutch)*. Pearson, Benelux, 2012.
- [23] T. Hsu and L. X. Zhang. Nonlinear analysis of membrane elements by fixed-angle softened-truss model. *ACI Structural Journal*, 94(5):483–492, 1997.
- [24] F. Isla, G. Ruano, and B. Luccioni. Analysis of steel fibres pull-out. Experimental study. *Construction and Building materials*, 100:183–193, 2015.
- [25] Joint ASCE-ACI Task Committee 426 on Shear and Diagonal Tension of the Committee on Masonry and Reinforced Concrete of the Structural Division. The shear strength of reinforced concrete members. *Journal of Structural Division*, 99(6):1091–1187, 1973.

-
- [26] G. N. J. Kani. The riddle of shear and its solution. *ACI Journal Proceedings*, 61(4):441–467, 1964.
- [27] P. Lava, S. Cooreman, S. Coppeters, M. De Strycker, and D. Debruyne. Assessment of measuring errors in DIC using deformation fields generated by plastic FEA. *Optics and Lasers in Engineering*, 47(7-8):747–753, 2009.
- [28] P. Lava, S. Cooreman, and D. Debruyne. Study of systematic errors in strain fields obtained via DIC using heterogeneous deformation generated by plastic FEA. *Optics and Lasers in Engineering*, 48(4):457–468, 2010.
- [29] M. K. Lee and B. I. G. Barr. An overview of the fatigue behaviour of plain and fibre reinforced concrete. *Cement and Concrete Composites*, 26(4):299–305, 2004.
- [30] I. Löfgren. *Fibre-reinforced concrete for industrial construction - a fracture mechanics approach to material testing and structural analysis*. PhD thesis, Chalmers University of Technology, Göteborg, Sweden, 2005.
- [31] J. W. Luo and F. J. Vecchio. Behaviour of steel fiber-reinforced concrete under reversed cyclic shear. *ACI Structural Journal*, 113(1):75–84, 2016.
- [32] F. Minelli. *Plain and fiber reinforced concrete beams under shear loading: structural behaviour and design aspects*. PhD thesis, University of Brescia, Italy, 2005.
- [33] F. Minelli and G. A. Plizzari. On the effectiveness of steel fibres as shear reinforcement. *ACI Structural Journal*, 110(3):379–389, 2013.
- [34] E. Mondo. Shear capacity of steel fibre reinforced concrete beams without conventional shear reinforcement. Master’s thesis, Royal Institute of Technology KTH, Stockholm, Sweden, 2011.
- [35] E. Mörsch. *Der Eisenbetonbau - Seine Theorie und Anwendung*. Verlag von Konrad Wittwer, Stuttgart, 1908.
- [36] A. Muttoni, J. Schwartz, and B. Thurlimann. *Design of Concrete Structures with Stress Fields*. Birkhäuser/Springer, Basel (Switzerland), 1997.
- [37] A. E. Naaman. Engineered steel fibers with optimal properties for reinforcement of cement composites. *Journal of Advanced Concrete Technology*, 1(3):241–252, 2003.
- [38] E. Nakamura, A. R. Avendano, and O. Bayrak. Shear database for prestressed concrete members. *ACI Structural Journal*, 110(6):909–918, 2013.
- [39] A. Nanni. Fatigue behaviour of steel fiber reinforced concrete. *Cement and Concrete Composites*, 13(4):239–245, 1991.
- [40] NBN. NBN EN 1990: Basics of structural design, 2002.

- [41] NBN. NBN EN 1992-1-1 ANB: Design of concrete structures - Part1-1: General rules and rules for buildings, 2010.
- [42] NBN. NBN EN 1992-1-1 ANB in eurocode 2: Ontwerp en berekening van betonconstructies - deel 1-1: Algemene regels en regels voor gebouwen (in dutch) - national application document, 2010.
- [43] M. P. Nielsen and L. C. Hoang. *Limit analysis and concrete plasticity, 3rd edition*. CRC Press, Boca Raton, FL (USA), 2011.
- [44] H. G. Park, K. K. Choi, and J. K. Wight. Strain-based shear strength model for slender beams without web reinforcement. *ACI Structural Journal*, 103(6):783–793, 2006.
- [45] A. Parvez and S. J. Foster. Fatigue behaviour of steel-fiber-reinforced concrete beams. *ASCE Structural Engineering Journal*, 141(4):04014117, 2014.
- [46] A. Pompo, P. R. Stupak, L. Nicolais, and B. Marchese. Analysis of steel fibre pull-out from a cement matrix using video photography. *Cement and concrete Composites*, 18:3–8, 1996.
- [47] J. A. Ramirez and et al. ASCE-ACI Committee 445 on Shear and Torsion: Recent approaches to shear design of structural concrete. *Journal of Structural Engineering*, 124(12):1375–1417, 1998.
- [48] K. H. Reineck. Ultimate shear force of structural concrete members without transverse reinforcement derived from a mechanical model. *ACI Structural Journal*, 22(5):592–602, 1991.
- [49] K. H. Reineck. Shear design of members without transverse reinforcement in DIN 1045-1. Technical report, University of Stuttgart, University of Leipzig, TU München, 1999.
- [50] K. H. Reineck, E. C. Bentz, B. Fitik, D. A. Kuchma, and O. Bayrak. ACI-DAfStb database of shear tests on slender reinforced concrete beams without stirrups. *ACI Structural Journal*, 110(5):867–875, 2013.
- [51] K. H. Reineck, D. A. Kuchma, K. S. Kim, and S. Marx. Shear database of reinforced concrete beams without shear reinforcement. *ACI Structural Journal*, 100(2):240–2495, 2003.
- [52] K. H. Reineck and L. Todisco. Database with shear tests on non-slender reinforced concrete beams without stirrups. *ACI Structural Journal*, 111(6):1363–1371, 2014.
- [53] W. Ritter. Die bauweise hennebique. *Schweizerische Bauzeitung*, 33:41–61, 1899.
- [54] J. Romualdi and G. Batson. Mechanics of crack arrest in concrete. *ASCE Engineering Mechanics Journal*, 89(3):147–168, 1963.

-
- [55] J. Romualdi and J. Mandel. Tensile strength of concrete affected by uniformly distributed closely spaced short lengths of wire reinforcement. *ACI Journal*, 61(6):657–671, 1964.
- [56] S. Sarkar, O. Adwan, and B. Bose. Shear stress contributions and failure mechanisms of high strength reinforced concrete beams. *Materials and Structures*, 32:112–116, 1999.
- [57] J. Schlaich, K. Schafer, and M. Jennewein. Toward a consistent design of structural concrete. *Journal Prestressed Concrete Institute*, 32(3):74–150, 1987.
- [58] B. Schnütgen. *Das Festigkeitsverhalten von mit Stahlfasern bewehrtem Beton unter Zugbeanspruchung*. PhD thesis, Ruhr-Universität Bochum, Germany, 1975.
- [59] S. P. Shah and et al. ACI Committee 554: Report 554.4R-88: Design considerations for steel fiber reinforced concrete. Technical report, American Concrete Institute, 1988.
- [60] T. Soetens. *Design models for the shear strength of prestressed precast steel fiber reinforced concrete girders*. PhD thesis, Faculty of Engineering Science and Architecture, UGent, Belgium, 2015.
- [61] T. Soetens, A. Van Gysel, S. Matthys, and L. Taerwe. A semi-analytical model to predict the pull-out behaviour of inclined hooked-end steel fibres. *Construction and Building materials*, 43:253–265, 2013.
- [62] H. P. Taylor. The fundamental behavior of reinforced concrete beams in bending and shear. In *ACI Special Publication SP-42: Shear in Reinforced Concrete*, pages 43–78, 1974.
- [63] L. Todisco, K. H. Reineck, and O. Bayrak. Database with shear tests on non-slender reinforced concrete beams with vertical stirrups. *ACI Structural Journal*, 112(6):761–769, 2015.
- [64] L. Vandewalle. *Ontwerp van constructiecomponenten: Beton, deel 1 (in Dutch)*. CuDi VTK vzw, Faculty of Engineering, KU Leuven, 2010.
- [65] L. Vandewalle. *Berekening en deaïllering van constructies in spanbeton (in Dutch)*. CuDi VTK vzw, Faculty of Engineering, KU Leuven, 2014.
- [66] L. Vandewalle and D. Dupont. Dwarskrachtcapaciteit van staalvezel-betonbalken (in Dutch). *Cement*, 8, 2002.
- [67] L. Vandewalle and et al. RILEM TC162-TDF: Test and design methods for steel fibre reinforced concrete - Design of steel fibre reinforced concrete using the σ - ε -method. *Materials and Structures*, 33(226):75–81, 2000.

- [68] L. Vandewalle and et al. RILEM TC162-TDF: Test and design methods for steel fibre reinforced concrete - Design of steel fibre reinforced concrete using the σ - ε -method - Final Recommendation. *Materials and Structures*, 36(262):560–567, 2003.
- [69] F. J. Vecchio. Disturbed stress field model for reinforced concrete: Formulation. *Journal of Structural Engineering - ASCE*, 126(9):1071–1077, 2000.
- [70] F. J. Vecchio and M. P. Collins. The modified compression-field theory for reinforced-concrete elements subjected to shear. *Journal of the American Concrete Institute*, 83(2):219–231, 1986.
- [71] J. C. Walraven. *Aggregate interlock: a theoretical and experimental analysis*. PhD thesis, Technische Universiteit Delft, TU Delft, The Netherlands, 1980.
- [72] J. C. Walraven. Fundamental analysis of aggregate interlock. *Journal of Structural Division - ASCE*, 107(11):2245–2270, 1981.
- [73] Y. Yang. *Shear behaviour of reinforced concrete members without shear reinforcement. A new look at an old problem*. PhD thesis, Technische Universiteit Delft, TU Delft, The Netherlands, 2014.
- [74] S. H. Zhang, J. and V. C. Li. Fatigue life prediction of fiber reinforced concrete under flexural load. *Internal journal of fatigue*, 21(10):1033–1049, 1999.

Master thesis filing card

Student: Maure De Smedt

Title: Experimental and analytical analysis of the shear capacity of prestressed steel fibre reinforced concrete beams

Dutch title: Experimentele en analytische analyse van de dwarskrachtcapaciteit van voorgespannen staalvezelversterkte betonbalken

UDC: 69

Abstract:

Steel fibre reinforced concrete (SFRC) is a cementitious composite material, consisting of a concrete matrix with discrete, randomly distributed steel fibres. Its application can be cost- and time-effective by (partially) replacing the conventional reinforcement. Despite the wide research and the continuously increasing structural applications of SFRC, the use is still restricted with respect to its potentials. This is mainly caused by the incomplete understanding of the complex behaviour and the lack of analytical models and international building codes for SFRC structural elements, specifically in the case of shear behaviour.

This research therefore aims to contribute to the understanding of the mechanical shear behaviour of prestressed SFRC beams, based on experimental and analytical investigations. Six beams are subjected to a four-point bending test. The main investigated parameters are (1) steel fibre dosage, (2) the amount of prestressing and (3) the amount of shear reinforcement. Not only failure mode and load are observed, but also shear behaviour is considered by deformations, displacements and cracking pattern properties during the loading. Both conventional measurement devices (i.e. demountable mechanical strain gauges, linear variable differential transformers and optical photoelectric sensor) and advanced optical techniques (Bragg grating optical fibres and stereo-vision digital image correlation) are used. Additionally, material identification tests are performed to characterise the material properties.

The experimentally determined results are analysed by a parameter study and a crack load discussion. Increasing the fibre dosage results in a larger post-cracking behaviour, a more gradual energy dissipation and an increased shear capacity. Increasing the prestress level results in an extended elastic region, a lower inclination of cracks and an increased shear capacity. Furthermore, the failure loads are compared to predictions using analytical models found in Eurocode 2, Model Code 2010, DRAMIX Guideline, RILEM, CNR and the model proposed by Soetens. All calculations of the shear capacity underestimate the actual failure load. The underestimation increases for a higher prestress level. In some models, the influence of a higher fibre dosage is better estimated and vice versa for others. Omitting partial safety factors and using mean material properties, an average experimental-to-predicted failure load ratio of 1.43 was found with a coefficient of variation of 7.2% for Eurocode 2 and Model Code 2010. The other models differ in shear design approach and including parameters, resulting in varying mean experimental-to-predicted ratios and model uncertainties.

BIBLIOGRAPHY

Thesis submitted for the degree of Master of Science in de Ingenieurswetenschappen:
Bouwkunde, optie Civiele Techniek

Thesis supervisors: Prof. dr. ir. L. Vandewalle
Dr. ir.-arch. K. De Wilder

Assessors: Ing. P. van der Zee
Ing. A. Hoekstra

Mentor: Dr. ir.-arch. K. De Wilder